UNIVERSITÀ DEGLI STUDI DI TRIESTE

XXIX CICLO DEL DOTTORATO DI RICERCA IN CHIMICA

FUNCTIONALISATION OF CARBON NANOSTRUCTURES TOWARDS HYBRID MATERIALS FOR DIFFERENT APPLICATIONS

Settore scientifico-disciplinare: CHIM/06

DOTTORANDO
DANIEL IGLESIAS ASPERILLA

COORDINATORE
CHIAR.MO PROF. MAURO STENER

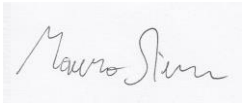

SUPERVISORE DI TESI
CHIAR.MO PROF. MAURIZIO PRATO

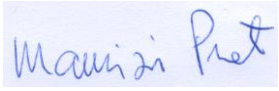

CO-SUPERVISORE DI TESI
DR. SILVIA MARCHESAN

ANNO ACCADEMICO 2015/2016

Acknowledgements

I am grateful to my supervisor Prof. Maurizio Prato for giving me the opportunity to develop my PhD thesis in such an inspiring environment. Sharing scientific knowledge and experiences with people from Italy, Spain, Greece, Argentina, France, Poland, Slovenia, Croatia, India, Japan, Russia, Mexico, Peru and China was just amazing.

I am especially grateful to Dr. Silvia Marchesan who co-directed this work. Thank you for transmitting me your enthusiasm and experience during these three years.

This thesis would had never happened without the help of collaborators. I am grateful to Thomas Swan Co., Ltd. for supplying the multi-walled carbon nanotubes and graphene used in the thesis. All CARINHYPH partners are acknowledged for their contribution in Chapter 2. My sincere thanks to Dr. Juan José Vilatela and his Group who made me feel at home during my periods at IMDEA Materials. Thanks to Alicia Moya and Dr. Laura Cabana, with whom I worked side by side.

I am grateful to Angela Giuliani and Dr. Michele Melchionna for their strong collaboration in the development of Chapter 3. I would like to extend the acknowledgements to Prof. Paolo Fornasiero and Prof. Claudio Tavagnacco for their constant help and support. Thanks Alessadro Beltram for your assistance with the thermal treatments. Thanks also Dr. Alejandro Criado for the XPS analyses.

Thanks to Prof. Mario Grassi, Prof. Romano Lapasin and Michela Abrami for their collaboration in the rheological part and their fruitful discussions.

I am grateful to the University Technical Support and Professors. Fabio Hollan performed the MS analyses. Thanks Claudio Gamboz and Paolo Bertoncin for your valuable TEM lessons. Thanks Manuela Bisiacchi for your patience and help in day-to-day activities.

Research can be sometimes discouraging, but getting over these moments is much easier if the best people surround you. Big thanks to Prato's Group and the new Superstructures Lab for making my life easier.

‘Grazie mille’ to Grillo, Stefano, Susanna, Luigi, Manuela, Bertoncin, Tanja and Fabri who helped me to understand the citizens of the intriguing city of Trieste.

‘Merci beaucoup’ to Caro for your many trainings and the great moments we lived outside the lab. Meryló, Ana, Álex, Adrian, Clarence, Cristina (Jerez), Jose, Arturo, Núria, Manu, Jenny, Francesco, Angela, Michele, Martu, Mauro, Alice, Eva, Marina, Cristina and many others for being my family during these years.

I look back to thank the Department of Organic Chemistry of the University of Castilla-La Mancha where everything begun. I am especially grateful to Dr. Pilar Prieto and Dr. Maria Antonia Herrero for their lessons at the very beginning. Thanks Marian also for placing your trust in me.

I wish to thank my parents and my family for their unconditional support.

I am most grateful to Ana. I have no words to thank your support during this adventure and I am looking forward to share new ones with you.

Muchas gracias,

Dani

Table of Contents

List of abbreviations

A	Anatase
AFM	Atomic Force Microscopy
ALD	Atomic Layer Deposition
AMRSF	Average Matrix Relative Sensitivity Factors
ATR-IR	Attenuated Total Reflectance InfraRed spectroscopy
BE	Binding Energy
BET	Brunauer–Emmett–Teller
BJH	Barrett-Joyner-Halenda
C_{60}	Fullerene made of 60 C atoms
C_{70}	Fullerene made of 70 C atoms
CARINHYPH	CARbon INorganic HYbrids for PHotocatalysis
CB	Conduction Band
CD	Circular Dichroism
CNH	Carbon Nanohorn
CNS	Carbon Nanostructure
CNT	Carbon Nanotube
CPL	Circularly Polarised Light
CV	Cyclic Voltammetry
CVD	Chemical Vapour Deposition
DC	Direct Current
DIPEA	*N*,*N*-Diisopropylethylamine
DMF	*N*,*N*-dimethylformamide
DNA	Deoxyribonucleic acid
DWCNT	Double-Walled Carbon Nanotube
EDLCs	Electrodes for all-solid and flexible electric double layer capacitors
EDX	Electron Dispersive X-ray
EIS	Electrochemical Impedance Spectroscopy
ES-MS	Electrospray Mass Spectrometry
Et_2O	Diethyl ether
EtOH	Ethanol
f-CNS	Functionalised CNS
FE	Faradaic Efficiency
Fmoc	Fluorenylmethyloxycarbonyl
FWHM	Full width at half maximum
G	Graphene
G'	Elastic or storage modulus
G"	Viscous or loss modulus
GCB	Graphitised Carbon Black
GCE	Glassy Carbon Electrode
GO	Graphene Oxide
HAADF-STEM	High Angle Annular Dark Field Scanning TEM

HBTU	*N,N,N′,N′*-Tetramethyl-*O*-(1*H*-benzotriazol-1-yl)uronium hexafluorophosphate
HOMO	Highest Occupied Molecular Orbital
HPLC	High-Performance Liquid Chromatography
ICP-OES	Inductively Coupled Plasma Optical Emission Spectroscopy
IR	Infrared
LbL	Layer-by-Layer
LCPL	Left Circularly Polarised Light
LUMO	Lowest Occupied Molecular Orbital
MB	Methylene Blue
MeOH	Methanol
MGC	Minimum Gelation Concentration
MO_x	Metal Oxides
MW	Microwaves
MWCNT	Multi-Walled Carbon Nanotubes
NIR	Near Infrared
NMR	Nuclear Magnetic Resonance
NP	Nanoparticle
ORR	Oxygen Reduction Reaction
PBS	Phosphate Buffered Saline
PDA	Polydopamine
PEG	Polyethylene glycol
pI	Isoelectric point
POZ	Primary ozonide
PSS	Poly(sodium 4-styrenesulphonate)
PVP	Polyvinyl pyrrolidone
R	Rutile
r.t.	Room temperature
RCPL	Right Circularly Polarised Light
RDE	Rotating Disc Electrode
RGO	Reduced Graphene Oxide
RHE	Reference Hydrogen Electron
RMB	Radial Breathing Mode
RRDE	Ring Rotating Disc Electrode
SAEDP	Selected Area Electron Diffraction Pattern
SEM	Scanning Electron Microscopy
SPPS	Solid-Phase Peptide Synthesis
SWCNT	Single-Walled Carbon Nanotube
TBOT	Tetrabutyl titanate
TEM	Transmission Electron Microscopy
TEOS	Tetraethoxysilane
TFA	Trifluoroacetic acid
TGA	Thermogravimetric analysis
TIPS	Triisopropylsilane
TPAOH	Tetrapropylammonium hydroxide

TS-1	Zeolite synthesised from silica and titania precursors
UHV	Ultra-High Vacuum
UV	Ultraviolet irradiation
UV-Vis	Ultraviolet-visible irradiation
VB	Valence Band
XPS	X-ray Photoelectron Spectroscopy
XRD	X-ray Diffraction

Abstract

During the last three decades, great scientific efforts led to the discovery and development of new carbon nanomaterials (*e.g.* carbon nanotubes or CNTs, carbon nanohorns or CNHs, and graphene or G). In the first chapter of this thesis, a general introduction on carbon nanostructures (CNS) and relevant characterisation techniques is provided (Chapter 1).

Despite their superior electrical, thermal, and mechanical properties, CNS inherent tendency to aggregate initially limited their applications. This issue can be addressed by various chemical functionalisation routes to improve their dispersibility in water and in polar solvents, thus allowing their handling in liquid phase, and their combination with other chemical entities. Assembly of such multicomponent nanomaterials considerably expands CNS use in fields ranging from biology to energy. In this work, CNS were functionalised to be combined with components of different nature into hybrids or composites for diverse applications.

In particular, Chapter 2 discusses the modification of CNTs and G via acid-mediated oxidation or diazo coupling routes to add hydrophilic appendages that favour *in situ* growth of metal oxide nanostructures (*e.g.* TiO_2). The resulting nanohybrids were tested for photocatalytic hydrogen production. Oxidation of CNT fibres (CNF) was also achieved, first through wet methods, and then by treatment with UV-generated ozone, with only the latter allowing preservation of their macroscopic integrity. The resulting hydrophilic CNF displayed enhanced performance for supercapacitors.

Chapter 3 focusses on *in situ* polymerisation of dopamine on the surface of CNTs and CNHs. The synthetic protocol was optimised to achieve homogeneous coatings that, after graphitisation through high temperature treatment under argon, became conductive. This two-step sequence resulted in the isolation of N-doped CNHs that catalysed the electrochemical reduction of O_2 into H_2O_2 with superior performance relative to current state-of-the-art catalysts.

Finally, hydrogel composites were prepared from either CNTs, CNHs, or G and a self-assembling tripeptide (Chapter 4). After an oxidative pre-treatment, each CNS was combined with the peptide and formed supramolecular hydrogels of improved rheological

properties (*i.e.* increased stiffness and resistance to applied stress). Interestingly, hydrogels containing CNTs showed self-healing capacity, thus opening a new window of application for these materials.

Riassunto

Negli ultimi trent'anni, abbiamo assistito alla scoperta e sviluppo di nuovi nanomateriali di carbonio (ad esempio, nanotubi o CNT, nanocorni o CNH e graphene o G). Nel primo capitolo di questa tesi viene fornita una introduzione sulle nanostrutture di carbonio (CNS) e sulle più comuni tecniche per caratterizzarle.

Nonostante le loro superiori properietà elettroniche, termiche e meccaniche, la loro tendenza ad aggregarsi ne ha inizialmente ostacolato l'uso. Questo limite può essere superato tramite funzionalizzazione chimica, di cui ne esistono diversi tipi, al fine di migliorarne la dispersiblità in acqua e in solvent polari, e permetterne la processabilità in fase liquida al fine di combinarli con altre entità molecolari di vario genere. L'assemblaggio di tali nanomateriali a più componenti permette di allargare il range applicativo delle CNS in vari ambiti (dalla biologia all'energia). In questo lavoro, le CNS sono state funzionalizzate e combinate con componenti di diversa natura in modo da generare materiali ibridi o compositi per varie applicazioni.

In particolare, nel Capitolo 2 viene discussa la modificazione di CNT e G attraverso protocolli ossidativi in acido o mediante reazione di diazocopulazione per introdurre gruppi idrofilici che favoriscano la crescita *in situ* di nanostrutture di ossidi di metalli (ad es. TiO_2). Gli ibridi così ottenuti sono stati testati per la produzione fotocatalitica di idrogeno. Il protocollo ossidativo è stato esteso alle nanofibre di CNT (CNF), prima in fase liquida, e poi con gas ozono prodotto da irradiazione UV. Solo quest'ultimo metodo ha mantenuto l'integrità della morfologia macroscopica delle CNF, che sono risultate più idrofiliche e hanno dimostrato ottime proprietà per l'uso in supercondensatori.

Il capitolo 3 si focalizza sull'ottimizzazione della polimerizzazione *in situ* di dopamina sulla superficie di CNT e CNH in modo da avere un rivestimento omogeneo che, in seguito a grafitizzazione ad alte temperature in atmosfera inerte, è diventato conduttivo. Questa sequenza a due step ha permesso la formazione CNH dopati con azoto che sono risultati essere eccezionali catalizzatori per la riduzione elettrochimica di ossigeno ad acqua ossigenata, con performance superiori rispetto agli esistenti catalizzatori stato dell'arte.

Infine, idrogel compositi sono stati ottenuti da CNT, CNH o G e un tripeptide in grado di auto-organizzazione supramolecolare. In seguito ad un pre-trattamento ossidativo, ogni CNS insieme al peptide ha formato idrogel con migliori proprietà reologiche (più rigidi e più resistenti a forze esterne). Inoltre, gli idrogel con CNT hanno dimostrato capacità di self-healing, che ne estende notevolmente le potenzialità applicative.

CHAPTER 1

Nanotechnology and carbon nanomaterials

1.1. Introduction

1.1.1. Nanotechnology and its impact on society

Nanotechnology introductions in scientific literature often quote the use of gold and silver nanoparticles (NPs) in the Roman Lycurgus cup, or the Egyptian blue pigment composed of single layers of calcium copper tetrasilicate.[1] However, nanomaterials are nowadays present in our everyday life, for instance, silver NPs are added to wound dressings or coatings for their antibacterial effect; titania NPs are a common ingredient in sunscreens, cosmetics, and even chewing gums and toothpastes.

Today, a countless variety of nanomaterials is available in literature. The nature of these materials presents a large diversity since they can be made of metals, metal oxides, polymers, carbon, dicalchogenides, etc. Remarkably, the library of nanomaterials is further enlarged thanks to the different nanomorphologies that they may form (*e.g.* round or square NPs, nanofilms or nanotubes). Moreover, the list would be even larger if we considered the structured nanomaterials formed by hierarchical organisation of multiple components. All these materials share in common the nanometric scale (*i.e.* 1-100 nm is the most agreed range for nanomaterials) in at least one of their dimensions. To put it in perspective, Figure 1.1 depicts object examples of different scalesize.

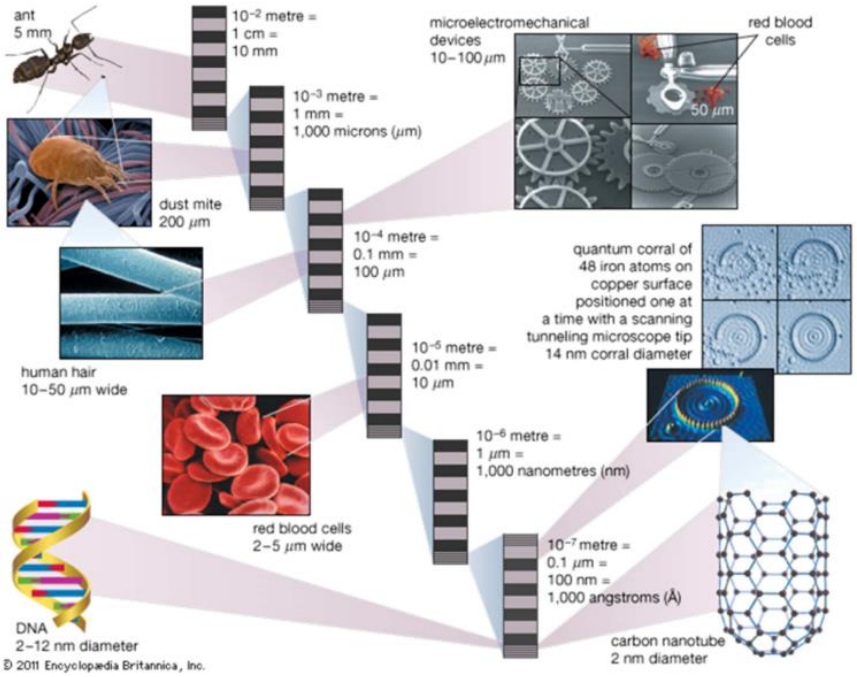

Figure 1.1. Examples of size of different objects from the milimetric to the nanometric scale.[2] Reprinted from (2) © 2011 Encyclopaedia Britannica.

1.1.2. Carbon nanomaterials

The advent of carbon nanomaterials had a great impact on nanotechnology. In 1985, James R. Heath, Sean O'Brien, Robert Curl and Richard Smalley discovered the Buckminsterfullerene, also called Bucky-ball or C_{60},[3] which is a spherical organic molecule composed of sixty sp^2 carbon atoms. It has often been considered as a 0D carbon nanomaterial and it proved useful especially in solar cells.[4] In 1991, a second push to the nanocarbon revolution was given by the discovery of carbon nanotubes (CNTs) by Iijima.[5] CNTs consist of a rolled-up layer of sp^2 carbon atoms (*i.e.* a graphene, G, sheet). The way in which the polyaromatic structure is rolled-up determines CNT properties, giving rise to metallic or semiconducting CNTs.[6] Besides, they can be formed by one, two, three or more concentric tubes in single-walled (SWCNTs), double-walled (DWCNTs), or multi-walled carbon nanotubes (MWCNTs), respectively. All these materials showed excellent thermal, mechanical and electronic properties and have been successfully used for various applications (*i.e.* photocatalysis, polymer reinforcement, flame retardants, etc.).[7] Isolation of G by Geim and Novoselov marked another key milestone since, until then, the 2D structure of G had been generally considered thermodynamically too unstable to be isolated.[8] This striking discovery opened a new

field of research with futuristic outcomes such as ultra-long-lasting batteries, super-efficient energy devices, flexible devices, etc.

A remarkable feature of carbon nanomaterials is the versatility of their outstanding performance (Figure 1.2). For instance, chemically modified C70 fullerene ([70] PCBM) blended with semiconducting polymers achieved the highest efficiency reported for bulk heterojunction solar cells.[9] Regarding biological applications, the combination of MWCNTs and gelatin afforded hybrid soft materials that allowed synchronous beating of cardiomyocytes that were grown into them.[10] With regards to mechanical properties, Qin *et al.* reported gyroids materials as dense as 4.6 % relative to mild steel, yet 10 times stronger.[11] The gyroids were 3D printed with G and VeroMagenta (*i.e.* a patented photo-reactive composition of polyacrylic precursors).

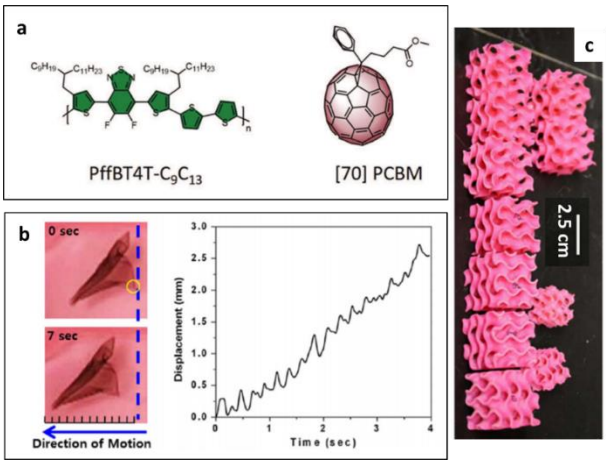

Figure 1.2. Examples of outstanding CNS performance: (a) semiconducting polymer and C_{60} derivative used for bulk heterojunction solar cells with 11.7% efficiency[9] Adapted with permissions from (4), © 2016 John Wiley and Sons[4]; (b) gelatin/CNT hydrogel hybrid seeded with rat cardiomyocytes that showed spontaneous synchronous beating[10]. Reprinted with permissions from (10). © 2013 American Chemical Society; and (c) image of the 3D printed G-based gyroids with superior mechanical properties.[11] Adapted from (11) © 2017 American Association for the Advancement of Science.

1.1.3. Terminology for graphene-related materials

There is debate regarding the terminology used to refer to carbon nanomaterials. Many authors refer to them as different carbon allotropes, while others prefer wording as carbon nanostructures (CNS), nanocarbon, G-based or G-related materials, The latter would appear appropriate considering a single layer of G as a sheet that can fold in different ways to give rise to all CNS (*e.g.* fullerenes, CNTs, carbon nanohorns (CNHs),

carbon nanoonions, carbon nanocones, Figure 1.3). It is worth noting that sp^2 carbon atoms shaping into curved morphologies is associated with higher strain (and reactivity)

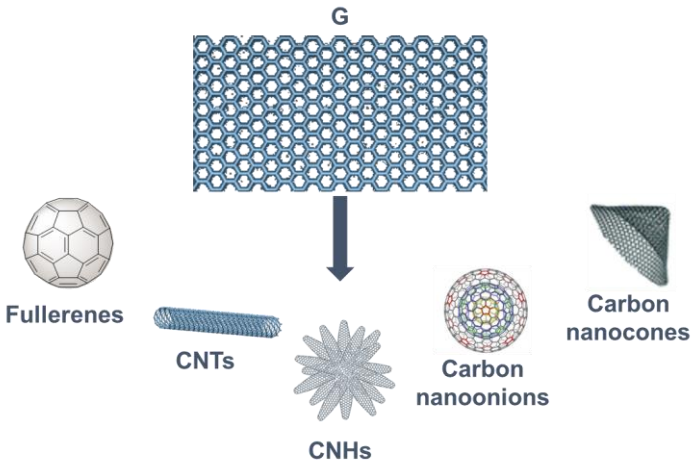

Figure 1.3. Schematic representation of G-based materials.

and, in extreme cases (*i.e.* tips, spheres), it may require presence of defects (*i.e.* pentagonal rings). Even though these materials are formed by G, they are rarely synthesised using it as a precursor. This PhD thesis focusses on the functionalisation, and the combination with other materials, of MWCNTs, CNT fibres (CNF), CNHs and G.

CNTs can be synthesised in different ways (*i.e.* arc discharge, laser ablation, chemical vapour deposition or CVD, flame pyrolysis, or in bottom-up approaches from organic molecules).[12] In the present study, high purity Elicarb® MWCNTs prepared by CVD were kindly supplied by Thomas Swan Co., Ltd. The typical tube diameter corresponded to 10-12 nm and the inorganic residue was <5%, due to traces of metal catalyst required for the synthesis. CNF were prepared by continuous spinning during CNT growth by CVD (for further details refer to Chapter 2. Section 3.3.).

CNHs are a less-known CNS that consists of horn-shaped, 30-50 nm long and 2-5 nm wide, SWCNTs that aggregate in spherical clusters.[13] They were produced by Carbonium S.R.L. by the Joule heating method, which does not require any metal catalyst and affords materials with neither amorphous carbon nor other graphitic impurities.[14] The absence of metal catalysts in the final material make CNHs very appealing for biological use (*e.g.* as gene delivery vectors)[15], and also interesting for energy (*i.e.* solar cells).[16]

The first preparation of G was carried out by ‘simply’ peeling off a single G layer from highly ordered pyrolytic graphite using scotch tape.[8] It is obvious that this approach

is not useful for the large scale production of pure G that is a key milestone to apply G in everyday life. G used in this project was kindly supplied by Thomas Swan Co., Ltd. and was prepared following a top-down approach by water exfoliation of graphite. This method afforded G whose large number of defects corresponded to edges and no to in-plane defects. Exfoliation of graphite in liquids is one of the most applied G production methods on large scale (Figure 1.4 a).[17]

The fact that G is often produced from graphite led to the imprecise definition of G as one of the layers that formed graphite. However, IUPAC stressed that the term graphite should not be used since it alludes to a 3D structure. To address this issue, *Carbon* (*i.e.* a recognised scientific journal specialised on CNS) published an editorial with appropriate definitions of G family members (*e.g.* G quantum dot, graphene oxide or GO, reduced graphene oxide or RGO, graphene nanoribbon, etc.).[18] G was defined as 'a single-atom-thick sheet of hexagonally arranged, sp^2-bonded carbon atoms that is not an integral part of a carbon material, but is freely suspended or adhered on a foreign substrate'. Scientists involved in the GRAPHENE Flagship European Project, designed to develop G-based materials and applications, noted recurrent imprecisions in literature in G-based materials nomenclature and called for a standardised system.[19] Wick *et al.* proposed a new way to define these new materials using two morphological aspects (*i.e.* the average lateral dimension and the number of stacked layers) and one chemical aspect (*i.e.* the C/O content), in a three-coordinate system (Figure 1.4 b).[19] Indeed, appropriate terminology is mandatory for correct comparison and reproduction of scientific data.

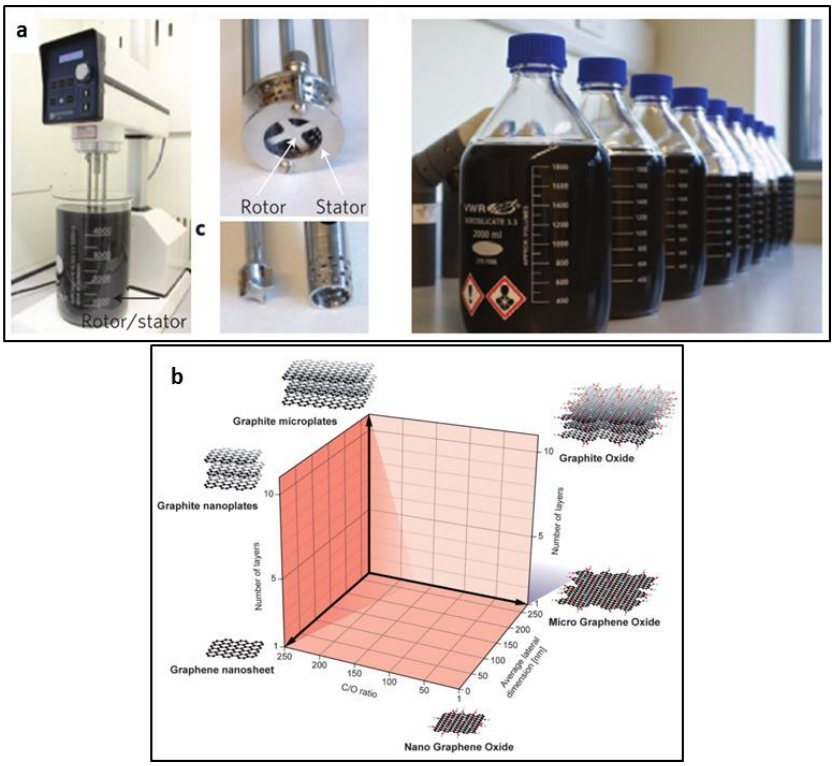

Figure 1.4. (a) Mechanical exfoliation of graphite to G showing (from left to right) the process, the utensils responsible of the shear exfoliation, and the large amounts of exfoliated G in solution.[17] **Reprinted by permission from MacMillan Publishers Ltd: Nature Materials (17) © 2014. (b) Proposed grid for the classification of G-based materials.**[19] **Reprinted with permission from (19) © 2013 John Wiley and Sons.**

Despite the great advantages of CNS, they are rarely used in their pristine form. This is due to low processability of CNS that are so hydrophobic to inevitably form aggregates in various forms, including: entangled CNT bundles, disordered CNH aggregates arising from Velcro-like interactions, and re-stacked G layers. This issue is usually resolved by CNS functionalisation, which can be covalent or non-covalent, as described in relevant chapters of this thesis (*i.e.* Chapter 2 and Chapter 3, respectively).

1.1.4. CNS-containing hybrid/composite materials

The preparation of multi-component nanostructured materials can be carried out in two different ways that lead to the formation of composites or hybrids (Figure 1.5). The differentiation of the two types starts from their synthesis. On one hand, nanocomposites are generally prepared by mechanical mixing of the nanostructure in the matrix of the main constituent of the material (*i.e.* CNS content is usually <5 % wt.). On the other hand, in the hybrids there is more parity in the ratio of the different components

and their synthesis happens *via* a designed interaction to generate a large interfacial contact. Hybrid synthesis can be addressed by *ex situ* or *in situ* approaches, as detailed in Chapter 3. Due to the more intimate contact, hybrids present new interfaces, which allow charge and energy transfers, thus improving or generating new properties. By contrast, nanocomposite properties are those of CNS (*i.e.* conductivity) added to those of the other component(s) (*i.e.* mechanically resistant polymers).

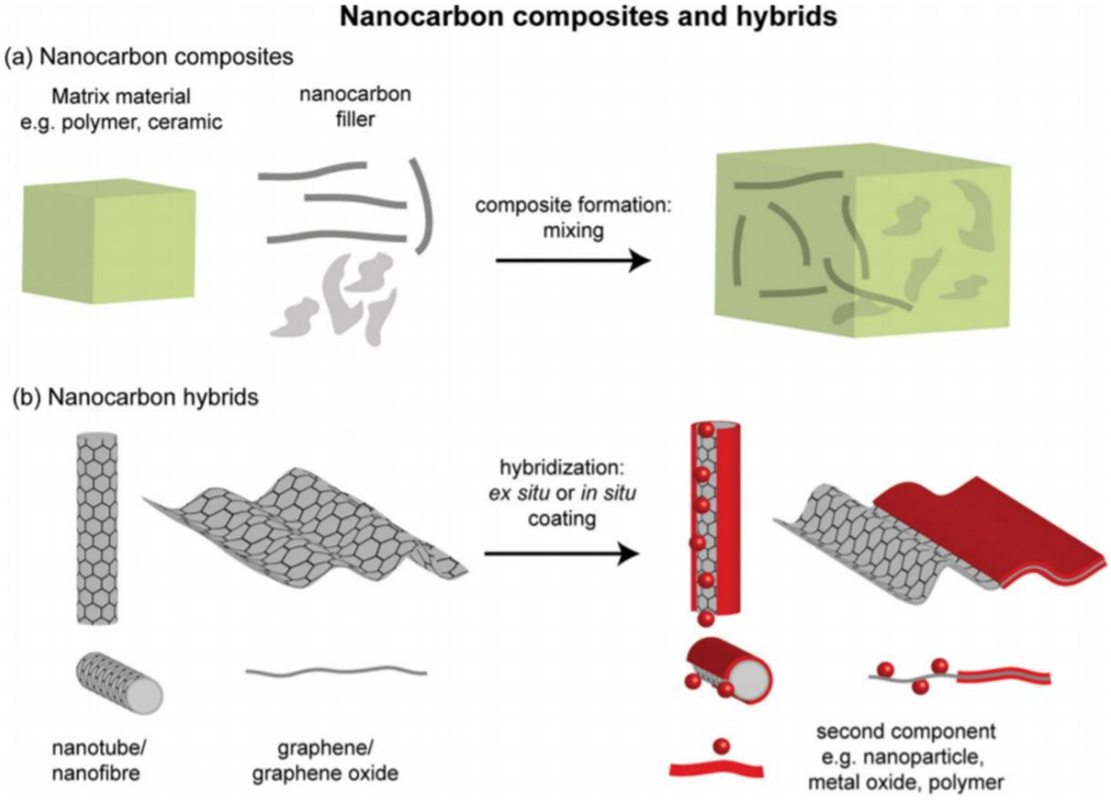

Figure 1.5. Schematic representation of different ways to combine CNS with other materials: (a) composites and (b) hybrids.[20] Reprinted with permissions from (20) © 2014 John Wiley and Sons.

1.2. Techniques used to characterise carbon nanomaterials

1.2.1. Thermogravimetric analysis (TGA)

In thermogravimetric analysis, a small sample (*e.g.* 1-10 mg) is introduced inside a furnace where temperature is increased, according to a specific program, and concomitantly the instrument monitors variations in the sample weight. The analysis can

be carried out under different atmospheres, being N_2 and air the most commonly used. In the case of carbon nanomaterials, both atmospheres are useful (Figure 1.6).

Under inert atmosphere, most pristine CNS are stable until high temperatures are reached. Functionalised CNS are less stable since the bonds formed in the functionalisation process are more labile. As a result, the degree of functionalisation can be estimated by comparison of the corresponding thermogram, with that of pristine CNS. The information extracted from a thermogram run in air is related to the thermal stability of the sample (*i.e.* temperature at which the material is calcined) or the amount of metal present in the sample (*i.e.* residue at high temperatures).

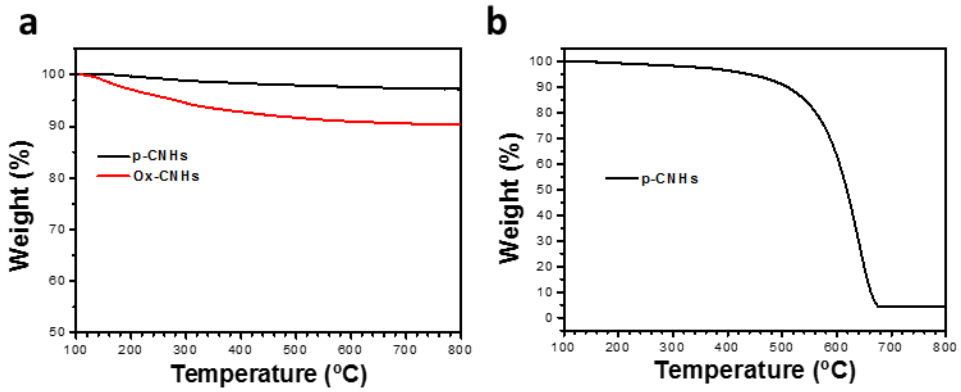

Figure 1.6. Example of a thermogram run under N_2 (a) and air (b).

1.2.2. Raman spectroscopy

This technique is one of the most powerful tools for CNS characterisation. However, there are other materials (*e.g.* metal oxides or peptides) that display Raman effect, which was first discovered by Prof. C. V. Raman that received the Nobel prize in physics in 1930. The Raman effect is observed when a sample, irradiated with photons at a certain frequency, scattered light at lower (Stokes scattering) or higher (anti-Stokes scattering) frequencies. These shifts are due to inelastic scattering and occur in a small fraction of incident photons, which are directly related with the phonons of the material (*i.e.* the quantised vibrational modes).

As a consequence of having similar chemical structure, all G-based nanomaterials (*i.e.* sp^2 carbon lattice) display similar Raman spectra (Figure 1.7). Common features are the so-called G-band and D-band at ~1580 cm^{-1} and ~1350 cm^{-1}. The G-band (so-called due

to its presence in graphite) is originated by the doubly degenerate E_{2g} mode.[21] The signal of this mode is affected by a number of factors, such as bond length, G interaction with other G layers, symmetry of sp^2 carbon atoms, and curvature.[22] The breathing modes of the hexagonal rings that form G originate the D-band, which is defect-related, since its activation necessitates a defect in the sp^2 lattice.[23] In some cases, the D'-band can be displayed at 1620 cm^{-1}. This band is also defect-related and appears after the interaction of the defect vibrational modes with the active modes of G.

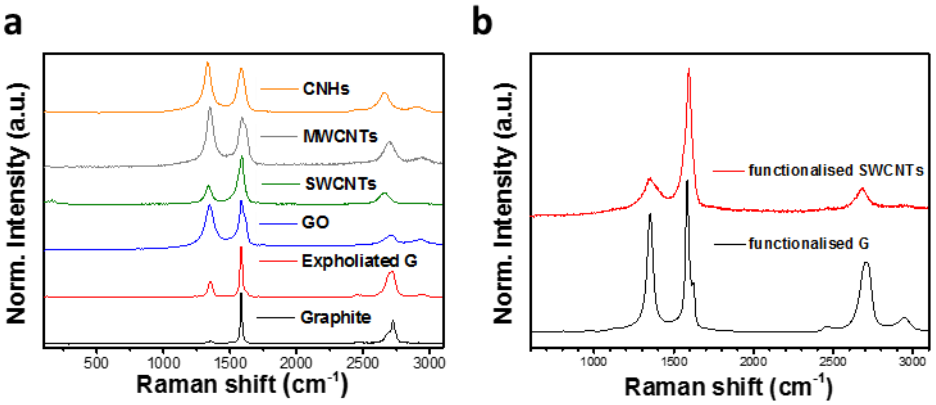

Figure 1.7. Raman spectra of pristine CNS used in this work (a) and functionalised G and SWCNTs (b). Raman spectrum of graphite was included as a reference material.

The intensity of the D band relative to the G band is used to assess the level of defects of these materials.[24] The so-called I_D/I_G ratio increases upon covalent functionalisation due to the introduction of sp^3 atoms in the carbon lattice, as exemplified by the increase of intensity of the D-band visible in G functionalisation. However, the D-band may have other contributions, such as the presence of amorphous carbon in conventional MWCNTs;[25] or the presence of heptagonal and pentagonal carbon rings needed for the formation of the tips in CNHs.[26]

Other relevant signals are the 2D band of G and the radial breathing mode (RBM) of SWCNTs. The 2D band of single-layer G appears at ~2700 cm-1. This mode is an overtone of the D-band and is a second order process where two inelastic processes are involved. The position of the band varies with the energy of the laser as its shape does with the number of stacked layers. Thus, the 2D band of single-layer G is composed of one single peak, while in few-layer G, the band can be deconvoluted in several components.[27,28] The RBM is a first order process that is due to the simultaneous stretching out-of-plane of all carbon atoms in a radial direction. This mode appears in the

100-500 cm^{-1} range and its exact position depends on the tube diameter. Besides, it gives information about chirality, electronic structure, and thus reactivity.[29]

1.2.3. UV-Vis spectroscopy

UV-Vis spectroscopy is one of the most common techniques used for various applications. In this work, it has been used in: i) peptide synthesis to calculate the initial loading of the resin and to follow the purification by HPLC; ii) to quantify the amount of primary amines as a way to confirm G functionalisation (*i.e.* Kaiser test); and iii) to assess the interaction between carbon nanomaterials and two different dyes.

The technique is based on light-mediated excitation of electrons to molecular orbitals with higher energy. Active functional groups are called chromophores and their position in a UV-Vis spectrum depends on the energy of the transition (*e.g.* $\sigma \rightarrow \sigma^*$, $\sigma \rightarrow \pi$, $\pi \rightarrow \pi^*$ depending on the orbitals involved). When sample concentration is appropriate, the Lambert-Beer law is followed, allowing analyte quantification.

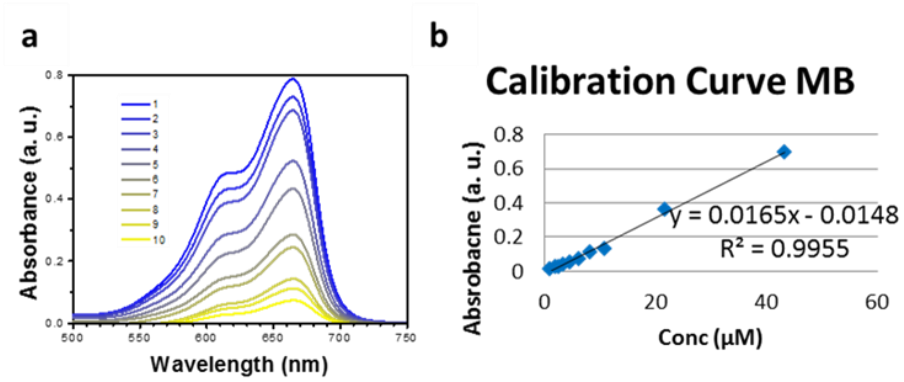

Figure 1.8. Visible light absorbance of methylene blue at different concentrations in water (a); calibration curve following Lambert-Beer law (b).

1.2.4. Infrared spectroscopy

Mid-infrared light is a low-energy radiation, of frequency within the 4000-400 cm^{-1} range, which is energetic enough to activate the vibrational modes of covalent bonds in a molecule (*i.e.* symmetric and asymmetric stretching, scissoring, rocking, wagging and twisting) giving rise to infrared spectroscopy. This technique is useful also for the characterisation of carbon nanomaterials, especially to confirm successful introduction of

characteristic functional groups upon functionalisation (*e.g.* azides), or when other techniques are not available. In particular, attenuated total reflectance infrared spectroscopy (ATR-IR) is a convenient mode for samples such as films that would otherwise be challenging to preserve during sample preparation for the traditional transmission mode. In ATR-IR, samples are pressed on top of a crystal (*e.g.* germanium or diamond), through which incident light is reflected on its path to the detector (Figure 1.9). Low sensitivity is an inherent limitation related to the low penetration of this mode.

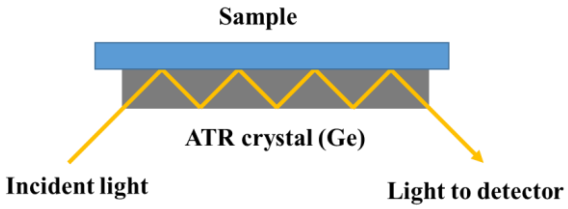

Figure 1.9. Schematic representation of the working mode of ATR-IR.

1.2.5 X-ray photoelectron spectroscopy

X-ray photoelectron spectroscopy (XPS) is a very useful technique in material science as it gives information about the chemical composition of the surface of the analysed material. In this technique, the sample is irradiated with an X-ray gun that is able to pull out the core level electrons, which eventually reach the detector. The fact that the core electrons are quantised, results in energy spectra whose peaks can be attributed to a characteristic electron structure. With high resolution equipment and mathematical data processing, we can get information not only on the atomic composition of the surface, but also on the chemical identity of the corresponding atoms.

Even though the X-ray gun is able to penetrate deep into the sample, this technique is usually used to characterised the surface (*i.e.* 10-30 nm depth, approximately). A drawback is that electrons ejected from the inner parts have many options to lose energy in their way out, which results in a high background signal rather than well-defined peaks. *Ad hoc* parameter settings and sample preparation are crucial to reduce this issue.

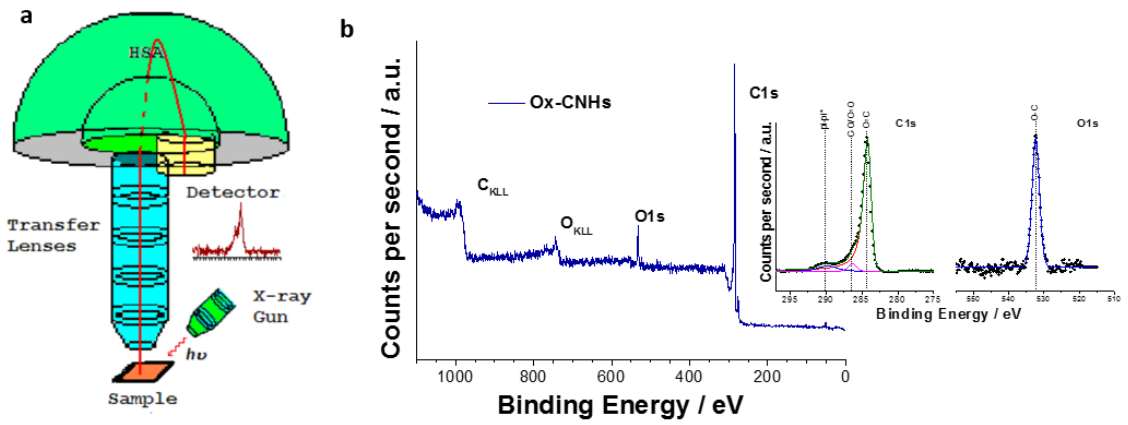

Figure 1.10. (a) Schematic representation of the XPS technique. . Reprinted from www.casaxps.com © 2013. (b) XPS survey spectrum and deconvolution of C1s and O1s peaks ox oxidised CNHs.

1.2.5. Microscopy techniques

The sizescale of nanomaterials necessitates high resolution microscopy techniques other than light microscopy. Popular techniques used are transmission electron microscopy (TEM) and scanning electron microscopy (SEM).

1.2.5.1.Transmission electron microscopy (TEM)

TEM allows the visualisation of samples with nanometric resolution. Samples are irradiated with a beam of electrons that will pass through the sample (*i.e.* transmission) and will eventually be detected by a camera, and processed by a software to create a 2D image. The interaction of the beam with the sample depends on its electron density: *e.g.* metal or metal oxide NPs have higher electron density that provides good contrast; organic matter has lower electron density that provides poor contrast. Besides, in case of organic matter other than CNS, sample decomposition due to irradiation may occur, requiring special care and *ad hoc* techniques.

Coupling the microscope with an Energy Dispersive Spectrometer allows the identification of the different elements that are present in the sample. This is very useful for core-shell materials, such as the coated CNHs prepared in Chapter 3.

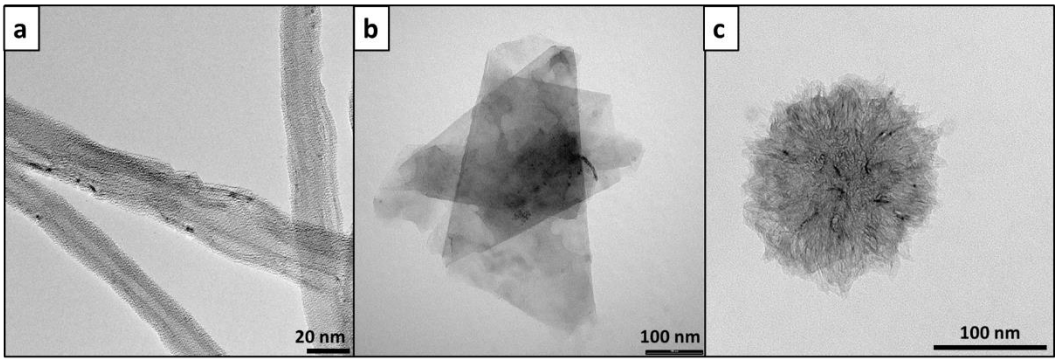

Figure 1.11. TEM images of some of CNS used in this work: (a) MWCNTs; (b) G; and (c) CNHs.

1.2.5.2.Scanning electron microscopy (SEM)

SEM is an electron microscopy technique used to study the surface topography of the analysed material at the micro and nanoscale. In this technique, the sample is irradiated with an electron beam and the image is generated from the electrons that the sample scatters.

A priori, any sample can be visualised by this technique without any specific pre-treatment, however, non-conductive samples get charged producing background signals. Thus, non-conductive samples require sputtering with a thin conductive material (*e.g.* gold) before imaging.

1.3. Thesis Outline

This thesis describes CNS functionalisation through different routes for the development of hybrid/composite materials for various applications. This research work is highly multidisciplinary and was possible thanks to several collaborations with other research groups with complementary expertise, as outlined in detail in each chapter. Besides, although CNS constitute the common core of all the nanomaterials described in this thesis, other components of various nature (*e.g.* metal oxide NPs, polymers, peptides) have been prepared too, and bound to the functionalised CNS. As a result, specific techniques other than those described in this chapter have been used for thorough material characterisation. The ones used more extensively by the PhD candidate (*e.g.* rheology)

are introduced in the relevant chapter, while those used mainly by collaborators are briefly mentioned.

Chapter 2 describes MWCNT, G and CNF covalent functionalisation using different routes to promote binding of metal oxide NPs into hybrids for photocatalytic applications. Chapter 3 describes MWCNT and CNH coating with polydopamine biopolymer for electrochemical applications. Chapter 4 describes MWCNT, CNH and G oxidation to allow for their incorporation into a self-assembled peptide hydrogel for biological use. Chapter 5 details the experimental sections relevant to the work described in the whole thesis. Where relevant, the use of various CNS allowed the investigation of CNS morphology impact on final nanomaterial preparation and performance, with the aim to identify the ideal CNS for the intended application.

1.4. References

(1) Johnson-mcdaniel, D.; Barrett, C. A.; Shara, A.; Salguero, T. T. *J. Am. Chem. Soc.* **2013**, *135*, 1677–1679.

(2) *Carbon Nanotub. Br. Encycl. Inc.* **2011**.

(3) Rooney, Cliona M, Rowe, M, Wallace, LE, Rickinson, A. *Nature* **1985**, *318*, 162–163.

(4) Martín, N. *Adv. Energy Mater.* **2016**, 1601102.

(5) Iijima, S. *Nature* **1991**, *354*, 56–58.

(6) Liu, H.; Tanaka, T.; Kataura, H.; Nishide, D. *Nat. Commun.* **2011**, *248*, 2524–2527.

(7) De Volder,Michael F. L. Sameh H. Tawfick, R. H. B. and; Hart, A. J.; De Volder, M. F. L.; Tawfick, S. H.; Baughman, R. H.; Hart, A. J. *Science* **2013**, *339*, 535–539.

(8) Novoselov, K. S.; Geim, A. K.; Morozov, S. V.; Jiang, D.; Zhang, Y.; Dubonos, S. V.; Grigorieva, I. V.; Firsov, A. A. *Science* **2004**, *306*, 666–669.

(9) Zhao, J.; Li, Y.; Yang, G.; Jiang, K.; Lin, H.; Ade, H.; Yan, H. *Nat. Energy* **2016**, *1*, n15027.

(10) Shin, S. R.; Jung, S. M.; Zalabany, M.; Kim, K.; Zorlutuna, P.; Kim, S.; Nikkhah, M.; Khabiry, M.; Azize, M.; Kong, J.; Wan, K.; Palacios, T. *ACS Nano* **2013**, *3*, 2369–2380.

(11) Qin, Z.; Jung, G. S.; Kang, M. J.; Buehler, M. J. *Sci. Adv.* **2017**, *3*, e1601536.

(12) Prasek, J.; Drbohlavova, J.; Chomoucka, J.; Hubalek, J.; Jasek, O.; Adam, V.; Kizek, R. *J. Mater. Chem.* **2011**, *21*, 15872–15874.

(13) Iijima, S.; Yudasaka, M.; Yamada, R.; Bandow, S.; Suenaga, K.; Kokai, F.; Takahashi, K. *Chem. Phys. Lett.* **1999**, *309*, 165–170.

(14) Carbonium SRL. http://www.carbonium.it http://www.carbonium.it (accessed Jan 28, 2017).

(15) Guerra, J.; Herrero, M. A.; Vázquez, E. *Rsc Adv.* **2014**, *4*, 27315–27321.

(16) Costa, R. D.; Feihl, S.; Kahnt, A.; Gambhir, S.; Officer, D. L.; Wallace, G. G.; Lucio, M. I.; Herrero, M. A.; Vázquez, E.; Syrgiannis, Z.; Prato, M.; Guldi, D. M. *Adv. Mater.* **2013**, *25*, 6513–6518.

(17) Paton, K. R.; Eswaraiah Varrla, C. B.; Ronan J. Smith, Umar Khan, Arlene O'Neill, Conor Boland, Mustafa Lotya, Oana M. Istrate, Paul King, Tom Higgins, Sebastian Barwich, Peter May, Pawel Puczkarski, Iftikhar Ahmed, Matthias Moebius, Henrik Pettersson, Edmund Long, João Coelho, Sean E. O'Brien, V. N.; Coleman, J. N. *Nat. Mater.* **2014**, *13*, 624–630.

(18) Bianco, A.; Cheng, H.-M.; Enoki, T.; Gotosi, Y.; Hurt, R.; Koratkar, N.; Kyotani, T.; Monthioux, M.; Park, C. R.; Tacson, J.; Zhang, J. *Carbon* **2013**, *5*, 1–6.

(19) Wick, P.; Louw-Gaume, A. E.; Kucki, M.; Krug, H. F.; Kostarelos, K.; Fadeel, B.; Dawson, K. A.; Salvati, A.; Vázquez, E.; Ballerini, L.; Tretiach, M.; Benfenati, F.; Flahaut, E.; Gauthier, L.; Prato, M.; Bianco, A. *Angew. Chemie Int. Ed.* **2014**, *53*, 7714–7718.

(20) Shearer, C. J.; Cherevan, A.; Eder, D. *Adv. Mater.* **2014**, *26*, 2295–2318.

(21) Ferrari, A. C.; Meyer, J. C.; Scardaci, V.; Casiraghi, C.; Lazzeri, M.; Piscanec, S.; Novoselov, K. S.; Roth, S.; Geim, A. K. *Phys. Rev. Lett.* **2006**, *97*, 187401–187405.

(22) Dresselhaus, M. S.; Jorio, A.; Hofmann, M.; Dresselhaus, G.; Saito, R. *Nano Lett.* **2010**, *10*, 751–758.

(23) Klar, P.; Lidorikis, E.; Eckmann, A.; Verzhbitskiy, I. a.; Ferrari, a. C.; Casiraghi, C. *Phys. Rev. B* **2013**, *87*, 205435.

(24) Graupner, R. *J. Raman Spectrosc.* **2007**, *38*, 673–683.

(25) Lehman, J. H.; Terrones, M.; Mansfield, E.; Hurst, K. E.; Meunier, V. *Carbon* **2011**, *49*, 2581–2602.

(26) Peña-Álvarez, M.; del Corro, E.; Langa, F.; Baonza, V. G.; Taravillo, M. *RSC Adv.* **2016**, 49543–49550.

(27) Park, J. S.; Reina, A.; Saito, R.; Kong, J.; Dresselhaus, G.; Dresselhaus, M. S. *Carbon* **2009**, *47*, 1303–1310.

(28) León, V.; Quintana, M.; Herrero, M. A.; Fierro, J. L. G.; Hoz, A. D. La; Prato, M.; Vázquez, E. *Chem. Commun.* **2011**, *47*, 10936.

(29) Dresselhaus, M. S.; Dresselhaus, G.; Saito, R.; Jorio, A. *Phys. Rep.* **2005**, *409*, 47–99.

CHAPTER 2

Covalent functionalisation of carbon nanostructures for photocatalysis and energy applications

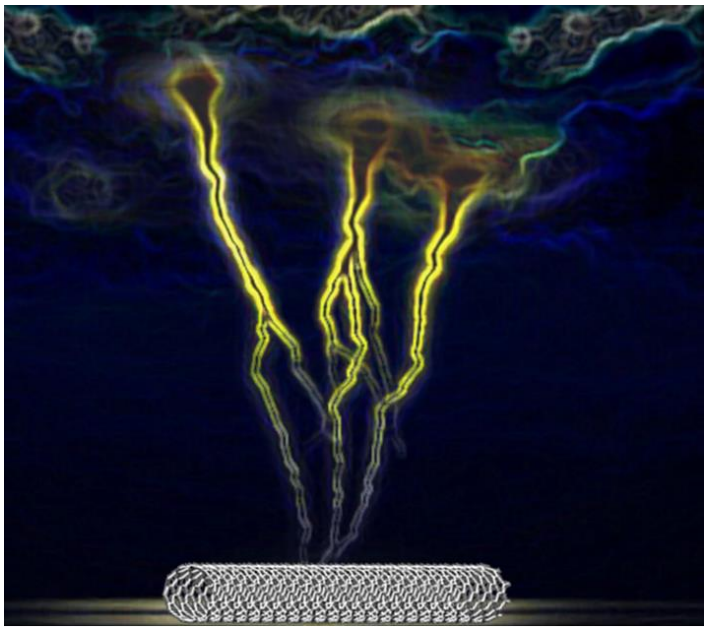

2.1. Introduction

Nowadays, implementation of green energy production methods and access to clean water have been identified as worldwide issues that must be addressed. The scientific community is called to join forces through multidisciplinary approaches to find viable solutions, and photocatalysis is emerging as an useful approach of versatile use.

In a photocatalytic protocol, a reaction rate is accelerated by a light-activated catalyst. Activation occurs after promotion of an electron from the HOMO to the LUMO band, with consequent generation of a hole in the HOMO band. The required incidental light energy thus depends on the HOMO-LUMO gap. The majority of photocatalysts reported in literature is composed of particles of reduced size (*e.g.* metal nanoparticles or NPs, metal oxides, zeolites, etc.), as opposed to discrete small molecules, thus, it is more correct to refer to these bands as valence band (VB) and conduction band (CB).

In terms of applications, photocatalysts have already proven to be useful in a variety of processes. For instance, with regards to water purification, several materials have been used to degrade pollutants such as dyes or drugs (*e.g.* methylene blue or ciprofloxacin, respectively).[1,2] Another key process where photocatalysts find use is water splitting for the production of H_2, a powerful energy vector. In this regard, it should be noted that even though many authors refer to H_2 production as water splitting, alcohols such as ethanol or methanol are usually added as sacrificial agents to trap the holes, and thus to prevent water oxidation. Therefore, 'hydrogen evolution' reaction appears as a more appropriate term when the molar ratio H_2:O_2 does not meet 2:1.

However, before realising the prediction by Jules Verne on *The Mysterious Island* (1874), in which the author foresaw that 'water will be the coal of the future', photocatalysts must be optimised. High chemical stability towards corrosion, and light absorbance in an adequate range (ideally including visible light), are two key requirements that the ideal catalyst should fulfill.

Nanotechnology plays a key role in the synthesis of innovative photocatalysts. Reducing particle size to the nanoscale is useful to: i) increase the surface area for the

reactants to interact with the catalyst active sites;[3] ii) shorten charge-transfer distances;[4] and iii) engineer the band-gap that may shift the absorption band towards visible light.[5]

2.1.1. CNS-inorganic hybrids

In addition to the use of nanosized photocatalysts, incorporation of a second or third component is an attractive approach to overcome inherent limitations of existing photocatalysts. In particular, combination of CNS and metal oxides such as TiO_2 has proven to enhance catalytic activity.[6] This effect was reported even when the presence of CNS reduced the surface area of TiO_2 suggesting that CNS do not simply act as scaffolds, but they also play a role in the catalytic process.[6] It is thus clear that the approach used to combine CNS and photocatalysts will affect the material properties and its performance.

Hybrids can be achieved by using similar volumetric fractions of different components, both *via ex situ* and *in situ* approaches. By contrast, nanocomposites arise when very different volume fractions are used, so that one component is dispersed in the other. Ideally, an intimate and homogeneous contact between components is desirable, while the presence of aggregates should be avoided. To this end, techniques such as chemical vapour deposition (*i.e.* CVD), sputtering, dip-coating, and wet impregnation are evolving rapidly to improve hybridisation. Research products are thus evolving from not homogenous towards highly homogeneous hybrids as shown in Figure 2.1.

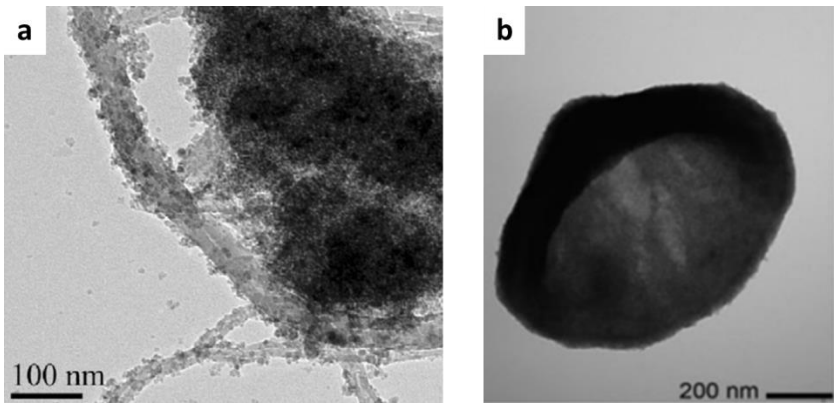

Figure 2.1. (a) TEM images of not homogenous TiO_2/CNTs hybrid.[7] Adapted from Ref. (7) with permission from Elsevier; and (b) very homogenous ox-CNC/Pd@TiO_2 (b).[8] Reproduced from (8) with permission of The Royal Society of Chemistry.

2.1.1.1.*Ex situ* approaches

Ex situ methods are understood as the combination of preformed materials. Major advantages include ease of preparation, and high control over the properties especially of the non-carbonaceous components (*e.g.* NP morphology or size distribution). For instance, cubic Pt NPs first synthesised by Xu *et al.*[9] were hybridised with MWCNTs for electrochemical oxygen reduction (Figure 2.2).[10] In this case, MWCNTs were previously functionalised with poly(sodium 4-styrenesulphonate) (*i.e.* PSS, a negatively charged polymer) for electrostatic interaction with the cationic shell of Pt nanocubes.

Alternatively, *ex situ* hybridisation can be promoted by hydrophobic forces or covalent binding. For instance, Rahman *et al.* exploited the hydrophobic shell of alkanethiolate-coated gold NPs synthesised by the Brust-Schiffrin and Murray method, to form hybrids with air-oxidised SWCNTs or MWCNTs.[11] Hybridisation resulted in a strong electronic interaction between the metal and the CNTs, with the gold NPs behaving as electron acceptors. Alternatively, covalent functionalisation can be achieved, for example *via* diazo coupling, by terminating the coating of the inorganic NPs with aryl diazonium species. Another popular approach exploits carboxylic groups on the CNS surface that can be introduced by means of oxidation. For instance, He *et al.* linked magnetic Fe_3O_4 NPs to GO by amide coupling for water purification.[12]

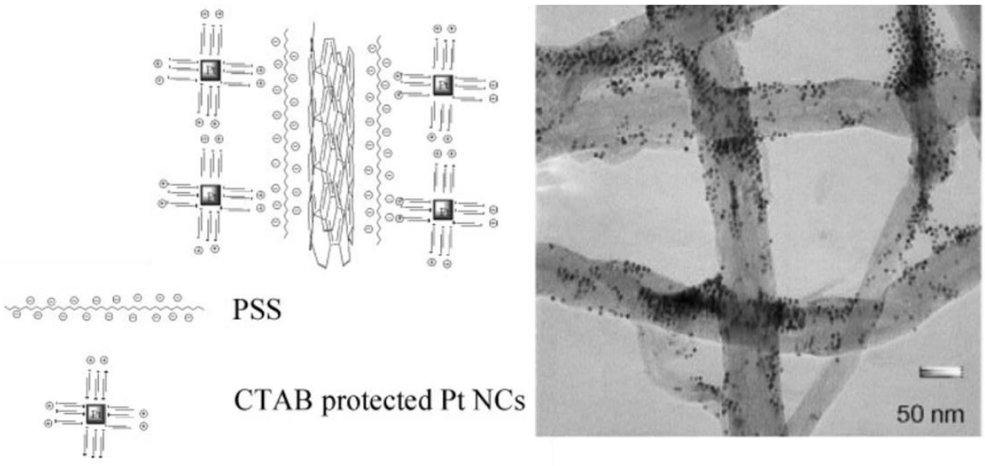

Figure 2.2. Schematic representation (a) and TEM image (b) of the hybrid composed of MWCNTs and Pt cubic NPs. Adapted with permissions from (10), Copyright 2014 John Wiley and Sons.

2.1.1.2.*In situ* approaches

This method involves the formation of one component in the presence of the other, and will be described in Chapter 3 for the *in situ* growth of polydopamine. By contrast, the focus of this chapter is on CNS hybridisation with inorganic components.

As illustrated in Figure 2.3, there are three main ways to carry out *in situ* hybridisation using: i) reduction of metal salts/complexes; ii) sol-gel process; and iii) atomic layer deposition (ALD).[13] The appropriate choice will vary based upon the characteristics of the different components.

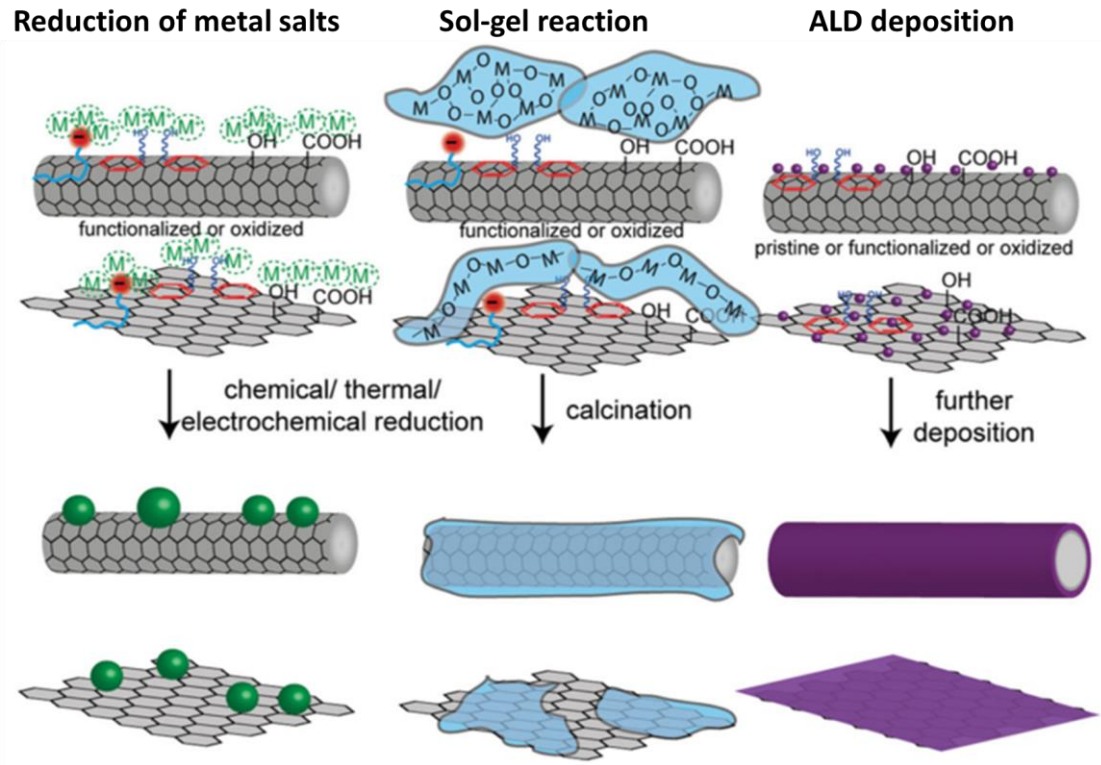

Figure 2.3. Most common ways of *in-situ* growth of inorganic materials on CNS. Adapted with permissions from (13), Copyright 2014 John Wiley and Sons.

For instance, water-soluble inorganic metal salts (*e.g.* $HAuCl_3$,[14] $FeCl_3$,[15] etc.) have been used as precursors of gold or iron oxide NPs. Reduction can be promoted by UV-light and heat, or chemicals (*e.g.*, sodium citrate, $NaBH_4$, ethylene glycol, etc.) that are convenient also for the concomitant repristinisation, to some extent, of the CNS.[16]

Currently, sol-gel processes are very popular to achieve a large interface between CNS and inorganic components. However, sol-gel protocols are not at all new, since they have been studied since the mid-1800.[17] During the process, the precursors (*i.e.* generally metal alkoxides) undergo a catalysed condensation to form a colloid in the presence of the corresponding CNS. Next, the colloidal system can be treated differently depending on whether hybrid fibres,[18] aerogels,[19] ceramic materials,[20] or films[21] are desired.

ALD is an elegant process to create films of a second component on top of a substrate. This approach is especially interesting for graphene deposited on substrates, or for CNT-based forests and films. Experimentally, numerous ALD cycles (*e.g.* 2000)[22] are carried out by flowing the metal precursor and the oxidising agent (*e.g.* metal alkoxides and water, respectively) into the reaction chamber. Key advantages of ALD include fine control over film thickness, system homogeneity, no need for purification steps, and possibility to introduce a third or fourth component in a layer-by-layer fashion.

All these methods do not specifically require prior CNS functionalisation to succeed, however this can be helpful to boost the interaction with the precursors. For instance, metal NP growth can ameliorate when the CNS disperse in water, otherwise the NPs will be distributed only on the outer part of CNS bundles. Besides, the sol-gel method necessitates the CNS surface to be hydrophilic for successful hybridisation. This can be achieved by non-covalent functionalisation with amphipathic aromatic molecules (*e.g.* benzyl alcohol) that adsorb onto the CNS surface thanks to π-π interactions, whilst exposing hydrophilic groups (*e.g.* hydroxyl) to the aqueous solution.[23] Covalent functionalisation (*e.g.* oxidation) is also possible to achieve similar results.[18] Eventually, it was demonstrated that ALD products improve significantly when CNTs are chemically modified.[24] Indeed, poor deposition of TiO_2 NPs on MWCNTs occurs when pristine tubes are used, whilst uniform coatings can be obtained with oxidised or N-doped CNTs.

2.1.2. CNS covalent functionalisation

Covalent functionalisation is useful to reduce CNS aggregation and to introduce additional properties (*e.g.* light harvesting or anchor points for metal oxides).[25,26] During the last decades, a large number of options were developed to graft different functional

groups in a stable manner (Figure 2.4).[27–29] Most of these protocols were first reported for CNTs, and later adapted to G, CNHs, etc.

In general, key advantages of covalent methods include high reproducibility, fine control over the degree of functionalisation and the stability and properties of the materials. For instance, with appropriate selection of oxidation conditions, important parameters such as the level of oxidation, or the length of oxidised MWCNTs can be fine-

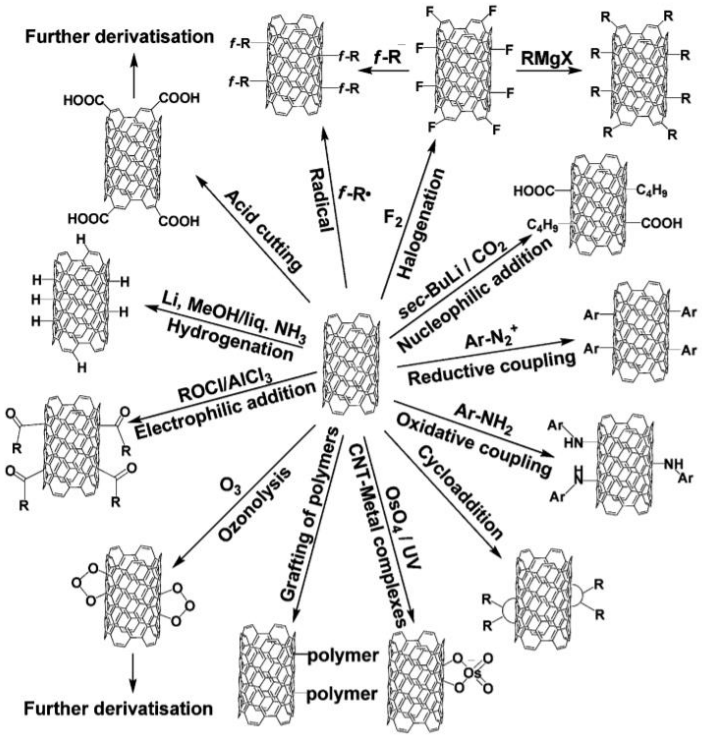

Figure 2.4. Chemical routes for CNT functionalisation.[30] Reproduced from (30) with permission of The Royal Society of Chemistry.

tuned (Figure 2.5), as well as purity (*i.e.* by oxidative removal of impurities).[31] XPS analysis revealed presence of varied oxygen-containing groups, with a high ratio of carboxylic acids. Importantly, another key advantage of covalent functionalisation with hydrophilic chains that reduce CNT bundling, is an overall alleviation of the asbestos like-pathogenicity associated with the formation of large CNT aggregates.[32]

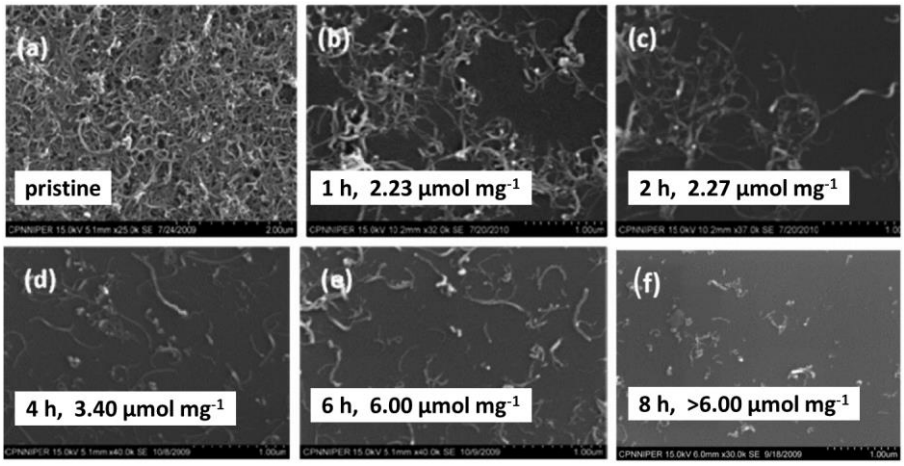

Figure 2.5. SEM images of oxidised MWCNTs at different reaction times show CNT progressive shortening.[31] Adapted with permission from (31). Copyright 2011 American Chemical Society.

Besides oxidation, diazo coupling is also widely used to functionalise CNTs, CNHs, or G[33–35] An aryl radical is typically generated *in situ* by decomposition of an aryl diazonium salt. Then, even though the exact reaction mechanism is not completely elucidated, there is consensus that one electron from the aromatic surface and one electron from the aryl radical form the new covalent bond and generate sp^3 carbon atoms in the CNS. Interestingly, this protocol is versatile since it permits the introduction of various functional groups depending on the substituent in the *metha-* and *para-* positions relative to the diazonium species. Besides, the use of nitrites (*e.g.* isopentyl or sodium nitrite) for the *in situ* preparation of diazonium salts from anilines avoids direct handling of unstable diazonium salts. Recently, Rubio *et al*. reported the optimisation of CNTs/CNHs diazo coupling in water using microwaves as energy source, towards green protocols.[34,36]

On the negative side, covalent functionalisation inherently damages the sp^2 carbon lattice and consequently compromises some of CNS unique properties due to the conjugated sp^2 structure. For instance, CNT conductivity decreases upon ozone-oxidation.[37] However, this process can be reversible to restore CNS properties, as shown for GO upon UV-light irradiation, or annealing at high temperatures (*e.g.* 900 ^{o}C).[38]

2.2. Aim of the work

This chapter focusses on CNS covalent functionalisation to boost interaction with different inorganic materials (*i.e.* zeolites and TiO_2) towards applications in energy or water purification. In particular, MWCNTs and water exfoliated G functionalisation aims

at introducing oxygen-containing species for their hybridisation with TiO_2 electrospun fibres for H_2 production. Alternatively, G functionalisation with quaternary ammonium groups will be performed to promote the *in situ* growth of nanocrystalline zeolites for photocatalytic applications. Special care will be taken to develop protocols that are as environmentally friendly as possible, in line with the EU objectives relevant to the CARINHYPH project, of which this research work takes part.[39]

A second part of this chapter focusses on the adaption of covalent functionalisation protocols for two types of CNT fibres (*i.e.* synthesised from butanol or toluene precursors). In this way, these notoriously hydrophobic materials should become more hydrophilic for the growth of metal oxides, towards catalytic or energy use.

2.3. Results and discussion

2.3.1. Functionalisation of MWCNTs and G for their hybridisation with TiO_2 for H_2 production

2.3.1.1. Production of TiO_2 nanofibres

In this work, a combination of sol-gel and electrospinning processes was used to synthesise long nanofibres composed of TiO_2 nanoparticles. The synthesis of these fibres was carried out by Alicia Moya in Dr. Juan José Vilatela's group at IMDEA Materials Institute (Getafe, Spain), where the PhD candidate spent two months to familiarise with the synthetic protocol. Photocatalytic tests were performed by Dr. Alexey Cherevan at Prof. Dr. Dominik Eder's laboratory at the Technical University of Vienna (Austria).

The preparation of TiO_2 electrospun fibres can be divided in three parts: i) the sol-gel reation; ii) the electrospinning process; and iii) the calcination step.[40,18] Initially, a solution of polyvinyl pyrrolidone (PVP) in ethanol (10 wt. %) and a solution of titanium ethoxide (*i.e.* the metal oxide precursor) were homogeneously mixed. Then, the sol-gel reaction was triggered upon the addition of a few drops of acetic acid. The PVP polymer was required to give the appropriate surface tension, viscosity and conductivity to allow for electrospinning. The solution was continuously flowed from the spinneret (*i.e.* needle) to a collector with 18 kV of potential difference between these two parts (Figure 2.6). The

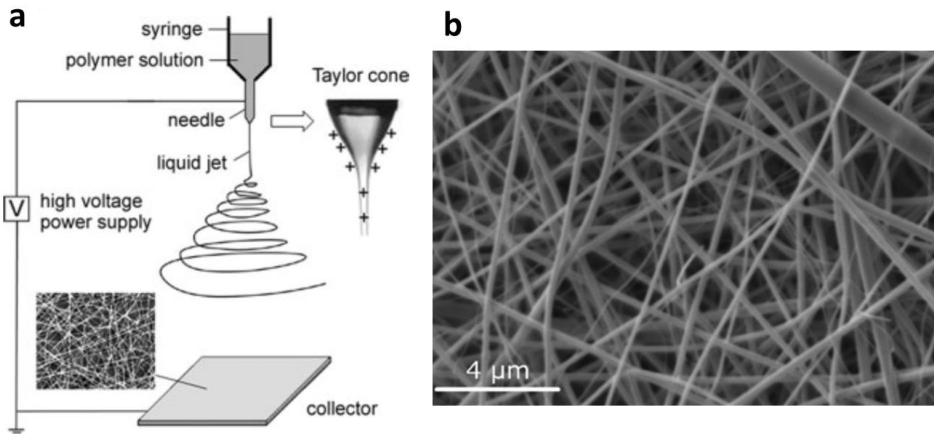

Figure 2.6. (a) Schematic representation of the electrospinning process. Adapted with permissions from (41), Copyright 2003 John Wiley and Sons.;[41] and (b) TiO_2 electrospun fibres synthesised by this method.[40] Adapted from (40) with permission of The Royal Society of Chemistry.

randomly oriented fibres were produced when the applied electric field overcame the surface tension of the polymer solution.[42] Next, a thermal treatment under air (*i.e.* 2.5 h at 400 ^{o}C) was carried out to remove the polymer, and a final thermal treatment at higher temperatures under argon (*i.e.* 1 h at 500 ^{o}C) crystallised TiO_2 anatase/rutile (A/R).

2.3.1.2.Functionalisation of MWCNTs and G

If CNS are to be introduced into TiO_2 electrospun fibres, ideally this should occur at the initial sol-gel step, by dispersing the CNS in the ethanol solution before electrospinning. Thus, the CNS must be functionalised to avoid aggregation in ethanol.

Indeed, pristine MWCNTs formed visible aggregates in ethanol (Figure 2.7) and thus, their functionalisation appeared to be indispensable for their incorporation into TiO_2 fibres. In line with the priorities set by the CARINHYPH project, preference was given for protocols in aqueous media (as opposed to organic solvents), and two different routes were chosen for this study, namely acid-mediated oxidation and diazo coupling. Experimental conditions were varied to produce five products: two types of oxidised MWCNTs (*i.e.* long-ox-MWCNTs and short-ox-MWCNTs), two types of MWCNTs functionalised through the diazo coupling reaction (*i.e.* phenol-MWCNTs and isophthalic-MWCNTs) and G functionalised also via diazo coupling (*i.e*. isophthalic-G).

Figure 2.7. Aggregates of MWCNTs in ethanol (1 mg ml^{-1}).

2.3.1.2.1. Functionalisation of MWCNTs

Two different acid treatments were applied to MWCNTs. In both cases, pristine MWCNTs were ultrasonicated at room temperature in acidic media. However, the use of harsh acid (*i.e.* concentrated H_2SO_4:HNO_3 = 3:1, 5h) or milder conditions (*i.e.* 69% HNO_3, 3 h) allowed to either cut the CNTs or preserve their length (Figure 2.8). In the first case, the majority of short-ox-MWCNTs have a length in the range of 100-500 nm, with negligible amounts longer than 1 micron. In the latter, the length of pristine MWCNTs was not altered, yielding long-ox-MWCNTs with a wide length distribution and as long as several microns. TEM analyses showed that in both cases the tubular structure was maintained and the materials were of high purity. The graphitic nature was

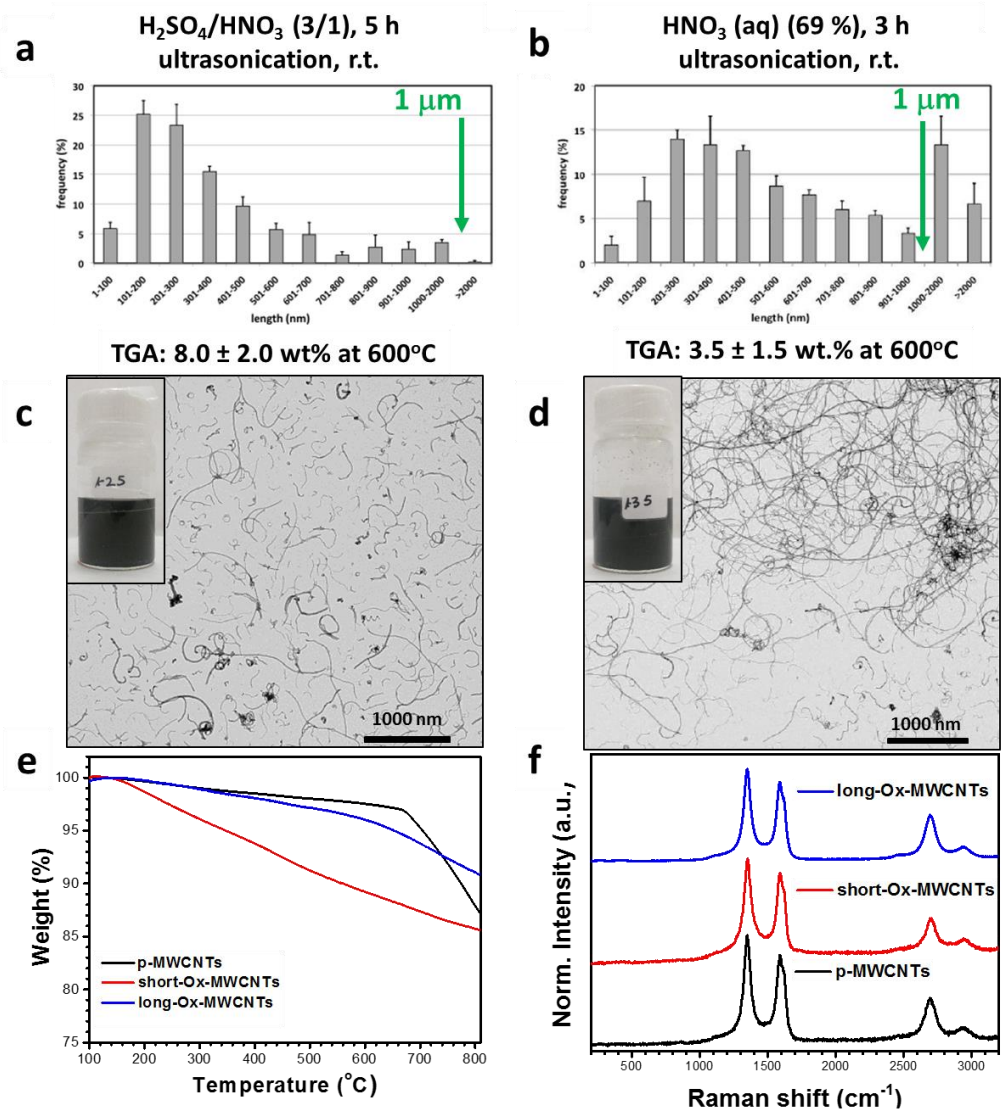

Figure 2.8. Characterisation of short-ox-MWCNTs (left) and long-ox-MWCNTs(right): (a) and (b) length distribution; (c) and (d) TEM images with the inset of the materials dispersed in ethanol; (e) TGA under N_2; and (f) Raman spectra.

confirmed by Raman analyses, with a high intensity D- and G- bands observed with no significant differences between the different materials, as expected for MWCNTs. TGA under inert atmosphere confirmed a weight loss at 600 °C of 8.0 ± 2.0 % and 3.5 ± 1.5 % for short-ox-MWCNTs and long-ox-MWCNTs, respectively, corresponding to 1777 and 777 µmol of carboxylic groups per gram of material (Figure 2.8 e). In this manner, the two products display a higher or lower level of functionalisation, since it was difficult to anticipate the ideal compromise between dispersibility and conductivity for the preparation of the hybrid. Thanks to the increase of hydrophilicity, both materials were

readily dispersed in ethanol (Figure 2.8 c and d, insets), while only the short-ox-MWCNTs dispersed well in water (not shown).

Diazo coupling (Figure 2.9) was performed with either 4-aminophenol or 5-aminoisophthalic acid and isopentyl nitrite in water to generate the diazonium species *in situ*.[43] Different conditions were tested, by varying both the reaction time and the amount of nitrate, using 4-aminophenol as a model. Minor differences were noted when the reaction time increased from 1 h to 2 h (Table 2.1). However, a significantly higher level of functionalisation was observed when a second aliquot of nitrite was added after 1 h, and the reaction proceeded overnight (Table 2.1). The latter conditions produced phenol-

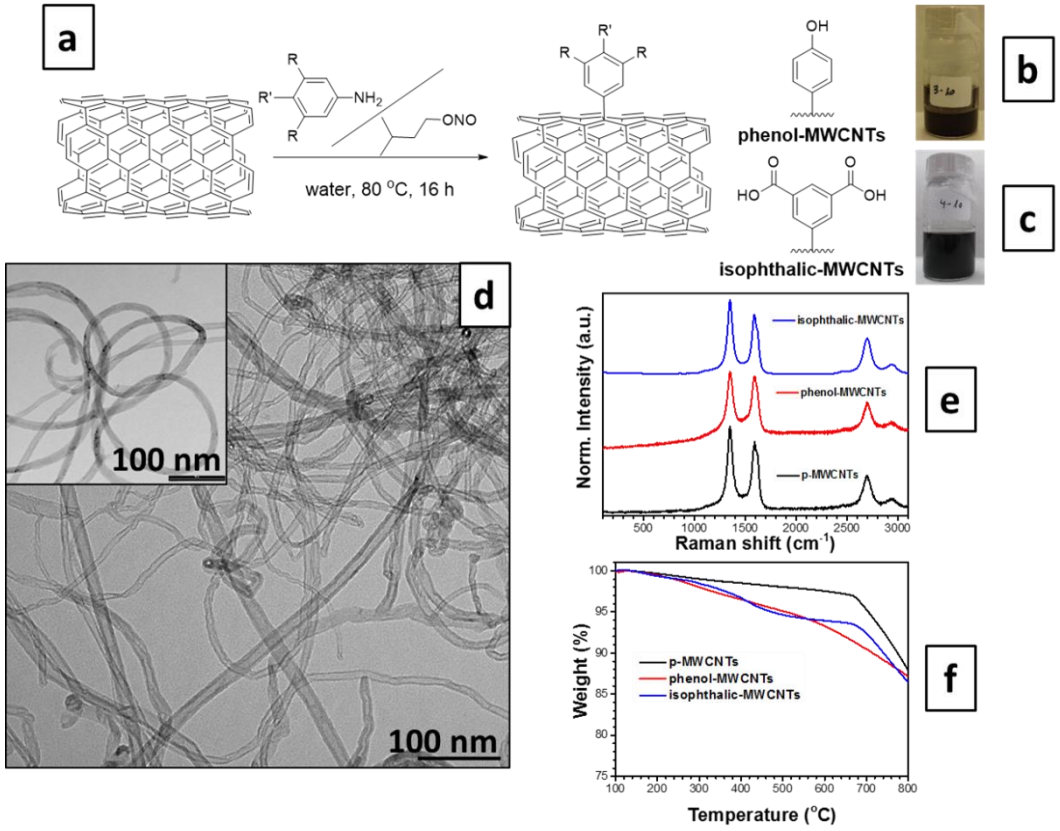

Figure 2.9. Preparation of phenol- and isophthalic-MWCNTs: scheme of synthesis (a); photographs of the dispersions in ethanol after 5 days (b,c); TEM images of phenol-MWCNTs (representative for both materials) (d); Raman spectra (e); and TGA under N_2 (f).

MWCNTs that led to homogeneous and stable dispersions in ethanol (Figure 2.9 b). Analogous data (*i.e.* 421 μmol g^{-1} after overnight reaction) was obtained for 5-aminoisophthalic acid (Fig. 2.9 e). This product dispersed well in ethanol too (Fig. 2.9 c).

Table 2.1. Optimisation of the reaction conditions for phenol-MWCNTs.

Reaction time	Time (h)	TGA weight loss at 600 ºC (%)	Degree of functionalisation (µmol FG/g)
Phenol-MWCNTs 1	1	3.0	322
Phenol-MWCNTs 2	2	3.7	376
Phenol-MWCNTs 3	16	7.4	795

2.3.1.2.2. Functionalisation of G

The pristine G used in this project was provided by Thomas Swan & and Co. Ltd. and consists of water exfoliated G with surfactants that is presented as solid or as a stable dispersion in water at high concentrations (*i.e.* 0.5-0.8 mg ml^{-1}). Unfortunately, the powder was not dispersible in ethanol, and G precipitated from the water dispersion when the solvent was exchanged to ethanol (Figure 2.11 b). This is likely ascribed to the loss of surfactants during solvent exchange and motivated the use of covalent functionalisation to achieve stable introduction of functional groups on G.

Initially, the reactions conditions described above for MWCNTs were applied to G, both in powder and water dispersion. However, TGA and Raman spectroscopy revealed that the protocol was unsuccessful, a significant increase of neither weight loss nor I_D/I_G ratio was observed, respectively. Clearly, this is ascribed to the higher reactivity of MWCNTs relative to G arising from their higher curvature of the sp^2 structure. Besides, the 2D band shape suggests that the exfoliated G flakes partially restack when water is removed. To address this issue, sodium cholate was added to the reaction media since this bile salt is known to stabilise large amounts of G in water.[44] Unfortunately, this approach did not result in successful G functionalisation.

Next, microwave irradiation was tested to promote the reaction, as this approach proved successful for CNTs and CNHs.[36,34] Although less studied for G, Dr. Verónica León reported preliminary good results in her doctoral thesis, thus similar conditions were applied here.[45] Since it is well-known that graphene-like materials display high absorbance of microwave irradiation, a control experiment was performed to assess whether the irradiation alone significantly affects G structure. An aqueous dispersion of G was irradiated and purified following exactly the same conditions used for the synthesis of isophthalic-G (see Experimental section for further details). The so-called blank-G was

characterised by Raman spectroscopy, and TEM, which proved no significant changes had occurred. TGA showed a minor decrease of the amount of surfactants (*i.e.* the weight loss is smaller, Figure 2.10), although this did not affect the water dispersibility of the material.

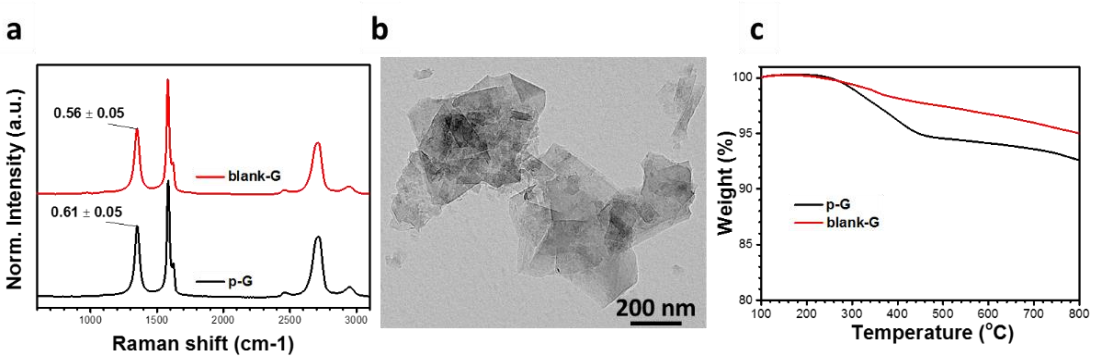

Figure 2.10. Characterisation of blank-G: (a) Raman analysis; (b) TEM image; and (c) TGA in N_2. The Raman spectrum and the thermogram of the corresponding p-G are included for comparison.

Despite the use of microwave irradiation, 0.3 eq. of aniline for C atom of G (*i.e.* ratio used for MWCNTs) were not enough to functionalise G. By contrast, an increase up to ten times of aniline resulted in successful functionalisation as observed by Raman spectroscopy (*i.e.* higher I_D/I_G ratio than the pristine G) and TGA (% wt. loss at 350 ºC due to the decomposition of the isophthalic moiety covalently attached to the G surface) (Figure 2.11 e and f). G functionalisation level was calculated by TGA taking into account the decrease of surfactant amount observed for the blank-G control.

Isophthalic-G formed stable dispersions in ethanol as required for hybridisation with TiO_2 fibres (Figure 2.11 c). This was confirmed by TEM analysis, which revealed high purity and preservation of G flake structure (Figure 2.11 d). The process was highly reproducible as confirmed by Raman spectroscopy and TGA (Figure 2.12 and Table 2.2.

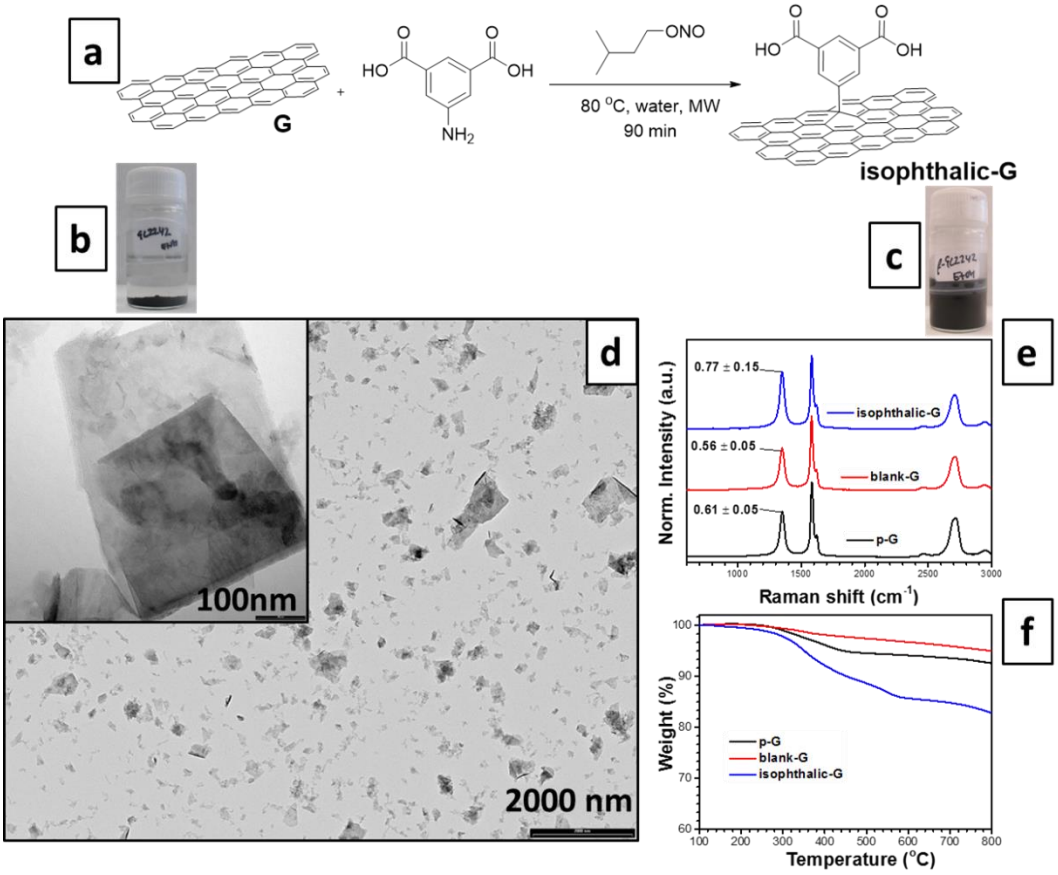

Figure 2.11. Preparation of isophthalic-G: scheme of synthesis (a); images of the dispersions in ethanol after 5 days (b) and (c); TEM images at low and high magnifications (d); Raman spectroscopy (e); and TGA under N_2 (f).

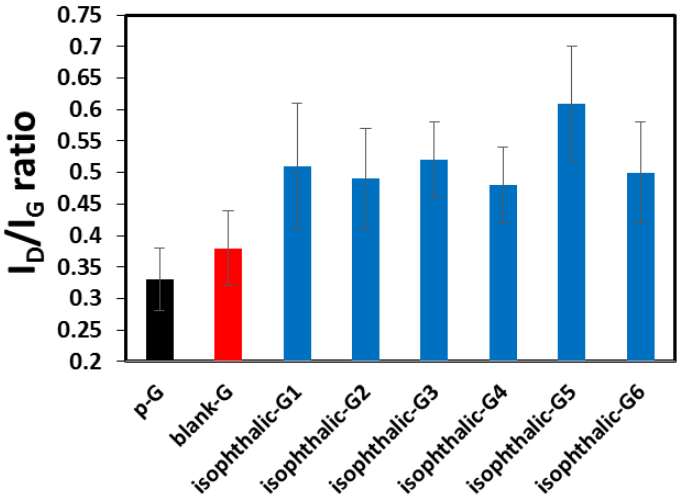

Figure 2.12. I_D/I_G ratio of different isophthalic-G batches.

Table 2.2. Degree of functionalisation calculated by TGA of different isophthalic-G batches. To calculate the degree of functionalisation the weight loss of blank-G was subtracted to the weight loss of the functionalised materials.

Reaction time	Weight loss at 600 ºC (%)	Degree of functionalisation (µmol FG/g)
p-G	8.7	--
blank-G	3.0	--
isophthalic-G1	10.8	472
isophthalic-G2	11.8	533
isophthalic-G3	11.4	509
isophthalic-G4	11.5	515
isophthalic-G5	10.8	472
isophthalic-G6	10.3	503
isophthalic-G (average ± std dev)	11.5 ±0.6	500 ± 24

Next, instead of 5-amino-isophthalic acid, the less sterically hindered 4-aminophenol was used for the synthesis of phenol-G. However, in this case, Raman spectroscopy revealed the appearance of additional signals that did not decrease despite extensive washes (Figure 2.13 a). These signals may be due to multiple arylation processes that occur simultaneously to the functionalisation, resulting in G flakes that were covalently functionalised with the grafted polymer (Figure 2.13 b). However, non-covalent interaction between G and the polymer could not be ruled out. These results were in agreement with a recent report on 4-nitrobenzenediazonium and 3,5-bis-*tert*-butylbenzenediazonium electrochemical grafting onto graphene and graphite.[46] In this work, Greenwood *et al.* reported that the grafting was limited to a monolayer when the sterically hindered compound was used, otherwise a multilayer dendritic-like grafting occurred. Since multiple arylation occurred even though a strong deactivating group was present, steric hindrance likely played a predominant role over the deactivating effect of the substituent. On the basis of these results, phenol-G was not pursued any further since uncontrolled polymerisation could increase the distance between TiO_2 NPs and the G surface.

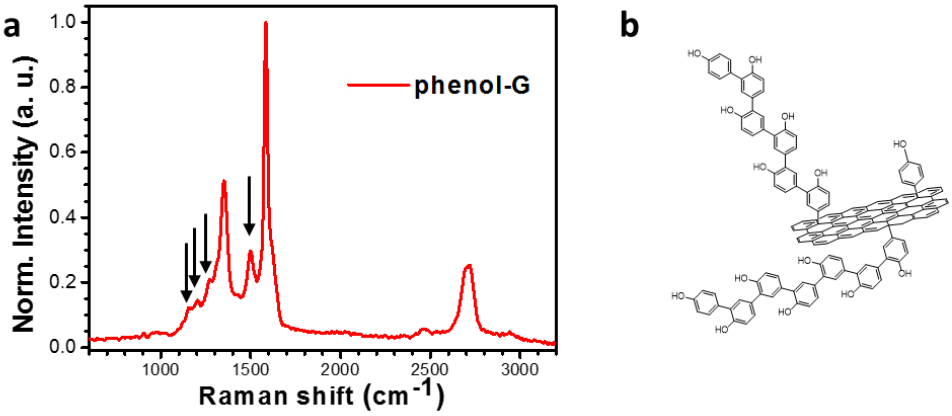

Figure 2.13. (a) Raman spectra of phenol-G; and (b) hypothesised structure of phenol-G.

2.3.1.3.Hybridisation of functionalised CNS with TiO_2 electrospun fibres

Preparation and characterisation of hybrid TiO_2 electrospun fibres was performed by the group of Dr. Vilatela (IMDEA Materials, Getafe, Spain), following the protocol described in Section 1.3.1.1, with the addition of functionalised CNS to the solution of titanium ethoxide and PVP, before the addition of the acid, in the first step. As a representative example, Figure 2.14 shows SEM and TEM images of the hybrid nanomorphology, consisting of nanofibres composed of CNS and TiO_2 nanocrystals of varying diameter (Table 2.3), thus confirming successful hybridisation, with an intimate contact between components.

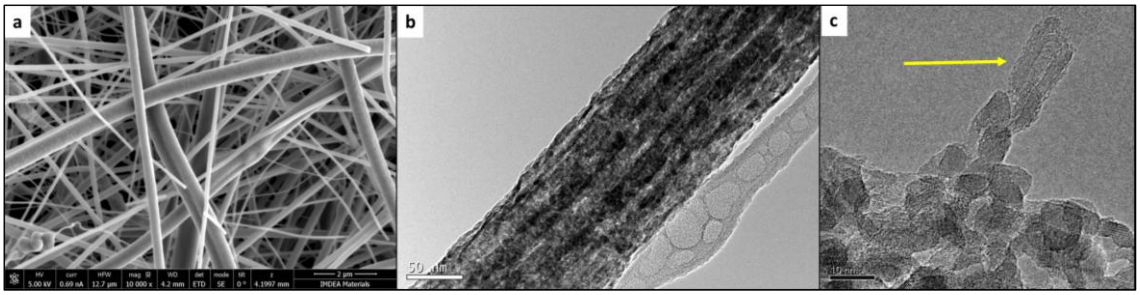

Figure 2.14. SEM (a) and TEM (b and c) images of short-Ox-MWCNTs@TiO_2. The yellow arrow point to a short-Ox-MWCNT. Courtesy of Alicia Moya.

The mesoporous structure of the final material was obtained after calcination, which caused a reduction of nanofibre thickness from ~800 nm to only a few hundred nanometres. The initial thermal treatment at 400 ºC in air removed the polymer at a relatively low temperature to preserve the CNS graphitic structure. It is worth noting that Alicia Moya *et al.* had previously demonstrated that despite the low temperature used, XRD spectra of the fibres presented the typical fingerprint of anatase phase.[18] By contrast, under the same conditions the crystal structure of TiO_2 NPs alone were significantly less crystalline. This favourable effect is likely due to the higher density of nanofibre materials that facilitate crystallisation. However, further annealing was required to increase the performance of the photocatalyst.

Although TiO_2 is a thermally resistant material, it undergoes phase transformation from A to R upon heating (*i.e.* from A/R 100/0 at 400 ºC to 0/100 at 800 ºC, both of them treated under Ar).[18] Regarding the photocatalytic properties, anatase is the most active phase, however, it is known that the best catalytic activity are obtained when both phases co-exist.[47,48] In this case, optimal photocatalytic conditions were achieved when the nanofibres were annealed at 500 ºC under Ar.[18] This was the result of optimisation studies, since at lower temperatures, A/R of 84/16 was obtained for the hybrid instead of pure A as expected for TiO_2 NPs alone. Besides, Askel and Eder reported that the presence of metal oxides could anticipate the decomposition of MWCNTs,[49] generally stable up to 650 ºC as evidenced by TGA under N_2 (Figure 2.9). Therefore, a low annealing temperature was required to guarantee that CNS is preserved, which was confirmed, amongst other techniques, by TEM (Figure 2.14).

As presented in Figure 2.15 a, XRD spectra of bare TiO_2 fibres and hybrids with different f-CNS were analogous. Overall, a slight increase of A phase was found in all hybrids tested (Table 2.3), which was higher in isophthalic-MWCNTs@TiO_2.

Raman spectra of the hybrids exhibited the D- and the G- bands in all cases confirming the preservation of the f-CNS in the final material. Raman spectra of TiO_2 NPs and fibres, and hybrid nanofibres, all presented the characteristic signals of A phase (Figure 2.15 b). The major difference was a blue shift of the whole set of fibres relative to TiO_2 NPs that had been attributed to differences in NP size.[50] However, the crystal size in all samples resulted to be very similar (Table 2.3), calling for a different effect. Anatase Raman response is very sensitive to O-O interactions, therefore, the blue shift could be

due to oxygen vacancies in the fibre structure. The O vacancies would likely create defects in the TiO_2-TiO_2 and the TiO_2-CNS interfaces, which could generate new electronic levels. In this regard, the generation of new inter-bandgap electronic levels was called to explain the high catalytic activity of mixed-phase TiO_2 materials.[47] The inert atmosphere during the annealing process was responsible for the appearance of the vacancies.[51] It is hypothesised that the dense morphology of the nanofibre, displaying very close proximity between A nanocrystals, favoured phase transformation into R. By contrast, this was not observed for TiO_2 NPs alone at 500 ºC.

Further characterisation of the hybrids was done by UV-Vis diffuse reflectance spectroscopy and physisorption studies (Figure 2.15 d and, Table 2.3). Both techniques are fundamental for the characterisation of photocatalysts. The UV-Vis spectra gives information on what kind of light (*i.e.* UV or visible) is required to activate photocatalysis. In this case, the absorbance of all materials was insignificant in the visible region (*i.e.* 390-700 nm), but displayed a large UV absorbance in the explored wavelengths. As a consequence, UV light will be required for hydrogen production with these materials.

Physisorption measurements were used to evaluate the materials surface area (Figure 2.15 d). This is a parameter of a high importance since it is directly related to the active sites in heterogeneous catalysis. The materials displayed pores of diameter between 2 and 50 nm, indicating a mesoporous nature. Agglomeration of TiO_2 into a fibrillary structure decreased surface area in all cases, with smaller particle size leading to higher surface area, and supposedly higher activity for H_2 production.

Table 2.3. Compendium of parameters of TiO_2 fibres and the different hybrids extracted from the characterisation in Figure 2.15. Courtesy of Alicia Moya.

	Anatase/rutile ratio	**Particle size (nm)**	**BET surface area (m^2 g^{-1})**
TiO_2 nanoparticles	1.00	14.94	95.5
TiO_2 fibres	0.75	11.85	41.4
Short-Ox-MWCNTs@TiO_2	0.79	7.59	48.4
Isophthalic-MWCNTs@TiO_2	0.87	17.15	34.52
Isophthalic-G@TiO_2	0.79	13.2	24.92

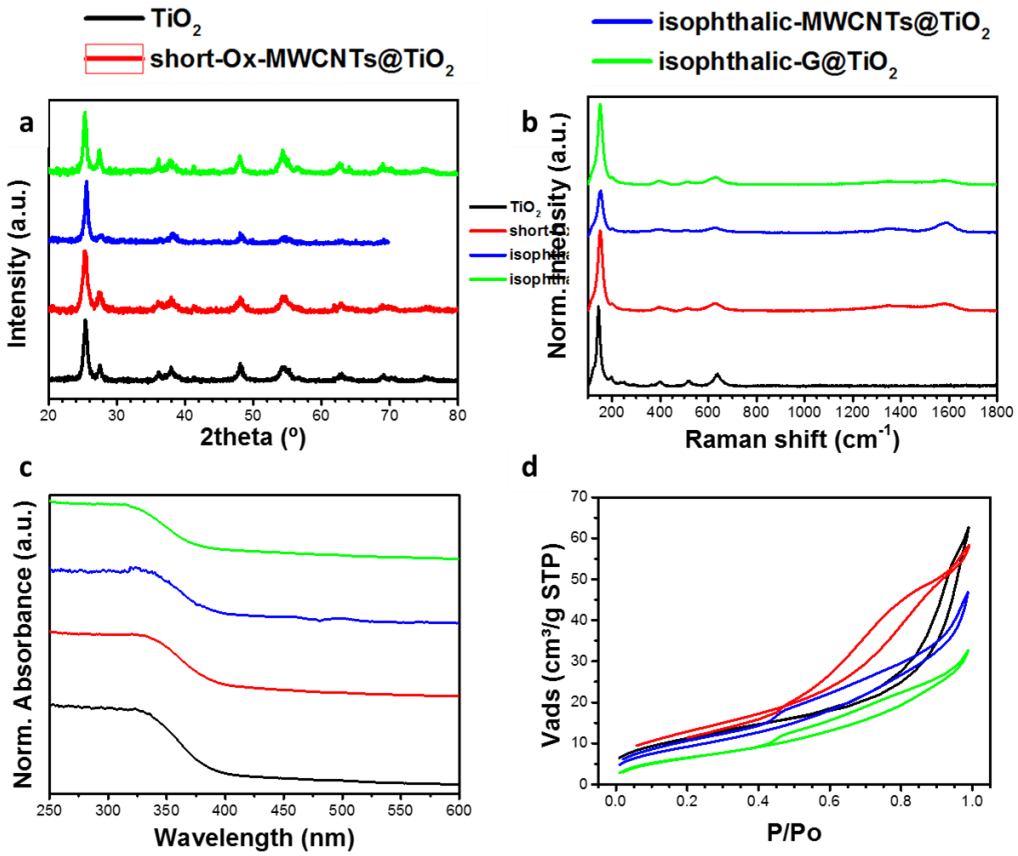

Figure 2.15. Characterisation of TiO_2 fibres and the different hybrids: (a) XRD, (b) Raman, (c) UV-Vis spectra in water; and (d) BET data. Courtesy of Alicia Moya.

2.3.1.4. Photocatalytic activity of the hybrids

Photocatalytic H_2 production experiments were conducted by the group of Prof. D. Eder at Technical Vienna University. A small amount (*i.e.* 30 mg) of the tested material was dispersed in the reaction mixture (water:methanol = 1:1). H_2PtCl_6 was added for *in situ* photodeposition of Pt NPs on the hybrid surface. The addition of Pt as co-catalyst enhanced catalytic activity, while methanol acted as sacrificial agent to trap the holes and prevent the oxidation of water. Then, the mixture was irradiated from the top with a UV-Vis lamp (*i.e.* 240-500 nm). The generated hydrogen was measured in-flow by an X-Stream gas analyser. A continuous flow of Ar was used to deliver products to the detector.

Moya *et al*. had previously demonstrated that A/R ratio was a determinant factor for high catalytic activity and also that the addition of short-ox-MWCNTs enhanced photocatalytic activity of electrospun fibres (Figure 2.16 and b).[18] This data suggested that short-ox-MWCNTs boosted electron transfers, in agreement with literature.[52,53]

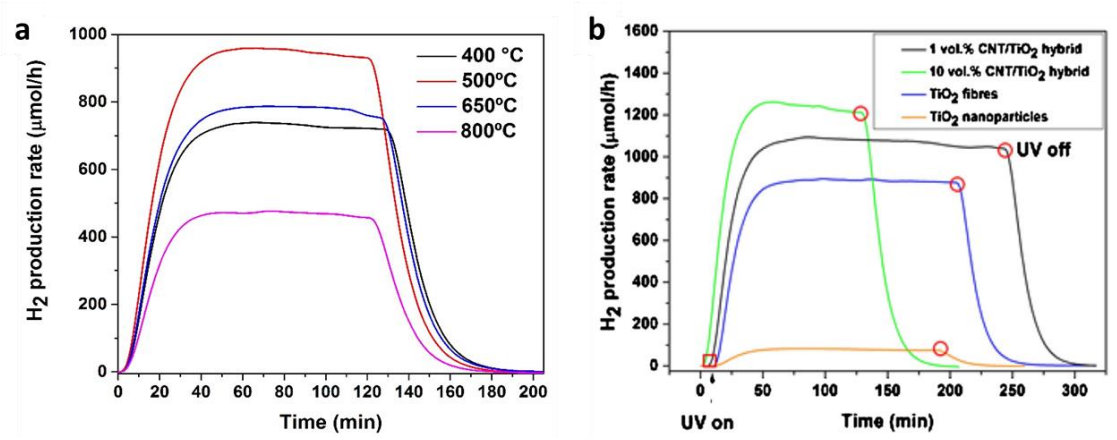

Figure 2.16. (a) H_2 production of pure TiO_2 fibres prepared at different annealing temperatures, consequently with different A/R ratios. A/R are 100/0, 84/16, 49/51 and 0/100 for 400 ºC, 500 ºC, 650 ºC and 800ºC, respectively. (b) Catalytic test of pure TiO_2 fibres, TiO_2 NPs and short-ox-MWCNTs@TiO_2. Adapted from (18) with permission of Elsevier.

H_2 production profiles revealed that photocatalytic processes started instantaneously after the illumination of the system and stopped when the UV lamp was switched off. The profiles indicated also stable activity in the explored reaction times (*i.e.* 4 h). Interestingly, electrospun fibre performance was much higher than that of NPs, despite NPs surface area being higher. This fact was explained by the intimate interfacial contact between components within the fibrillary structure, which facilitated charge transfers. Besides, a positive effect may also arise from better adsorption/desorption of the reactants/products thanks to fibre mesoporosity.

The activities of the new hybrids prepared with isophthalic-MWCNTs and isophthalic-G are summarised in Table 2.4 and Figure 2.17. For comparison, the performance of pure TiO_2 fibres, TiO_2 NPs and short-ox-MWCNTs@TiO_2 at different MWCNTs content are included. It is worth noting that the performance of the hybrids was in all cases better than that of TiO_2 NPs.

The performance of short-ox-MWCNTs@TiO_2 appeared to be the highest amongst the materials tested, especially with a MWCNT content up to 10% vol. In the case of isophthalic-G hybrids, at all amounts of f-G tested (*i.e.* 1, 3 or 5 vol. %), photocatalytic activity was very similar to that of pure TiO_2 fibres. We hypothesise that the different CNS morphology played a key role in the process, possibly due to different CNS orientation in the fibrillary structure, with a role played by the anisotropy of MWCNTs.[54–56] It is hypothesised that short-ox-MWCNTs were oriented along the

longitudinal axes of the fibres, due to the electrospinning process that involved longitudinal stretching of the material through the nozzle.[57] Alignment of MWCNTs could supress the recombination of charge carriers (*i.e.* electron and holes).[58] The fact that electrospun fibres hybrids containing short-ox-MWCNTs@TiO_2 performed better than those containing isophthalic-MWCNTs@TiO_2 is likely ascribed to better dispersibility of the former. Indeed short-ox-MWCNTs were individualised, as seen by TEM imaging (Figure 2.8 c and d), while isophthalic-MWCNTs aggregated to some extent. The differences in the alignment of individual and non-individualised tubes were already observed in the synthesis of electrospun polyethylene oxide fibres.[59]

Table 2.4. Summary of the H_2 production of the different tested materials. Courtesy of Dr. A. Cherevan.

Sample	f-CNS vol. %	H_2 production (mmol g^{-1} h^{-1})
TiO_2 nanoparticles	0	3.0
TiO_2 fibres	0	27.7
Short-Ox-MWCNTs@TiO_2	1	34.0
	10	40.6
	40	38.7
Isoph-MWCNTs@TiO_2	5	6.7
Isoph-G@TiO_2	1	20.9
	3	22.0
	5	26.0

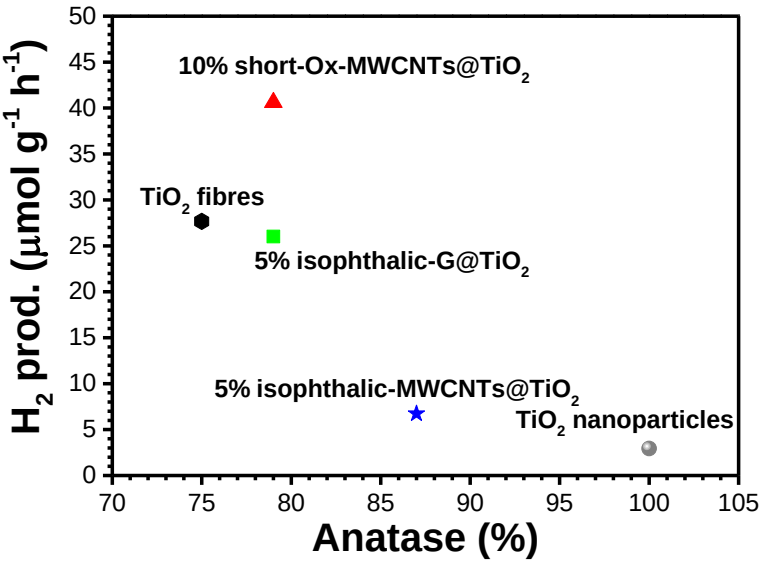

Figure 2.17. Comparison of the catalytic activity of the different f-CNS@TiO_2 fibres. The hybrids presented in the chart correspond to the best hybrids tested for every f-CNS.

2.3.2. G functionalisation for its hybridisation with zeolites for water purification

2.3.2.1. Zeolites

Zeolites are naturally occurring crystalline aluminosilicates with small pores and large surface area that can be used as molecular sieves, catalyst supports, or in gas/ion exchange membranes.[60] Thanks to synthetic advancements in achieving fine control over their properties, they have become widely used catalysts for oil cracking in gasoline production.[60]

Popular methods for zeolite synthesis are solvothermal, hydrothermal or sol-gel processes that use organometallic or inorganic precursors.[61,62,63] Common precursors are tetraethylorthosilicate as silica source, and sodium aluminate as alumina source. Their substitution with other oxides (*e.g.* tetraethylorthotitanate instead of sodium aluminate),[64] yields new zeotypes with titania, instead of alumina. The so-called TS-1 zeolites (*i.e.* synthesised from silica and titania precursors) are very interesting since they have demonstrated promising photocatalytic activity.[65] Another common component in zeolite synthesis is the structural directing agent, which serves as template for zeolite growth. Typically, this is an organic compound (*i.e.* tetrapropylammonium hydroxide, TPAOH) that directs zeolite growth around itself, thus fine-tuning mesoporosity.[60,62] Finally, the structural directing agent is removed in the calcination step.

2.3.2.2. CNS-zeolite hybrids in photocatalysis

The zeolitic materials here reported were prepared by the combination of a sol-gel and a hydrothermal process. The synthesis was carried out by Dr. Paul Gebhardt in Prof. Dominik Eder's group at Technical University Vienna, and will be detailed in the Experimental Section. This group has large experience on the hybridisation of inorganic materials with CNS and recently they have reported CNS-TS-1 zeolite hybrids.[61,63,65] In contrast with the trends observed for the photocatalytic performance of TiO_2 fibres upon addition of CNS, photocatalytic activity of G-TS-1 hybrids was up to 6-7 times higher than the corresponding MWCNTs-TS-1, at the same CNS concentration (Figure 2.18). Outstandingly, the activity observed for 10 wt. % G-TS-1 hybrids surpassed that of state of the art catalysts, such as TiO_2-P25 (Degussa), and was 25 times higher than TS-1.

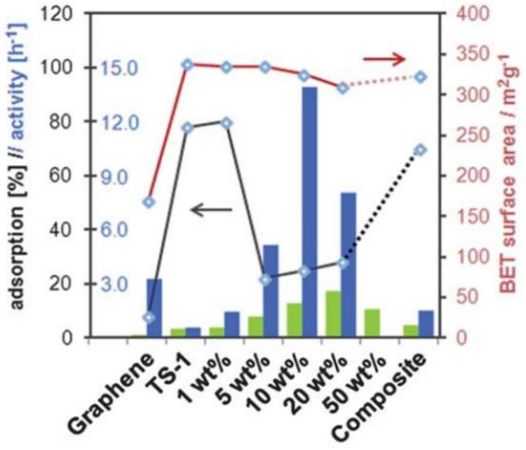

Figure 2.18. Photocatalytic activity for the degradation of 4-nitrophenol under UV irradiation of: G-TS-1 (blue bars) and MWCNTs-TS-1 (green bars) with different CNS amount; G and CNS-TS-1 composites (prepared by different synthetic route). BET (red line) and dye adsorption (black line) data for G-TS-1 hybrids.[61] Adapted from (61) with permission of The Royal Society of Chemistry.

Addition of CNS resulted in very different particle size and morphology. On one hand, MWCNTs caused a gradual decrease in particle size as their concentration increased (*i.e.* 23, 14 or 6 nm for 5, 30 or 50 wt. % of MWCNTs).[65] On the other hand, the use of G at different concentrations caused dramatic changes in shape and size of TS-1 NPs (*i.e.* ellipsoidal, rectangular or spherical nanoparticles for 1, 5 or > 5 wt. % G, respectively, Figure 2.19 a, b and c).[61] By contrast, no significant change was observed when either RGO or GO were added, regardless of concentration (Figure 2.19 d, e and f).

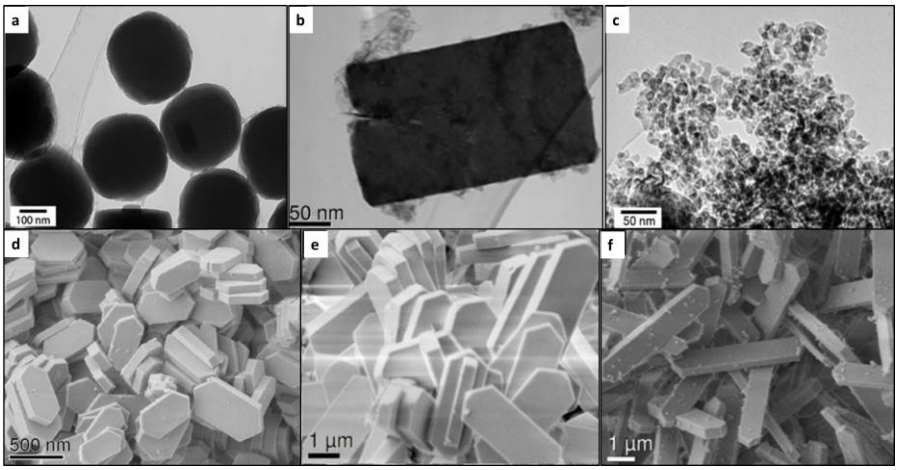

Figure 2.19. (Top) TEM images of 1 % G-TS-1 (a); 5 % G-TS-1 and 10 % G-TS-1 (c); (bottom) SEM images of TS-1 (d); 10 % GO-TS-1 (e); and 10 % RGO-TS-1 (f). Adapted from (61) and (63) with permission of The Royal Society of Chemistry.

2.3.2.3.Design of G functionalisation for zeolite *in situ* growth into hybrids

These observations indicate a key role played by the chemical structure of G and its functionalisation (if present). To enhance the interfacial interaction between G and zeolite, G functionalisation for this work was appropriately chosen to introduce tripropylammonium moieties covalently linked to G to exploit them as structural directing agents, similarly to those used previously as small molecules (*i.e.* tetrapropylammonium hydroxide, TPAOH).[61,63] Since the quaternary nitrogen atoms will mark the function of the f-G for the synthesis of the hybrids, we referred to this material as quaternary-G. The synthetic route was designed to be as environmentally friendly as possible (Scheme 2.1). First the desired aniline bearing the quaternary moiety was prepared, and then it was grafted onto G via diazo coupling as a last step.

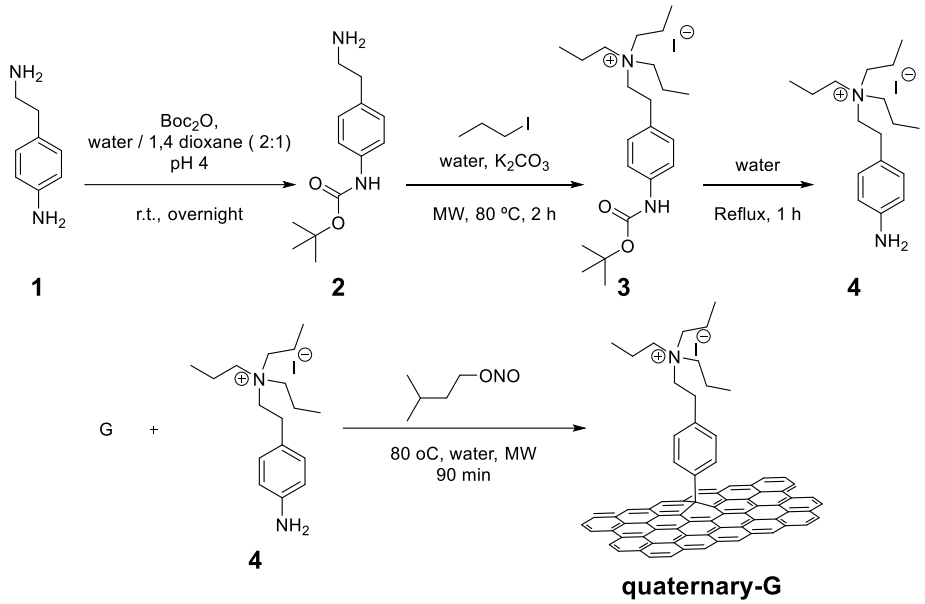

Scheme 2.1. Synthetic route for quaternary-G.

The first step involved selective protection of aniline **1** at mildly acidic pH, exploiting the difference in pKa between the aniline (*i.e.* pK_a 4.2) and the aliphatic amine (*i.e.* pK_a 9.2).[66] Purification of product **2** was done by liquid extraction to limit the generation of toxic waste (*i.e.* large amounts of solvents, and silica) otherwise required for column chromatography. Next, the free amine in **2** was alkylated by propyl iodide. Selective formation of the quaternary ammonium product is typically achieved by refluxing in organic solvent (*e.g.* toluene) with an excess of alkylating agent. To develop

a green route, we modified the protocol developed by Yu and Varma to get the quaternary salt **3** in a biphasic mixture of water/propyl iodide using microwave irradiation as green energy source.[67] The reaction was done at 80 ºC instead of 120 ºC, to avoid undesired Boc deprotection that would lead to aniline alkylation. Lowering the temperature implied increasing the reaction time (*i.e.* from 20 min to 2 h), otherwise **2** was not fully quaternarised. The crude appeared as a triphasic system in which **3** was between aqueous and organic phases (Figure 2.20). After water removal, the addition of hexane resulted convenient to precipitate **3**, which was isolated by filtration.

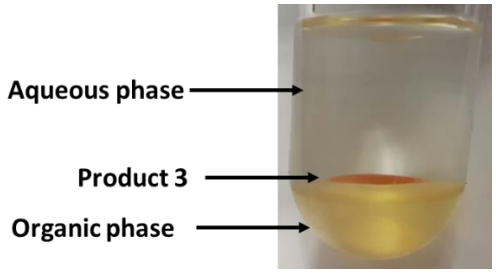

Figure 2.20. Image of the crude of alkylation reaction showing the triphasic system.

Boc-amine deprotection is usually performed in acidic, organic media (*i.e.* HCl in dioxane, or TFA in CH_2Cl_2). Instead, we opted for water at elevated temperatures, which promotes both acid- and base-catalysed reactions in an environmentally friendly way.[68,69] Compound **3** was dissolved by refluxing in water, and yielded **4** in 1 h. The exact reaction mechanism is unclear, but it likely leads to the formation of CO_2 and *tert*-butanol as the only by-products. Freeze-drying removed both from **4** in good yield (85 %).

G functionalisation was done following the same conditions than for the synthesis of Isophthalic-G but using **4** as grafting agent. The functionalisation was confirmed by Raman spectroscopy and TGA (Figure 2.21). The increase of the I_D/I_G ratio from 0.35 to 0.56 and the degree of functionalisation calculated by TGA under inert atmosphere were similar to the degree of functionalisation of isophthalic-G (*i.e.* 500 and 340 µmol g^{-1} for isophthalic-G and quaternary-G, respectively). Besides, Raman spectra revealed no sign of multiple arylation, confirming the key role played by steric hindrance on the aniline. Homogeneous distribution of the functional groups in f-G was confirmed by exploiting their affinity to reactant free gold NPs, which can be easily visualised by TEM (Figure 2.22). This approach had been successfully used in our group for f-G and f-CNTs.[33,70,71]

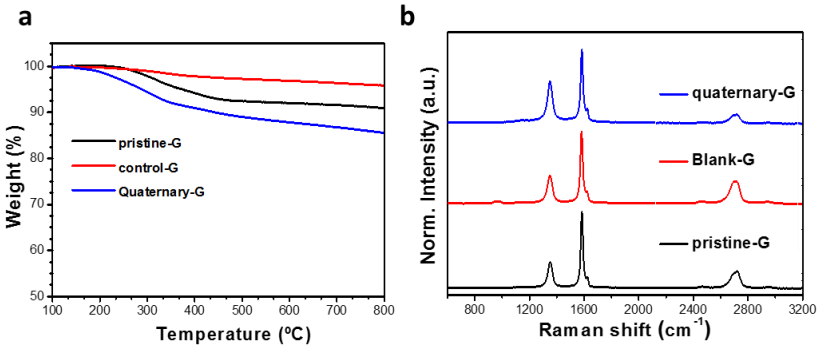

Figure 2.21. Characterisation of quaternary-G: (a) TGA under N_2; and (b) Raman analysis.

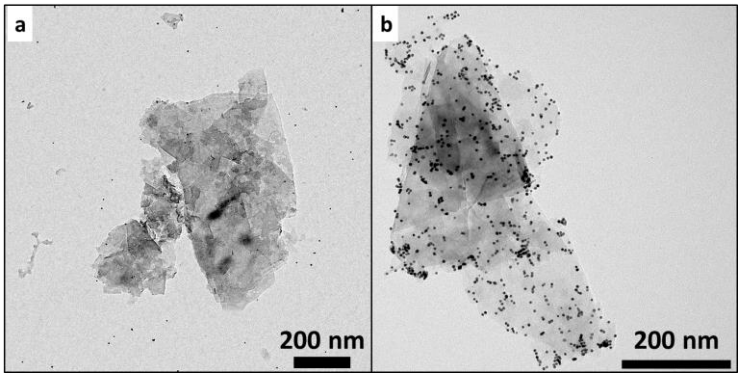

Figure 2.22. TEM images of pristine G (a) and quaternary-G after the addition of gold NPs.

Quaternary-G was thus used by our collaborators to obtain TS-1 hybrid. Unfortunately, TEM analysis revealed G flakes covered by a layer of agglomerated NPs of random shapes and sizes (Figure 2.23 a). This material is likely an amorphous titanosilicate, rather than an ordered zeolite, and may arise from the presence of iodide, which was reported to hinder zeolite crystallisation.[72]

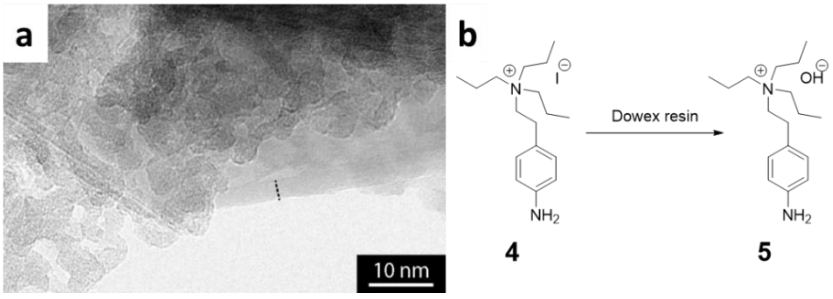

Figure 2.23. (a) TEM image of the amorphous particles present in quaternary-G-TS-1. Courtesy of Dr. Paul Gebhardt; and (b) scheme for the anion exchange.

To address this issue, Dowex® resin was used to exchange the iodide for a hydroxyl group (*i.e.* the former has affinity for the resin that is 175 times higher than the latter). The absence of iodide in aniline **5** was confirmed by ESI-MS in the negative mode.

Next, aniline **5** was grafted to G as before, to yield quaternary(OH^-)-G. Remarkably, the final TS-1 quaternary(OH^-)-G hybrids containing high amounts of f-G (*i.e.* 25 wt. %) were homogeneously covered by zeolitic NPs of 2-5 nm diameter. By contrast, hybrids containing lower levels of f-G (*i.e.* 9 wt. %) displayed amorphous material similar in appearance to Figure 2.23 a (not shown). Interestingly, by TEM no free NPs were seen, even though the materials were ultrasonicated during sample preparation. This fact underlines a strong interaction between TS-1 NPs and G, which is likely ascribed to the structural directing agent role played by the quaternary ammonium moieties on G.

Interestingly, G flakes were preserved after calcination (*i.e.* 600 ^oC, 5 h), contrarily to 10 wt. % pristine-G hybrids.[61] It is worth noting that it was reported that the presence of TiO_2 anticipates the combustion of MWCNTs,[49] while SiO_2 postpones it,[73] suggesting a stronger influence of the latter in determining the hybrid thermal behaviour. The crystal structure of the zeolites after calcination could not be properly evaluated due to the reduced particle size (*i.e.* average 4.37 nm, Figure 2.24 f), yet in the diffraction pattern TS-1 reflection weak signals could be discerned (Figure 2.24 d).

In conclusion, an intimate G-TS-1 interface was created by *ad hoc* design of G functionalisation, which prevented the aggregation of TS-1 NPs with the smallest size for the G-TS-1 hybrids reported by Eder and co-workers. We foresee a great potential of quaternary(OH^-)-TS-1 hybrid use in photocatalysis.

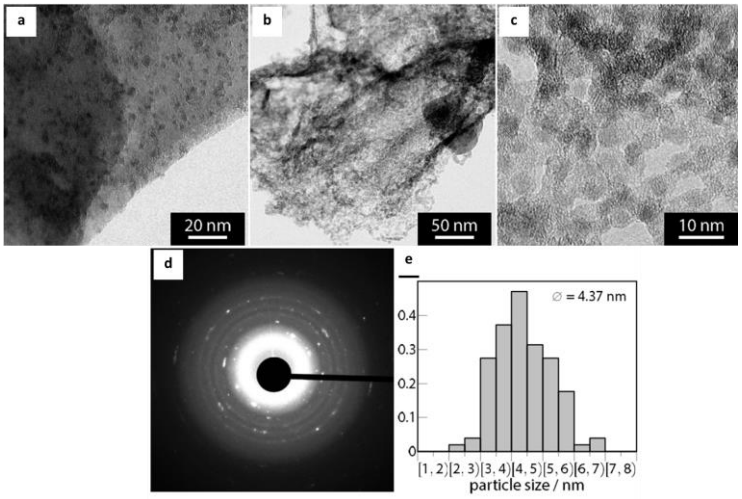

Figure 2.24. 25 wt. % G-TS-1. TEM images (a) before and (b-c) after calcination; (d) selected area electron diffraction pattern (SAEDP); and (e) NP size after calcination. Courtesy of Dr. Gebhardt.

2.3.3. CNT-fibre functionalisation for ALD growth of metal oxides for photocatalysis

CNS can assemble together or in combination with other materials making foams, films or fibres.[74–77] In this regard, CNT fibres (*i.e.*, CNF) are very attractive since they combine the mechanical properties of high-performance textiles with the superior electrical properties of CNTs. Besides, the high porosity of the as-prepared CNF will favour the interaction with materials of different nature (*e.g.* polymers or metal oxides). This part of the work was done in collaboration with Dr. Juan José Vilatela's group at IMDEA Materials Institute (Getafe, Spain) that have expertise in the synthesis and application of CNF. The CNF used in this study were synthesised by Víctor Reguero or Dr. Laura Cabana. They are synthesised through the direct spinning of the CNT aerogel produced at high temperature during the gas-phase CNT growth. When the temperature is decreased, the CNT aerogel is collected in the form of a film by wrapping the CNF around a substrate (Figure 2.25 a). The CNF can then be densified with acetone, as the capillary forces make it condense into a continuous rope (Figure 2.25 b). In this work, we have used both films and ropes made of continuously spun CNF.[78] In particular, the rope is very convenient to handle as it can bend, twist or be knitted as desired. CNF synthesis was conducted using two different carbon precursors. CNF produced from butanol are easily scalable, while those produced from toluene have better electronic properties.

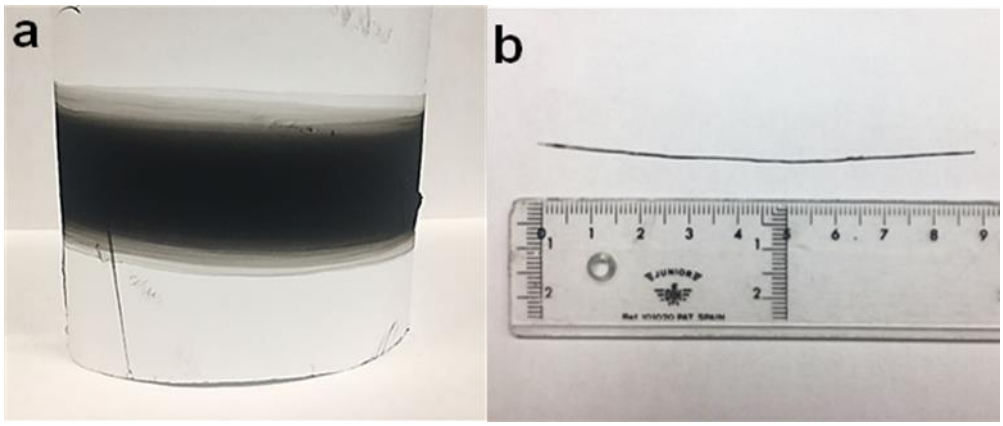

Figure 2.25. Photographs of CNF produced as film (a) or rope (b). Courtesy of Dr. Laura Cabana.

CNF can be applied in sensing, for instance to monitor resin curing, by exploiting CNT changes in resistance.[79] There are many other potential uses for CNF, however, their high hydrophobicity limits their application in water or polar solvents, giving scope for their covalent functionalisation to introduce hydrophilic groups.

Initially, protocols used for CNT and G functionalisation were attempted on CNF, including the routes described above (*i.e.* diazo coupling and acid-based oxidation), or in previous works from our group (*i.e.* 1,3-dipolar cycloaddition under microwave in the absence of solvents).[36] A summary of these preliminary experiments is reported in (Figure 2.26). TGA and Raman data confirmed functionalisation in all cases, and to a different degree according to the reaction time. However, the treatment dramatically damaged the macroscopic CNF morphology, which is essential for their potential application.

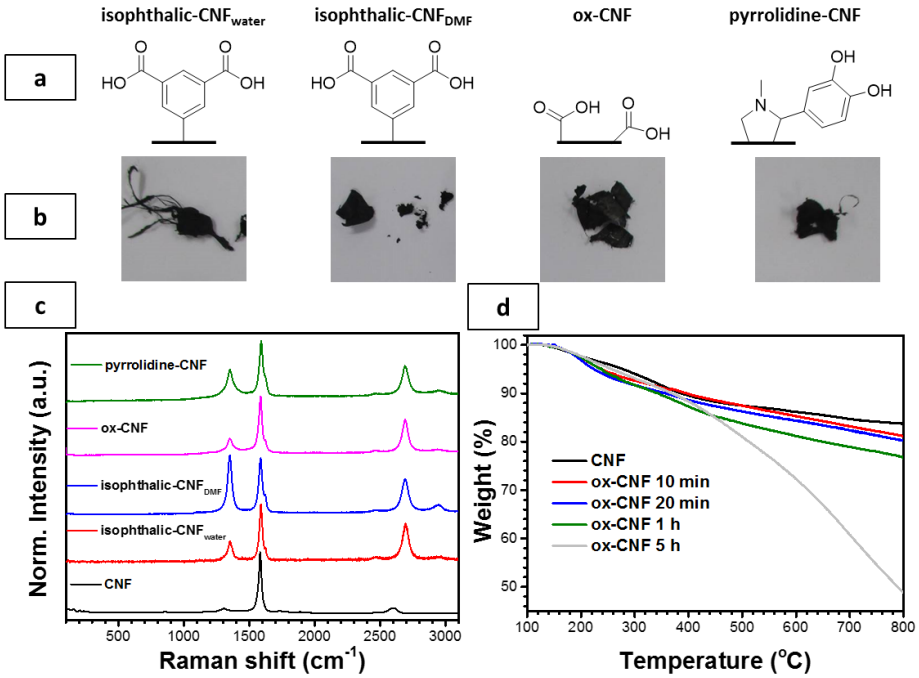

Figure 2.26. Preliminary data for CNF functionalisation by using different routes: (a) Schematic representation of the functional group linked to CNF; (b) images of the functionalised materials; (c) Raman spectra; and (d) TGA under N2 of oxidised CNF in a sulfonitric mixture.

Thus, we attempted gas-phase reactions to address this issue. Plasma oxygen, halogens or ozone are the most common gases used to functionalise CNTs.[80–83,37] The use of ozone for this purpose is of particular interest since it is easily prepared *in situ* by irradiation of air with a high energy lamp. The simplicity of this method has attracted interest during the last years for CNS functionalisation.[38,84,85]

Ozone treatment of CNF was performed using a ProCleaner^{TM} Plus. The instrument consists of a high energy light source (λ = 185 nm) that produces ozone from atmospheric oxygen. Initially, CNF ropes were treated for different reaction times to follow the process kinetics (*i.e.* 5 min, 15 min, 30 min or 2 h) by Raman analysis (Figure 2.27). Interestingly, CNF reactivity varied according to the carbon precursor used. In the case of butanol, short reaction times (*i.e.* 5 min or 15 min) were already effective (Figure 2.27 a). By contrast, in the case of toluene, I_D/I_G ratio slowly increased during the first 30 min, and bursted after 2 h. This trend could be ascribed to the incubation of defects and intermediates, as the ozonide form described by Yim and Johnson as explained below.[86]

This sort of treatment had been shown to be reversible under certain conditions, such as UV irradiation or pyrolysis at relatively low temperatures (*i.e.* 250 °C) [38.87,]For

this reason, stability of the functionalisation was assessed by monitoring the I_D/I_G ratio over time (Figure 2.27 c,d). Over 3 weeks, the level of functionalisation was very stable for butanol CNF, and showed a minor decrease during the first 7 days for toluene CNF. Therefore, CNF ozone oxidation is not spontaneously reversible at ambient conditions.

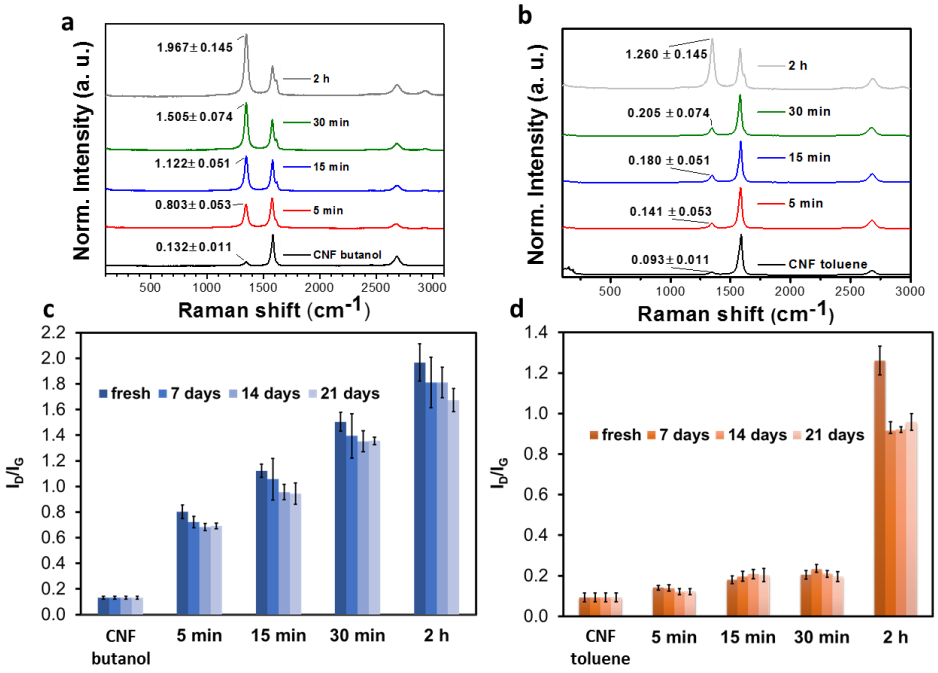

Figure 2.27. Normalised Raman spectra of pristine and functionalised CNF ropes (top). Evolution of I_D/I_G ratio over time (bottom). Data for butanol (a, c) or toluene (b, d) CNF.

TEM imaging of CNF oxidised for 30 minutes revealed damage occurring in the CNT tubular structure, while the metal catalyst was still encapsulated (Figure 2.28). TGA in air (Figure 2.29) revealed multiple steps of weight loss for the pristine CNF, while only one for ox-CNF. Considering that weight loss of graphitic material occurs at high temperatures, and that of amorphous material occurs at lower temperature, TGA suggested concomitant CNF purification. Besides, ox-CNF weight loss was anticipated by 70 °C relative to pristine CNF, confirming the presence of hydrophilic functional groups that are known to favour oxidative decomposition during calcination.

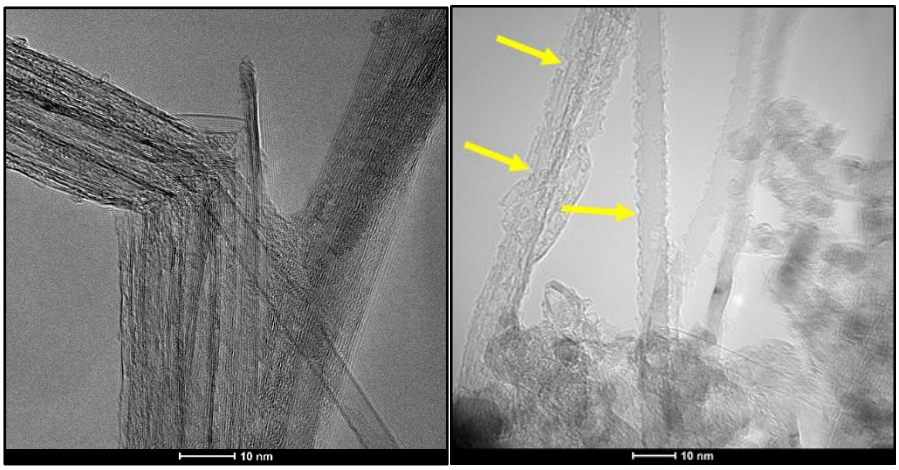

Figure 2.28. TEM image of CNF made of toluene (a) before and (b) after 30 min oxidation. The yellow arrows indicate the holes in the nanotubes. Courtesy of Dr. Laura Cabana.

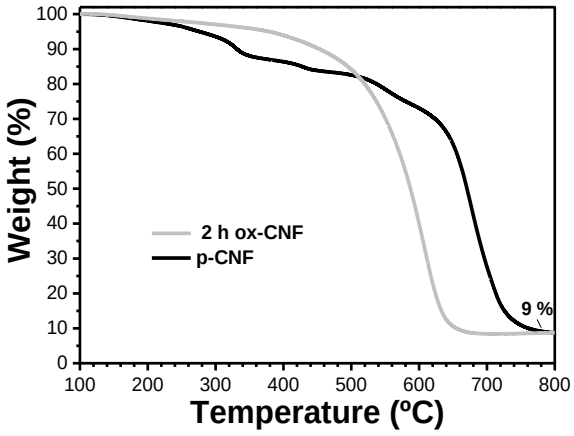

Figure 2.29. TGA under air of pristine and 2 h ozone-treated CNF made of toluene.

The identification of the functional groups introduced with ozone treatment is not straightforward since the involved reaction mechanisms are still unclear. Yim and Johnson reported a detailed *in silico* study in which two possible mechanisms were investigated (Figure 2.30).[86] Both are initiated by the formation of a five-membered heterocycle between ozone and a C=C double bond (primary ozonide, POZ). The authors analysed its evolution *via* classical Criegge's mechanism or through the formation of an epoxide intermediate. In Criegge's route, the heterocycle breaks forming a ketone and a superoxide (Criegge's intermediate) with the subsequent rupture of the C=C bond of the carbon lattice (Figure 2.30 a). This intermediate would evolve to two different lactones (very similar in energy) that would require very high energy (c. a. 39 kcal mol-1) to produce either a pyran or CNT etching, thus liberating CO and CO_2, respectively.

Alternatively, the primary ozonide forms an epoxide, liberating O_2 (Figure 2.30 b). This step has a much lower energy barrier (*i.e.* 7.9 against 17.0 in Kcal mol^{-1}) than the analogous step in Criegge's mechanism since there is no C-C bond to break. The eventual evolution of the epoxide would form an ether with affordable energetic cost at r.t.

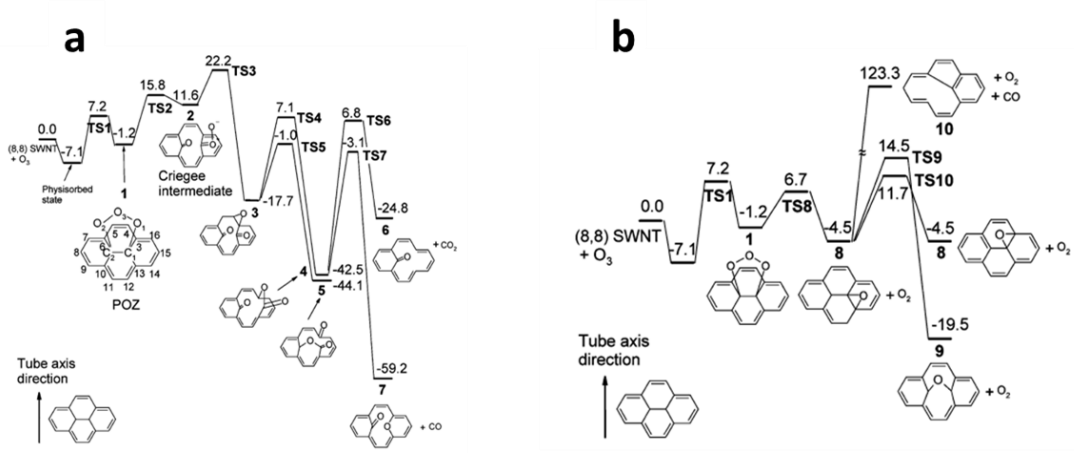

Figure 2.30. Different reaction mechanisms proposed in literature.[86]. Adapted with permission from (87). Copyright 2006 American Chemical Society.

However, XPS data on experimental works reports the presence of many different kinds of oxygen containing functional groups including carboxylic acids, alcohols, ketones and epoxides.[82,37] The mismatch between the experimental and theoretical data is explained as a consequence of side reactions between the intermediates/final products and the O_3 present in the reaction media. Therefore, XPS characterisation is required to know the nature of the functional groups linked to the CNF.

Figure 2.31 shows XPS spectra of pristine and functionalised CNF. Deconvolution of the C1s region revealed components at higher binding energies (286-289 eV) in ox-CNF relative to pristine CNF. They were originated from carbon atoms bound to oxygen with one (C-O), two (C=O) and three (O-C=O) bonds.[88] In the case of pristine CNF, the appearance of a band at higher binding energies (285.6 eV) can be due to sp^2 carbon not in a regular structure. The C1s area presented in Figure 2.31 a and c displayed two components at 288.8 eV and 285.0 eV. Figure 2.31 e shows the C% and O% obtained from XPS spectra of both pristine and functionalised toluene CNF. It is evident that the oxygen content increases with the treatment, being a clear indication of

the successful functionalisation of the CNTs. Moreover, in less than 2 hours of reaction, C and O contents are stabilised, implying no need to increase the reaction time any further.

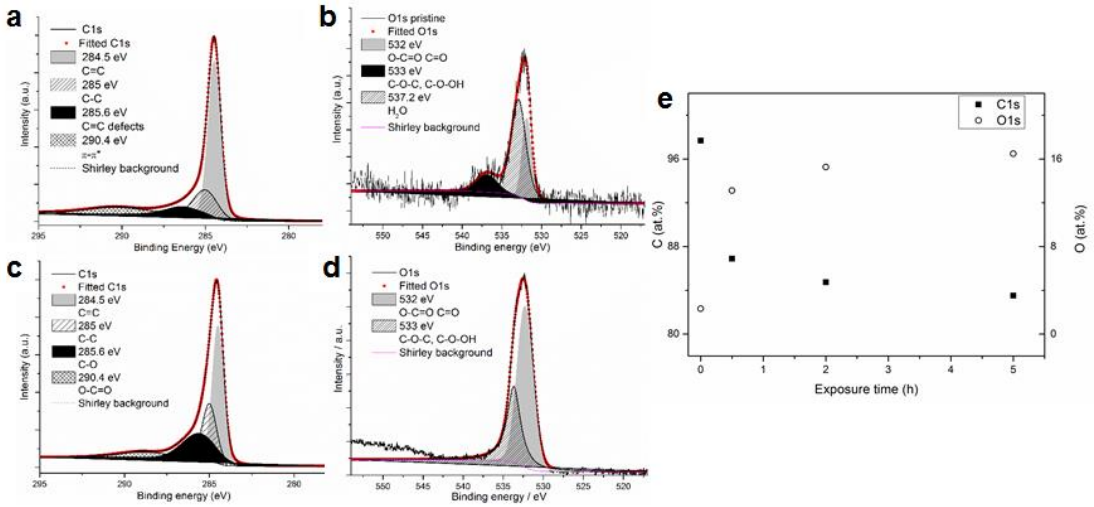

Figure 2.31. XPS spectra in the C1s region of (a) pristine and (b) ozone-treated for 30 min, toluene CNF. XPS spectra of the O1s region of (c) pristine and (d) ozone-treated for 30 min toluene CNF. e) Relative content of C% and O% depending on CNF exposure time to ozone.

Quantitative deconvolution of C1s and O 1s signals is presented in Table 2.5. Evidence of functionalisation was found in the decrease of sp^2 carbon content from ~60 % (taking into account sp^2 defects) to ~30 %, and in the appearance of C-O and O-C=O signals. Moreover, double bonds also reacted with active oxygen, as previously reported for plasma functionalisation.[88,89] The double bonds were dissociated and then reacted with active oxygen producing the C-O bonds that became C-OH. Within 30 min, oxygen content is stabilised (Figure 2.31 e).

As a proof of how functionalisation may change the properties of CNF in terms of wettability, Figure 2.32 shows a CNF rope immersed in toluene/water biphasic system. While pristine CNF remained in toluene, ox-CNF were found in water.

Table 2.5. Deconvolution of XPS spectra of toluene CNF in the C1s and O1s region. % is calculated taking into account C1s and O1s areas.

C1s	sp^2 (%)	sp^3 (%)	sp^3 defects or C-O (%)	sp^2 defects or C=O (%)	O-C=O (%)	Π- Π* (%)
pristine	50.7	15.8	0	9.2	0	18.7
30 min	37.3	8.6	16.0	0	11	0
2 h	30.1	17.1	16.1	0	6	0
5 h	32.0	12.3	10.6	0	12.3	0

O1s	C-O-C, C-O-OH (%)	O-C=O, C=O (%)	Adsorbed H_2O (%)
Pristine	3.4	1.5	0.7
30 min	10.9	16.2	0
2 h	11.4	19.3	0
5 h	17.5	15.2	0

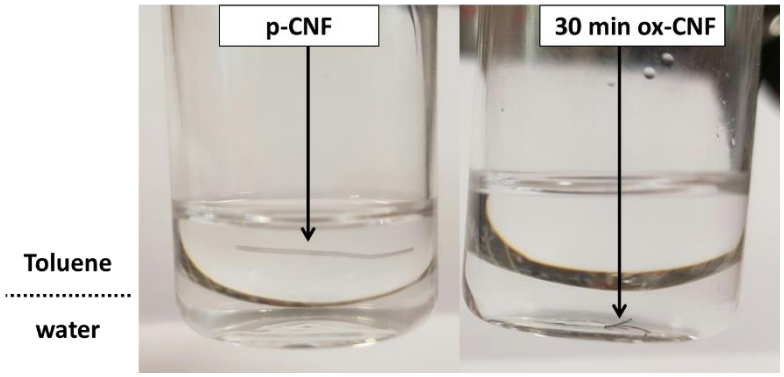

Figure 2.32. Photograph of a CNF rope immersed in toluene/water biphasic system before (left) and after (right) ozone oxidation for 30 min.

Next, the mechanical performance of CNF was assessed, and stress/strain curves are presented in Figure 2.33. Ox-CNF elongated less, yet the material became more rigid, as the tensile strength increased, with Young modulus value of 0.23 N/tex (30 min) and 0.21 N/tex (2h) relative to 0.11 N/tex of pristine CNF. Moreover, the plastic component of deformation behaviour disappeared with functionalisation, leaving only elastic behaviour. Tenacity was reduced. These results can be explained by removal of disordered amorphous carbon that provided charge paths when strain was applied to pristine CNF rope, which could elongate more than ox-CNF. However, even though

absence of amorphous carbon in ox-CNF reduced the connection points between CNTs, those became stronger, thanks to the interaction between the hydrophilic functional groups of different CNTs within the CNF. This fact results in an increase of the rigidity of the material. A similar response was reported in literature for thermal and plasma oxygen-treated CNF, [81,90] as well as in fibres that were irradiated with an electron beam.[91]

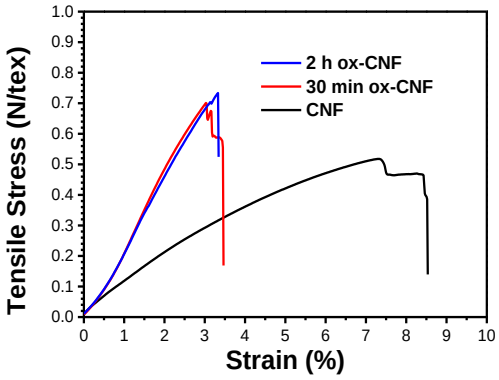

Figure 2.33. Mechanical test of pristine and functionalised toluene CNF ropes.

In terms of applications for ox-CNF so produced, although the electrical properties are compromised by this type of treatment,[37] conductivity (*e.g.* 59 S cm^{-1} and 53 cm^{-1} for 30 min and 2 h treated ox-CNF, respectively) is good enough for their implementation in devices, such as sensors or supercapacitors.

Pristine CNF are so hydrophobic that their electrical conductivity suffers no modification when they are immersed in water, as there is no water infiltration within the CNT bundles. However, when ox-CNF were immersed in water, their electrical resistance dramatically increased up to 60% or almost 100%, depending on the degree of functionalisation (Figure 2.34 a). The change in resistance occurred within seconds, and it was not due to a loss of ox-CNF Ohmic response in water or after functionalisation (Figure 2.34 b). This change in the resistance of ox-CNF also confirmed the increased hydrophilicity. This behaviour could be exploited in industrial procedures where water generation is indicative of evolution of a specific process.

Such enhanced hydrophilicity of ox-CNF significantly extended CNF application in supercapacitors (in collaboration with Evgeny Senokos, IMDEA Materials). CNF electrochemical behaviour had demonstrated promising potential as multifunctional

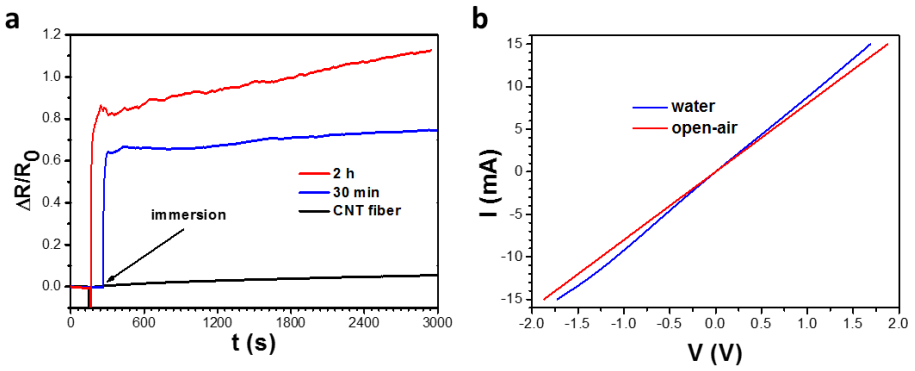

Figure 2.34. (a) Resistance response of pristine and ox-CNF immersed in water. (b) I vs V curve from -1.8 to 1.8 V on 2 h treated toluene CNF under water and in open-air conditions.

electrode for all-solid and flexible electric double layer capacitors (EDLCs).[92] However, despite the good performance achieved in ionic liquids, CNF electrochemical application remained limited thus far in aqueous electrolytes due to poor water infiltration. CNF oxidation reported herein enabled use of water-based electrolytes with low cost and high ionic conductivity, which are both attractive for high power density applications. Besides, it increased the specific capacitance of the CNF due to reversible redox reactions of oxygen-containing functional groups.

To characterise the electrochemical performance of ox-CNF, samples of similar weight were tested by CV in 3-electrode cell. The results are shown in Figure 2.35. CV curves indicated presence of two peaks at -0,35V and -0,45V (vs Hg_2Cl_2) corresponding to redox reactions of carboxylic groups. Longer functionalisation times resulted in an evident increase of the peak area due to higher concentration of functional groups providing pseudocapacitive response. Moreover, the increase of CV curves total area confirmed improved electrochemical properties for ox-CNF. This could be ascribed to better infiltration of aqueous electrolyte in the electrode material, which resulted in higher specific surface area available for electrolyte ions.

Specific capacitance calculated at different scan rates by integrating the area under CV curves and normalising by mass of active material is presented in Figure 2.35 b. Specific capacitance obtained at 5 mV s^{-1} for samples functionalised for 5 min and 2 h doubled from 23 F g^{-1} to 46 F g^{-1}, respectively. This data was in agreement with the hypothesis of higher pseudocapacitive contribution to the total capacitance of ox-CNF. Moreover, the capacitance drop observed for 2 h treated toluene CNF (*i.e.* from 46 F g^{-1}

to 42 F g^{-1}) at higher scan rate showed excellent rate capability. Specific capacitance for ox-CNF was comparable to that of pristine CNF characterised in ionic liquid electrolyte with 2-3 times higher potential window,[92] while rate capability was significantly improved. Overall, such data demonstrated great prospects for ox-CNF use in supercapacitors.

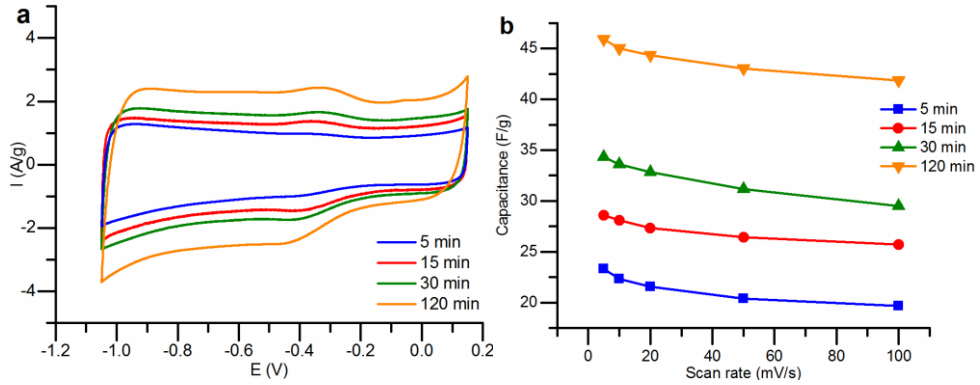

Figure 2.35. (a) CV curves at scan rates of 50 mV/s and (b) capacitance plot obtained for ox-CNF with different treatment time. Courtesy of Evgeny Senokos.

2.4. Conclusions

CNS covalent functionalisation for hybridisation with TiO_2 fibres was successfully demonstrated. Different functional groups were introduced both by means of oxidation protocols and diazo coupling, in a stable and reproducible way. Photocatalytic performance of the so-obtained electrospun hybrids highlighted short-ox-MWCNTs as ideal CNS candidates for this application.

Functionalisation of G was developed using green protocols. This project showed the strong influence that functional groups might have for the *in situ* growth of inorganic components toward hybrids. The obtained hybrid quaternary(OH^-)-zeolite appeared a promising material for photocatalysis, due to the small particle size of nanocrystals, close interaction with G and likely higher surface area.

Functionalisation of CNF was achieved by UV-generated ozone treatment with overall preservation of their macroscopic morphology. Although the CNT components were damaged ay the oxidative treatment, ox-CNF resulted to be more hydrophilic relative to pristine CNF, allowing their electronic characterisation in water, and with very promising results in the field of supercapacitors. Eventually, the hydrophilicity of ox-CNF could be exploited in ALD processes to hybridise the materials with metal oxides.

2.5. References

(1) Zhang, X.; Li, R.; Jia, M.; Wang, S.; Huang, Y.; Chen, C. *Chem. Eng. J.* **2015**, *274*, 290–297.

(2) Houas, A.; Lachheb, H.; Ksibi, M.; Elaloui, E.; Guillard, C.; Herrman, J.-M. *Appl. Catal. B Environ.* **2001**, *31*, 145–157.

(3) Im, J. H.; Yang, S. J.; Yun, C. H.; Park, C. R. *Nanotechnology* **2011**, *23*, 35604.

(4) Zhang, Y.; Zhang, N.; Tang, Z.-R.; Xu, Y.-J. *Phys. Chem. Chem. Phys.* **2012**, *14*, 9167–9175.

(5) Henderson, M. A. *Surf. Sci. Rep.* **2011**, *66*, 185–297.

(6) Melchionna, M.; Prato, M.; Fornasiero, P. *Catal. Today* **2016**, *277*, 202–213.

(7) Tian, L.; Ye, L.; Deng, K.; Zan, L. *J. Solid State Chem.* **2011**, *184*, 1465–1471.

(8) Melchionna, M.; Beltram, A.; Montini, T.; Monai, M.; Nasi, L.; Fornasiero, P.; Prato, M. *Chem. Commun.* **2016**, *52*, 764–767.

(9) Hu, X.; Wang, T.; Dong, S. *J. Nanosci. Nanotechnol.* **2006**, *6*, 2056–2061.

(10) Yang, W.; Wang, X.; Yang, F.; Yang, C.; Yang, X. *Adv. Mater.* **2008**, 2579–2587.

(11) Rahman, G. M. A.; Guldi, D. M.; Zambon, E.; Pasquato, L.; Tagmatarchis, N.; Prato, M. *Small* **2005**, *1*, 527–530.

(12) He, F.; Fan, J.; Ma, D.; Zhang, L.; Leung, C.; Chan, H. L. *Carbon* **2010**, *48*, 3139–3144.

(13) Shearer, C. J.; Cherevan, A.; Eder, D. *Adv. Mater.* **2014**, *26*, 2295–2318.

(14) Zhang, J.; Lei, J.; Pan, R.; Leng, C.; Hu, Z.; Ju, H. *Chem. Commun.* **2011**, *47*, 668–670.

(15) Piovesana, S.; Capriotti, A. L.; Cavaliere, C.; Ferraris, F.; Iglesias, D.; Marchesan, S.; Lagana, A. *Anal. Chem.* **2016**, *88*, 12043–12050.

(16) Adhikari, B.; Biswas, A.; Banerjee, A. *Appl. Mater. Interfaces* **2012**, *4*, 5472–5482.

(17) Hench, L. L.; West, J. K. *Chem. Rev.* **1990**, *90*, 33–72.

(18) Moya, A.; Cherevan, A.; Marchesan, S.; Gebhardt, P.; Prato, M.; Eder, D.; Vilatela, J. J. *Appl. Catal. B Environ.* **2015**, *179*, 574–582.

(19) Lan, Y.; Li, X.; Li, G.; Luo, Y. *J. Nanoparticle Res.* **2015**, *17*, 395.

(20) Grobert, N.; Chu, B. T. T.; Tobias, G.; Salzmann, C. G.; Todd, R. I.; Green, M. L. H. *J. Mater. Chem.* **2008**, *44*, 5344–5349.

(21) Innocenzi, P.; Malfatti, L.; Lasio, B.; Pinna, A.; Loche, D.; Casula, M. F.; Alzari, V.; Mariani, A. *New J. Chem.* **2014**, *38*, 3777–3782.

(22) Hu, H.; Dong, B.; Hu, H.; Chen, F.; Kong, M.; Zhang, Q.; Luo, T.; Zhao, L.; Guo, Z.; Li, J.; Xu, Z.; Wang, S.; Eder, D.; Wan, L. *ACS Appl. Mater. Interfaces* **2016**, *8*, 17999–18007.

(23) Cherevan, A. S.; Gebhardt, P.; Shearer, C. J.; Matsukawa, M.; Domen, K.; Eder, D. *Energy Environ. Sci.* **2014**, *7*, 791–796.

(24) Acauan, L.; Dias, A. C.; Pereira, M. B.; Horowitz, F.; Bergmann, C. P. *ACS Appl. Mater. Interfaces* **2016**, *8*, 16444–16450.

(25) Barrejon, M.; Pla, S.; Berlanga, I.; G, M. J. G.-E.; Martin-Gomis, L.; Fierro, L. G.; Zhang, M.; Yudasaka, M.; Langa, F. *J. Mater. Chem. C* **2015**, *3*, 4960–4969.

(26) Beltram, A.; Melchionna, M.; Montini, T.; Nasi, L.; Gorte, R. J.; Prato, M.; Fornasiero, P. *Catal. Today* **2015**, *253*, 142–148.

(27) Karousis, N.; Tagmatarchis, N.; Tasis, D. *Chem. Rev.* **2010**, *110*, 5366–5397.

(28) Tasis, D.; Tagmatarchis, N.; Bianco, A.; Prato, M. *Chem. Rev.* **2006**, *106*, 1105–1136.

(29) Chua, C. K.; Pumera, M. *Chem. Soc. Rev.* **2013**, *42*, 3222.

(30) Wu, H.; Chang, X.; Liu, L.; Zhao, Y. *J. Mater. Chem.* **2010**, *20*, 1036–1052.

(31) Jain, S.; Thakare, V. S.; Das, M.; Godugu, C.; Jain, A. K.; Mathur, R.; Chuttani, K.; Mishra, A. K. *Chem. Res. Toxicol.* **2011**, *24*, 2028–2039.

(32) Ali-boucetta, H.; Nunes, A.; Sainz, R.; Herrero, M. A.; Tian, B.; Prato, M.; Bianco, A.; Kostarelos, K. *Angew. Chemie - Int. Ed.* **2013**, *52*, 2274–2278.

(33) González-Domínguez, J. M.; Santidrín, A.; Criado, A.; Hadad, C.; Da Ros, T.; Kalbàc, M. *Chem. - A Eur. J.* **2015**, *21*, 18631–18641.

(34) Rubio, N.; Herrero, M. A.; Meneghetti, M.; Díaz-Ortiz, Á.; Schiavon, M.; Prato, M.; Vázquez, E. *J. Mater. Chem.* **2009**, *19*, 4407.

(35) Criado, A.; Melchionna, M.; Marchesan, S.; Prato, M. *Angew. Chemie - Int. Ed.* **2015**, *54*, 10734–10750.

(36) Rubio, N.; Herrero, M. A.; de la Hoz, A.; Meneghetti, M.; Prato, M.; Vázquez, E. *Org. Biomol. Chem.* **2010**, *8*, 1936–1942.

(37) Simmons, J. M.; Nichols, B. M.; Baker, S. E.; Marcus, M. S.; Castellini, O. M.; Lee, C.; Hamers, R. J.; Eriksson, M. A. *J. Phys. Chem. B* **2006**, *110*, 7113–7118.

(38) Mulyana, Y.; Uenuma, M.; Ishikawa, Y.; Uraoka, Y. *J. Phys. Chem. C* **2014**, *118*, 27372–27381.

(39) CARINHYPH Project www.carinhyph.eu.

(40) Molina-Mendoza, A. J.; Moya, A.; Frisenda, R.; Svatek, S. A.; Gant, P.; Gonzalez-Abad, S.; Antolin, E.; Agraït, N.; Rubio-Bollinger, G.; Perez de Lara, D.; Vilatela, J. J.; Castellanos-Gomez, A. *J. Mater. Chem. C* **2016**, *4*, 10707–10714.

(41) Li, D.; Xia, Y. *Adv. Mater.* **2004**, *16*, 1151–1170.

(42) Chronakis, I. S. *J. Mater. Process. Technol.* **2005**, *167*, 283–293.

(43) Price, B. K.; Tour, J. M. *J. Am. Chem. Soc.* **2006**, *128*, 12899–12904.

(44) Lotya, M.; King, P. J.; Khan, U.; De, S.; Coleman, J. N. *ACS Nano* **2010**, *4*, 3155–3162.

(45) Verónica León. Non-conventional techniques for the generation and modification of graphenes: applications to the synthesis of electro-active scaffolds for on demand drug delivery, University of Trieste, 2014.

(46) Greenwood, J.; Phan, T. H.; Fujita, Y.; Li, Z.; Ivasenko, O.; Vanderlinden, W.; Van Gorp, H.; Frederickx, W.; Lu, G.; Tahara, K.; Tobe, Y.; Uji-i, H.; Mertens, S. F. L.; De Feyter, S. *ACS Nano* **2015**, *9*, 5520–5535.

(47) Hurum, D. C.; Gray, K. A.; Rajh, T.; Thurnauer, M. C. *J. Phys. Chem. B* **2005**, *109*, 977–980.

(48) Zhang, J.; Xu, Q.; Feng, Z.; Li, M.; Li, C. *Angew. Chemie - Int. Ed.* **2008**, *47*, 1766–1769.

(49) Aksel, S.; Eder, D. *J. Mater. Chem.* **2010**, *20*, 9149–9154.

(50) Zhu, K. R.; Zhang, M. S.; Chen, Q.; Yin, Z. *Phys. Lett. A* **2005**, *340*, 220–227.

(51) Eder, D.; Windle, A. H. *J. Mater. Chem.* **2008**, *18*, 2036–2043.

(52) An, T.; Chen, J.; Nie, X.; Li, G.; Zhang, H.; Liu, X.; Zhao, H. *ACS Appl. Mater. Interfaces* **2012**, *4*, 5988–5996.

(53) Pan, X.; Zhao, Y.; Liu, S.; Korzeniewski, C. L.; Wang, S.; Fan, Z. *Appl. Mater. Interfaces* **2012**, *4*, 3944–3950.

(54) Nair, A. S.; Peining, Z.; Babu, V. J.; Shengyuan, Y.; Ramakrishna, S. *Phys. Chem. Chem. Phys.* **2011**, *13*, 21248–21261.

(55) Sadhu, S.; Poddar, P. *J. Phys. Chem. C* **2014**, *118*, 19363–19373.

(56) Yang, L.; Luo, S.; Liu, S.; Cai, Q. *J. Phys. Chem. C* **2008**, *112*, 8939–8943.

(57) Naebe, M.; Lin, T.; Wang, X. *Carbon Nanotubes Reinforced Electrospun Polymer Nanofibres, Nanofibers*; Kumar, A., Ed.; InTech, 2010.

(58) Zhu, K.; Neale, N. R.; Miedaner, A.; Frank, A. J. *Nano Lett.* **2007**, *7*, 69–74.

(59) Dror, Y.; Salalha, W.; Khalfin, R. L.; Cohen, Y. *Langmuir* **2003**, No. 11, 7012–7020.

(60) Cundy, C. S.; Cox, P. a. *Chem. Rev.* **2003**, *103*, 663–702.

(61) Ren, Z.; Kim, E.; Pattinson, S. W.; Subrahmanyam, K. S.; Rao, C. N. R.; Cheetham, a. K.; Eder, D. *Chem. Sci.* **2012**, *3*, 209–216.

(62) Choi, M.; Cho, H. S.; Srivastava, R.; Venkatesan, C.; Choi, D.-H.; Ryoo, R. *Nat.*

Mater. **2006**, *5*, 718–723.

(63) Gebhardt, P.; Pattinson, S. W.; Ren, Z.; Cooke, D. J.; Elliott, J. a; Eder, D. *Nanoscale* **2014**, *6*, 7319–7324.

(64) Notari, B. *Structure-Activity and Selectivity Relationships in Heterogeneous Catalysis*; Grasselli, R. K., A.W. Sleight, Eds.; Elsevier Science Publishers B.V., Amsterdam, 1991.

(65) Krissanasaeranee, M.; Wongkasemjit, S.; Cheetham, A. K.; Eder, D. *Chem. Phys. Lett.* **2010**, *496*, 133–138.

(66) Perron, V.; Abbott, S.; Moreau, N.; Lee, D.; Penney, C.; Zacharie, B. *Synthesis* **2009**, *2*, 283–289.

(67) Ju, Y.; Varma, R. S. *Org. Lett.* **2005**, *7*, 2409–2411.

(68) Wang, J.; Liang, Y.-L.; Qu, J. *Chem. Commun.* **2009**, 5144–5146.

(69) Medina-Ramos, W.; Mojica, M. A.; Cope, E. D.; Hart, R. J.; Pollet, P.; Eckert, C. A.; Liotta, C. L. *Green Chem.* **2014**, *16*, 2147–2155.

(70) Quintana, M.; Montellano, A.; Castillo, R.; Tendello, G. Van; Bittencourt, C.; Prato, M. **2011**, *47*, 9330–9332.

(71) Quintana, M.; Spyrou, K.; Grzelczak, M.; Browne, W. R.; Rudolf, P.; Prato, M. *ACS Nano* **2010**, *4*, 3527–3533.

(72) Toktarev, A. V; Echevskii, G. V. *Pet. Chem.* **2009**, *49*, 33–38.

(73) Bourlinos, A. B.; Georgakilas, V.; Zboril, R.; Dallas, P. *Carbon* **2007**, *45*, 2136–2139.

(74) Niu, Z.; Chen, J.; Hng, H. H.; Ma, J.; Chen, X. *Adv. Mater.* **2012**, *24*, 4144–4150.

(75) Tang, C.; Long, G.; Hu, X.; Wong, K.; Lau, W.; Fan, M.; Mei, J.; Xu, T.; Wang, B.; Hui, D. *Nanoscale* **2014**, *6*, 7877–7888.

(76) Wu, Z.; Wu, Z.; Chen, Z.; Du, X.; Logan, J. M.; Sippel, J.; Nikolou, M.; Kamaras, K.; Reynolds, J. R.; Tanner, D. B.; Hebard, A. F.; Rinzler, A. G. *Science* **2013**, *305*, 1273–1276.

(77) Koziol, K.; Vilatela, J.; Moisala, A.; Motta, M.; Cunniff, P.; Sennett, M.; Windle, A. *Science* **2007**, *318* (5858), 1892–1895.

(78) Li, Y.-L.; Kinloch, I. A.; Windle, A. H. *Science* **2004**, *304* (5668), 276–278.

(79) Fernández-Toribio, J. C.; Íñiguez-Rábago, A.; Vilà, J.; González, C.; Ridruejo, Á.; Vilatela, J. J. *Adv. Funct. Mater.* **2016**, *26*, 7139–7147.

(80) Kim, J. H.; Kim, D. Y.; Jeong, E.; Lee, Y. S. *Appl. Surf. Sci.* **2016**, *360*, 1009–1015.

(81) Park, O.-K.; Young Kim, W.; Min Kim, S.; You, N.-H.; Jeong, Y.; Su Lee, H.; Ku, B.-C. *Mater. Lett.* **2015**, *156*, 17–20.

(82) Pal, P. P.; Larionova, T.; Anoshkin, I. V.; Jiang, H.; Nisula, M.; Goryunkov, A. A.; Tolochko, O. V.; Karppinen, M.; Kauppinen, E. I.; Nasibulin, A. G. *J. Phys. Chem. C* **2015**, *119*, 27821–27828.

(83) Byl, O.; Liu, J.; Yates, J. T. *Langmuir* **2005**, *21*, 4200–4204.

(84) Cataldo, F.; Putz, M. V.; Ursini, O.; Hafez, Y.; Iglesias-Groth, S. *Fullerenes, Nanotub. Carbon Nanostructures* **2015**, *23*, 1095–1102.

(85) Cataldo, F.; Iglesias-Groth, S. *Fullerenes, Nanotub. Carbon Nanostructures* **2015**, *23*, 253–258.

(86) Yim, W.; Johnson, J. K. *J. Phys. Chem. C* **2009**, *113*, 17636–17642.

(87) Aria, A. I.; Gharib, M. *Langmuir* **2011**, *27*, 9005–9011.

(88) Ago, H.; Kugler, T.; Cacialli, F.; Salaneck, W. R.; Shaffer, M. S. P.; Windle, A. H.; Friend, R. H. *J. Phys. Chem. B* **1999**, *103*, 8116–8121.

(89) Chen, C.; Liang, B.; Ogino, A.; Wang, X.; Nagatsu, M.; Chen, C.; Liang, B.; Ogino, A.; Wang, X.; Nagatsu, M. *J. Phys. Chem. C* **2009**, *113*, 7659–7665.

(90) Li, W.; Xu, F.; Wang, Z.; Wu, J.; Liu, W.; Qiu, Y. *Mater. Lett.* **2016**, *183*, 117–121.

(91) Miller, S. G.; Williams, T. S.; Baker, J. S.; Sola, F.; Lebron-Colon, M.; McCorkle, L. S.; Wilmoth, N. G.; Gaier, J.; Chen, M.; Meador, M. A. *ACS Appl. Mater. Interfaces* **2014**, *6*, 6120–6126.

(92) Senokos, E.; Reguero, V.; Palma, J.; Vilatela, J.; Marcilla, R. *Nanoscale* **2016**, *8*, 3620–3628.

CHAPTER 3

In situ polymerisation on carbon nanostructures for electrocatalysis

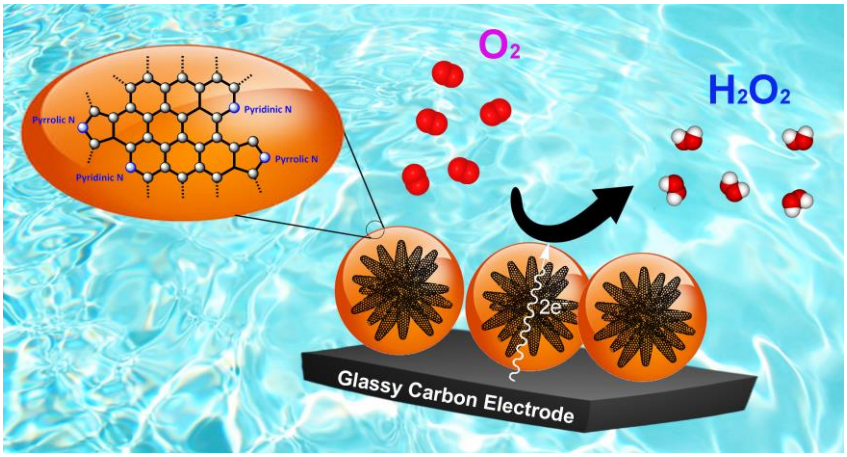

3.1. Introduction

Polymers comprehend a vast class of macromolecules that are formed by a large number of repeating structural units (*i.e.* monomers) covalently linked to each other, or non-covalently linked in the so-called supramolecular polymers. The number of monomers and their organisation give rise to different types of polymers: linear, branched, alternating copolymers, block copolymers, etc. Polymers can also be classified as natural (*e.g.* polydopamine or cellulose), semi-synthetic (*i.e.*, their derivatives), or synthetic (*e.g.* nylon or polypropylene). Over the years, many approaches were developed for polymer synthesis (*e.g.* radical, reversible addition-fragmentation chain transfer, photo-polymerisation, atom-transfer radical polymerisation, oxidative polymerisation, etc.). Besides, they can be inorganic or organic depending on monomer chemical nature.

Today, research on polymers is directed towards the development of functional and smart polymers.[1,2] Smart refers to materials responsive to changes in the environment, while the term functional is related to the chemical activity of the material. The implementation of functional polymers has been explored in applications such as solar devices or catalysis to avoid the use of expensive metals in more environmentally friendly processes. Figure 3.1 includes some promising examples for solar cells devices and polymer catalysts.

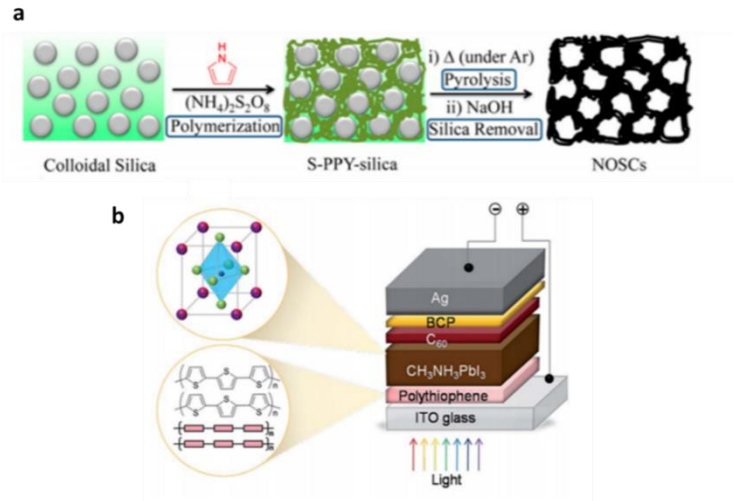

Figure 3.1. (a) Schematic representation of the synthesis of a calcined polyaniline based catalyst for the oxygen reduction reaction, [3] adapted with permission from (3). © 2017 American Chemical Society; and (b) scheme of dye-sensitised solar cells built up using polythiophene,[4] adapted from (4) with permission of The Royal Society of Chemistry.

These examples reflect in turn, that the combination of the mature polymer technology with younger scientific disciplines such as nanotechnology, could afford exceptional results in many different applications. Such combination has been exploited during the last years to prepare materials very diverse in nature. For instance, the innovative metamaterials prepared by Gómez-Graña *et al.* by step-wise combination of silica nanoparticles, a cationic polymer electrolyte, and silver NPs.[5]

CNS hybridisation with polymers is being studied nearly since CNT discovery in 1991.[6] Mamedov *et al.* reported some of the first examples of successful hybridisation between CNTs and polymers.[7] The authors followed a layer-by-layer strategy to prepare free-standing membranes with tensile stress values close to hard ceramics.

The high interest of the scientific community on polymer-CNS combinations is reflected in the large number of publications (>20,000 in the last two decades). Advances in this field brought some of these materials to the market. For example, Nanotect® (Takenaka Seisakusho Co., Ltd.) is a robust CNT-polymer composite that alleviates corrosion and damage caused by external impacts. Thus, this product can be applied in many different applications such as aircrafts or chemical plant components (Figure 3.2).

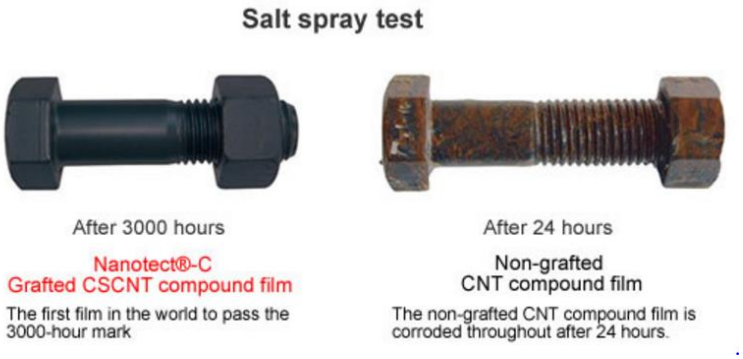

Figure 3.2. Example of a screw coated with Nanotect® and a normal screw upon corrosion with a salt spray (http://www.takenaka-mfg.com/technologies/nanotect.html).

3.1.1. Non-covalent functionalisation of CNS

In the examples illustrated above, the polymer coating is chemically grafted onto the wall of CNTs with the consequent damage of some of the properties of the nanomaterial (*e.g.* conductivity). Preservation of CNS electronic properties can be

achieved by means of non-covalent approaches that do not disrupt the conjugated sp^2 structure.[8] In this case, there is a vast array of non-covalent interactions that can be used with π-π stacking, CH-π, NH-π or hydrophobic forces amongst the most popular options. Non-covalent approaches present pros and cons relative to covalent protocols. Experimental procedures are much simpler in the former case, although long-term stability is a notorious issue.

In general, ultrasonication of the different components in the appropriate solvent is sufficient to hybridise the materials. Next, the removal of the unbound molecules is carried out by sonication/filtration cycles, dialysis, centrifugation, etc. In the literature, the most common adjuvants used for the non-covalent functionalisation of CNS are discrete aromatic molecules or surfactants (*e.g.* pyrene, sodium dodecyl sulphate, respectively) and polymers.[9–12]

Aromatic molecules or surfactants create a micelle-like structure, in which hydrophobic motifs interact with the CNS and the more polar motifs face the solution. Therefore, inherent to the formation of these systems there is an equilibrium between free and bound molecules. The presence of unbound compounds is essential to get stable solutions that otherwise would form aggregates upon dilution/purification (Figure 3.3).

For the functionalisation of tubular CNS, such as CNTs, the use of polymers is an attractive alternative, since they can afford more stable materials. Polymer chains are generally long enough to literally wrap the CNTs all around their curved surface. This wrapping appears stable towards dilution/purification, thus offering many possibilities to the application of CNS-polymer systems. Depending on the final use, it may be preferable to eventually remove the polymer, especially when the organic residue reduces the device performance, for instance in semi-conducting applications.[13] In this case, polymers act merely as dispersants for CNS. For example, Mulla *et al.* recently reported the selective dispersion of semiconducting SWCNTs using a π-conjugated polymer.[14] Once isolated, the interaction between the polymer and SWCNTs can be break by electrolysis of the polymer or solvent changing, appearing as a very interesting strategy obtain high-quality SWCNTs. In literature, examples exist whereby the polymer forms also the bulk composite and improves the performance by direct blending;[15] or whereby a polymer like polyacrylic acid wraps CNTs that are embedded in a different matrix, such as a protein hydrogel.[16]

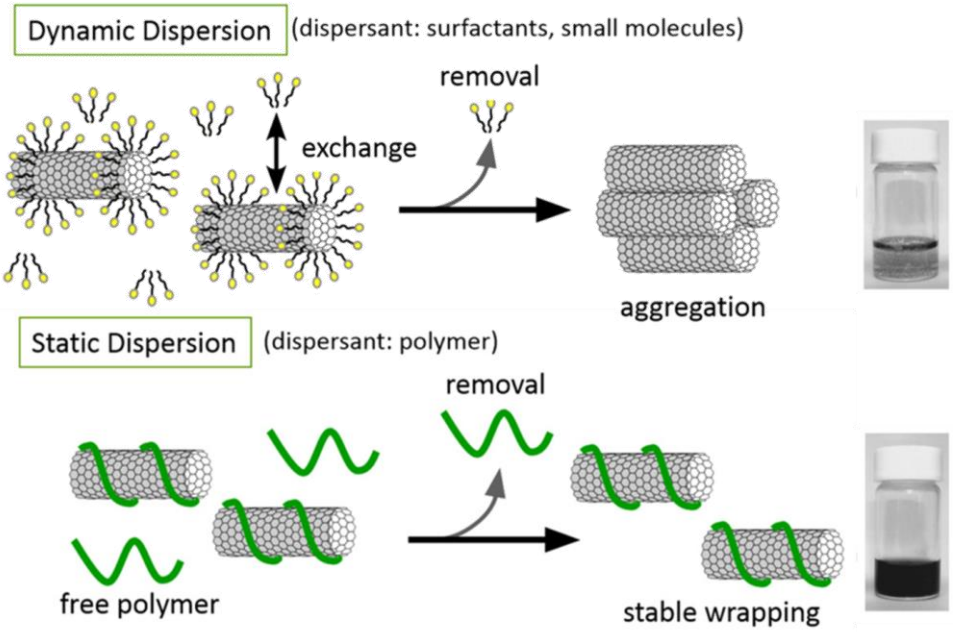

Figure 3.3. Different types of non-covalent interaction depending on the dispersant used. Adapted from reference (12) © 2015 IOP Publishing.

Functional polymers confer new properties to CNS and are necessary in the final application. For instance, use of polymers with visible light absorbance is useful to prepare dye-sensitised polymer solar cells.[17] For this application, poly(3-alkyl-thiophenes)-CNT materials are typically exploited. Advances in this field go together with advances in the successful isolation of semiconducting SWCNTs (from mixtures containing also metallic SWCNTs), since the HOMO-LUMO match between the donor (polymer) and the acceptor (metallic SWCNTs) does not favour charge separation.[18] Interestingly, as reported by Lee *et al.* poly(3-alkylthiophene)s can be also used to isolate semiconducting SWCNTs.[19] Besides, such combinations appeared mutually convenient since, on one hand, the polymer gives light response to the SWCNTs, and on the other hand, CNTs increase polymer photo-stability and extend device lifetime.[20]

Also biological polymers, such as proteins (refer to Chapter 4 for details) or DNA, can wrap around CNS. SWCNTs coated with single-stranded DNA were designed for electronic detection of various small molecules (*e.g.* alkyl amines, alcohols, carboxylic acid, etc.), for application in the area of 'electronic noses' or 'electronic tongues' (*i.e.* sensors with molecular recognition in air or water, respectively).[21] Polymer-wrapped CNS find also application in electrocatalysis, both as support for metal catalysts;[22] or for the generation of N-doped coated CNS (see section 3.1.3 for details).[23]

3.1.1.1. *In situ* polymerisation on CNS

In situ polymerisation directly on CNS is an attractive alternative that offers many advantages: i) possibility to disperse higher amounts of CNS; ii) convenient formation of polymers that otherwise are difficult to handle (*e.g.* due to low solubility or thermal instability); and iii) generation of intimate polymer-CNS interface. For example, polyaniline is a rigid polymer that aggregates in small particles with low specific surface area, thus polymer wrapping is more challenging than *in situ* polymerisation, which is often the preferred choice.[24,25] Fang *et al.* reported an example of a typical procedure, whereby the monomer is first dispersed with the CNS in the reaction media, and then polymerisation is initiated by the addition of an oxidant (*e.g.* ammonium persulfate).[26] CNS dispersion is facilitated *via* non-covalent interaction with the monomer. Besides, it was demonstrated that CNTs used as template for the polymerisation do not alter the structure or the crystallinity of the polymer.[27] Similarly, *in situ* polymerisation was applied to coat CNS with polypyrrole,[28] nylon,[29] polyethylene,[30] polystyrene,[31] polydopamine (PDA),[32] etc. with different properties and uses in each case. For instance, polystyrene is excellent for the dispersion of MWCNTs in polymer matrices but less effective to disperse thinner tubes such as DWCNTs.[31] Conducting polymers, such as polyaniline, polypyrrole or poly-(3,4-ethylenedioxythiophene), are useful for the construction of supercapacitors.[33]

3.1.1.2. CNS coated with polydopamine (PDA)

PDA is formed upon oxidative polymerisation of dopamine (3,4-dihydroxyphenethylamine, Figure 3.4). This universally-adhesive biopolymer can coat virtually any kind of material ranging from MWCNTs,[34] GO,[35] SnO_2 NPs,[36] SiO_2/Si,[37] to even tomatoes.[38] Research on polydopamine coatings attracted wide interest (*i.e.* approximately 1,000 research articles) since the first report of Lee *et al.*.[39] This boom is well-understood on the basis of the polymer properties:

1. Biocompatibility. PDA was found to be one of the major components of the natural glue used by mussels to adhere to different surfaces in nature.[40] Importantly, biocompatible coatings can reduce nanomaterials toxicity.[41]

2. Facile polymerisation that occurs in aqueous conditions at r.t. at slightly basic pH, although alternatives exist (*e.g.* enzyme catalysis or electropolymerisation),[42,43]
3. Amino or catechol units can be used as chemical handles for derivatisation, allowing the use of PDA in numerous applications. For example, they are useful to bind TiO_2 NPs for use in dye-sensitised solar cells,[44] or as synthetic membranes for micro or nanofiltration;[45] and in many other applications.[46]
4. Conductivity. PDA graphitisation under reductive atmosphere affords N-doped graphitised films with a conductivity of 1200 S/cm^{-1}, similar to that of polycrystalline graphite and superior to that of GO.[37] Given that coatings as thin as a few nanometres were reported, this strategy could be used to create films of N-doped pseudo-graphene on different substrates.

Despite great research efforts to elucidate the polymerisation mechanism, this topic is still subject of active debate, although key steps are now established. O_2 is essential, otherwise the reaction does not proceed even in the presence of a strong base such as NaOH.[47] There is a general consensus on the initial oxidation of the precursor into a quinone, and on the following intramolecular cyclisation to leukodopamine-chrome or insaturated 5,6-hydroxyindole (Figure 3.4). Belawski *et al.* reported the key contribution of supramolecular interactions (*i.e.* π-π stacking or hydrogen bonding) based on their ^{15}N solid-state NMR and crystallographic studies. Non-covalent interactions could explain PDA affinity for diverse surfaces. Vecchia *et al.* suggested different mechanisms depending on reaction conditions, such as the concentration of dopamine or the type of buffer used. For instance, when Tris-buffer (*i.e.* the buffer used in this work)

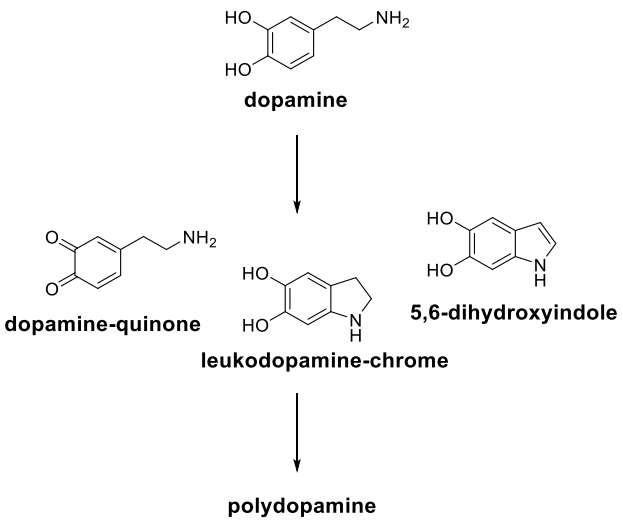

Figure 3.4. Structure of dopamine and PDA intermediates.

is present, it is accommodated in the polymeric structure, which displays various functional groups including carboxylic acids, cathecols, amines, quinones, etc. The mechanism may get even more intriguing when the polymerisation is performed in the presence of CNS. The vast polyaromatic surface would probably boost supramolecular interactions through CH-π, cation-π, π-π stacking.

3.1.2. Electrochemical application of N-doped CNS

Electrochemistry studies the relation between electricity and chemical processes. It can be used to characterise materials (*e.g.*, fullerenes),[48] to deposit metals,[49] in sensing,[50] or in fuel cell technology.[51] Fuel cells produce energy from a chemical reaction. In contrast with batteries, they will work continuously if the system is fed with fuel (*i.e.* oxygen and hydrogen). They are generally classified by the electrolyte between the anode and the cathode that serves as media to bring protons to the cathode and complete the chemical reaction. The most common types are: i) phosphoric acid-; ii) proton exchange membrane-; iii) molten carbonate-; iv) solid oxide-; vi) direct methanol-; and vi) alkaline-fuel cells.

These devices are already present in our everyday life supplying clean energy to big buildings such as hospitals or banks. However, the research on these kind of devices is still very active. Yamanaka *et al.* developed a new concept to simultaneously produce H_2O_2 and energy (Figure 3.5).[51] The improvements of this kind of alkaline fuel cells may have beneficial consequences in global production of H_2O_2.

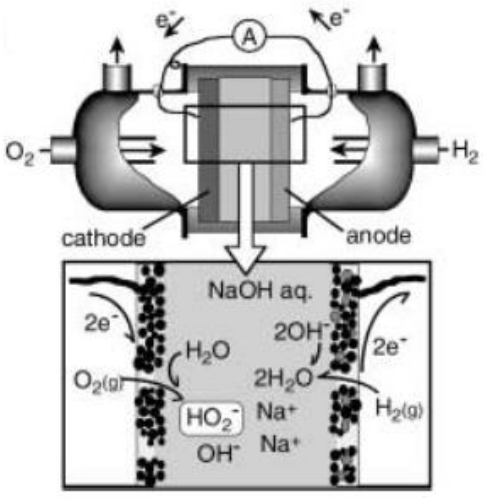

Figure 3.5. Fuel cell designed for H_2O_2 production. Adapted from (51), © 2003 John Wiley and Sons.

Nowadays, 4 x 10^6 tons of H_2O_2 are produced annually for industrial use. Production relies on the reduction of anthraquinone, a non-environmentally friendly process. Most catalysts used in this area contain expensive metals (*e.g.* Pt, Au, etc.).[52,53,54] Thus, implementation of metal-free catalysts is highly desirable and could have a great impact on society. Carbon-based materials are promising candidates, since they have already been used to substitute metal catalysts in different energy applications.[55] In particular, N-doped CNS proved valuable in a number of electrochemical approaches.[23] PDA is an attractive option to introduce nitrogen atoms in close contact with the graphitic walls of the CNS, and create efficient catalytically active sites.[56] It was suggested that the carbon atoms adjoining pyridinic nitrogen atoms have Lewis basicity and can adsorb O_2. Surprisingly, to the best of our knowledge, there is only one report in which PDA has been used to prepare an N-doped GO metal free catalyst.[57] PDA-GO was produced with different polymer thicknesses (*e.g.* 2.5 nm, 5 nm and 10 nm), that were calcined at high temperatures. Best catalytic efficiency was demonstrated for the 5 nm-thick PDA-GO calcined at 900 ^oC.

3.2. Aim of the work

This part of the thesis focusses on the synthesis of PDA-coated CNS and subsequent graphitisation to achieve N-doped CNS for use as electrochemical catalysts. Different CNS will be evaluated, as well as various reaction conditions to optimise the *in situ* polymerisation of dopamine on the CNS. A range of temperatures will be tested to optimise the calcination step of PDA. Finally, electrocatalytic performance of obtained PDA-CNS material will be investigated in collaboration with other colleagues from our research group as well as Prof. Claudio Tavagnacco (expertise in electrochemistry) and Prof. Paolo Fornasiero (expertise in catalysis), all based at the University of Trieste.

3.3. Results and discussion

3.3.1. Towards homogeneous PDA coatings

Table 3.1 shows experimental conditions reported in literature to coat MWCNTs with PDA. All protocols have in common the use of aqueous Tris-buffer as media and long reaction times. MWCNTs and dopamine concentrations vary, and so does the thickness of PDA coatings. Differences that may arise from CNT characteristics (*e.g.* thickness, length, level of impurities) may affect polymerisation. Thus, the first step was the optimisation of reaction conditions to obtain homogeneous and fully-coated materials in a reproducible way. From Table 3.2 it can be seen that the process is influenced by five key variables: i) type of CNTs (*e.g.* pristine or functionalised); ii) reaction time; iii) dopamine concentration; iv) CNT concentration; and v) buffer concentration.

Table 3.1. Different experimental conditions reported in literature.

Ref.	Conc. MWCNTs(mg/ml)	Conc. dopamine (mg/ml)	Conc. base (mM)	Reaction time (h)	Thickness (nm)
Carbon, **2008**, *46*, 1792[32]	1	2	10 mM	10	12
				36	26
Carbon, **2010**, *48*, 2347[58]	1	0.1	10 mM	24	5
ACS App. Mater. Interfaces, **2013**, *5*, 7770[34]	Not specified	4	2 mM	10	5

Despite the low processability of pristine MWCNTs, they were the first choice as CNS scaffold Fei *et al.* reported that the use of oxidised MWCNTs could prevent coating, due to CNT hydrophilicity.[32] However, in our hands, both pristine and ox-CNTs led to similar results. TEM analysis revealed that the coatings were not homogeneous (Figure 3.6 a and b). Reaction time was thus extended (*i.e.* to 48 h, Table 3.2.), but TEM revealed presence of undesired free polymer that was embedding CNTs (Figure 3.6 c).

In the following optimisation steps, we changed monomer amount and base concentration (Table 3.2 entries d, e and f). Interestingly, PDA coatings so-obtained were more homogeneous (Figure 3.6 d, e). In general, coatings were very similar in terms of thickness (*i.e.* 15 ± 7 nm or 19 ± 7 for pristine and ox-MWCNTs, respectively), yet when pristine MWCNTs were used, some parts of the tubes appeared bare. When the concentration of dopamine was increased towards its maximum solubility in water (*i.e.* 100 mM, Table 3.2 f), coatings of analogous thickness (15 ± 3 nm) were formed, yet formation of self-standing PDA aggregates also occurred (Figure 3.6 f).

Table 3.2. Experimental polymerisation conditions to prepare fully covered materials.

Ref.	MWCNTs	Time (h)	Buffer (mM)	MWCNTs amount (mg ml^{-1})	Dopamine amount (mg ml^{-1})	Final amount (mg)	Thickness (nm)
a	Pristine	16	2	0.2	2	18	-
b	Oxidised	16	2	0.2	2	16	-
c	Oxidised	48	2	0.2	2	17	-
d	Pristine	16	10	0.2	8	40	15 ± 7
e	Oxidised	16	10	0.2	8	41	19 ± 7
f	Oxidised	16	10	0.2	20	49	15 ± 3

Note 1. All reactions were carried out with 10 mg of MWCNTs.

This data suggested that 10 mM base concentration and 8 mg ml^{-1} of dopamine were sufficient to reach a plateau in terms of coating thickness. Bernsmann *et al.* demonstrated that this plateau was due to O_2 consumption in the media, and it can be overcome by refreshing the dopamine solution.[59] However, when more cycles of polymerisation were carried out, PDA coatings were partially peeled off. In light of these

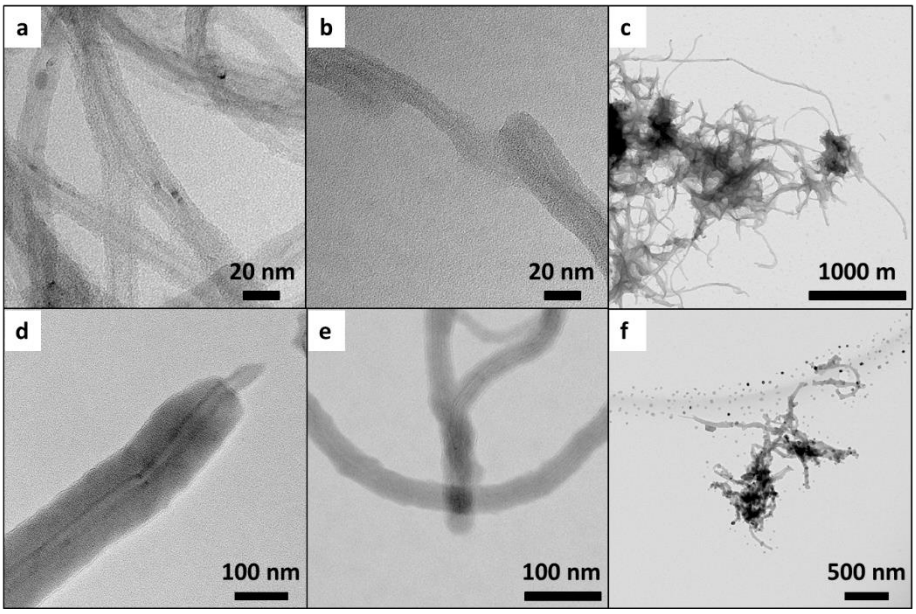

Figure 3.6. TEM images of the different PDA-coated CNT samples.

observations, conditions outlined in Table 3.2, entry c were selected for further studies. An advantage of working at plateau conditions is higher batch-to-batch reproducibility, thus addressing a known drawback in non-covalent functionalisation. Raman spectroscopy revealed mainly PDA signals (*i.e.* ~1350 and ~1580 cm-1, Figure 3.7), not only due to the low penetration of the technique, but also thanks to the homogeneous coverage of ox-MWCNTs by PDA.

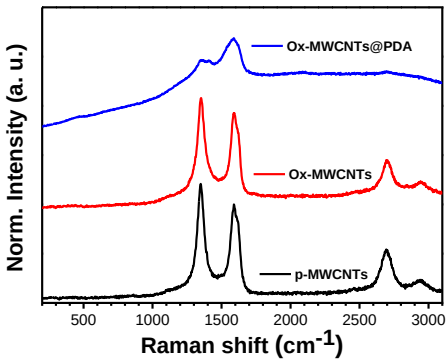

Figure 3.7. Raman spectra of pristine, oxidised and PDA coated MWCNTs. All the reported spectra is the average of 10 data points confirming the uniformity of the materials.

TGA was performed both in nitrogen and air (Figure 3.8). Thermograms under inert atmosphere permitted the quantification of 9% wt. of carboxylic groups (*i.e.*, 2.0 mmol/g ox-CNTs) introduced after CNT oxidation pre-treatment. On the contrary, it was not possible to quantify the amount of PDA since the polymer did not fully decompose,

instead, it graphitised in the explored range of temperatures. TGA in air did not allow PDA quantification either, since PDA decomposed gradually from 200 ºC to 560 ºC.

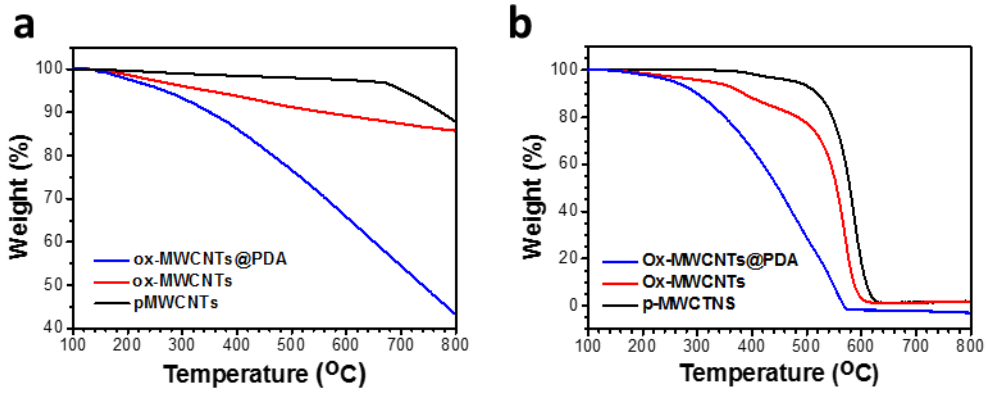

Figure 3.8. TGA in N_2 (a) and air (b) of pristine , oxidised and PDA-coated MWCNTs.

Consequently, we used gravimetric analysis to calculate the proportion of PDA relative to CNTs in the final material. The amount of ox-MWCNTs (*i.e.* 10 mg) is considered constant throughout the protocol. Using this methodology, the amount of PDA was estimated to 76.8 ± 2.0 % relative to 23.2 ± 2.0 % of ox-MWCNTs by weight. As expected, the percentage of polymer was very similar across different batches as reported in Table 3.3.

Table 3.3. Total amount of ox-MWCNTs and PDA in the coated materials.

Ref.	Ox-MWCNTs (%)	PDA (%)
Ox-MWCNTs@PDA_1	27.7	72.3
Ox-MWCNTs@PDA_2	23.2	76.7
Ox-MWCNTs@PDA_3	24.4	75.6
Ox-MWCNTs@PDA_4	21.7	78.3
Ox-MWCNTs@PDA_5	22.7	77.3
Ox-MWCNTs@PDA_6	21.5	78.5
Ox-MWCNTs@PDA_7	21.9	78.1
Ox-MWCNTs@PDA_8	22.6	77.4
Ox-MWCNTs@PDA_{media}	23.2 ± 2.0	76.8 ± 2.0

3.3.2. Preliminary studies on PDA calcination

As reported in literature, conductivity of PDA films is a function of the temperature of calcination.[37] Many articles report calcination steps at temperatures >800 ºC, however, data on PDA materials calcined at lower temperatures is still scarce. Therefore, we decided to investigate the minimum temperature at which PDA coatings became conductive. If it was possible to reduce the calcination temperature, this would result in fewer costs, extended equipment lifetime, and overall less energy consumption.

The experimental protocol involved the coating of quartz slides with PDA. We decided to avoid MWCNTs for this study since their inherent conductivity could falsify the results. As presented in Scheme 3.1, quartz slides were coated following the protocol optimised for MWCNTs. Briefly, a quartz slide was introduced in a 8 mg ml^{-1} aqueous solution of dopamine for 30 min. After that, Tris-buffer (10 ml, 50 mM) was added and stirring continued for 16 h. Then, the films were rinsed with water and ethanol.

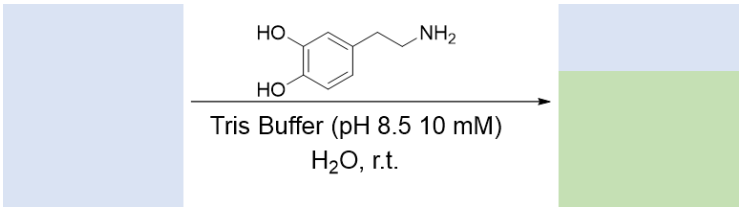

Scheme 3.1. PDA polymerisation on quartz slides. The blue square represents the bare quartz slide and the greenish square represents the coated slide.

As presented in Figure 3.9 a, quartz slides were successfully coated. Raman spectra revealed presence of PDA all over the substrate (Figure 3.9 a). Calcination was next performed under Ar for 3 h[36] at 500 ºC, 600 ºC or 700 ºC. Presence of the calcined polymer was confirmed by Raman spectroscopy (Figure 3.9 b, c and d). The data showed a clear evolution of the two bands at ~1350 cm^{-1} and at ~1580 cm^{-1} that became increasingly sharper as temperature was increased, while the baseline fluorescence was reduced and the background became more stable. Interestingly, the band shape of the film calcined at 700 ºC was well in agreement with the formation of a structured carbon nanomaterial. Thus, we assigned these bands to the D and the G active Raman modes of graphene-related materials. Interestingly, these bands lose their characteristic shape with lower calcination temperature.

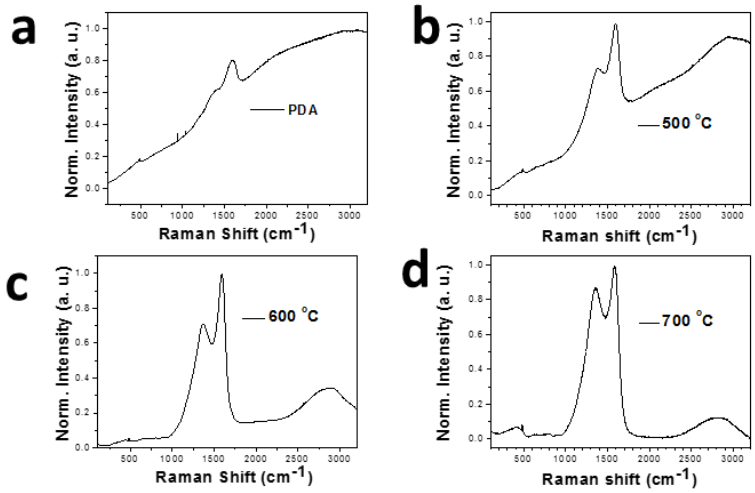

Figure 3.9. Raman spectra of PDA fresh (a) and calcined at 500 C (b), 600 ºC (C) or 700 ºC (d).

Next, we measured the conductivity of the films (Figure 3.10). PDA-coated quartz slides were spray-coated with Au at both ends. I vs V curves were recorded at different applied potential from -10 V to 10 V. Only the material calcined at 700 ^{0}C appeared to be conductive. Film resistance increased linearly with applied potential.

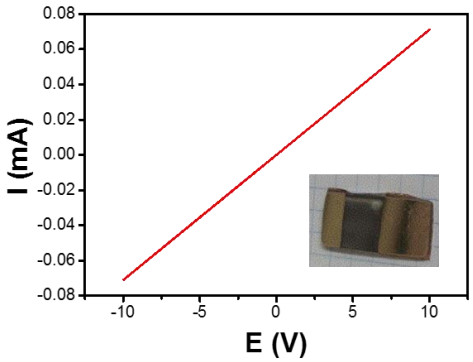

Figure 3.10. I vs V curve of PDA-coated quartz slide calcined at 700 ºC. Inset photo shows the Au-coated and PDA-coated quartz slide.

3.3.3. Calcination of ox-MWCNTs@PDA

In light of the data discussed above, ox-MWCNTs@PDA were calcined under Ar at 700 °C for 3h. The calcined material (g-N-MWCNTs$_{700}$) was characterised by TEM, Raman spectroscopy and TGA in nitrogen and air. Additionally, we performed a colorimetric test to assess presence of amines at each step (*i.e.* the Kaiser test).

The Kaiser test is very popular in peptide synthesis for the detection of primary amines. The test allowed quantitative determination of primary amines thanks to the formation of a Schiff base that was coloured (*i.e.* 2-(1,3-dioxolan-2-yl)imino indane-1,3-dione). The test was considered positive (*i.e.* presence of primary amines) if the solution turned purple. As illustrated in the Figure 3.11 a, only the test for ox-MWCNTs@PDA was positive. UV-Vis spectroscopy analysis allowed quantification of amines, which corresponded to 885.64 µmol of amine per gram of material. From this data, we can also extract that the thermal treatment removed all the amines possibly through inclusion of nitrogen in the N-doped graphitic structure.

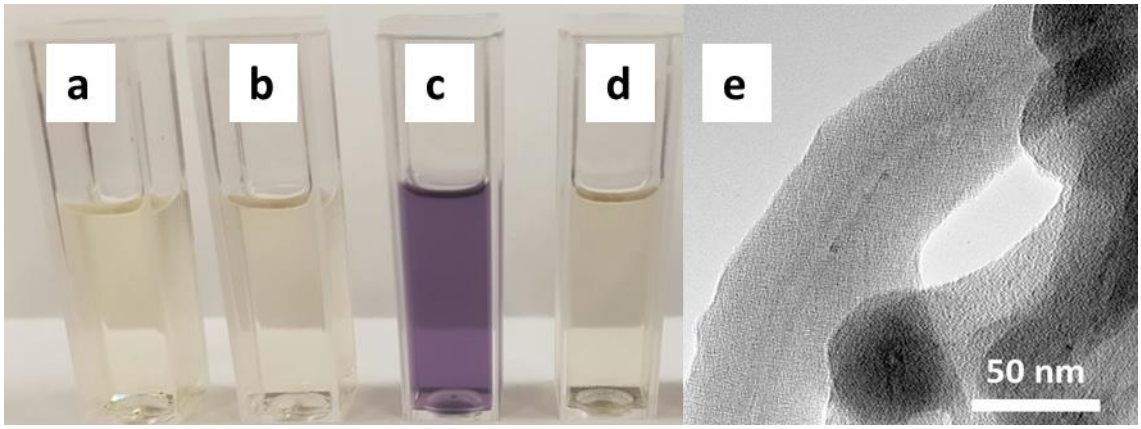

Figure 3.11. Kaiser test solutions of pMWCNTs (a), ox-MWCNTs (b), ox-MWCNTs (c) and ox-MWCNTs@PDA (d); and TEM image of g-N-CNHs$_{700}$ (e).

TEM micrographs of the calcined material showed no significant change in the polymer coating (Figure 3.11 b), including its thickness (*i.e.* 15 ± 5 nm). Figure 3.12 shows the Raman spectrum and the TGA of g-N-CNHs$_{700}$. It is clear that the thermal treatment sharpened Raman features relative to fresh samples, in agreement with PDA graphitisation (Figure 3.9). Besides, TGA in air revealed combustion of g-N-MWCNTs$_{700}$ occurred within a narrow temperature range, in contrast with the fresh sample, and it was anticipated relative to both pristine and oxidised CNTs. Moreover, TGA in N_2 highlighted high stability of the material, with 3% wt. loss observed below 300 ºC.

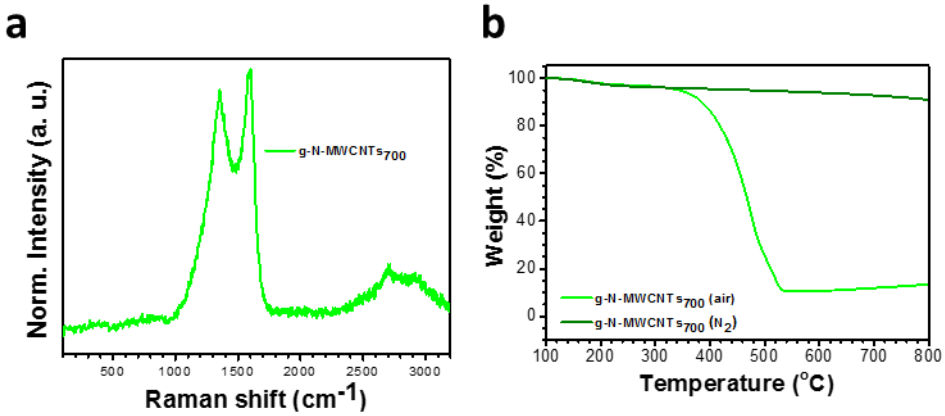

Figure 3.12. Raman spectrum (a) and thermograms under air and N2 of g-N-MWCNTs$_{700}$..

3.3.4. Coating of CNHs

As mentioned in Chapter 1, CNHs are horn-shaped SWCNTs that cluster together in spherical aggregates. Importantly, they are produced in the absence of metal catalysts, and are thus devoid of metal-contamination as opposed to other CNS. Besides this fact being an advantage in terms of safety, biocompatibility, and environmental impact, it is essential to guarantee that the performance in electrocatalysis is due to hybridisation with the calcined PDA layer and not to the presence of metal traces. This parameter should not be omitted since as it was reported in literature that the presence of metal impurities enhanced electrochemical performance of various graphene-based materials.[60,61]

The experimental protocol optimised for the preparation of g-N-MWCNTs$_{700}$ was thus applied to prepare g-N-CNHs$_{700}$ (Scheme 3.2) from acid-oxidised CNHs. The materials were characterised at each step by TEM, TGA and Raman spectroscopy. TEM images revealed no significant change after the mild oxidation treatment, while after polymerisation a thick layer coated ox-CNHs (Figure 3.13). In this case, the similar electron density for ox-CNHs and PDA and the unique morphology of CNHs hinder accurate quantification of PDA thickness, which was estimated to be ~35 ± 8 nm. It is possible that, due to their unique structure and high surface area, the freshly made PDA layer was more porous relative to the one obtained on CNTs, and thus thicker. After graphitisation, the thickness of the shell in the core-shell structure was 18 ± 6 nm, which was very similar to the coating measured for ox-MWCNTs.

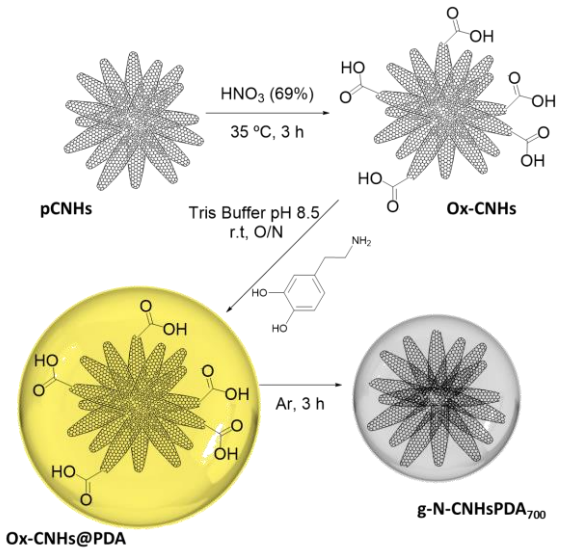

Scheme 3.2. Synthesis of g-N-CNHs$_{700}$.

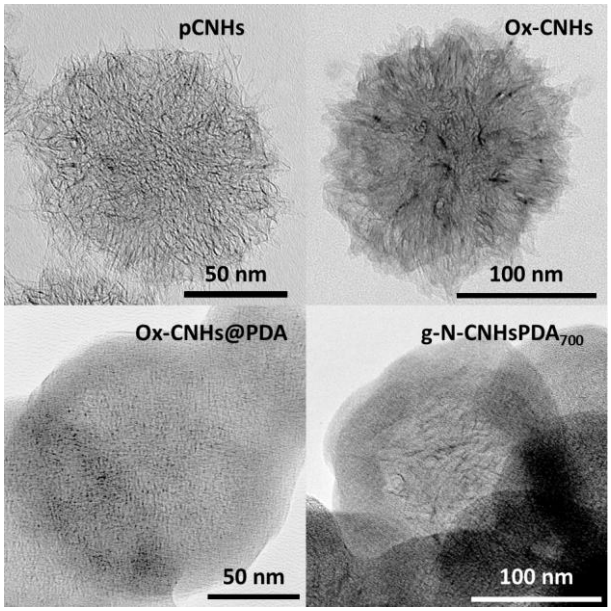

Figure 3.13. TEM images of all the CNHs derivatives.

Composition of the surface of oxCNHs@PDA and g-N-CNHs$_{700}$ were analysed by TEM-EDX imaging in collaboration with Dr. Lucia Nasi at the CNR-IMEM Institute (Parma, Italy, Figure 3.14). Apart from H, the only elements present were C, O and N. In accordance with the core-shell structure, O and N atoms were co-localised in the outer layer, while C atoms were homogeneously distributed throughout the structure.

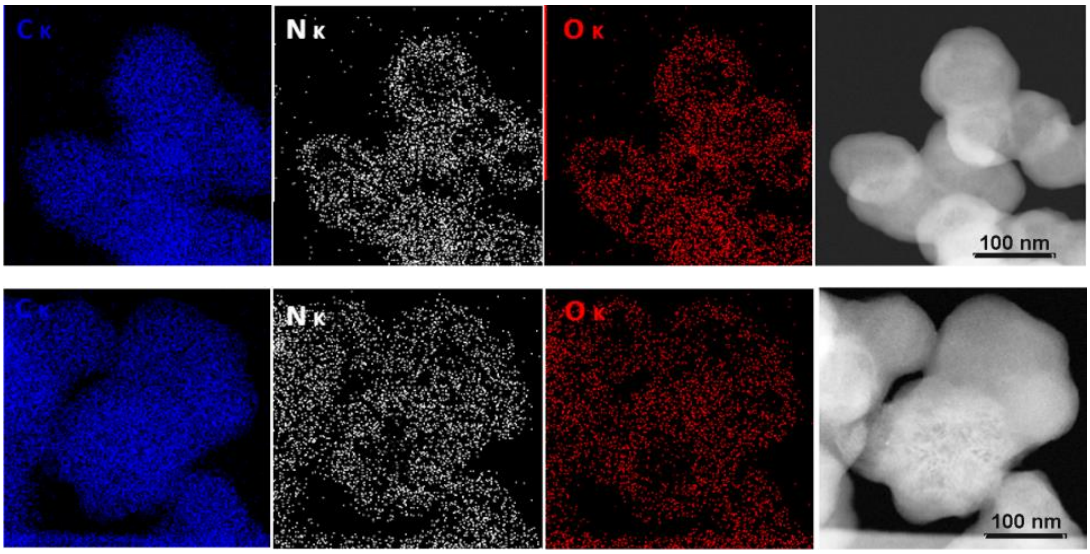

Figure 3.14. EDX-TEM of ox-CNHs@PDA and g-N-CNHs$_{700}$.

TGA and Raman analysis for CNH derivatives is presented in Figure 3.15. Analogously to what discussed above for g-N-MWCNTs, TGA in inert atmosphere did not allow PDA quantification, but were useful to quantify oxidation (*i.e.* 9 % wt., corresponding to 2.0 mmol of carboxylic groups per gram of material). TGA in air did not allow PDA quantification either but revealed a sharp combustion step at lower temperatures for g-N-CNHs$_{700}$ relative to p-CNHs and ox-CNHs. Besides, the combustion step occurred rapidly in contrast with fresh ox-CNHs@PDA indicating that there was more order in the shell after calcination, thus confirming Raman data. Mild functionalisation after thermal treatment was confirmed by Raman spectroscopy since there was an increase in the I_D/I_G ratio (Figure 3.15 d). Moreover, the absence of any residues at high temperatures after calcination in air confirmed that the materials were metal-free. PDA was quantified by gravimetric means (Table 3.4). CNHs and MWCNTs represent similar wt. percentage of the final material (*i.e.* 22.6 and 23.6%, respectively).

XPS spectra were recorded by Dr. Criado at CIG BiomaGUNE (San Sebastián, Spain) at each step of the protocol to gain information on the functional groups present on the surface of the nanostructures. The survey spectra of all derivatives is presented in Figure 3.16. p-CNHs displayed one single peak whose binding energy (BE) was assigned to the presence of C=C bonds all along the surface of the nanoform. As expected from the TGA in N_2, the mild oxidation treatment introduced a very low level of O-containing functional groups (Figure 3.18, Table 3.5). After dopamine polymerisation, the peak of N arose as a single peak after the deconvolution of the spectra. Interestingly, if we

subtracted the 5.49 % of O contribution from the oxidised surface from the total amount of O in ox-CNHs@PDA, we found a N:O atomic ratio very similar to the ratio found in

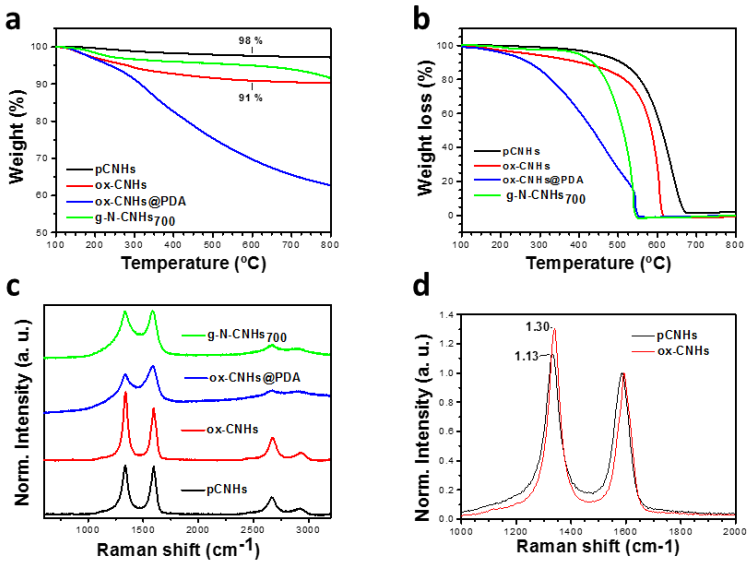

Figure 3.15. Characterisation of pCNHs, ox-CNHs, ox-CNHs@PDA and g-N-CNHs$_{700}$ by TGA in N_2 (a), TGA in air (b) and Raman spectroscopy (c); zoom in the D- and G- band of CNHs (d).

Table 3.4. Gravimetric analysis of the non-calcined hybrid material for PDA quantification.

Sample	Ox-CNHs (%)	PDA (%)
ox-CNHs@PDA$_1$	21.0	79.0
ox-CNHs@PDA$_2$	20.6	79.4
ox-CNHs@PDA$_3$	20.4	79.6
ox-CNHs@PDA$_4$	20.4	79.6
ox-CNHs@PDA$_5$	23.4	76.6
ox-CNHs@PDA$_6$	26.3	73.7
ox-CNHs@PDA$_7$	26.3	73.7
Average	22.6 ± 2.7	77.4 ± 2.7

the monomer (*i.e.* 2:1 for the monomer and 1.9:1 for ox-CNHs@PDA). Finally, the annealing of the material caused very important changes. On one hand, the percentage of O decayed dramatically from 19.45 % to 3.80 % in agreement with EDX data. On the other, deconvolution of the N 1s peak clearly revealed two components, whose BE (400.3 and 398.9 eV, respectively) suggested presence of both pyrrolic and pyridinic motifs.

These results are in line with the Kaiser test performed for MWCNT samples, which confirmed the absence of primary amines after the thermal treatment, but in

contrast with some literature articles in which the N atoms were reported to evolve to graphitic N rather than pyrrolic and pyridinic.[62,63] Besides, XPS characterisation did not reveal presence of any metal. This was in agreement with TGA in air data. However, the low penetration of the XPS technique did not permit the detection of metal traces in the inner part of the hybrids and TGA is not accurate to detect element traces. Thus, hybrids were characterised by Dr. M. Crosera by using inductively coupled plasma optical emission spectroscopy (ICP-OES), in collaboration with Prof. Gianpiero Adami at the University of Trieste. As expected, no metal traces above 0.0005 wt % were found in g-N-CNHs$_{700}$, therefore we are certain that the synthesised materials are metal-free.

N and O content reduction after thermal treatment was not correlated with significant changes in coating thickness either for MWCNTs or for CNHs. To enlighten this aspect, Dr. Michele Melchionna performed the analysis of the textural properties of g-N-CNHs$_{700}$ at liquid N_2 temperature. The material displayed high microporosity with a large Langmuir surface area of 481 $m^2\ g^{-1}$, 26 $m^2\ g^{-1}$ of which were located on the external

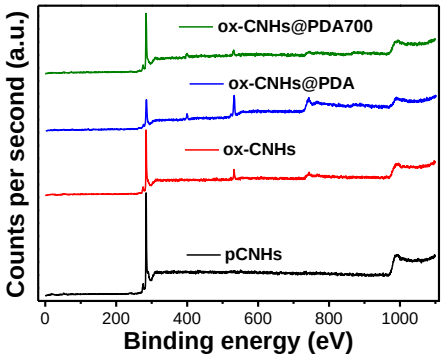

Figure 3.16. XPS survey spectra of pristine, oxidised, coated and calcined CNHs.

Table 3.5. Atomic ratio of pristine, oxidised, coated and calcined CNHs.

Sample	Core	Atomic %		Sample	Core	Atomic %
pCNHs	C_{1s}	99.10		Ox-CNHs	C_{1s}	94.51
	O_{1s}	0.90			O_{1s}	5.49
	N_{1s}	-			N_{1s}	-

Ox-CNHs@PDA	C_{1s}	73.08		Ox-CNHs@PDA$_{700}$	C_{1s}	90.63
	O_{1s}	19.45			O_{1s}	3.80
	N_{1s}	7.47			N_{1s}	5.56

hybrid surface. The isotherm of adsorption presented a type I, according to IUPAC recommendations (Figure 3.17), and a microporous volume of 0.15 cm^3 g^{-1}. This data thus suggested that the thermal treatment caused formation of the pores rather than thinning of the PDA coating. Surface areas of g-N-CNHs700 were lower than those of ox-CNHs. The tip opening of the horn-shape structures upon acid treatment made the internal part of the tubes accessible (i.e. 928 m^2 g^{-1}). The graphitised PDA layer blocked access to the inside of the tube, yet it guaranteed high gas adsorption that could be exploited for material function.

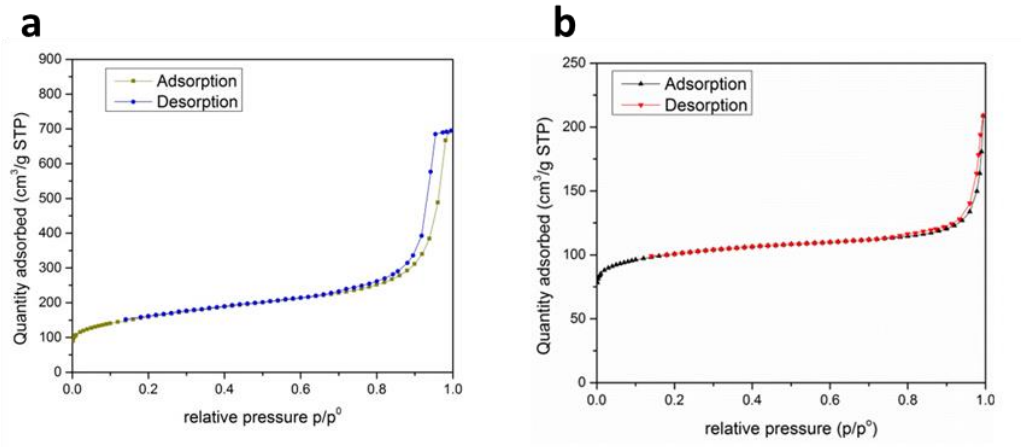

Figure 3. 17. N_2 physisorption isotherm of ox-CNHs (a) and g-N-$CNHs_{700}$ (b) at liquid N_2 temperature.

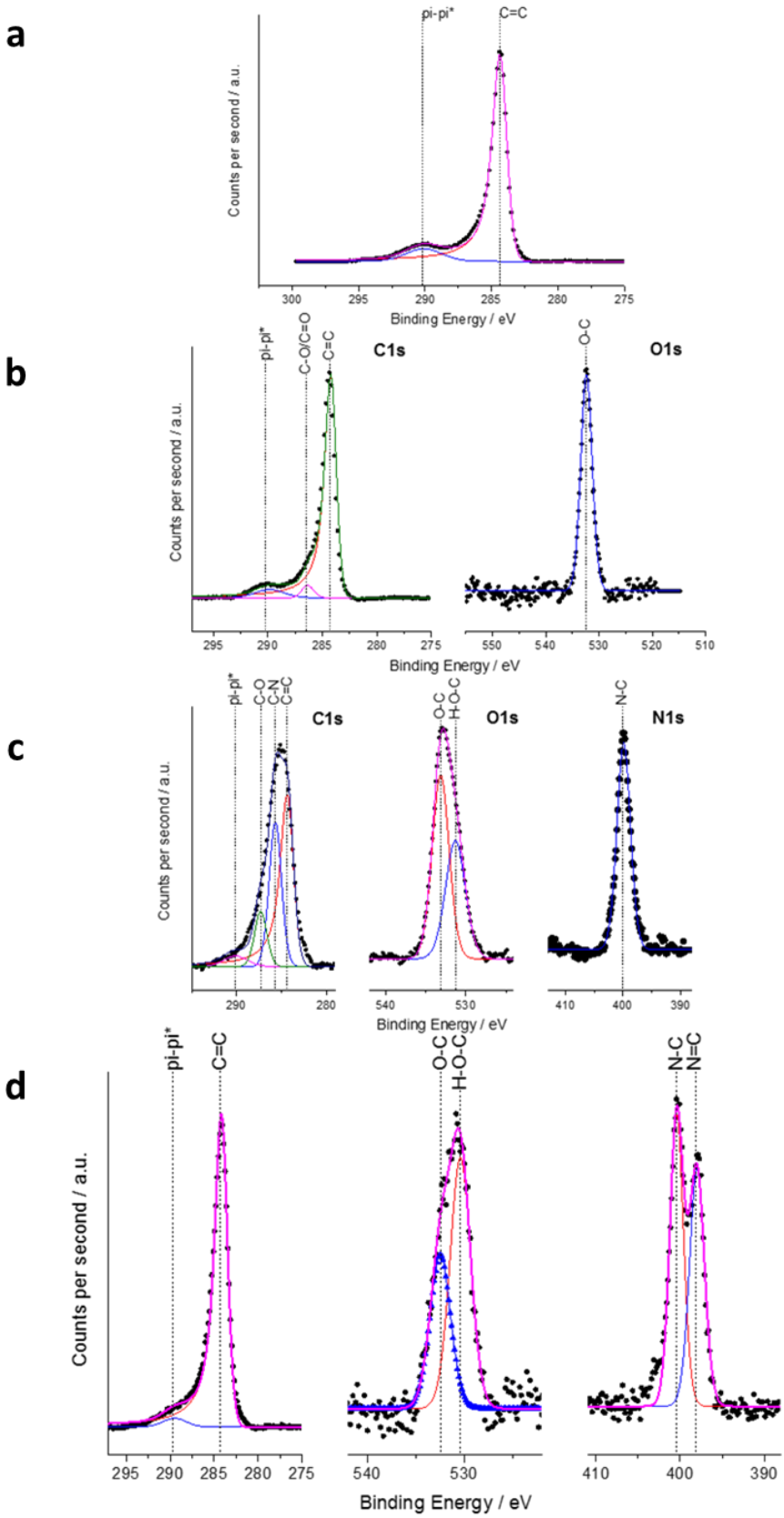

Figure 3.18. Deconvolution of the C, N and O peaks in all CNHs derivatives: (a) pristine CNHs; (b) oxidised CNHs; (c) ox-CNHs@PDA; and (d) g-N-CNHs$_{700}$. Note that no signs of N and O or N were found in the pristine and the oxidised materials respectively.

3.3.5. Electrochemical properties of g-N-CNHs$_{700}$

As mentioned in section 3.1, one potential application of N-doped graphitised materials regards the electrochemical reduction of oxygen for their implementation in fuel cells. To date, only g-N-CNHs$_{700}$ has been electrochemically characterised.

Unless otherwise indicated, the electrochemical characterisation of the materials was performed by Angela Giuliani.

3.3.6. Cyclic Voltammetry

Cyclic voltammetry (CV) was carried out under N_2, in phosphate buffer at pH 7.4 between -0.34 V and +1.65 V vs RHE using a scan rate of 0.050 V s^{-1}. The capacitive current of ox-CNHs@PDA was much smaller than that of ox-CNHs and g-N-CNHs$_{700}$. This was due to the isolating properties of fresh PDA layer that impeded charge carrier mobility (Figure 3.19 a). The broad peaks displayed by ox-CNHs and g-N-CNHs$_{700}$ at +0.82 V and +0.60 V were assigned to O and N functional groups, respectively.

Consecutive CV, up to 20 cycles, were done to get more information on the electrochemical properties of the materials. Minor changes presented by Ox-CNHs and g-N-CNHs$_{700}$ were likely due to gradual wetting of the sample (Figure 3.19 b and d). Contrarily, initial cycles of the fresh sample were completely different to the twentieth cycle. This phenomenon was probably due to the redox process of dopamine/dopaminequinone,[64,65] and disappeared after the fifth cycle in agreement with the incorporation of these species in the polymer matrix.

3.3.7. Electrocatalytic performance of the N-doped hybrids for ORR to H_2O_2

Initial tests of the electrocatalytic activity of ox-CNHs, ox-CNHs@PDA and g-N-CNHs$_{700}$ were performed. Ox-CNHs and ox-CNHs@PDA required much more negative potential to afford low currents comparing with the calcined sample. Therefore, a more detailed characterisation of g-N-CNHs$_{700}$ was performed. The activity of g-N-CNHs$_{700}$ was investigated at acidic, neutral and basic pH values (*i.e.* 1.0, 7.4 and 13.0). As shown

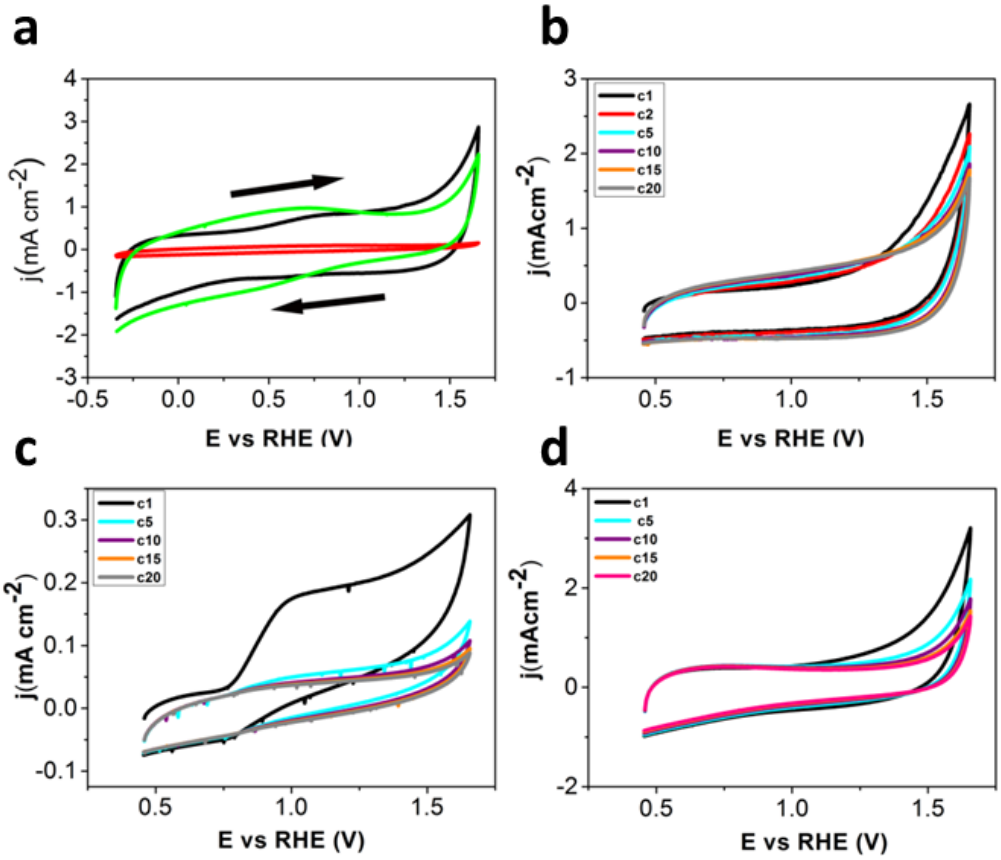

Figure 3.19. CVs obtained on glassy carbon electrode (GCE) modified with ox-CNHs (—), ox-CNHs@PDA (—) and g-N-CNHs$_{700}$ (—) in 0.10 M phosphate buffer solution pH 7.4 under N2. (a). Multicycle (up to 20 cycles) CVs obtained on GCE modified with ox-CNHs (b), ox-CNHs@PDA, (c) and g-N-CNHs (d) in 0.10 M phosphate buffer solution pH 7.40 under N_2. Scan rate: 0.05 V s^{-1}.

in Figure 3.20, activation occurred at different potential values for every pH. At first sight, the current at acidic pH seemed to be much higher than in the other tested conditions, however, after the subtraction of the capacitive currents, the activity of g-N-CNHs$_{700}$ at different pH was very similar. Therefore, the electrocatalyst can work in the whole range of pH revealing a superior O_2 activation.

Table 3.6 summarises very important parameters for the activity of g-N-CNHs$_{700}$ at the different pH values. The current density was normalised using hydroquinone as redox probe to calculate the active area of the electrode (not shown). The number of electron and therefore the product of electrocatalysis were identified using a rotating disc electrode (RDE). The Koutecky-Levich plots (i.e. j-1 vs ω-1/2, Figure 2.21) revealed that there was an order 1 dependent on the concentration of dissolved O2. Besides, we calculated also the number of electrons involved in the process also from these graphs

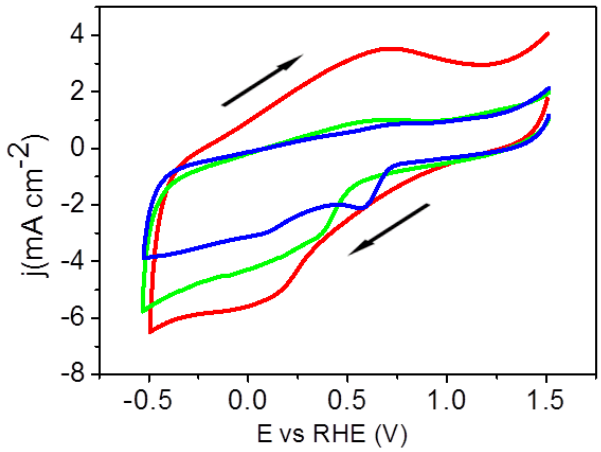

Figure 3. 20. CVs obtained on GCE modified with g-N-CNHs$_{700}$ at pH 1.0 in 0.1 M H_2SO_4 (—), at pH 7.4 in 0.10 M phosphate buffer solution (—) and at pH 13.0 in 0.1 M NaOH (—) under pure O_2. Scan rate: 0.05 V s^{-1}.

that appeared to be 2.6 ± 0.2, 2.0 ± 0.1 and 3.1 ± 0.2 at pH 1.0, 7.4 and 13.0, respectively (Figure 3.21). The number of electrons calculated using the RDE were quite in agreement with the values calculated using the rotating ring disk electrode (RRDE) that were measured at the laboratories of Prof. Vizza at the IMEM-CNR Institute in Florence (Table 3.6).

Table 3.6. The potential values here reported are referred to the RHE reference electrode.

pH	ORR onset (V)	E_{peak} (V)	j_{peak} (mA cm^{-2})	j_{norm} mA mg^{-1}	Ne^- (RRDE)
1.0	0.40	0.18	-3.6	8.7	2.4
7.4	0.53	0.40	-2.3	5.5	2.1*
13.0	0.71	0.59	-1.79	4.3	3.2
* The RRDE experiments performed in neutral media were affected by instability problems of the ring current attributed to phosphate surface adsorption; the Ne^- value was derived from Koutecky-Levich plots obtained with the same experimental setup.					

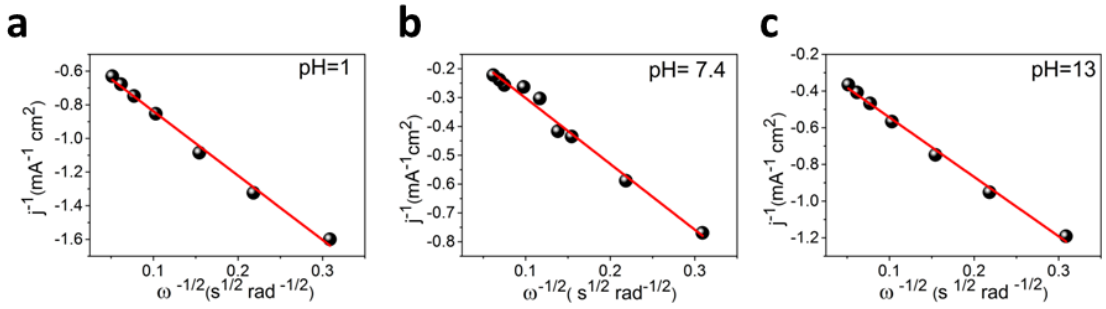

Figure 3.21. Calculated K-L plots for the ORR performed in a) pH 1 in 0.1 M H_2SO_4; b) pH 7.4 in 0.1 M PBS; c) pH 13 0.1 M NaOH. The current density j is normalized by the geometric area of the RDE.

All these data suggested that H_2O_2 was the main product at acidic and neutral pH while the process was less selective at high pH values. In this regard, a 3 electron process

was in accordance with the production of a molecule of H_2O for every molecule of H_2O_2 (*i.e.* 4 electrons process and 2 electrons process, respectively).

Further insight into electrochemical performance was achieved by quantifying the amount of H_2O_2 through bulk electrocatalytic experiments at three different potentials for every pH value (Figure 3.22). The applied potentials were chosen based on the onset potential calculated by the tangential mode from CV data (Figure 3.19). All the studied systems displayed good Faradaic efficiencies (FEs) with higher values for the more positive potentials (*i.e.* 0.30 V, 0.45 V and 0.60 V for pH 1.0, 7.4, and 13.0, respectively).

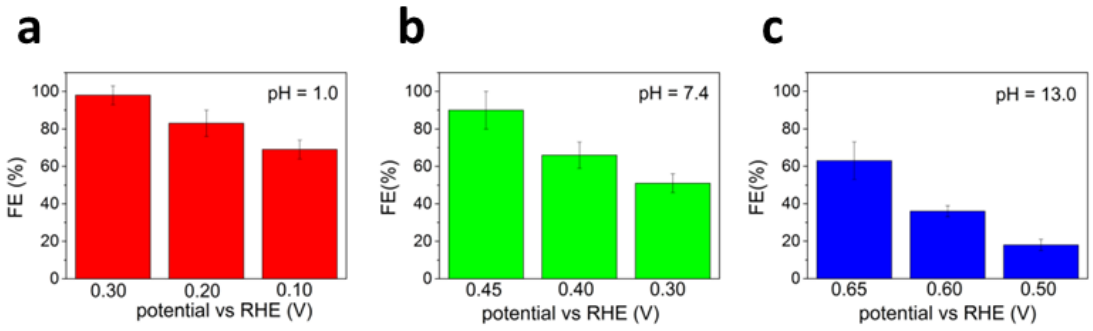

Figure 3.22. FE% of H_2O_2 produced after 1 hour of electrolysis at three different fixed potentials (for each pH value) using g-N-CNHs modified electrode at pH 1.0 (a), pH 7.4 (b), pH 13.0 (c) at three different potential values for each medium.

H_2O_2 is a natural oxidant that may compromise the activity of the catalyst when the amount of oxidant is high enough, and it could damage the materials reducing its activity. In our case, the performance at acidic and basic pH suffered small variations within the first 6 h while samples at physiological pH developed a gradual decrease of FE (Figure 3.23 a). However, the electric current appeared to be very stable at all the tested conditions during 24 h (Figure 3.23 b). This indicated that FE decrease was due to reduction of H_2O_2 to H_2O, rather than to the loss of catalytic activity of g-N-CNHs$_{700}$. This hypothesis was confirmed by performing several measurements with the same materials. The FE for the first hours was always very similar to the initial tests. Therefore, these systems appeared to be ideal for a continuous flow production of H_2O_2 and energy with no accumulation of the product.

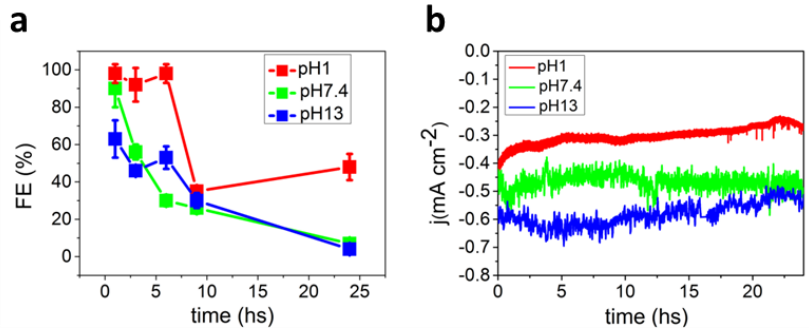

Figure 3.23. Plots of FE% vs time (a) and stability test at pH 1.0, pH 7.4 and pH 13.0 over 24 h collected using a three electrode cell: working electrode made of g-N-CNHs modified glassy carbon, Counter Electrode made of Pt net separate from the bulk solution using a porous membrane and reference electrode Ag/AgCl (b).

3.3.8. g-N-CNHs at different temperatures

Once we studied the electrocatalytic activity g-N-CNHs$_{700}$, we prepared two new materials increasing the temperature of the thermal treatment up to 800 ^{o}C and 900 ^{o}C, respectively. A complete characterisation including TGA, Raman spectroscopy and TEM imaging of the two new materials and the rest of the series is presented in Figure 3.24. Notably, none of these techniques revealed significant differences between samples.

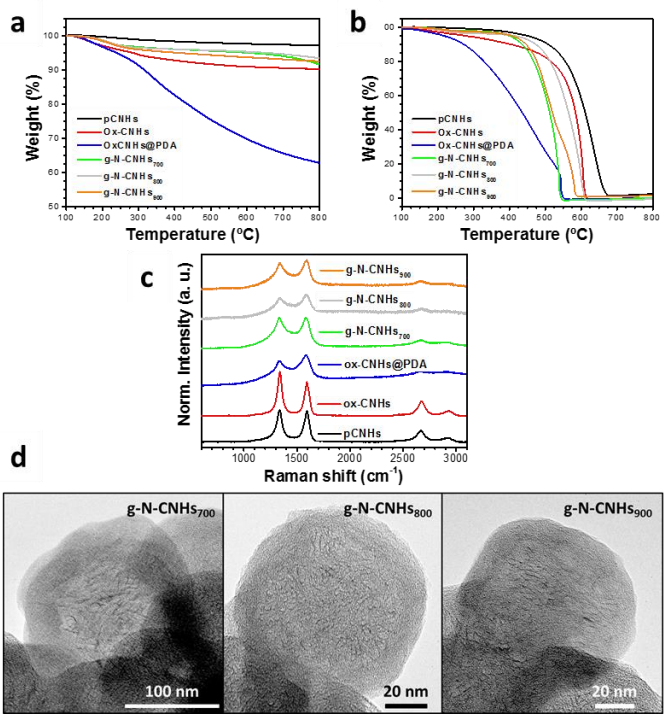

Figure 3.24. TGA in N_2 (a); TGA in air (b); Raman spectra (c) of CNHs derivatives; TEM images of the g-N-CNHs calcined at different temperatures (d).

In terms of electrochemical characterisation, the CV of g-N-CNHs$_{800}$ and g-N-CNHs$_{900}$ showed the same trend as g-N-CNHs$_{700}$, but the capacitive currents were smaller (Figure 3.25). Therefore, the electrocatalytic activity of the materials calcined at 800 ºC and 900ºC was expected to be lower.

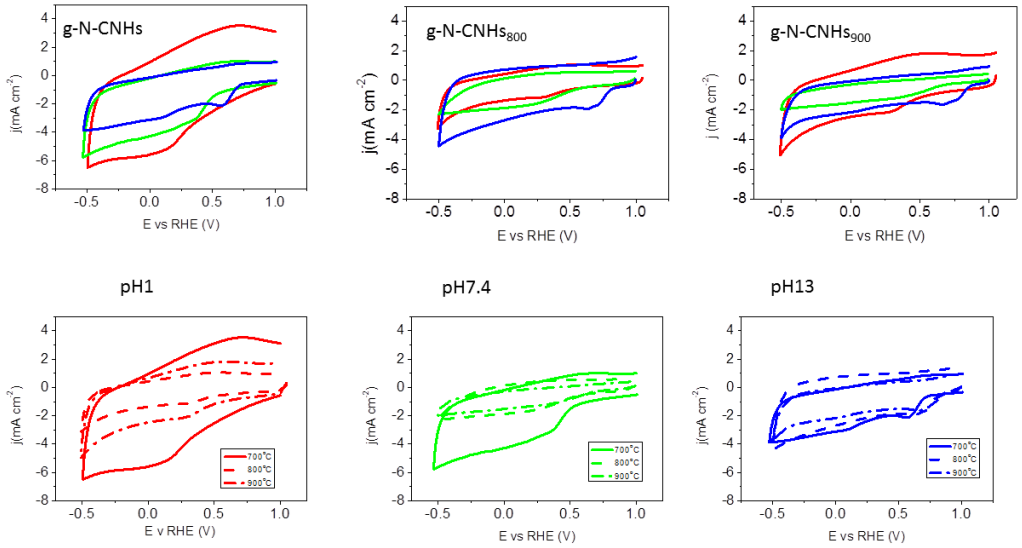

Figure 3.25. Top: CV profiles for the three final materials calcined at the three different temperature at pH 1.0 in 0.1 M H_2SO_4 (—), at pH 7.4 in 0.10 M phosphate buffer solution (—) and at pH 13.0 in 0.1 M NaOH (—) under pure O_2. Bottom: Comparison of CV based on the pH.

On the search of a plausible explanation for the reduction of activity, we acquired XPS data (analysis performed by Dr. Criado at CIC Biomagune in San Sebastián, Spain) also on the last two materials (Figure 3.26). XPS data were similar to those of samples calcined at 700 °C. Remarkably, N % decreased gradually with the increase of calcination temperature (Table 3.7) and it was not due to N graphitisation, as only pyrrolic and pyridinic N types were identified after deconvolution of survey spectra.

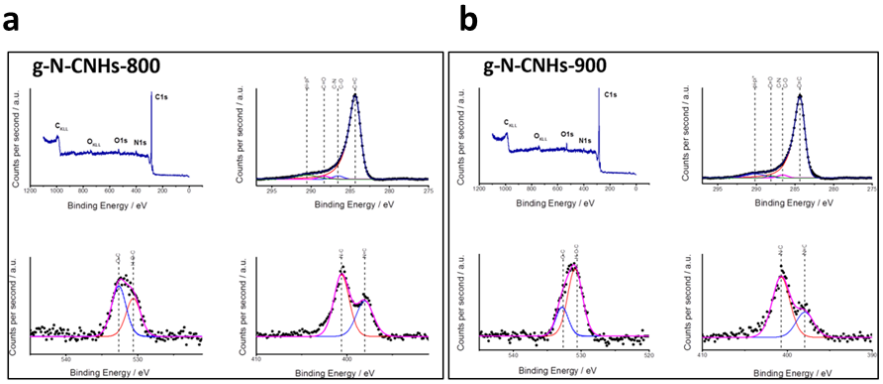

Figure 3.26. XPS characterisation of g-N-CNHs$_{800}$ (a) and g-N-CNHs$_{900}$ (b).

Table 3.7. Comparison between C%, O% and N% of g-N-CNHs calcined at different temperatures

Core	g-N-CNHs$_{700}$	g-N-CNHs$_{800}$	g-N-CNHs$_{900}$
C_{1s}	90.63	93.05	93.05
O_{1s}	3.80	2.68	4.37
N_{1s}	5.56	4.27	2.57

3.3.9. Insights on mechanistic aspects

The exact mechanisms underpinning the electrochemical ORR using metal-free catalysts are still unclear. However, we know from literature that the process can follow two different pathways where two or four electrons are exchanged towards the production of H_2O and H_2O_2, respectively.[56] It also known that the *in situ* decomposition of H_2O_2 to H_2O spontaneously occurs.[66–68] Parameters such as porosity or N content will influence important aspects, such as mass transport or electron mobility.[68,69] Therefore, in our case, the presence of N atoms in the surface of the nanomaterial enhanced electron mobility and likely determined the selectivity of the 2 electrons process. Besides, the presence of pyridinic N atoms was recently reported to be the N-active positions for the reaction under study.[70] Moreover, the loss of activity when the N percentage decreases (*i.e.* decrease of the FEs, Figure 3.27) supported the strong influence of the N atoms.

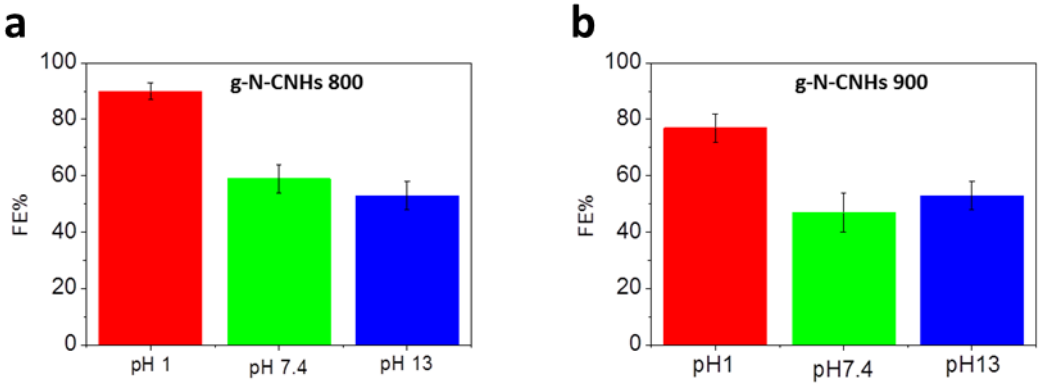

Figure 3.27. FEs of g-N-CNHs$_{800}$ (a) and g-N-CNHs$_{900}$ (b) at the three different studies pH values.

The different values obtained at the different working pH made also reasonable to think that the mechanism of the process followed different pathways depending on the working conditions. To prove this, Tafel plots from RDE at the different pH were

calculated (Figure 3.28). Indifferently of the pH, the Tafel plots presented a linear region (*i.e.* slopes 95 mV dec^{-1}, 84 mV dec^{-1} and 71 mV dec^{-1} for pH 1.0, 7.4 and 13.0, respectively) that was then lost at potential values close to 0 V when the reaction was done in acidic or neutral media or at higher potential values (*i.e.* 0.6 V) for the experiment at basic pH. This fact clearly reflected a variation on the mechanism depending on pH.

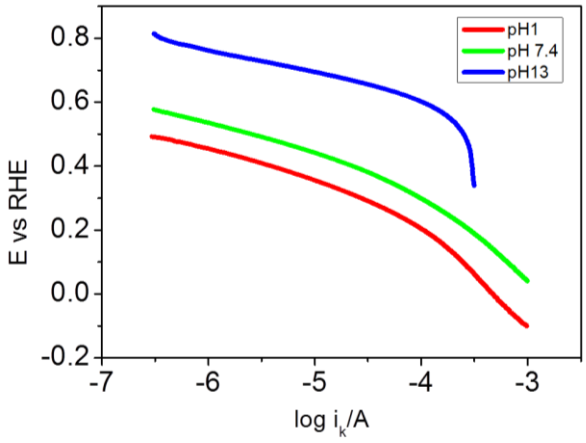

Figure 3.28. Tafel plots of log I_K vs. E (V) for the ORR on the g-N-CNHs electrode in oxygen-saturated solution at pH 1.0 (—), at pH 7.4 (—) and at pH 13.0 (—) under O_2. Scan rate: 0.05 V s^{-1}. RDE rotation rate: 1200 rpm.

3.4. Conclusions

In this Chapter, different reaction conditions for the coating of MWCNTs with PDA as biopolymer have been discussed. Then, investigation on the calcination conditions of the polymer led to the synthesis of MWCNTs coated with a thick layer of N-doped graphitised polymer with intimate interface with MWCNTs. Moreover, the protocol resulted to be very reproducible across different batches.

Optimised conditions were successfully applied to the synthesis of g-N-$CNHs_{700}$. Through scientific collaboration, the electrochemical properties of the material were characterised. Outstandingly, it turned out that g-N-CNHs could produce H_2O_2 with very high efficiencies, in the whole range of pH, and the electrochemical response was stable up to 24 h. Therefore, with these products we overcome two important issues for this kind of PDA-coated CNS materials, such as stability and batch-to-batch reproducibility. The g-N-CNHs reported herein position as front-runner electrocatalysts for the production of H_2O_2 (Figure 3.29, Table 3.8)

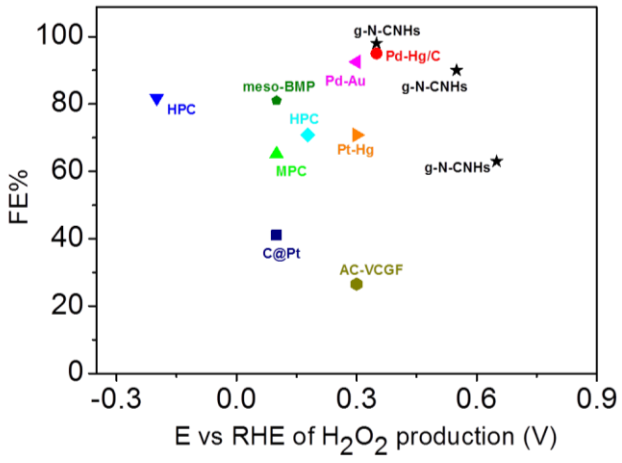

Figure 3.29. Graphical comparison with state-of-the-art catalysts (references in Table 2.8). The comparison considers FEs and applied potential as the two variables. In the table, FE% at the three different pH have been reported for g-N-CNHs$_{700}$.

Table 3.8. Comparison with latest benchmark catalysts for ORR to H_2O_2.

Catalyst	Reference	Medium	Working potential	FE % on H_2O_2
Pd-Hg/C	*Nano Lett.*, **2014**, 14, 1603-1608	0.1 M $HClO_4$	0.35-0.75V vs RHE	95
Mesoporous N-doped carbon	*J. Am. Chem. Soc.*, **2012,** 134, 4072-4075	0.1 M $HClO_4$	0.1 vs RHE	65.15
Hierarchical porous carbon	*Angew. Chem. Int. Ed.*, **2015**, 54, 6937-6841	pH 1-7	0 vs RHE 0.45 vs RHE	91 70.8
Pd-Au	*J. Am. Chem. Soc.* **2011**, 133, 19432-19441	pH 1	0.1-0.3 V vs RHE	92.5
Pt-Hg	*Nat. Mat.* , **2013**, 12, 1137-1142	pH 1	0.1-0.3 V vs RHE	70.8
AC+VGCF	*Angew. Chem. Int. Ed.*, **2008**, 47, 1900-1902	Neutral water	0.3V vs RHE	26.5
meso-BMP	*J. Energy Chem.*, **2016**, **doi:** 10.1016/j.jechem.2016.01.024	pH 1-13	0.1vs RHE	81
C@Pt	*J. Phys. Chem. C*, **2014**, 118, 30063−30070	1M $HClO_4$	0.1V vs RHE	41
g-N-CNHs$_{700}$	**Our work**	**0.1M H_2SO_4 pH 1**	**+0.3V vs RHE**	**98**
g-N-CNHs$_{700}$	**Our work**	**0.1M PBS pH 7.4**	**+0.45V vs RHE**	**90**
g-N-CNHs$_{700}$	**Our work**	**0.1M NaOH pH 13**	**+0.65V vs RHE**	**63**

3.5. Perspective

The research work described in this chapter opens the way to various potential developments for applications of these nanostructured materials. For instance, we can envisage the implementation of g-N-CNHs$_{700}$ in actual fuel cell devices. Besides, the activity of g-N-MWCNTs$_{700}$ will be studied and compared with the already characterised CNHs derivative. Other possibilities could involve the utilisation of other CNS such as SWCNTs, G, GO, graphitised carbon black (GCB) to relate the activity with the morphology and/or electrical properties of the CNS.

Another plausible line of research would include nanostructured metal oxides such as TiO_2 or Ta_2O_5 to study the effect of the graphitised PDA layer on CNS@MO_x hybrids for hydrogen production. Boosting the interaction between the nanomaterial and the metal oxide could be done before the graphitisation step (*e.g.* exploiting the cathecol units of the polymer) or after the generation of the N-doped graphitic layer. In this regard, the functionalisation of the N-doped graphitic surface using chemical reactions optimised for the functionalisation of CNS (*e.g.* diazo coupling reaction) could expand dramatically the applicability of these systems.

3.6. References

(1) Schulz, D. N.; Patil, A. O. *ACS Symp. Ser.* **1998**, *704*, 1–14.

(2) Gil, E. S.; Hudson, S. M. *Prog. Polym. Sci.* **2004**, *29*, 1173–1222.

(3) Ding, W.; Li, L.; Xiong, K.; Wang, Y.; Li, W.; Nie, Y.; Chen, S.; Qi, X.; Wei, Z. *J. Am. Chem. Soc.* **2015**, *137*, 5414–5420.

(4) Yan, W.; Li, Y.; Li, Y.; Ye, S.; Liu, Z.; Wang, S.; Bian, Z.; Huang, C. *Nano Res.* **2015**, *8*, 2474–2480.

(5) Kravets, V. G.; Grigorenko, S.; Peyyety, N. A.; Ponsinet, V.; Richetti, P.; Baron, A.; Torrent, D.; Barois, P. *Mater. horizons* **2016**, *3*, 596–601.

(6) Iijima, S. *Nature* **1991**, *354*, 56–58.

(7) Mamedov, A. A.; Kotov, N. A.; Prato, M.; Guldi, D. M.; Wicksted, J. P.; Hirsch, A. *Nat. Mater.* **2002**, *1*, 190–195.

(8) Melchionna, M.; Prato, M. *ECS J. Solid State Sci. Technol.* **2013**, *2*, M3040–M3045.

(9) Liang, Y.-L.; Stoodart, F. *Acc. Chem. Res.* **2012**, *8* (3), 1161–1171.

(10) Economopoulos, S. P.; Tagmatarchis, N. *J. Phys. Chem. C* **2015**, *119*, 8046–8053.

(11) Fernandes, R. M. F.; Abreu, B.; Claro, B.; Buzaglo, M.; Regev, O.; Furó, I.; Marques, E. F. *Langmuir* **2015**, *31*, 10955–10965.

(12) Fujigaya, T.; Nakashima, N. *Sci. Technol. Adv. Mater.* **2015**, *16*, 24802.

(13) Arnold, M. S.; Green, A. A.; Hulvat, J. F.; Stupp, S. I.; Hersam, M. C. *Nat. Nanotechnol.* **2006**, No. 1, 60–65.

(14) Mulla, K.; Neelima, K.; Liang, S.; Shaik, H.; Younes, E.; Adronov, A.; Zhao, Y. *Chem. Commun.* **2015**, 5*1*, 149–152.

(15) Fukumaru, T.; Fujigaya, T.; Nakashima, N. *Macromolecules* **2013**, *46*, 4034–4040.

(16) Paul, A.; Shao, W.; Shum-tim, D.; Prakash, S. *Biomaterials* **2012**, *33*.

(17) Alturaif, H. A.; Alothman, Z. A.; Shapter, J. G.; Wabaidur, S. M. *Molecules* **2014**, *19*, 17329–17344.

(18) Kanai, Y.; Grossman, J. C. *Nano Lett.* **2008**, *3*, 908–912.

(19) Lee, H. W.; Yoon, Y.; Park, S.; Oh, J. H.; Hong, S.; Liyanage, L. S.; Wang, H.; Morishita, S.; Patil, N.; Park, Y. J.; Park, J. J.; Spakowitz, A.; Galli, G.; Gygi, F.; Wong, P. H.; Tok, J. B.; Kim, J. M.; Bao, Z. *Nat. Commun.* **2011**, *2*, 541–548.

(20) Pradhan, B.; Batabyal, S. K.; Pal, A. J. *J. Phys. Chem. B* **2006**, *110*, 8274–8277.

(21) Staii, C.; Johnson, A. T.; Chen, M.; Pennsyl, V. *Nano Lett.* **2005**, *5*, 1774–1778.

(22) Zhang, S.; Shao, Y.; Yin, G.; Lin, Y. *J. Mater. Chem.* **2010**, *20*, 2826–2830.

(23) Ozaki, J. I.; Tanifuji, S. I.; Kimura, N.; Furuichi, A.; Oya, A. *Carbon* **2006**, *44*, 1324–1326.

(24) Suckeveriene, R. Y.; Zelikman, E.; Mechrez, G.; Narkis, M. *Rev. Chem. Eng.* **2011**, *27*, 15–21.

(25) Ciric-Marjanovic, G. *Synth. Met.* **2013**, *170*, 31–56.

(26) Li, F.; Shi, J.; Qin, X. *Chinese Sci. Bull.* **2010**, *55*, 1100–1106.

(27) Jiménez, P.; Castell, P.; Sainz, R.; Ansón, A.; Martínez, M. T.; Benito, A. M.; Maser, W. K. *J. Phys. Chem. B* **2010**, *114*, 1579–1585.

(28) Chen, G. Z.; Shaffer, M. S. P.; Coleby, D.; Dixon, G.; Zhou, W.; Fray, D. J.; Windle, A. H. *Adv. Mater.* **2000**, *12*, 522–526.

(29) Saeed, K.; Park, S.-Y.; Haider, S.; Baek, J.-B. *Nanoscale Res. Lett.* **2009**, *4*, 39–46.

(30) Kim, J.; Hong, M.; Seo, Y. *Phys. Chem. Chem. Phys.* **2009**, *11*, 10851–10859.

(31) Lahelin, M.; Annala, M.; Nykänen, A.; Ruokolainen, J.; Seppälä, J. *Compos. Sci.*

Technol. **2011**, *71*, 900–907.

(32) Fei, B.; Qian, B. T.; Yang, Z. Y.; Wang, R. H.; Liu, W. C.; Mak, C. L.; Xin, J. H. *Carbon* **2008**, *46*, 1795–1797.

(33) Frackowiak, E.; Khomenko, V.; Jurewicz, K.; Lota, K.; Béguin, F. *J. Power Sources* **2006**, *153*, 413–418.

(34) Shi, C.; Deng, C.; Zhang, X.; Yang, P. *ACS Appl. Mater. Interfaces* **2013**, *5*, 7770–7776.

(35) Han, X.; Zhang, L.; Li, C. *RSC Adv.* **2014**, *4*, 30536–30541.

(36) Kong, J.; Yee, W. A.; Yang, L.; Wei, Y.; Phua, S. L.; Ong, H. G.; Ang, J. M.; Li, X.; Lu, X. *Chem. Commun.* **2012**, *48*, 10316–10318.

(37) Li, R.; Parvez, K.; Hinkel, F.; Feng, X.; Müllen, K. *Angew. Chemie Int. Ed.* **2013**, *52*, 5535–5538.

(38) Kim, B. H.; Lee, D. H.; Kim, J. Y.; Shin, D. O.; Jeong, H. Y.; Hong, S.; Yun, J. M.; Koo, C. M.; Lee, H.; Kim, S. O. *Adv. Mater.* **2011**, *23*, 5618–5622.

(39) Lee, H.; Dellatore, S. M.; Miller, W. M.; Messersmith, P. B. *Science* **2007**, *318*, 426–430.

(40) Harrington, M. J.; Masic, A.; Holten-Andersen, N.; J. Herbert Waite; Fratzl, P. *Science* **2011**, *328*, 216–220.

(41) Adeli, M.; Soleyman, R.; Beiranvand, Z.; Madani, F. *Chem. Soc. Rev.* **2013**, *42*, 5231–5256.

(42) Kobayashi, S.; Makino, A. *Chem. Rev.* **2009**, *109*, 5288–5353.

(43) Ouyang, R.; Lei, J.; Ju, H.; Xue, Y. *Adv. Funct. Mater.* **2007**, *17*, 3223–3230.

(44) Nam, H. J.; Kim, B.; Ko, J.; Jin, M.; Kim, M.; Jung, D.-Y. *Chem. - A Eur. J.* **2012**, *18*, 14000–14007.

(45) Mccloskey, B. D.; Bum, H.; Ju, H.; Rowe, B. W.; Miller, D. J.; Jae, B.; Kin, K.; Freeman, B. D. *Polymer* **2010**, *51*, 3472–3485.

(46) Liu, Y.; Ai, K.; Lu, L. *Chem. Rev.* **2014**, *114*, 5057–5115.

(47) Ju, K.; Lee, Y.; Lee, S.; Park, S. B.; Lee, J. *Biomacromolecules* **2011**, *12*, 625–632.

(48) Echegoyen, L.; Echegoyen, L. E. *Acc. Chem. Res.* **1998**, *31*, 593–601.

(49) Zhang, X.; Shi, F.; Yu, X.; Liu, H.; Fu, Y.; Wang, Z.; Jiang, L.; Li, X. *J. Am. Chem. Soc.* **2004**, *126*, 3064–3065.

(50) Bracamonte, M. V.; Melchionna, M.; Giuliani, A.; Nasi, L.; Tavagnacco, C.; Prato, M.; Fornasiero, P. *Sensors Actuators B* **2017**, *239*, 923–932.

(51) Yamanaka, I.; Onizawa, T.; Takenaka, S.; Otsuka, K. *Angew. Chemie - Int. Ed.* **2003**, *42*, 3653–3655.

(52) Edwards, J. K.; Solsona, B.; N, E. N.; Carley, A. F.; Herzing, A. a; Kiely, C. J.; Hutchings, G. J. *Science* **2009**, *323*, 1037–1041.

(53) Edwards, J. K.; Pritchard, J.; Lu, L.; Piccinini, M.; Shaw, G.; Carley, A. F.; Morgan, D. J.; Kiely, C. J.; Hutchings, G. J. *Catal. Sci. Technol.* **2014**, *4*, 3244–3250.

(54) Edwards, J. K.; Edwin, N. N.; Carley, A. F.; Herzing, A. A.; Kiely, C. J.; Hutchings, G. J. *Angew. Chemie - Int. Ed.* **2009**, *48* (45), 8512–8515.

(55) Marchesan, S.; Melchionna, M.; Prato, M. *ACS Nano* **2015**, *9*, 9441–9450.

(56) Guo, D.; Shibuya, R.; Akiba, C.; Saji, S.; Kondo, T.; Nakamura, J. *Science* **2016**, *351*, 361–365.

(57) Qu, K.; Zheng, Y.; Dai, S.; Qiao, S. Z. *Nanoscale* **2015**, *7*, 12598–12605.

(58) Hu, H.; Yu, B.; Ye, Q.; Gu, Y.; Zhou, F. *Carbon* **2010**, *48*, 2347–2353.

(59) Bernsmann, F.; Ball, V.; Addiego, F.; Ponche, A.; Michel, M.; Gracio, J. J. D. A.; Toniazzo, V.; Ruch, D. *Langmuir* **2011**, *27*, 2819–2825.

(60) Wong, C. H. A.; Chua, C. K.; Khezri, B.; Webster, R. D.; Pumera, M. *Angew. Chemie - Int. Ed.* **2013**, *52*, 8847–8850.

(61) Wang, L.; Ambrosi, A.; Pumera, M. *Angew. Chemie - Int. Ed.* **2013**, *52*, 13818–13821.

(62) Yang, S.; Feng, X.; Wang, X.; Müllen, K. *Angew. Chemie - Int. Ed.* **2011**, *50*, 5339–5343.

(63) Ding, W.; Wei, Z.; Chen, S.; Qi, X.; Yang, T.; Hu, J.; Wang, D.; Wan, L. J.; Alvi, S. F.; Li, L. *Angew. Chemie - Int. Ed.* **2013**, *52*, 11755–11759.

(64) Bernsmann, F.; Ponche, A.; Ringwald, C.; Hemmerle, J.; Raya, J.; Bechinger, B.; Voegel, J.; Schaaf, P.; Ball, V. *J. Phys. Chem. C* **2009**, *113*, 8234–8242.

(65) Bernsmann, F.; Voegel, J.; Ball, V. *Electrochim. Acta* **2011**, *56*, 3914–3919.

(66) Zhang, P.; Sun, F.; Xiang, Z.; Shen, Z.; Yun, J.; Cao, D. *Energy Environ. Sci.* **2014**, *7*, 442–450.

(67) Wei, W.; Liang, H.; Parvez, K.; Zhuang, X.; Feng, X.; Müllen, K. *Angew. Chemie - Int. Ed.* **2014**, *53*, 1570–1574.

(68) Liang, J.; Du, X.; Gibson, C.; Du, X. W.; Qiao, S. Z. *Adv. Mater.* **2013**, *25*, 6226–6231.

(69) He, W.; Jiang, C.; Wang, J.; Lu, L. *Angew. Chemie - Int. Ed.* **2014**, *53*, 9503–9507.

(70) Tuci, G.; Zafferoni, C.; D'Ambrosio, P.; Caporali, S.; Ceppatelli, M.; Rossin, A.; Tsoufis, T.; Innocenti, M.; Giambastiani, G. *ACS Catal.* **2013**, *3*, 2108–2111.

CHAPTER 4

Supramolecular hydrogels from a heterochiral tripeptide and a carbon nanostructure

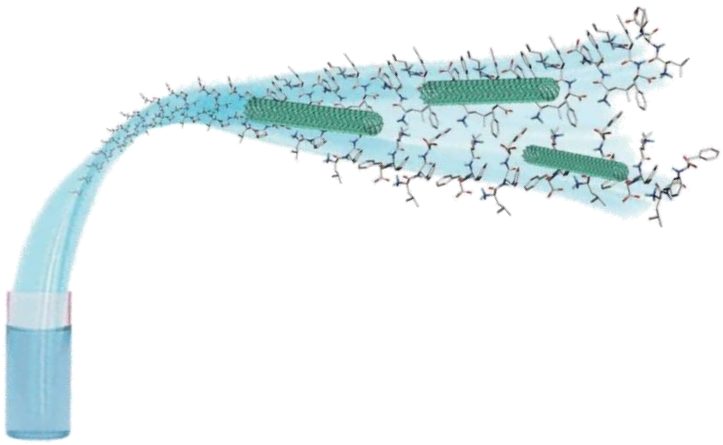

4.1. Introduction

4.1.1. Hydrogels

Hydrogels are viscoelastic materials that are able to entrap a large amount of water in a 3D network matrix. This sort of materials is widely present in nature. The scientific community has dedicated great efforts to apply hydrogels in medicine.[1] Their properties make them appealing for drug delivery applications, wound healing, or tissue engineering. Biologically-relevant hydrogels can be composed of molecules of different chemical nature including peptides or proteins and carbohydrates (*e.g.* collagen or hyaluronic acid), synthetic or semi-synthetic polymers, alone or in combination.

Hydrogel properties can be improved or expanded by including nanomaterials. In particular, the combination of carbon nanostructures (CNS, *e.g.* CNTs or G) is very appealing and can lead to the formation of smart biomaterials that are mechanically more resilient, and that respond to physicochemical stimuli (*e.g.* near-infrared (NIR) light irradiation, electrical stimulation, etc.).[2]

Amongst the various hydrogel building blocks, proteins have been historically very attractive due to their natural abundance, well-known chemistry, bioactivity, and biodegradability. However, even though research on protein hydrogels is a mature field, not often have they reached the stage of clinical trials or the market. Among the main disadvantages, there are batch-to-batch low reproducibility, pathogen transfer from natural sources, physicochemical instability, and immunogenicity. It is thus preferable to replace them with short peptides that could mimic some of their functions, whilst minimising side effects. Sequences as short as tripeptides are very attractive since they can convey powerful biological messages (*e.g.* Arg-Gly-Asp for cell adhesion)[3] and confer self-assembling abilities into hydrogels (*e.g.* Phe-Phe motif containing sequences).[4]

4.1.2. Ultra-short peptide hydrogels

Since the cost of peptide synthesis and purification increases exponentially with amino acid number, ultra-short peptides (*i.e.* composed of two to three amino acids) represent an affordable option.[5] They can be prepared also by means of enzymatic catalysis, biotechnology methods, or liquid-phase synthesis, which offer easier scale-up relative to solid-phase peptide synthesis (SPPS). [6]

Research on ultra-short peptide self-assembly in *superstructures* (*i.e.* structures that span across sizescales notably larger than that of the individual components) blossomed after the seminal work by Reches and Gazit in 2003.[7] In this work, through a minimalist approach, they identified Phe-Phe as a key self-assembling motif from amyloid beta peptide. This motif leads to diverse nanostructures, including nanotubes, nanorods, nanowires, and nanospheres, thanks to subtle chemical variations on the peptide structure or in the self-assembly process (Figure 4.1).[4] The topic has attracted great interest and generated vast literature on derived materials, including hydrogels.

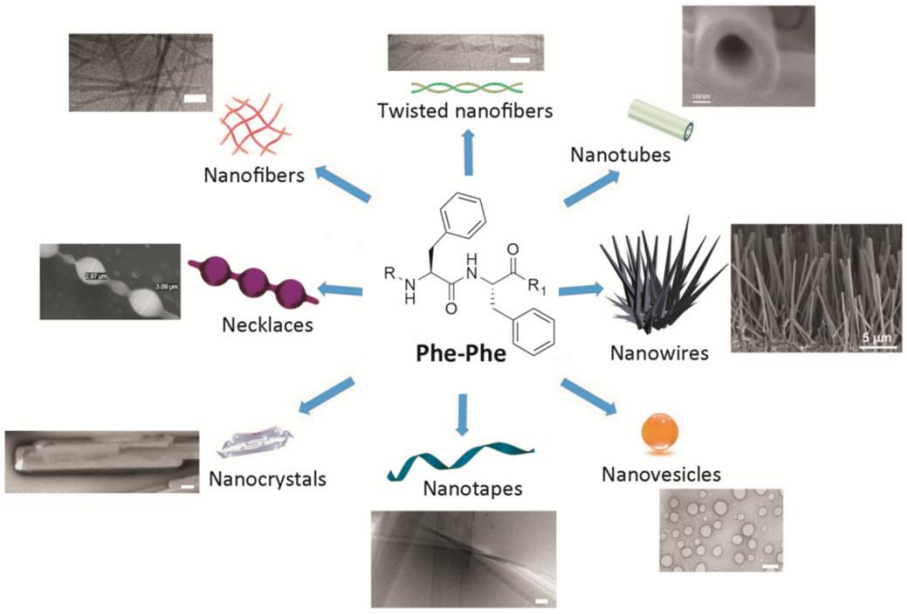

Figure 4.1. Examples of different supramolecular nanostructures were the Phe-Phe motif was present.[4] Reproduced with permission from (4), Copyright 2015

Unless a crossed-linking reaction is involved,[8,9,10] the obtained materials are physical or supramolecular hydrogels. 3D-matrix formation is driven by the cooperative interplay of weak forces such as hydrogen bonding, hydrophobic interactions, π-π

stacking, and electrostatic forces.[5] Typically, hydrophobic or amphipathic compounds are good candidates for gelators, however, it is very difficult to predict self-assembly and gelation, since its cooperative nature leads to dramatic macroscopic changes arising from subtle differences in their components or in the process conditions.

Indeed, there is relatively little chemical diversity in the reported gelators, which belong mainly to two groups. A popular approach consists in peptide derivatisation with synthetic end-capping groups, especially aromatic motifs (*e.g.* Fmoc, naphthalene, pyrene, etc.), that act as rigid templates driving π-π stacking.[5] However, use of such moieties is not ideal, especially for biological use and due to their persistence in the environment, for which unprotected di- or tripeptides would be preferable. Unfortunately, design of the latter is challenging, as exemplified by a study by Frederix *et al.* where only four new hydrogelators (*i.e.* Lys-Tyr-Phe, Lys-Tyr-Tyr, Lys-Phe-Phe, Lys-Tyr-Trp) were identified in experiments driven by an *in silico* screen of all 8000 combinations of L-amino acids in tripeptides.[11]

An alternative approach consists of introducing D-amino acids at selected positions to favour conformation and self-assembly. This approach offers key advantages, such as increased protease resistance and stability of secondary structure.[12] The first reports date back to 2012, where introduction of a D-amino acid at the N-terminus of a hydrophobic sequence bearing the Phe-Phe motif, led to rapid gelation at physiological conditions, whereas the L-tripeptide analogue did not gel.[13,14] Also other combinations of L- and D-amino acids can lead to hydrogels at neutral pH from hydrophobic sequences bearing two phenylalanines (Figure 4.2),[15,16,17] and with different rheological properties.

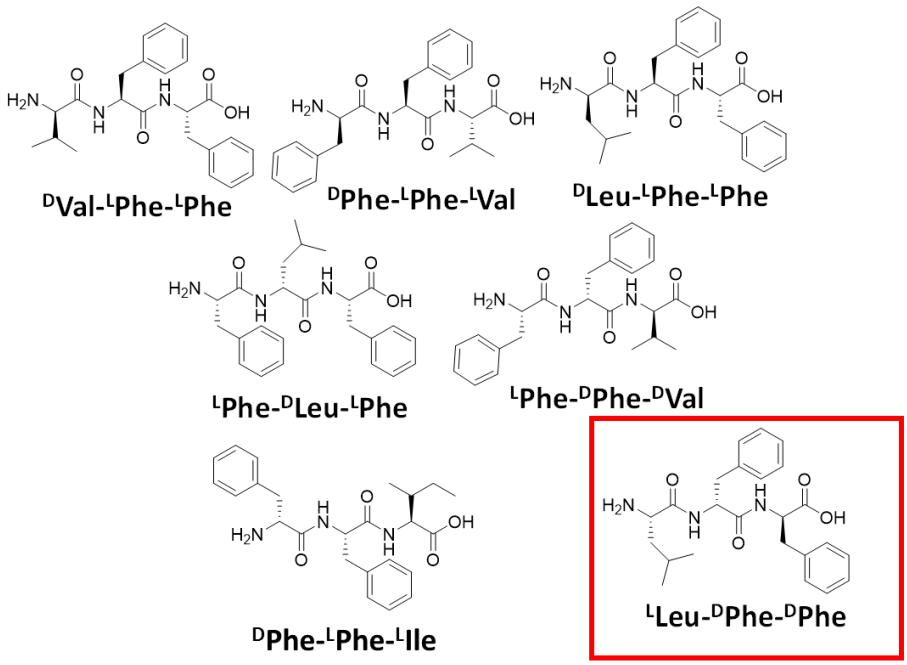

Figure 4.2. Unprotected heterochiral tripeptides forming hydrogels reported to date. In the red box the gelator prepared in this work.

Spectroscopic and *in silico* studies highlighted a tendency for these hydrogelators to form antiparallel β-sheets that stack into amyloid-like structures, although *in vitro* cell culture studies did not reveal cytotoxicity. Usually these tripeptides are dissolved at alkaline pH, where they exist as anions and repel each other; a pH trigger to neutral forms the zwitterions which rapidly self-assemble. In particular, the tripeptide ^{D}Leu-^{L}Phe-^{L}Phe is a particularly good hydrogelator that can co-assemble with aromatic dyes[18] or drugs[19] in loadings as high as 30 wt.% relative to the peptide. Its self-assembly behaviour was monitored over time, revealing formation of spherical nucleation zones, from which fibrils rapidly emerge, elongate and bundle in various directions. Peptide stacks in beta-sheets held by hydrogen bonding and electrostatic interactions between termini. Importantly, interlocking of different sheets occurs via a Phe zipper that creates a highly hydrophobic region that excludes water and stabilises the assembly (Figure 4.3).[14]

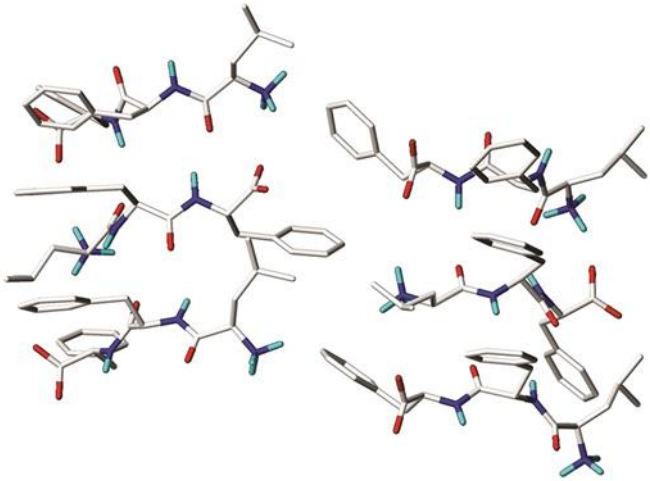

Figure 4.3. Optimised structures of ^{D}Leu-^{L}Phe-^{L}Phe. Adapted from (14) with permission of The Royal Society of Chemistry.

4.1.3. Interaction of CNS with proteins or peptides

Hybridisation of CNS and proteins or peptides has been widely studied over the last years for applications in the biomedical field, such as cancer therapy, bioimaging, biosensors, tissue engineering or drug delivery.[20] However, the very different chemical nature of the two components makes the design of a hybrid material technically challenging.[21]

In line with protein/peptide complex structure-function relationship, it is important to consider parameters such as the temperature, pH or ionic strength. Molecules displaying ionisable groups may change drastically their zeta potential and therefore their function by subtle changes in the pH of the media. Besides, folding, and thus biological function, may be irreversibly impaired by a number of factors. For instance, denaturation may occur if the peptide or protein is exposed to harsh chemical conditions, typically used for CNS functionalisation. CNS curvature is another parameter that can affect protein folding on its surface as the two components are brought together. In addition, protein and peptide folding is usually an orchestrated sequence of chemical interaction-driven events that aim to mask hydrophobic regions from the aqueous environments; presence of a large hydrophobic surface, as that of CNS, is likely to interfere with such process. Despite such technical challenges, a vast number of studies exist on protein/peptide

interaction with CNS, that can be grouped mainly in non-covalent or covalent approaches, as described by recent reviews on the topic.[22,23]

4.1.3.1. Non-covalent functionalisation

Given the chemical diversity of amino acids, a variety of non-covalent interactions can be exploited for CNS binding, including Van der Waals, hydrophobic, aromatic, and/or electrostatic interactions. For instance, peptides rich of phenylalanine and tryptophan will be used for aromatic interaction,[24] whereas those rich of arginine or lysine may form cation-π pairs.[25]

Direct interaction between the biomolecule and the CNS can be useful to disperse the CNS in water. Dieckmann *et al.* dispersed SWCNTs by simple mixing with an amphipathic helical peptide upon ultrasonication.[24] The hydrophobic residues (Val and Phe) faced the SWCNTs, while the hydrophilic residues (Lys, Glu or His) were exposed to media (Figure 4.4). Similarly, MWCNTs were dispersed with an ionic complementary peptide in water.[26] Dispersions were stable at both acidic and basic pH (*i.e.* pH <5 or >8), but unstable with pH ~ pI of the peptide, highlighting pH influence on peptide structure. Unfortunately, this approach has several drawbacks, including non-specific protein binding, low stability (*i.e.* peptide dissociation upon dilution), and potential loss of protein function due to unfolding.[27] Non-specific binding can be mitigated by introducing appropriate linkers. Examples include pyrene sulfonic acid to bind positively charged proteins;[28] or poly(diallyldimethylammonium chloride) to anchor negatively charged peptide nanofibres on RGO.[29] CNS PEGylation is a useful method to alleviate non-specific protein adsorption onto CNS *in vivo*.[30]

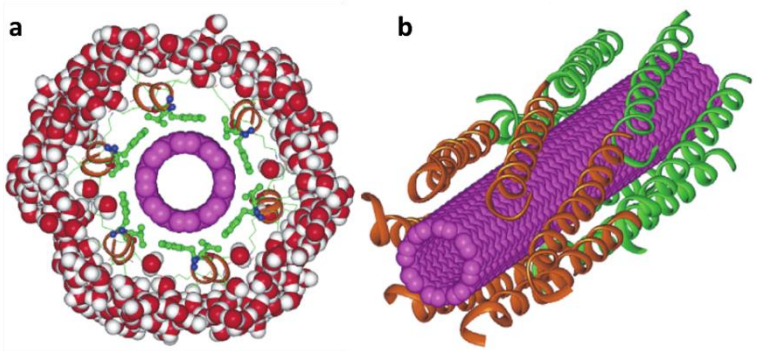

Figure 4.4. Molecular modelling illustrating the interaction between SWCNTs and an amphipatic α-helix. The green motifs in (a) represent hydrophobic amino acids that interact with SWCNTs. (b) represents the interaction of 12 α-helix with a SWCNT. It shows that the α-helix structure is maintained. Adapted with permission from (24). Copyright 2013 American Chemical Society.

4.1.3.2. Covalent functionalisation

This method is less common, due to technical challenges. A popular approach involves CNS oxidation, which may compromise CNS properties, for subsequent coupling *via* activation of COOH groups. Besides, amide coupling with protein/peptide amines may also rigidify the latter structure, affecting function.[22] This method has been used, for example, to bind an antimicrobial peptide to GO for water purification.[31]

The changes in the structure of the protein can be alleviated by the introduction of a linker (*e.g.* PEG) between CNS and peptide. For instance, Dordick *et al.* reported higher bactericidal activity for CNTs conjugated to proteins when a PEG_{12} chain was interlocked between the enzyme and the graphitic wall.[32]

4.1.3.3. Combination of covalent and non-covalent functionalisation

This approach involves either CNS covalent modification with groups that favour interaction with peptides (*e.g.* carboxylic or sulfonic acids)[33,28]; or peptide covalent derivatisation with aromatic motifs (*e.g.* pyrene) to boost CNS interaction. The former has been widely used to enhance GO and CNT interaction with peptide-based gelators.[2,23]

4.1.4. Self-assembling short peptide-CNS hydrogels

As mentioned above, literature on hydrogels composed of short peptides and CNS is still scarce, due to technical challenges. Banerjee and co-workers reported the hybridisation of oxidised SWCNTs and RGO in two hydrogels made of a protected amino acid (*i.e.* Fmoc-Phe-OH) or a protected dipeptide (*i.e.* Fmoc-Tyr-Asp-OH or Fmoc-Phe-Asp-OH), respectively.[34,35] CNS presence increased hydrogel stiffness in both cases. Yang *et al.* controlled the supramolecular assembly of gluthathione tripeptide by adjusting the amount of GO.[36]

4.2. Aim of the work

The aim of this work is to prepare a hydrogel at physiological pH from an unprotected, heterochiral self-assembling tripeptide and a CNS. The unreported gelator ^{L}Leu-^{D}Phe-^{D}Phe was chosen as the potentially more protease-stable enantiomer of a well-characterised gelator,[14] which rapidly leads to stable gels within seconds upon application of a pH trigger, and which also has the advantage to tolerate presence of other (small) molecules up to 30% its weight.[19,18]

CNS oxidation can reduce toxicity and allow excretion *in vivo*,[37,38] besides allowing CNS dispersion in aqueous media. Importantly, CNS inclusion in the hydrogel could add interesting responsiveness (*e.g.* to NIR irradiation, electrical stimuli, etc.) that could be exploited in the future for drug release *on demand*. Therefore, oxidised CNS were chosen for this work. In particular, the aim is to assess the influence of CNS morphology on the final material, by testing: GO (as 2D model), ox-CNTs (as 1D model), ox-CNHs (as 3D model). They will be mixed with the peptide and the properties of the final material will be assessed by different techniques: IR, TEM, rheometry and CD.

4.3. Results and discussion

4.3.1. Peptide synthesis

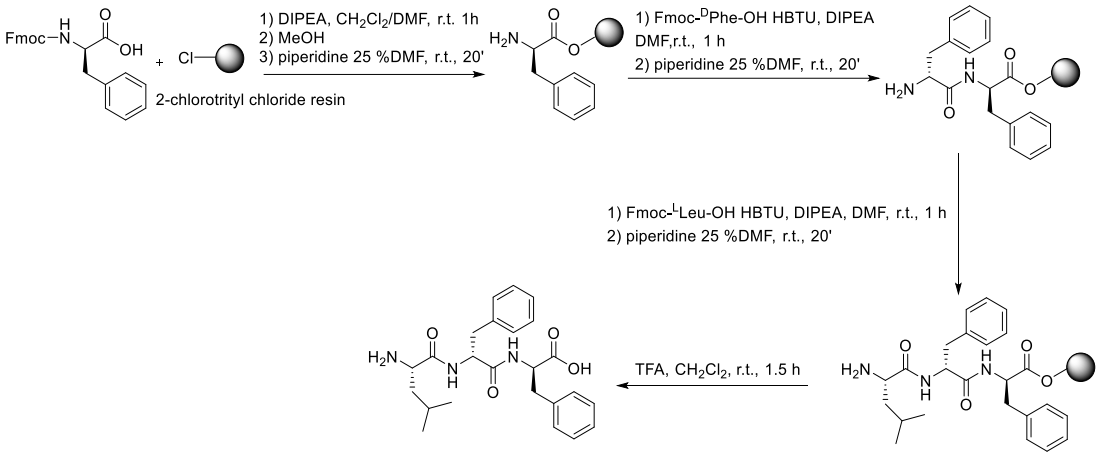

Scheme 4.1. Solid-phase synthesis of ^{L}Leu-^{D}Phe-^{D}Phe.

The peptide sequence ^{L}Leu-^{D}Phe-^{D}Phe was synthesised by Fmoc-based SPPS. Peptide chain elongation occurs stepwise from C- to N-terminal through repetitive cycles of coupling and deprotection (Scheme 4.1). Each step was monitored by two colourimetric tests: i) Kaiser test (refer to Chapter 1 for further details); and ii) the bromophenol blue test, in which the dye changes colour from yellow to blue due to pH increase when free amines are present. Our strategy involved use of the popular 2-chlorotrityl chloride resin, onto which the first amino acid was loaded and its amount quantified by spectroscopic absorbance of the coloured solution obtained from Fmoc-hydrolysis in a test sample (see Experimental Section for details). *N,N,N′,N′*-Tetramethyl-*O*-(1*H*-benzotriazol-1-yl)uronium hexafluorophosphate (HBTU) was used as coupling agent. The mechanism of the activation is driven by the tetramethylurea and ends up with hydroxybenzotriazole ester (*i.e.* a good leaving group) that would eventually favour the formation of the peptide bond (Scheme 4.1). A final cleavage in acidic medium hydrolysed the ester that bound the C-terminus of the peptide to the resin. Reverse-phase HPLC purification yielded pure ^{L}Leu-^{D}Phe-^{D}Phe, which was characterised by mass spectrometry (ES-MS), ^{1}H-NMR and ^{13}C-NMR (see Experimental Section).

4.3.2. Hydrogel characterisation

Enantiomers have identical physical and chemical behaviour except when they interact with circularly polarised light or with other chiral molecules. Thus, the gelling ability exhibited by the enantiomer ^{D}Leu-^{L}Phe-^{L}Phe was also expected for ^{L}Leu-^{D}Phe-^{D}Phe, and this was confirmed by using the vial inversion test. Briefly, the peptide was dissolved in alkaline phosphate buffer (pH~12) and subsequent addition of a mildly acidic phosphate buffer (pH~6) led to a gel at a final pH of 7.4 (Figure 4.5).

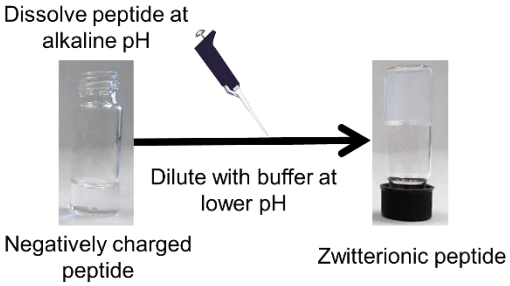

Figure 4.5. Inversion test of ^{L}Leu-^{D}Phe-^{D}Phe (final concentration 2.5 mg ml^{-1}).

Rheology studies flow and deformation of soft matter and is the preferred choice to define a liquid or gel state, and their mutual transitions. An oscillatory rheometer (Figure 4.6) displays two metal plates that hold the material to be tested; one of the plates oscillates onto the other at a defined frequency, and exerts a defined stress to the material. The material response to such forces is measured by means of the elastic or storage (G') modulus and the viscous or loss (G'') modulus. Briefly, a gel state displays G' > G'', while a viscous solution will have G'' > G'. The gel-to-sol or sol-to-gel transitions occur when G' = G''. A *frequency sweep* test is performed to evaluate the gel nature, as gels should display not only G' > G'', but also both G should be independent of the oscillation frequency. A *stress sweep* test is useful to determine the resistance of the gel to applied stress before its structure collapses. Finally, a *time sweep* test can be performed at defined frequency and stress to monitor gelation kinetics. All three tests were performed.

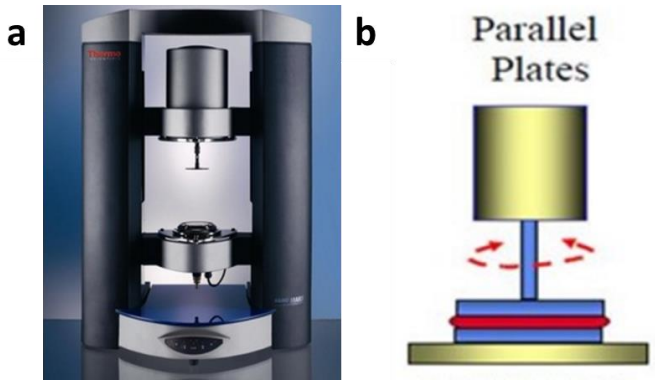

Figure 4.6. (a) rheometer used in this work and (b) schematic representation of the parallel plates. The red arrows represent the applied stress and the red area represent the hydrogel.

Frequency sweep measurements allowed the determination of ^{L}Leu-^{D}Phe-^{D}Phe minimum gelling concentration (MGC), *i.e.* 0.5 mg ml^{-1} (0.05 % wt. or 1.17 mM) (Figure 4.7). However, gels at MGC are weak (*i.e.* G'~400 Pa and G''~100 Pa), thus 2.5 mg ml^{-1} of ^{L}Leu-^{D}Phe-^{D}Phe was chosen as an ideal concentration for further tests, since it allows to use relatively small amounts of peptide whilst yielding hydrogels with more applicable mechanical properties (*i.e.*~1.7 kPa and 0.1 kPa for G' and G'' respectively after 30 min).

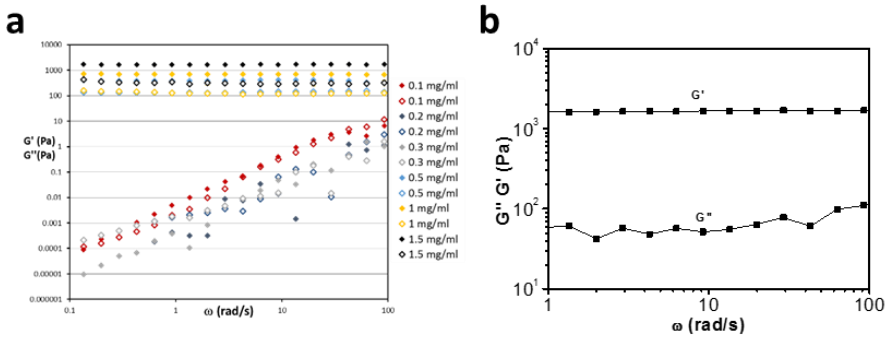

Figure 4.7. Frequency sweep data for the calculation of the MGC (left) and frequency sweep data of 2.5 mg ml-1 hydrogel.

Stress sweeps showed that loss of the linear viscoelastic response of the material, which can be related to loss of stability, occurred at ~80 Pa (Figure 4.8). Gelation kinetics were probed at conditions whereby the gel structure is not altered, *i.e.* in the so-called *linear viscoelastic region*. G' and G'' were thus monitored over time at 1 Pa every second (1 Hz) (Figure 4.8 b). In agreement with visual observations, gelation occured almost immediately, thus not allowing monitoring of the gelation point. After approximately 30

minutes, a plateau was reached where both G' and G'' did not further vary significantly. At this time, the peptide was expected to be completely assembled into fibrils. Eventually, such fibrils will bundle in thicker fibres with the consequent further stiffening of the material as observed after 24 h.[14]

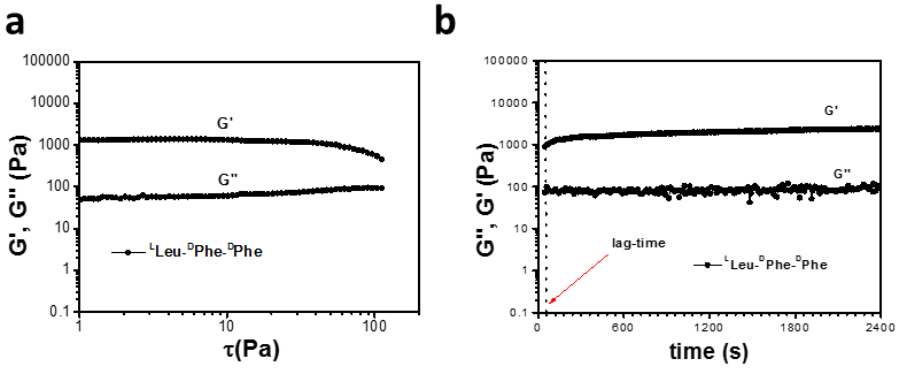

Figure 4.8. (a) Stress sweep and (b) time sweep experiments for ^{L}Leu-^{D}Phe-^{D}Phe (2.5 mg ml^{-1}).

^{L}Leu-^{D}Phe-^{D}Phe hydrogel at the nanoscale was characterised by TEM. Peptide nanostructures are very challenging to visualise with this technique since: i) their low electron density renders low signal/noise ratio (*i.e.* undefined features are observed); and ii) the continuous irradiation with the electron beam damages the sample. Besides, artefacts due to sample preparation or drying are to be avoided. Cryo-TEM is thus ideal for these samples, but it requires specific instrumentation and the vitrification of the sample in liquid ethane or propane that demands special safety measures. In practice, TEM and AFM imaging are popular alternatives. In this work, ^{L}Leu-^{D}Phe-^{D}Phe was analysed by negative staining TEM, by using potassium phosphotungstate to increase the electronic contrast and image fine features of the entangled fibre bundles (Figure 4.9).

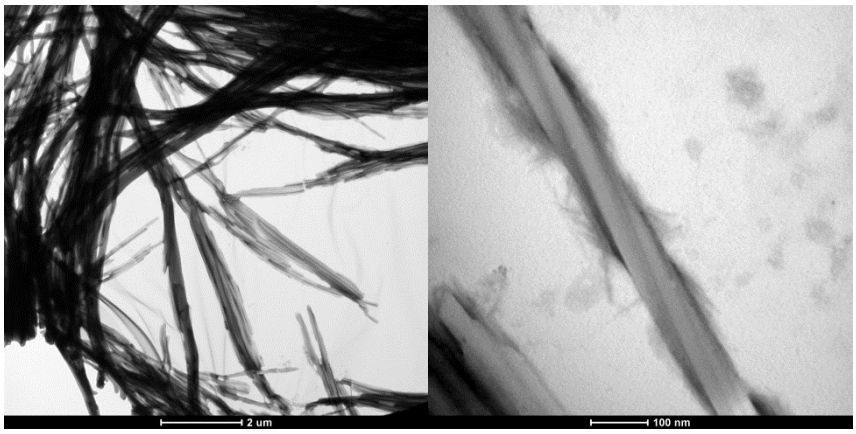

Figure 4.9. Negative staining TEM images of ^{L}Leu-^{D}Phe-^{D}Phe hydrogel.

Self-assembled peptide fibres were analysed also by Raman microspectrometry. Short peptides such as Phe-Phe have already been studied by this technique.[39] In a combined *in silico*-experimental work, Lekprasert *et al.* assigned most of the active Raman modes of the dipeptide in the nanotube arrangement and identified two active modes related to the aromatic ring at 1002 cm^{-1} and 1032 cm^{-1}. The signal with higher intensity (~ 1003 cm^{-1}) was used to map images of the thick fibre bundles using Raman microscopy (Figure 4.10).

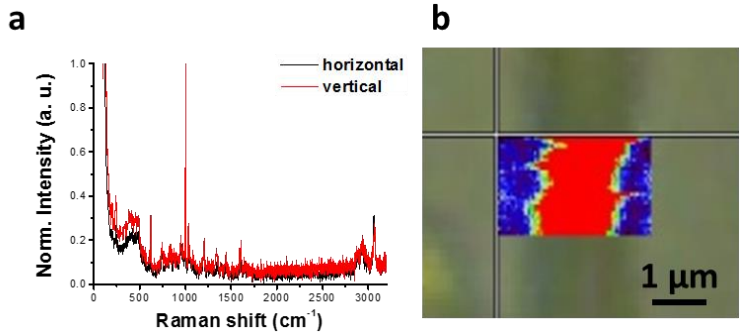

Figure 4.10. Raman spectra of ^{L}Leu-^{D}Phe-^{D}Phe fibres (a) and Raman imaging of one thick fibre (in red the zone with high intensity at 1003 cm^{-1} and in blue the background).

4.3.2.1. Secondary structure of the peptide sequence

The primary structure of the tripeptide was well characterised by the common techniques (*i.e.* NMR and MS-spectrometry). However, the identification of the

secondary structure was not trivial, especially the peptide being heterochiral and short, and it required the combination of different analyses, such as CD and ATR-IR.

UV-light absorption of ^{L}Leu-^{D}Phe-^{D}Phe was ascribed to three different electronic transitions, located in two chromophore groups: i) the aromatic ring of the phenylalanines and ii) the amide groups of the backbone. Figure 4.11 a shows the absorption of ^{L}Leu-^{D}Phe-^{D}Phe at neutral pH at concentration below the MGC to avoid self-assembly. The lowest energy absorption (λ = 258 nm) is due to the $\pi \rightarrow \pi^*$ transition on the aromatic ring. Due to the symmetry of the molecular orbitals implicated in the transition, the process is considered forbidden and therefore the intensity of the band is very low (ε = 195 cm^{-1} M^{-1}). The two remaining transitions, $n \rightarrow \pi^*$ and another $\pi \rightarrow \pi^*$, lay on the peptide bonds (λ = 190-200 nm). The $n \rightarrow \pi^*$ process should result in a low intensity band since the orbitals do not overlap being this transition forbidden (ε = 100 cm^{-1} M^{-1}). However, due to the broadening of the absorption bands in UV-Vis spectroscopy the former overlaps with the highest intensity band (ε = 7000 cm^{-1} M^{-1}) assigned to the $\pi \rightarrow \pi^*$.

The CD signal (Figure 4.11 b) shows that the sample absorbs preferably right circularly polarised light (*i.e.* negative signal) in the region 200-230 nm. No CD signal was found at 258 nm suggesting no effect of the chirality on the aromatic motifs. The

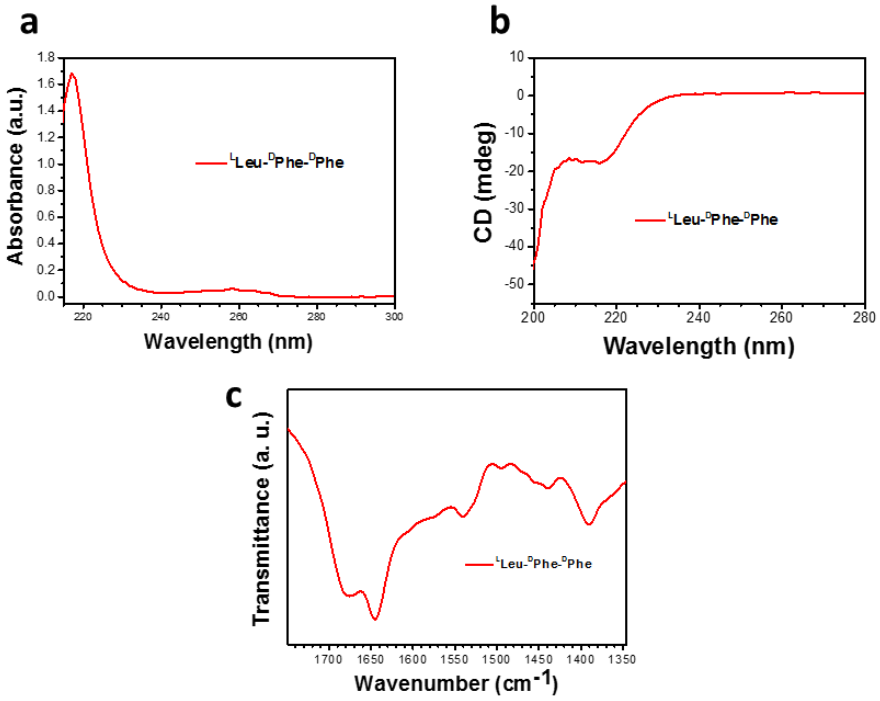

Figure 4.11. (a) UV-Vis, (b) CD and (c) ATR-IR spectra of the disassembled peptide.

ATR-IR spectrum of the amide I region of the peptide in solution was characterised by very broad signals that suggest absence of an organised supramolecular structure with a defined H-bonding pattern (that would result in narrow signals for the amide I band at specific positions depending on the conformation, Figure 4.11 c).

Hydrogelation caused dramatic changes both in ATR-IR and CD spectra (Figure 4.12 a and b, respectively). Both are compatible with anti-parallel β-sheet formation as reported for the enantiomer. The amide I region of ATR-IR is dominated by the characteristic two maxima at 1689 cm^{-1} and 1641 cm^{-1}. The CD spectrum shows a negative peak at 224 nm and a broad positive signal in the region of 200-220 nm. The spectrum is the mirror-image of that of the enantiomer, as expected.

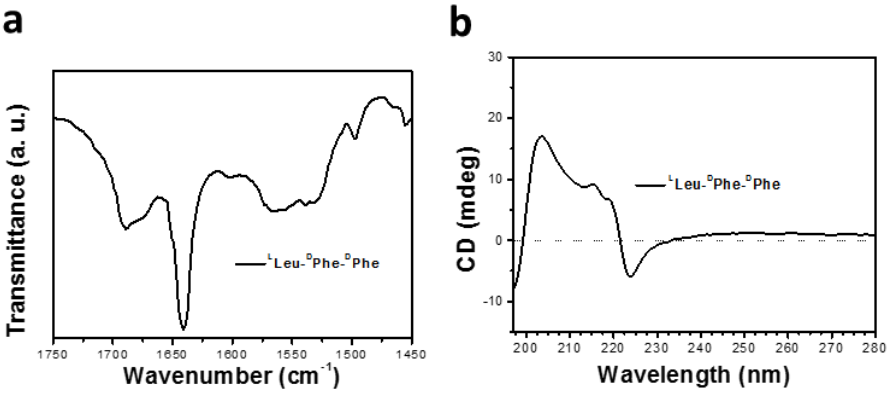

Figure 4.12. (a) ATR-IR and (b) CD data of the peptide hydrogel.

4.3.3. Functionalisation of carbon nanostructures

To overcome the low processability of CNSs due to their inherent tendency towards aggregation, and even more so in polar solvents, each CNS was oxidised by using different protocols, according to their different level of chemical reactivity (Scheme 4.2).

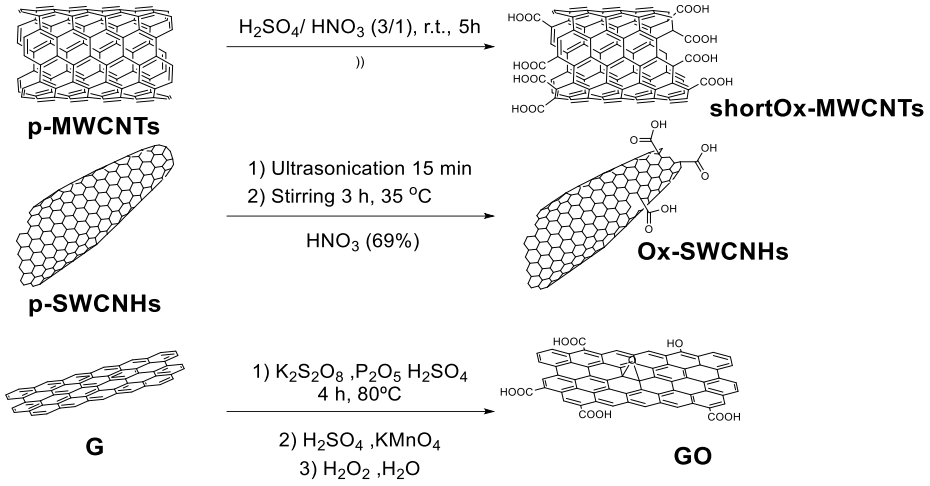

Scheme 4.2. Oxidation protocols for the different nanostructures.

In this way, carboxylic moieties were introduced in each CNS, yet maintaining their overall structure as determined by TEM and Raman analyses (Figure 4.13). TGA under N_2 confirmed analogous level of oxidation for each CNS, corresponding to ~10 % wt. (*i.e.* 2.2 mmol carboxylic groups per gram of material).

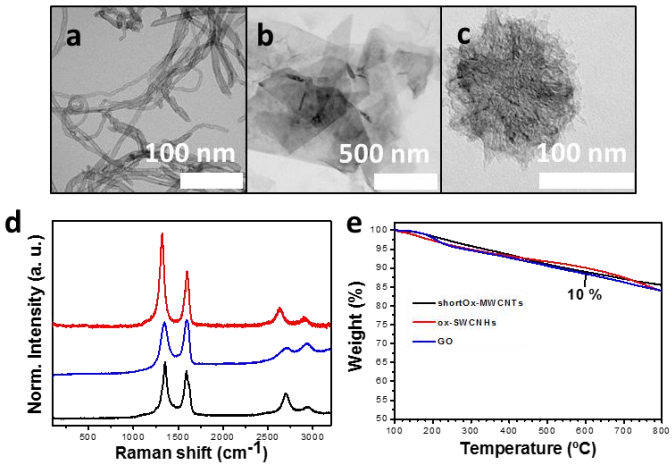

Figure 4.13. (a-c) TEM images of ox-MWCNTs, GO and ox-CNHs; (d) Raman spectra of oxidised CNS; and (e) TGA in N_2 of oxidised CNS.

4.3.4. CNS-peptide interaction in solution

Hydrogel formation was assessed by using the pH trigger at analogous experimental conditions as reported above in section 3.3.2. In line of principle, the CNSs could be added to either solution, *i.e.* at pH ~12 or pH ~6. However, despite the good

dispersibility of ox-CNSs in water, they aggregated in either solution, and this is likely due to the high ionic strength of the buffers. Fortunately, the amphiphilic nature of the peptide allows its use as a surfactant, effectively debundling the ox-CNSs when both components were mixed in the alkaline buffer, thus leading to homogeneous dispersions (Figure 4.14).

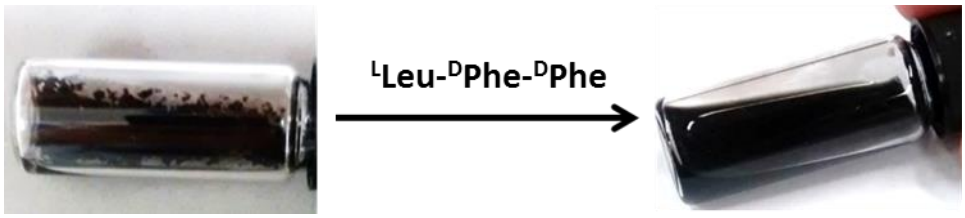

Figure 4.14. . Ox-MWCNTs dispersions (2 mg ml^{-1}) in alkaline buffer at pH 12 before (left) and after (right) the interaction with the peptide.

To shed light on the interaction between peptide and ox-CNS in solution, ATR-IR and CD analyses were carried out (Figure 4.15). The low signal-to-noise ratio of ATR-IR data due to the weak amide I signal, together with the lack of molecular order at high pH, rendered the analysis quite challenging. Overall, no significant shift in the amide I band was seen relative to the solutions containing only the peptide, although the sample with ox-CNHs clearly displayed far broader signals, suggesting more disorder. Besides, it should be noted that variations in 1670 cm^{-1} signal intensity may be ascribed to batch-to-batch differences in TFA content (note: TFA is the peptide counterion after HPLC purification). Similarly, CD analyses revealed no red- or blue-shifts in the peptide spectrum upon CNS addition.

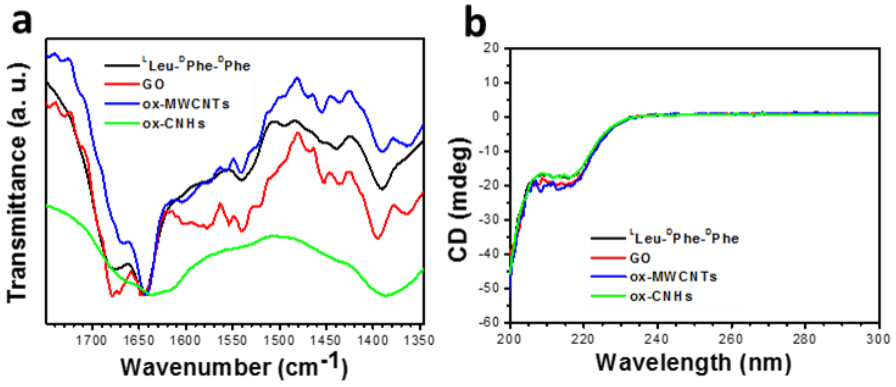

Figure 4.15. (a) ATR-IR and (b) CD of solution 1 (*i.e.* 5 mg ml^{-1} of peptide and 2 mg ml^{-1} of the corresponding ox-CNS in phosphate buffer pH~12).

Thus, considering: i) the vast C sp^2 lattice of all the employed CNSs, ii) the absence of any significant variation in the ATR-IR and CD peptide signals, and iii) the increase of dispersibility of the ox-CNSs, we hypothesised that ^{L}Leu-^{D}Phe-^{D}Phe interacted with CNSs through π-π stacking facing the solution with the more polar groups, in a similar manner as other amphiphilic surfactants or aromatic small molecules interact with CNS.[40]

4.3.5. Peptide hydrogels containing CNS

Solutions were prepared in alkaline buffer containing 5 mg ml^{-1} (5.8 mM) of tripeptide and 2 mg ml^{-1} of ox-CNS, to test whether the tripeptide could bear a high loading of nanomaterial during self-assembly. Upon dilution with an equal volume of mildly acidic buffer to reach a final neutral pH, rapid gelation occurred in all cases (Figure 4.16 a). Hydrogel stability over time was confirmed in the case of ox-MWCNTs and GO. By contrast, ox-CNHs appeared to segregate from the peptide into visible aggregates within a few hours (Figure 4.16 b). Remarkably, the presence of any of the ox-CNSs at such high loading, not only did not hamper hydrogel formation, but also it did not alter the kinetics of the process, which happened too rapidly to register the sol-to-gel transition

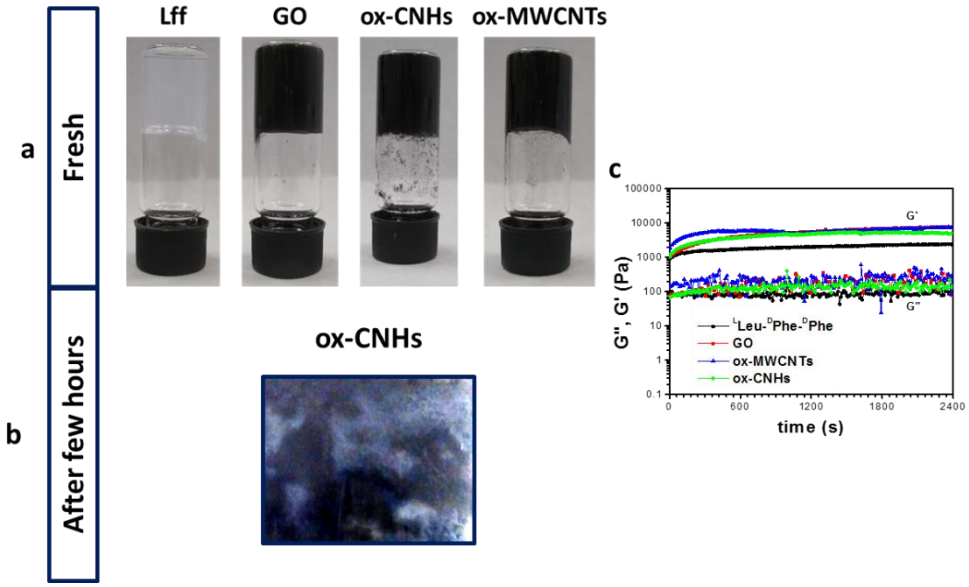

Figure 4.16. (a) Images of hydrogels freshly made (a); (b) image of ox-CNHs hydrogel a few hours after its preparation; and (c) time sweep experiments of the native hydrogel and composites.

by rheometric analysis (Figure 4.16 c). Presence of the robust CNSs, resulted in all cases in hydrogels with elastic moduli (G') that were significantly higher relative to the peptide alone (Figure 4.16 c). Frequency sweeps confirmed the data (Figure 4.17). The viscous component (G'') was not significantly different amongst samples (i.e. 0.1 kPa), while the elastic modulus (G') increased notably (i.e. 4.2 kPa for ox-MWCNTs, 3.3 kPa ox-CNHs, and 6.2 kPa for GO), relative to the peptide alone (i.e. 1.7 kPa). These results confirmed the improvement of the rheological properties of peptide hydrogels upon CNS addition.

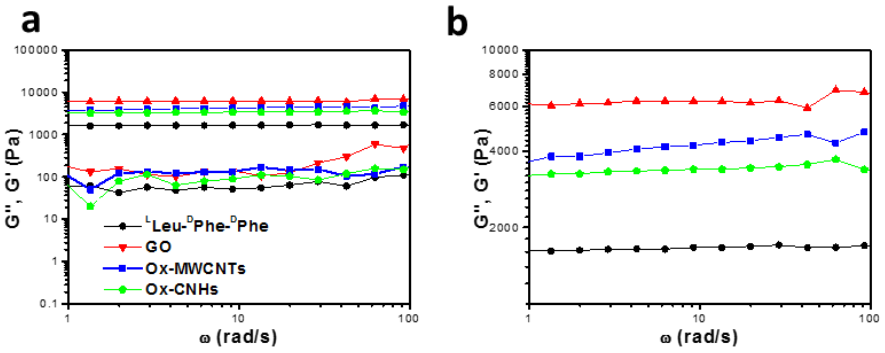

Figure 4.17. (a) Frequency sweep measurements of the native hydrogel and of the composites; and (b) zoom in of the G' region for better appreciation of the changes.

Next, composite hydrogels were prepared with a low loading of CNS (*i.e.* 0.1 mg ml^{-1} or 0.01%) to assess whether the effects on the rheological properties of the final materials were maintained (Figure 4.18). Frequency sweeps revealed that the elastic

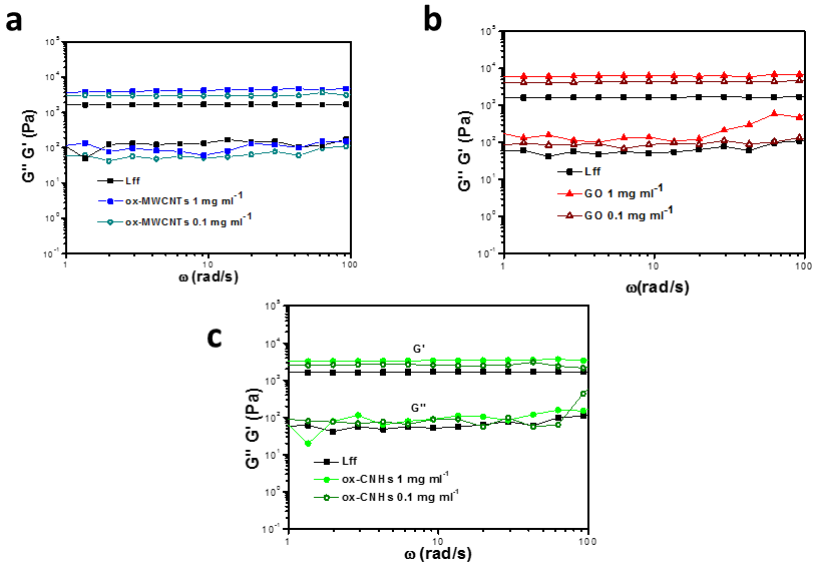

Figure 4.18. Frequency sweep of native hydrogel and the composites at high (1 mg ml^{-1}) and low content (0.1 mg ml^{-1}) hydrogels: (a) ox-MWCNTs; (b) GO; and (c) ox-CNHs.

moduli G' decreased (2.9 kPa for ox-MWCNTs, 2.5 kPa for ox-CNHs, and 4.2 kPa for GO), but they were still higher relative to the peptide alone (1.7 kPa).

CNS are well-known for their resilience, thus the effect of their presence was assessed also by means of stress sweeps, where the material is subjected to increasing amounts of external forces until the gel network is disrupted (Figure 4.19). Loss of linearity of elastic and viscous moduli against applied stress is an early indication of significant alteration of the gel network structure. Only in the case of GO or ox-CNTs, both at low and high content, the composite hydrogels displayed higher resistance to stress, while ox-CNHs did not have a significant effect.

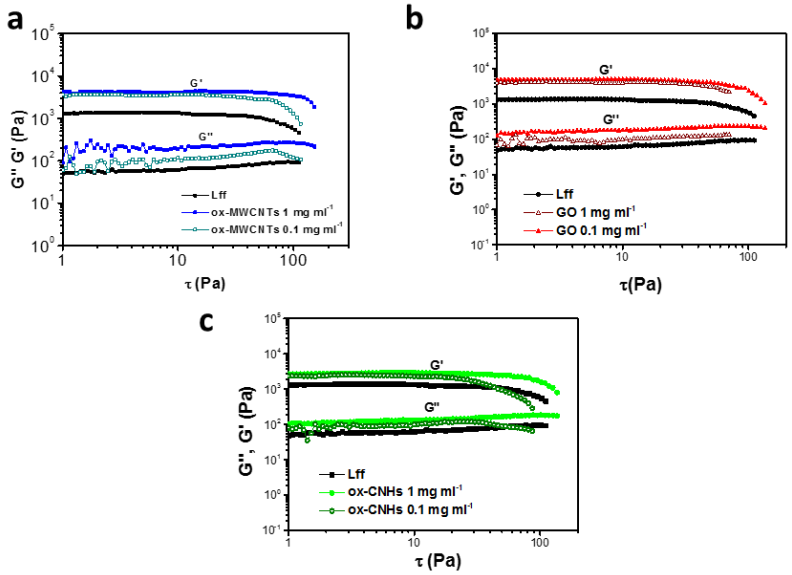

Figure 4. 19. Stress sweep of native hydrogel and the composites at high (1 mg ml^{-1}) and low content (0.1 mg ml^{-1}) hydrogels: (a) ox-MWCNTs; (b) GO; and (c) ox-CNHs.

Negative staining TEM analysis of the composite hydrogels at high loading of CNS were in agreement with the visual observations (Figure 4.20). Interaction was confirmed between the peptide fibres and either ox-MWCNTs or GO, but to a much lesser extent for ox-CNHs. Ox-MWNCTs and GO were distinctly immersed into the gel matrix interacting with numerous fibres. On the contrary, ox-CNHs appeared to aggregate and not always interacted with the peptide fibres.

The morphology and width of peptide fibres was preserved in all cases. This observation suggested that the peptide conformation, and thus its secondary or tertiary structure, were not significantly altered. This is in agreement with ATR-IR and CD data

of the composites, in which neither red- or blue-shifts, nor significant differences in the vibrational or CD peaks were observed (Figure 4.21). It should be noted that CD data was normalized since signal intensities were affected by scattering, due to the CNS.

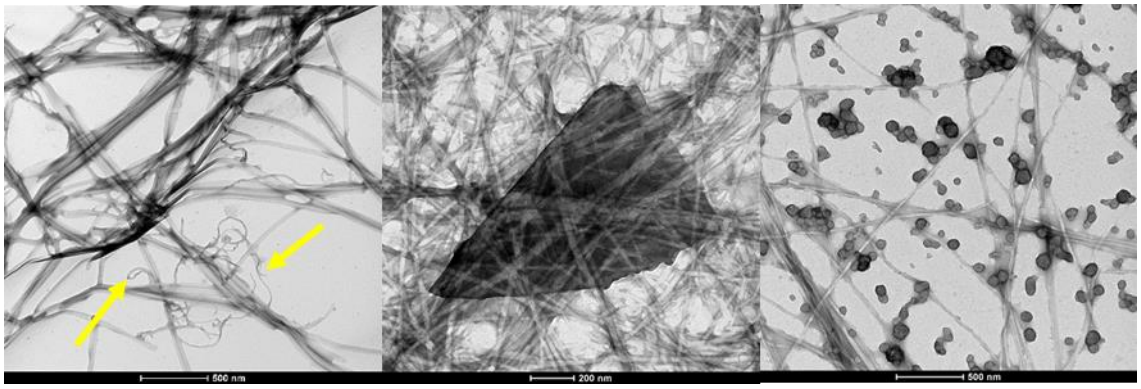

Figure 4.20. Negative staining TEM imaging of the composite hydrogels: (a) ox-MWCNTs, (b) GO and (c) ox-CNHs. The yellow arrows point to ox-MWCNTs.

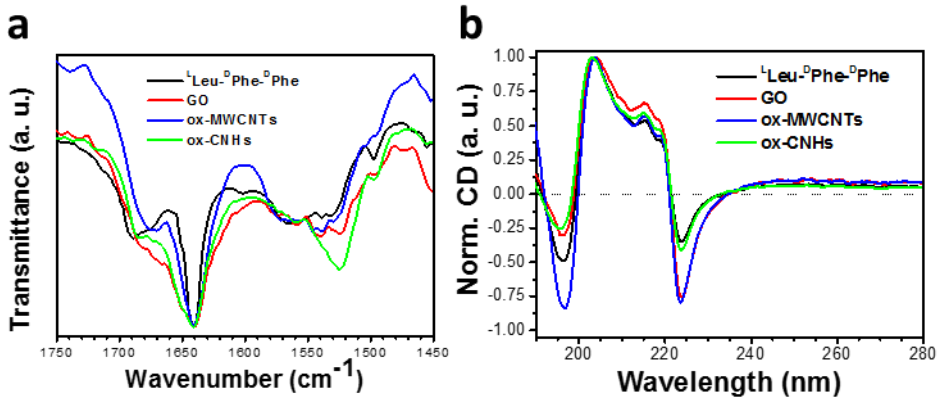

Figure 4.21. ATR-IR (a) and CD (b) data of the native peptide and the composite hydrogels. CD data was normalised due to significant scattering from the hydrogels, thus affecting signal intensity.

Similar results were reported by Banerjee and co-workers when combining RGO with an Fmoc protected dipeptide, although with a lower RGO concentration than what we used (*i.e.* 0.05 mg ml^{-1}, 20 or 2 times less relative to our composites). When oxidised SWCNTs were mixed with an Fmoc protected amino acid, the morphology of the peptide nanostructures changed from helical nanofibres to nanotapes with the SWCNTs aligned along the nanotapes.[34,35] Higher concentrations led to the segregation of the material in different phases.

The observed differences in the rheological performance of the composites have to be ascribed to the CNS morphology in which the C sp^2 lattice is arranged. In the case

of ox-CNHs, their peculiar 3D structure favoured aggregation, as opposed to interaction with peptide fibres. When this occurred, the interaction was localised typically in one fibre (*i.e.* one or a few ox-CNHs interacted with a single fibre). By contrast, the flat surface of GO allowed simultaneous interaction with numerous fibres; thus resulting in increased elastic moduli and resistance to stress. Finally, the interaction of ox-MWCNTs with ^{L}Leu-^{D}Phe-^{D}Phe fibres was favoured by similar anisotropy and diameter of the elongated structures. These interactions could be cooperative, with ox-MWCNTs acting as a bridge connecting several peptide fibres. TEM images supported this hypothesis (Figure 4.22).

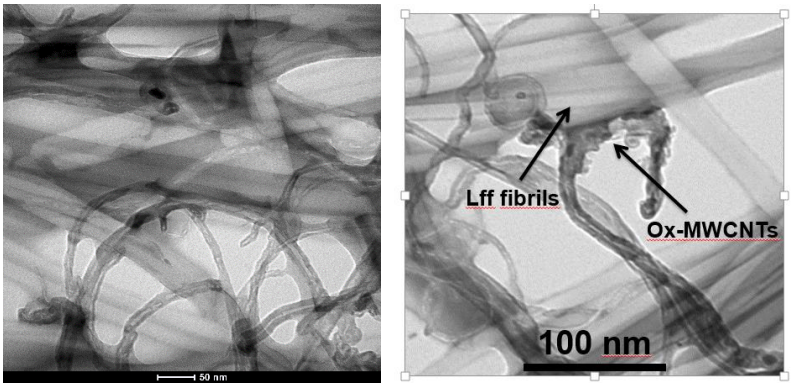

Figure 4.22. High magnification TEM images of the composite hydrogel containing ox-MWCNTs.

4.3.5.1. Self-healing tests

When hydrogels are exposed to external stimuli, they may undergo modifications that disrupt the gel network, and self-healing ability may be an attractive feature for a number of applications. For instance, in tissue engineering, a supramolecular hydrogel structure may be assembled *in vitro* from multiple components, disrupted into a solution to allow injection *in vivo*, and ideally recovered *in situ* as a biomaterial. However, self-healing is more established for macromolecular hydrogels,[41] while for supramolecular gels made from short peptides, it is not yet well understood and thus difficult to predict.

A recovery test was designed to probe the self-healing ability of the peptide and of the composite hydrogels. The experiment was designed based upon the rheometric data discussed above and was carried out as follows:

1. Hydrogels were prepared *in situ* on the rheometer to avoid damage during transfer.
2. Gelation was allowed to occur for 30 min. until reaching a plateau indicating successful self-assembly and stabilisation of the material.
3. Next, the materials were challenged for 30 s at increasing stress values (i.e. 50, 100, 150, 200, or 250 Pa) with 10 min intervals for recovery.

The peptide hydrogel suffered a considerable loss in both moduli when stressed at 50 Pa, although the gel state was maintained (*i.e.* G' > G'') . By contrast, the material underwent an irreversible transition to a viscous solution (*i.e.* G'' > G') at 100 Pa.

GO and ox-CNHs composites revealed similar behaviour. Perturbations at 50 Pa and 100 Pa reduced hydrogel moduli, yet preserving their gel nature. Stress at 150 Pa irreversibly led to solutions.

By contrast, the composite containing ox-MWCNTs resisted notably higher stress values, up to 250 Pa, well in agreement with the rheometric data discussed in previous sections (Figure 4.23). Remarkably, after the gel-to-sol transition, the hydrogel state was quickly recovered (*i.e.* G'> G''). Composites with low loading of CNTs also displayed

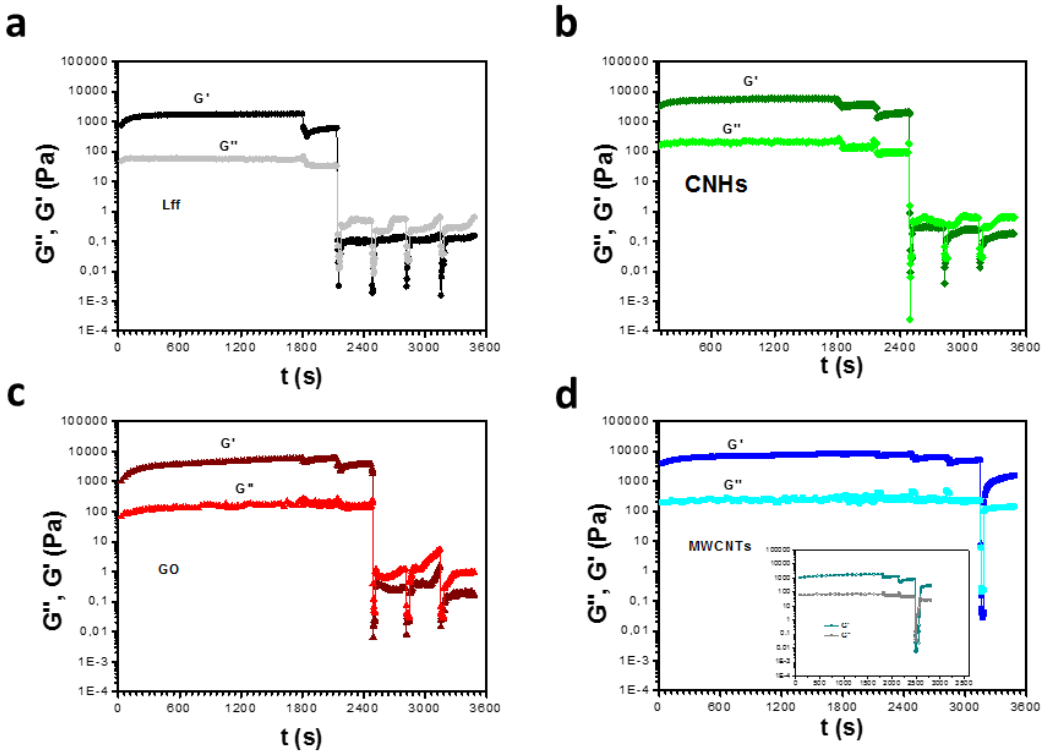

Figure 4.23. Rheological recovery test of native and composites hydrogels: (a) native hydrogel; (b) ox-CNHs; (b) GO; and (d) ox-MWCNTs. Inset in (d) shows the recovery test of low content ox-MWCNTs composite hydrogel.

self-healing ability. We propose that the favourable interaction between peptide fibres and ox-MWCNTs, both elongated structures of similar morphology and size, could be a key factor to re-interconnect the fibres in the self-healing process.

In addition, for a deeper understanding of the effect of CNS morphology on peptide self-assembly, SWCNTs were also tested to complete the study. This form of carbon is notably more difficult to manipulate than MWCNTs, due to increased propensity towards aggregation. Therefore, the degree of functionalisation required to obtain good dispersions in water is significantly higher. Besides, in light of the higher reactivity of SWCNTs, due to their higher curvature, fine control over the level of oxidation is more challenging, relative to MWCNTs.

The Figure 4.24 shows the SWCNTs different oxidation levels obtained by changing reaction time or temperature. Oxidation was confirmed by Raman spectroscopy (*e.g.* reduction of the RBM peaks and broadening of the D-band). Even when using highly oxidised SWCNTs (*i.e.* 18 % by TGA analysis), they were not dispersible in either the basic or the acidic buffer. Contrarily with the other ox-CNS, ox-SWCNTs dispersion did not improve after the addition of the peptide, not even when longer ultrasonication times were applied (*e.g.* 3 hours in contrast with 10-15 min required for the rest ox-CNS). It is

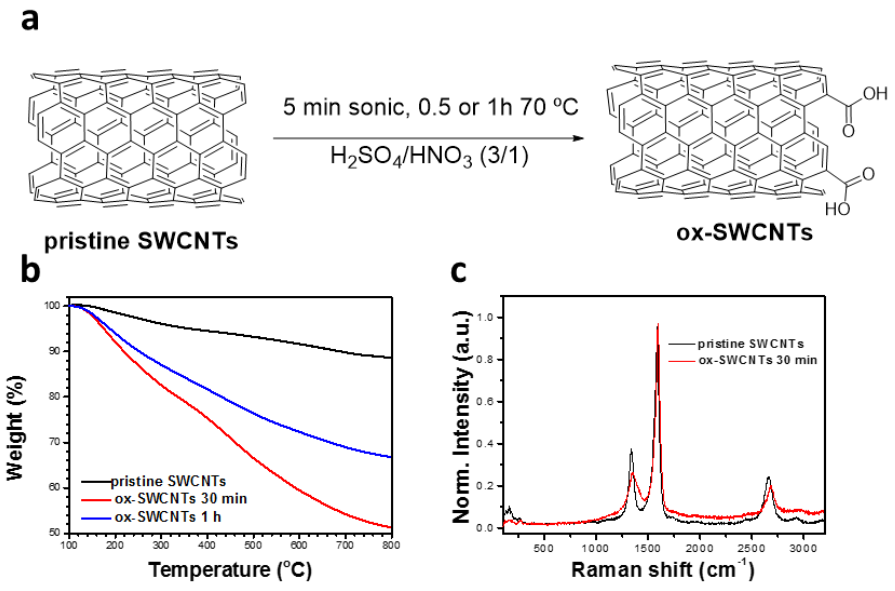

Figure 4.24. (a) Scheme for the oxidation of SWCNTs; (b) TGA under N_2 of SWCNTs with different oxidation times and (c) Raman spectra of pristine and oxidised SWCNTs.

possible that the peptides adsorbed preferentially on MWCNTs, as opposed to the highly curved SWCNTs. The use of other functionalisation protocols (*e.g.*1,3-dipolar cycloaddition with more hydrophilic appendages, or covalent linkage of ^{L}Leu-^{D}Phe-^{D}Phe) could better address the issue of low SWCNT dispersibility in buffer, to allow formation of homogeneous hydrogels, and may constitute the topic of future studies.

4.4. Conclusions

In this project, a heterochiral peptide sequence (^{L}Leu-^{D}Phe-^{D}Phe) was synthesised by standard Fmoc-based SPPS and purified by HPLC. The tripeptide proved to be a new gelling sequence whose properties were analogous to its enantiomer (^{D}Leu-^{L}Phe-^{L}Phe) as determined by rheology, TEM or ART-IR and CD.

CNTs, G and CNHs were subjected to different oxidation treatments to obtain materials with the same level of oxidation as determined by TGA under N_2. The nanomaterials were used to assess the effect of CNS morphology on the self-assembly of the peptide into a hydrogel at neutral pH in phosphate buffer.

Overall, the presence of CNS resulted in an improvement of the rheological performance of the hydrogels whilst maintaining the structural features observed by TEM or ATR-IR for the peptide alone. Outstandingly, only the presence of ox-CNTs at both high (1 mg ml^{-1}) and low content (0.1 mg ml^{-1}) gave the hydrogels self-healing ability. It is worth to note that this behaviour has not yet been reported for this kind of hydrogels. In the future, these materials could be used in drug delivery applications exploiting the properties of CNS such as their NIR responsiveness or their conductivity.

4.5. Perspective

As mentioned in the introduction of this chapter, hydrogels obtained at physiological conditions could be used for cell culture or drug release applications. Most of the knowledge on this field is related to polymeric hydrogels.[42] The so-called 'smart' hydrogels are a special class whereby a specific response (*e.g.* drug release) can be induced upon application of specific stimuli, such as changes of pH, or temperature.

As explained in a recent review by Merino *et al.*, research on *on-demand* nanocomposite hydrogels should move towards the rational preparation of materials with reversible on-off switching capacity.[43] In this regard, light, magnetic fields or electrical currents are among the most used triggers. The inclusion of nanomaterials (*e.g.* CNS or metal NPs) with marked responsiveness to these stimuli can notably improve the hydrogel performance in this area. For instance, the effect of CNS was studied by Giri *et al.* in a composite hydrogel of carboxymethyl guar gum and MWNCTs for the transdermal delivery of diclofenac sodium.[44] Apart from the transdermal capacity, the nanomaterial increased the loading of the drug and the thermal stability of the composite.

In our group, mechanically exfoliated G and MWCNTs have been recently used to dope poly(methacrylic acid) hydrogels.[45] Remarkably, low concentration of G alleviated drastically the heating produced by electrical stimulation (*i.e.* resistive heating). Besides, mild electrical stimulation (*e.g.* DC, 10 V, 5 min) resulted in a reproducible on-off system for the release of ^{14}C-sucrose (Figure 4.25).

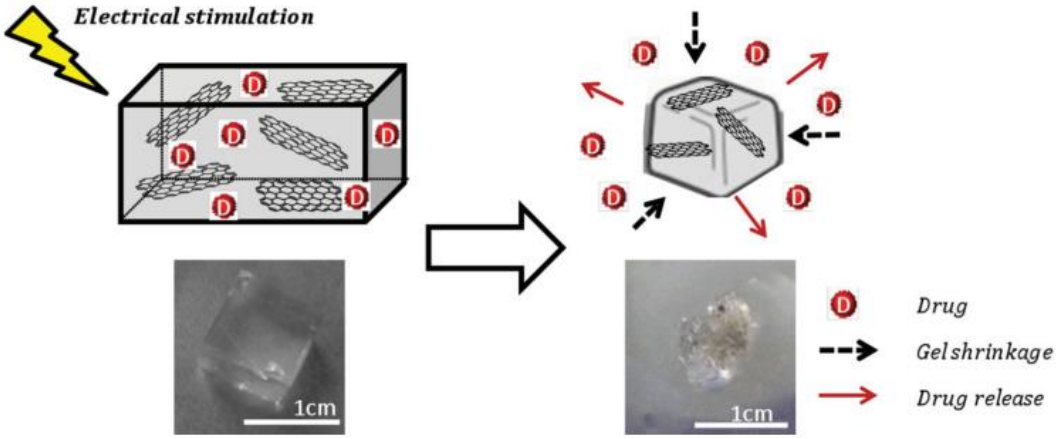

Figure 4.25. Schematic representation of the drug delivery of poly(methacrylic acid) hydrogel loaded with graphene upon electrical stimulation. The pictures show the state of the hydrogel before and after the drug delivery. Reproduced with permissions from (45) Copyright 2014 John Wiley and Sons.

Examples of drug release of supramolecular hydrogels composed of short peptides and CNS are still scarce. The hierarchical approach reported by Wu *et al.* stands as a breaking example on the field.[46] They exploited the NIR responsiveness of GO for the on-demand release of doxorubicin, a water-insoluble drug. The injection of the hydrogel *in vivo* showed therapeutic potential against a specific kind of tumour.

In line with this research trend, it would be interesting to test *on-demand* drug release on our composite systems, for instance, upon application of an electrical stimulus. As mentioned in previous sections, sustained drug release of the hydrophobic antibiotic ciprofloxacin was achieved by using a supramolecular hydrogel formed by the co-assembly of the drug and the ^{D}Leu-^{L}Phe-^{L}Phe tripeptide.[19]

In this preliminary study, rheological experiments and TEM imaging were carried out to study the three-component systems made of peptide, ox-CNS, and ciprofloxacin. Due to the low stability of composites containing ox-CNHs, only ox-MWCNTs and GO were tested. The strategy reported by Marchesan *et al.* was thus used for the preparation of the drug loaded hydrogels.[19] Use of a pH trigger from alkaline to neutral resulted in all cases in the instant formation of the hydrogels as confirmed by frequency sweep measurements (Figure 4.26 a, b and c). In agreement with literature data, drug addition lowered the elastic moduli, although no significant morphological difference was seen by TEM (Figure 4.26 d, e and f).

Now that the ternary hydrogels have been formed, it will be interesting in future studies to examine their ability towards *on-demand* drug release upon application of electrical stimuli that exploit CNS responsiveness.

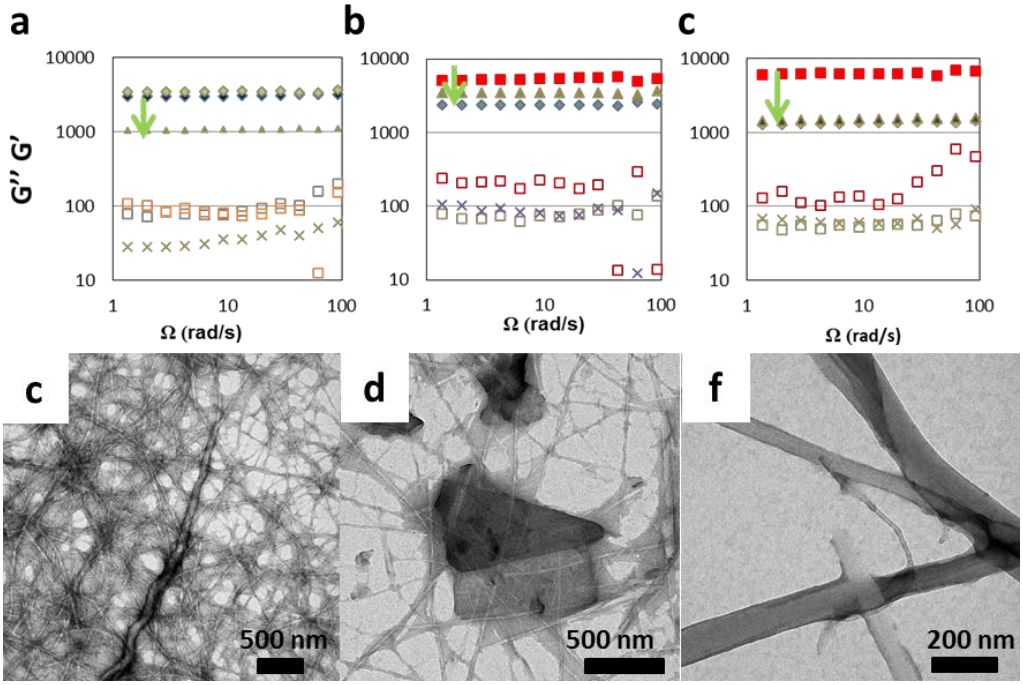

Figure 4.26. Frequency sweep experiments with and without CIP for the native (a), GO (b), and ox-MWCNTs (c) containing hydrogels. TEM images of CIP containing hydrogels: (c) native peptide, (b) GO, and (c) ox-MWCNTs composite hydrogels.

4.6. References

(1) Hoffman, A. S. *Adv. Drug Deliv. Rev.* **2002**, *43*, 3–12.

(2) Iglesias, D.; Bosi, S.; Melchionna, M.; Ros, T. Da; Marchesan, S. *Curr. Top. Med. Chem.* **2016**, *16*, 1976–1989.

(3) Ung, P.; Winkler, D. A. *J. Med. Chem.* **2011**, *54*, 1111–1125.

(4) Marchesan, S.; Vargiu, A. V.; Styan, K. E. *Molecules* **2015**, *20*, 19775–19788.

(5) Adams, D. J. *Macromol. Biosci.* **2011**, *11*, 160–173.

(6) Basu, K.; Baral, A.; Basak, S.; Dehsorkhi, A.; Nanda, J.; Bhunia, D.; Ghosh, S.; Castelletto, V.; Hamley, I. W.; Banerjee, A. *Chem. Commun.* **2016**, *52*, 5045–5048.

(7) Reches, M.; Gazit, E. *Science* **2003**, *625*, 625–627.

(8) Ding, Y.; Li, Y.; Qin, M.; Cao, Y.; Wang, W. *Langmuir* **2013**, *29*, 13299–13306.

(9) Khalily, M. A.; Goktas, M.; Guler, M. O. *Org. Biomol. Chem.* **2015**, *13*, 1983–1987.

(10) Seow, W. Y.; Hauser, C. A. E. *Adv. Healthc. Mater.* **2013**, *2*, 1219–1223.

(11) Frederix, P. W. J. M.; Scott, G. G.; Abul-haija, Y. M.; Kalafatovic, D.; Pappas, C. G.; Javid, N.; Hunt, N. T.; Ulijn, R. V; Tuttle, T. *Nat. Chem.* **2014**, *7*, 30–37.

(12) Melchionna, M.; Styan, K. E.; Marchesan, S. *Curr. Top. Med. Chem.* **2016**, *2016*, 1–10.

(13) Marchesan, S.; Easton, C. D.; Kushkaki, F.; Waddington, L.; Hartley, P. G. *Chem. Commun.* **2012**, *48*, 2157–2256.

(14) Marchesan, S.; Waddington, L.; Easton, C. D.; Winkler, D. A.; Goodall, L.; Forsythe, J.; Hartley, P. G. *Nanoscale* **2012**, *4*, 6752–6760.

(15) Marchesan, S.; Easton, C. D.; Styan, K. E.; Waddington, L. J.; Kushkaki, F.; Goodall, L.; McLean, K. M.; Forsythe, J. S.; Hartley, P. G. *Nanoscale* **2014**, *6*, 5172–5180.

(16) Marchesan, S.; Styan, K. E.; Easton, C. D.; Waddington, L.; Vargiu, A. V. *J. Mater. Chem. B* **2015**, *3*, 8123–8132.

(17) Vargiu, A. V.; Iglesias, D.; Styan, K. E.; Waddington, L. J.; Easton, C. D.; Marchesan, S. *Chem. Commun.* **2016**, *52*, 5912–5915.

(18) Marchesan, S.; Waddington, L.; Easton, C. D.; Kushkaki, F.; McLean, K. M.; Forsythe, J. S.; Hartley, P. G. *Bionanoscience* **2013**, *3*, 21–29.

(19) Marchesan, S.; Qu, Y.; Waddington, L. J.; Easton, C. D.; Glattauer, V.; Lithgow, T. J.; McLean, K. M.; Forsythe, J. S.; Hartley, P. G. *Biomaterials* **2013**, *34*, 3678–3687.

(20) Oliveira, S. F.; Bisker, G.; Bakh, N. A.; Gibbs, S. L.; Landry, M. P.; Strano, M. S. *Carbon* **2015**, *95*, 767–779.

(21) Calvaresi, M.; Zerbetto, F. *Acc. Chem. Res.* **2013**, *46*, 2454–2463.

(22) Prato, M.; Marchesan, S. *Chem. Commun.* **2015**, *51*, 4347–4359.

(23) Li, D.; Zhang, W.; Yu, X.; Wang, Z.; Su, Z.; Wei, G. *Nanoscale* **2016**, *8*, 19491–19509.

(24) Dieckmann, G. R.; Dalton, A.; Johnson, P. a; Razel, J.; Chen, J.; Giordano, G. M.; Munoz, E.; Musselman, I. H.; Baughman, R. H.; Draper, R. K. *J. Am. Chem. Soc.* **2003**, *84*, 1770–1777.

(25) Zawari, M.; Haghighizadeh, M.; Derakhshandeh, M.; Barmaki, Z.; Farhami, N.; Monajjemi, M. *J. Comput. Theor. Nanosci.* **2015**, *12*, 5472–5478.

(26) Sheikholeslam, M.; Pritzker, M.; Chen, P. *Langmuir* **2012**, *28*, 12550–12556.

(27) Katoch, J.; Kim, S. N.; Kuang, Z.; Farmer, B. L.; Naik, R. R.; Tatulian, S. A.; Ishigami, M. *Nano Lett.* **2012**, *12*, 2342–2346.

(28) Li, C.; Mezzenga, R. *Langmuir* **2012**, *28*, 10142–10146.

(29) Wang, J.; Zhao, X.; Li, J.; Kuang, X.; Fan, Y.; Wei, G.; Su, Z. *ACS Macro Lett.* **2014**, *3*, 529–533.

(30) Liu, Z.; Davis, C.; Cai, W.; He, L.; Chen, X.; Dai, H. *Proc. Natl. Acad. Sci. U. S. A.* **2008**, *105*, 1410–1415.

(31) Kanchanapally, R.; Viraka Nellore, B. P.; Sinha, S. S.; Pedraza, F.; Jones, S. J.; Pramanik, A.; Chavva, S. R.; Tchounwou, C.; Shi, Y.; Vangara, A.; Sardar, D.; Ray, P. C. *RSC Adv.* **2015**, *5*, 18881–18887.

(32) Pangule, R. C.; Brooks, S. J.; Dinu, C. Z.; Bale, S. S.; Salmon, S. L.; Zhu, G.; Metzger, D. W.; Kane, R. S.; Dordick, J. S. *ACS Nano* **2010**, *4*, 3993–4000.

(33) Voge, C. M.; Johns, J.; Raghavan, M.; Morris, M. D.; Stegemann, J. P. *J. Biomed. Mater. Res. - Part A* **2012**, *101*, 231–238.

(34) Adhikari, B.; Banerjee, A. *Soft Matter* **2011**, *7*, 9259.

(35) Roy, S.; Banerjee, A. *RSC Adv.* **2012**, *2*, 2105.

(36) Yang, Q.; Wang, Z.; Weng, J. *Soft Matter* **2012**, *8*, 9855–9863.

(37) Ali-boucetta, H.; Nunes, A.; Sainz, R.; Herrero, M. A.; Tian, B.; Prato, M.; Bianco, A.; Kostarelos, K. *Angew. Chemie - Int. Ed.* **2013**, *52*, 2274–2278.

(38) Marchesan, S.; Kostarelos, K.; Bianco, A.; Prato, M. *Mater. Today* **2015**, *18*, 12–19.

(39) Lekprasert, B.; Korolkov, V.; Falamas, A.; Chis, V.; Roberts, C. J.; Tendler, S. J. B.; Notingher, I. *Biomacromolecules* **2012**, *13*, 2181–2187.

(40) Li, H.; Song, S. I.; Song, G. Y.; Kim, I. *J. Nanosci. Nanotechnol.* **2014**, *14*, 1425–

1440.

(41) Taylor, D. L.; Panhuis, M. *Adv. Mater.* **2016**, *28*, 9060–9093.

(42) Qiu, Y.; Park, K. *Adv. Drug Deliv. Rev.* **2001**, *53*, 321–339.

(43) Kostarelos, K.; Prato, M.; Vázquez, E.; Merino, S.; Martín, C. *ACS Nano* **2015**, *9*, 4686–4697.

(44) Giri, A.; Bhowmick, M.; Pal, S.; Bandyopadhyay, A. *Int. J. Biol. Macromol.* **2011**, *49*, 885–893.

(45) Servant, A.; Leon, V.; Jasim, D.; Methven, L.; Limousin, P.; Fernandez-Pacheco, E. V.; Prato, M.; Kostarelos, K. *Adv. Healthc. Mater.* **2014**, *3*, 1334–1343.

(46) Wu, J.; Chen, A.; Qin, M.; Huang, R.; Zhang, G.; Xue, B.; Wei, J.; Li, Y.; Cao, Y.; Wang, W. *Nanoscale* **2015**, *7*, 1655–1660.

CHAPTER 5

Experimental Section

5.1. Materials and Methods

5.1.1. Materials

High purity MWCNTs and G were kindly supplied by Thomas Swan and Co. Ltd. CNHs were purchased at Carbonium s.r.l. Super-purified Unydim SWCNTs were purchased from NanoIntegris. CNF were provided by Dr. Juan José Vilatela at IMDEA Materials, Getafe, Spain.[1] Chemicals were purchased from Sigma-Aldrich, Acros or Fluka and they were used without further purification.

5.1.2 Methods

5.1.2.1.NMR

NMR spectra was recorded on a Varian Inova 500 MHz. Chemical shifts are reported in ppm using the solvent residual signal as internal reference ($CDCl_3$ δ H = 7.26 ppm or δ C = 77.23; DMSO-d_6: δ H = 2.50 ppm or δ C = 39.51 ppm; and CD_3OD: δ H = 4.78 ppm or δ C = 49.15 ppm). The resonance multiplicity is described as s (singlet), d (doublet), t (triplet), dd (doublet of doublets), ddd (doublet of doublets).

5.1.2.2.TGA

TGA of approximately 1 mg of each compound were recorded on a TGA Q500 (TA Instruments) under air or nitrogen, by equilibrating at 100 °C for 20 min., and following a ramp of 10 °C min^{-1} up to 800 °C.

5.1.2.3.Raman spectroscopy

Raman spectra were recorded with an Invia Renishaw microspectrometer (50) equipped with He−Ne laser at 532 nm. For G samples, the powders were dispersed in EtOH, drop-cast onto a silicon wafer and the solvent evaporated; at least 20 spectra per sample were recorded on different areas of the sample in order to assess the uniformity of the materials. MWCNTs and CNHs samples were dispersed in EtOH and filtrated through a Millipore membrane (JHWP, 0.45 μm). Et_2O was added to dry the material. Then, a uniform layer of material was transferred to a double sided scotch tape. At least 10 spectra per sample were recorded on different areas of the sample in order to check

the uniformity of the materials. No sample preparation was required for the Raman analysis of CNF or the PDA-coated quartz slides. For the hydrogels, a small portion of the hydrogels was deposited on a quartz slide and the sample was dried under vacuum.

5.1.2.4.TEM imaging

Typically, a concentrated dispersion of the sample was drop-cast on a copper grid (200 mesh, copper, carbon only), after evaporation of the solvent under vacuum, the samples were analysed with a Philips EM 208 microscope operating at 100 kV. Additional TEM images of TiO_2 fibres and CNT fibres were acquired with a Talos F200X, FEI, operating at 80 KV. HAADF-STEM were acquired by Dr. Lucia Nasi on a JEOL 2200FS microscope operating at 200 kV, equipped with an Energy Dispersive Spectrometer (EDX), in-column energy (Omega) filter. For the TEM images of the hydrogels, a small portion of the gel (*i.e.* 20 µl) was deposited on top of a copper grid (200 mesh, copper, carbon only). After 30 s of contact, the water was drawn from the sample. Then, the grid was deposited on top of a drop of 2% aqueous potassium phosphotungstate at pH 7.2 for 30 s and the grid was dried under vacuum before its visualisation. Samples were analysed on a TEM FEI Tecnai G2 operating at 100 kV at the University of Padova.

5.1.2.5.Microwave-assisted reactions

Microwave-assisted reactions were carried out in CEM Discover reactor, with infrared pyrometer, pressure controlled system, stirring and air cooler option. Functionalisation of G was done in round bottom flasks 100 ml volume with a condenser connected. Alkylation reaction was done on sealed microwave quartz vessels 35 ml volume.

5.1.2.6.UV-ozone treatments

Ozone treatment of CNF was carried out in a Cleaner ProCleaner^{TM} Plus. The instrument has a lamp of high energy ($\lambda = 185$ nm) that produces ozone from atmospheric oxygen.

5.1.2.7.XPS spectroscopy

The XPS data for the CNF were collected by Dr.Belén Alemán in a home-built analysis chamber equipped with a Focus 500 monochromatic Al-Kα (hν = 1468.71 eV) X-Ray source and a Phoibos 100 hemispherical energy analyser, both from SPECS GmbH. The detector is a 1 dimensional delay line detector from Surface Concept. The deconvolutions shown were fitted by Gaussian/Lorentzian peak shapes and Shirley background profile subtraction. Atomic quantification from XPS spectra was carried out taking into account the peak area after background removal and the average matrix relative sensitivity factors (AMRSF).[2,3] XPS data of pristine CNHs, ox-CNHs, ox-CNHs@PDA$_{700}$, CNHs@PDA$_{800}$ and CNHs@PDA$_{900}$ were acquired by Dr. Alejandro Criado in a SPECS Sage HR 100 spectrometer with a non-monochromatic X ray source of Magnesium with a Kα line of 1253.6 eV energy and 250 W. The samples were placed perpendicular to the analyser axis and calibrated using the 3d5/2 line of Ag with a full width at half maximum (FWHM) of 1.1 eV. An electron flood gun was used to compensate for charging during XPS data acquisition. The selected resolution was 30 and 15 eV of Pass Energy and 0.5 and 0.15 eV/step for the survey and high resolution spectra, respectively. Measurements were made in an ultra-high vacuum (UHV) chamber. Fitting of the XPS data were done using CasaXPS 2.3.16 PR 1.6 software. For this data, the Shirley-type background subtraction was used and all curves were defined as 40% Lorentzian, 60% Gaussian.

5.1.2.8.Mechanical measurements

Mechanical measurements of CNF were performed with a Textechno Favimat using a gauge length of 20 mm. Several samples for each condition were tested. Fibre lineal density was determined by the vibroscopic method.

5.1.2.9.XRD

XRD on TiO_2 electrospun fibres was performed in a XíPert MD Analytical by Alicia Moya. From XRD patterns, average crystal size was calculated using Scher-rer's equation and the anatase/rutile ratio according to Spurr's equation.[4,5] Adsorption–desorption isotherms were carried out on Micrometrics ASAP 2010 at 77 K with N_2 as adsorbate.

5.1.2.10. BET-BJH

The specific surface area (according to BET) and porosity (according to BJH) of TiO_2 fibres were determined assuming 0.162 nm^2 as the nitrogen molecule area. The analysis were performed by Alicia Moya. The textural characterisation ox-CNHs and ox-CNHs@PDA_{700} was done by Dr. Michele Melchionna. To do so, the atomic ratios were computed from experimental intensity ratios and normalised by atomic sensitivity factors N_2 physisorption at the liquid nitrogen temperature was collected using a Micromeritics ASAP 2020 analyser. Prior to the analysis, the samples were degassed at 120 °C for at least 12 h at a pressure lower than 10 mmHg. The specific surface area of the samples was calculated applying the BET method. Pore size distributions were calculated applying the BJH method to the adsorption branch of the isotherms.

5.1.2.11. UV-Vis spectroscopy

UV-Vis spectra were recorded with a Varian Cary 5000 spectrophotometer using 1 cm pathlength quartz cuvettes. The UV-Vis characterisation of the TiO_2 fibres was performed by UV–Vis Diffuse Reflectance Spectroscopy by Alicia Moya. Rotating ring disk electrode (RRDE) measurements were performed was used to perform the experiments. The working electrode was a Pine™ ring-disk electrode (E7R9 Series) with platinum ring electrode and glassy carbon disk electrode covered with the catalysts layer.

5.1.2.12. Circular dichroism (CD)

CD spectra were acquired on a Jasco J-815 spectropolarimeter equipped with a Peltier temperature control system. Experiments were performed at 25 ^oC, from 190-300 nm, using a 0.1mm pathlength quartz cuvette.

5.1.2.13. ATR-IR spectroscopy

FT-IR measurements were performed in a Cary 660 spectrometer operating at the ATR mode. 128 scans were acquired for every sample with a resolution of 4 cm^{-1}. For the preparation of the samples, a portion of the gel (*i.e.* 0.5 ml) was deposited on top of silicon wafer and was dried under vacuum.

5.1.2.14. Rheometry

Rheological analyses were performed on a stress-controlled rotational rheometer Haake MARS III equipped with a Peltier temperature control system. 60 mm titanium flat plates were used for all measurements with a gap of 0.345 mm. Time sweeps were performed at 1 Pa and 1 Hz for 1 h. Frequency sweeps were recorded at 2 Pa from 0.1 Hz to 100 Hz. Stress sweeps were performed from 1 Pa up to gel failure at 1 Hz. Further explanation for the recovery tests can be found in the main text. All measurements were recorded at 25 ºC.

5.1.2.15. ICP-OES (Optical Emission Spectrometry)

ICP-OES analysis was recorded by Prof. G. Adami and Dr. M. Crosera on an Optima 8000 Perkin-Elmer instrument.

5.1.2.16. Electrical and electrochemical characterisation of CNF

The electrical characterisation of the CNF was performed using a microprobe station combined with a 2450 Keithley source-measurement unit. Indium was used to create contact with CNF.

CV was carried out by Evgeny Senokos at IMDEA Materials (Getafe, Spain), using a Biologic VMP multichannel potentiostatic–galvanostatic system and 3 electrode cell configuration with platinum mesh as the counter electrode and calomel reference electrode. 1M KOH solution was used as the electrolyte. Scan rates applied ranged from 5 to 100 mV s^{-1} and the voltage window used was 1.2 V. The specific capacitance was obtained by integrating the area under CV curves and normalising by the mass of active material.

5.1.2.17. Electrochemical characterisation of CNHs coated with PDA

The electrochemical characterisation and the catalytic tests of PDA-coated materials was performed by Angela Giuliani. CV and chrono-amperometry experiments were performed on a Autolab 302 N electrochemical workstation (Metrohm, The Netherlands) at room temperature, using a conventional three-electrode system composed of a modified glassy carbon electrode (GCE; CH Instrument, CH 104) as a working

electrode, a platinum wire as an auxiliary electrode and a Ag/AgCl (3 M NaCl) (CH Instrument, CH 111) as a reference electrode. The working electrode was assembled by drop-casting a dispersion of 2 mg ml^{-1} of the specific sample in milliQ water onto a glassy carbon supporting electrode (GCE). Tris buffer (0.1 M, pH 7.4) was employed as the supporting electrolyte solution for the initial screening of the materials by CV. The buffer solution was purged with high purity nitrogen for 15 min prior to experiments and left under the same gas atmosphere during the measurements. Rotating ring disk electrode (RRDE) measurements were performed instead using a model 636A rotating ring-disk electrode. A PGSTAT 100N bi-potentiostat was used to perform the experiments. The working electrode was a Pine™ ring-disk electrode (E7R9 Series) with platinum ring electrode and glassy carbon disk electrode covered with the catalysts layer. Measurements were performed using a ring-disk electrode from Pine Instrument Co. consisting of a glassy carbon (GC) disk insert (⌀ 5 mm; A = 0.196 cm^2) and a Pt ring (A = 0.11 cm^2). The RRDE measurements were carried out using a modulated speed rotator (MSR) from Pine Instrument Co. All the measurements were carried out using an Autolab potentiostat/galvanostat in a single compartment glass cell using a three-electrode arrangement. In the RRDE the working electrode was prepared as follows: a proper amount of g-N-CNTs (10 mg) was dispersed in 0.220 g of water, 0.112 g of ethanol, and 0.084 g of a Nafion solution (5 wt % in lower aliphatic alcohols and water). The resulting ink was sonicated for 30−45 min and drop-casted onto the glassy carbon electrode (3 mg). The as-prepared electrode was then dried at room temperature. A platinum wire was used as counter electrode, and a double junction Ag/AgCl/KCl sat. electrode served as reference electrode. All RRDE experiments were carried out at a scan rate of 20 mV/s in the potential range from −0.85 to +0.1 V vs Ag/ AgCl/KCl sat. for alkaline medium or from -0.35 to +0.750 V vs Ag/ AgCl/KCl sat. for acidic medium. Linear sweep voltammograms are recorded for each electrolyte solution at different spin rates (quiet; 400; 800; 1200; 1600; 2000), while the electrode with a Pt ring held at a potential of +0.50 V or +1.2 V in alkaline or acidic medium respectively. Nitrogen or oxygen was used to purge the solution to achieve an oxygen-free or an oxygen-saturated electrolyte solution. Relevant data are reported in Table S3. The Tafel plots were obtained by linear sweep voltammetry experiments collected by scanning the disk potential of RDE from 0 to 1.0 V vs. RHE at a 5 mVs^{-1} in the three different oxygen-saturated electrolyte solutions (pH=1, 7.4 and 13) under a rotation speed of 1200 r.p.m. The ORR polarisation curve

was extracted by subtracting the capacitive current. The kinetic current, $\mathbf{I_k}$, was calculated from the mass transport correction of RDE total current by equation:

$$\mathbf{I_k} = \boldsymbol{I_T} \times \boldsymbol{I_L} / (\boldsymbol{I_L} - \boldsymbol{I_T})$$

where $\boldsymbol{I_T}$ is the experimental total current and $\mathbf{I_L}$ the limiting current.

For the screening of catalytic activity, CVs under O_2 flow were performed using the same setting but using three different electrolyte: H_2SO_4 (0.1 M) to obtain pH 1, PBS for the measurement at pH 7.4, and NaOH (0.1 M) to obtain pH 13. Amperometric experiments were conducted in a stirred electrolyte solution by applying the desired working potential.

The amount of H_2O_2 after the electrolysis experiments has been detected by permanganometric titration, the value reported is the average of nine independent samplings; the reproducibility of the material performance has been tested using three different batches of material. The amount of produced H_2O_2 was further validated by an electro-sensing method developed recently within our group,[6] and the two methods are in excellent agreement.

5.1.2.18. Electrochemical Impedance Spectroscopy (EIS)

Electrochemical Impedance Spectroscopy (EIS) measurements were conducted by Dr. Manuela Bevilacqua by using a Metrohm Autolab Instrument equipped with the FRA32M impedance analyser module at the potential under which FE reaches the maximum value for each experimental condition.

5.1.2.19. Quantification of amino acid loading on resin in SPPS

In duplicate, 5 to 10 mg of chlorotrityl resin loaded with the first amino acid were transferred to an Eppendorf tube. Then, piperidine 25 % in DMF (1 ml) was added and the mixture was stirred at room temperature for 20 min. The resin was centrifuged down (12000 rpm, 5 min) and 100 µl of the supernatant were transferred to a glass vial containing DMF (10 ml). The absorbance the final solution was measured at 301 nm and the loading was calculated using the formula in the Figure 5.1.

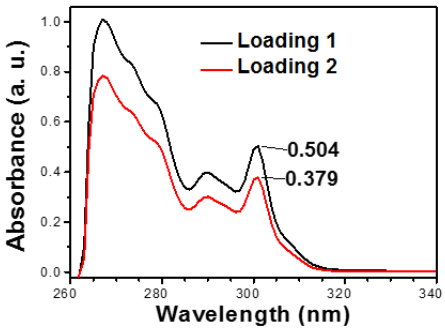

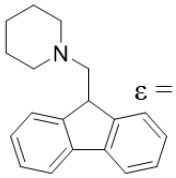

$\varepsilon = 7800\ \mathrm{l\ mol^{-1}\ cm^{-1}}$

$$\frac{mmol(Fmoc)}{g(resin)} = \frac{A * 101}{(7.8 * m\ (mg))} \quad (1)$$

Figure 5.1. Example of the colorimetric assay to calculate the loading of the resin.

5.1.2.20. Bromophenol blue test

This test was used to verify presence/absence of amines after a deprotection/coupling step in SPPS. A few resin beads were placed in a test tube and some drops (5-10) of bromophenol blue 0.05 % in dimethylacetamide were added to the beads. The beads were immediately inspected. The test was positive (i.e. presence of amines) if the solution turned from yellow to blue.

5.1.2.21. Kaiser test

Kaiser tests were performed using the Sigma-Aldrich kit. Briefly, 1 mg of the corresponding carbon nanomaterial was ultrasonicated for 5 min with 75 µl of solution 1 (*i.e.* phenol 80% in ethanol) and 100 µl of solution 2 (*i.e.* KCN in H_2O/pyridine). Then, 75 µl of solution 3 (*i.e.* ninhydrin 6 % in ethanol) and the mixture was incubated for 10 min at 120 ºC. Next, once the mixture cooled down, they were made up to 3 ml with a solution of EtOH/H_2O (60%). Samples were centrifuged (*i.e.* 3000 rpm 10 min) and absorbance of the supernatant at 570 nm was recorded. Equation 1 was used to calculate the amount of amines per gram of material. A_{570nm} is the absorbance at 570 nm, 3 is the final volume in ml, 15000 is the absorptivity of the colourful compound at 570 nm and mass is the exact mass of the analysed materials in mg.

$$NH_2\ \mu mol\ /_g = \frac{3 \times 10^6 \times A_{570nm}}{15000 \times mass} \quad (1)$$

5.1.2.22. Hydrogel preparation

For the peptide hydrogel, 5mg of ^{L}Leu-^{D}Phe-^{D}Phe were ultrasonicated in 1 ml alkaline sodium phosphate buffer (0.1 M, pH 11.8) until complete dissolution (*i.e.* 5 min) in a Branson sonicator bath 40 kHz at room temperature. Then the hydrogel was formed when the pH of the solution was brought to neutral upon the addition of 1 ml of mildly acidic sodium phosphate buffer (0.1 M, pH 5.8).

For the peptide hydrogel containing ox-CNS, 5mg of ^{L}Leu-^{D}Phe-^{D}Phe and 2 mg of ox-CNS were ultrasonicated in 1 ml alkaline sodium phosphate buffer (0.1 M, pH 11.8) until homogeneity (*i.e.* 15 min). Then the hydrogel was formed when the pH of the solution was brought to neutral upon addition of 1 ml of mildly acidic sodium phosphate buffer (0.1 M, pH 5.8).

For the low ox-CNS content, a stock solution of the peptide (5 mg ml^{-1}) and the corresponding ox-CNS (0.2 mg ml^{-1}) were prepared in the same buffer as outlined above. Then, gels were prepared using 1 ml from the stock solution and 1 ml of the acidic sodium phosphate buffer.

For the rheological experiments, the gels were prepared *in situ* in the plate of the rheometer to avoid the damaging of the gel. Briefly, 600 µl of the peptide dissolved at alkaline pH (with or without ox-CNS) were pipetted straight in the inferior plate. Then, 600 µl of the acidic buffer were added on top of the solution generating a homogeneous hydrogel.

5.1.2.23. Interaction of Au nanoparticles and G

1 mg of G (non-functionalised or functionalised with the ammonium groups) was ultrasonicated in MeOH (1 ml) for 5 min in a Branson sonicator bath 40 kHz at room temperature. Then, reactant free gold nanoparticles (Sigma-Aldrich, 5 nm, 0.1 M PBS) were added to the previous dispersion and the mixture was stirred overnight at room temperature. After that, the dispersion was drop-cast on the TEM grids and samples were dried under vacuum before their visualisation.

5.1.2.24. Quartz slides coated with PDA

A quartz slide (1 cm x 2 cm, approximately) was immersed in a 8 mg ml^{-1} of dopamine (8 ml) 30 min. After that, Tris buffer pH 8.5 (2 ml, 50 mM) was added and the polymerisation proceeded for 16 h at room temperature. Next, the coated quartz slide was taken from the solution and thoroughly rinsed with H_2O and ethanol and the material was dried under vacuum. Eventually, the coated slides were annealed at 500 ºC, 600 ºC and 700 ºC for 3 h under Ar in a tubular furnace. Figure 5.2 describes the ramp of temperatures used to calcine all the materials in this chapter.

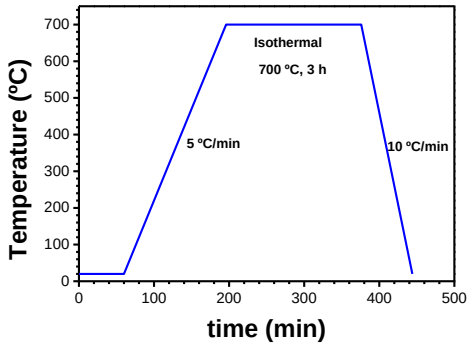

Figure 5.2. Example of the ramp of temperatures used for the calcination of the different PDA materials. The isotherm varies from 500 ºC to 900 ºC depending of the material.

5.2. Synthetic procedures

5.2.1. Small molecules

4-(2-aminoethyl)-N-(*tert*-butoxycarbonyl)phenylamine (**2**)

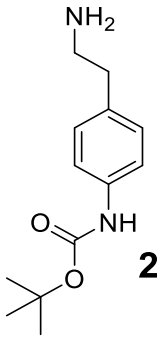

A reported protocol was followed for the synthesis of **2**.[7] In a round-bottom flask, 4-(2-aminoethyl)-N-(*tert*-butoxycarbonyl)phenylamine (1 g, 734 mmol) was dissolved in acetic acid (aq) 10 % (60 ml). To this solution Boc_2O (1.64 g, 7.5 mmol) in 1,4-dioxane

(60 ml) were slowly added. After stirring for 16 h at r.t., the crude was diluted with deionised water (150 ml) and then washed with Et_2O (3 x 75 ml). The aqueous phase was basified with NaOH 2M to pH 14 and extracted with Et_2O (3 x 100 ml). The combined organic phases were washed with deionised H_2O (2 x 50 ml), dried with Na_2SO_4 and filtered. The solvent was eliminated under reduced pressure affording product **2** (1.14 g 66 %). **^{1}H NMR** (500 MHz, CD_3OD) δ 7.26 (d, *J* = 8.3 Hz, 2 H, Ar-H), 7.05 (d, *J* = 8.3 Hz, 2 H, Ar-H), 2.78 (t, *J* = 7.2 Hz, 2H, Ar-CH_2), 2.63 (t, *J* = 7.2 Hz, 2 H, -CH_2-N), 1.45 (s, 9 H, 3 x –CH_3). **^{13}C NMR** (125 MHz, CD_3OD): δ 155.6, 138.9, 135.3, 130.2, 120.3, 80.9, 44.3, 39.5, 28.9 **MS (ESI)**: m/z 234.8 $[M]^+$,179.6 [M-56.5]; 163.1 [M-90]. $C_{13}H_{20}N_2O_2$ requires 236.1

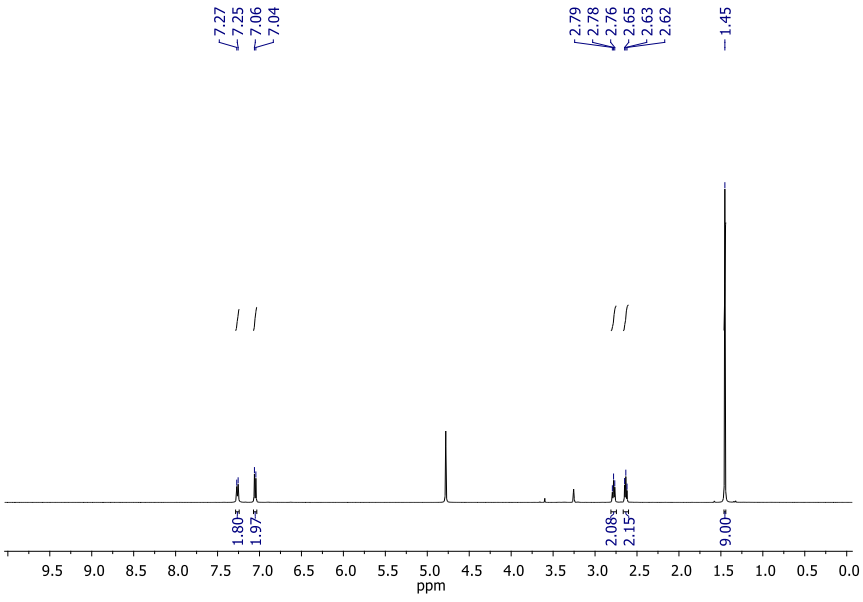

Figure 5.3. ^{1}H-NMR spectrum of 1 in CD_3OD.

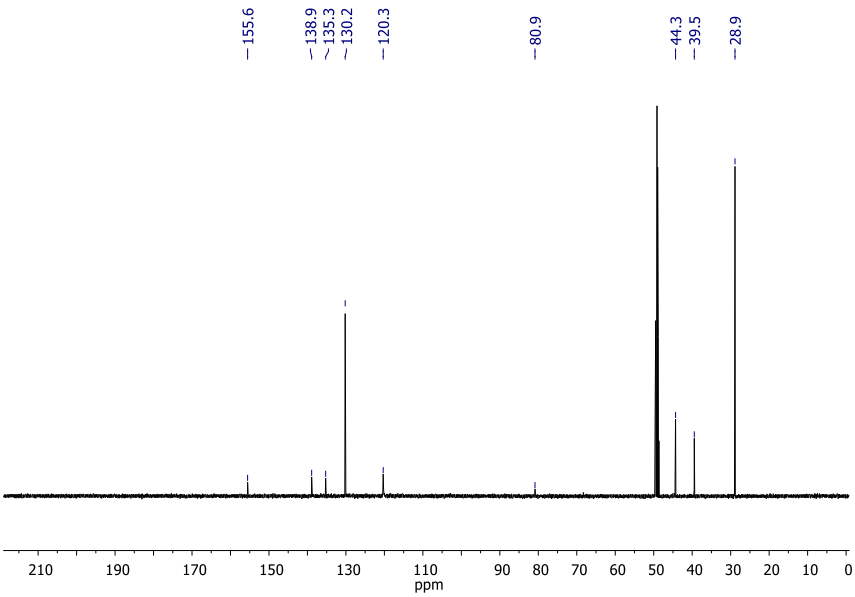

Figure 5.4. ^{13}C-NMR of product 2 in CD_3OD.

1-(triisopropilammonioethyl)-4-(*N*-tertbutoxicarbonyl)phenylamine iodide (**3**)

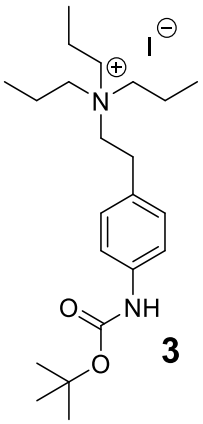

2 (0.75 g, 3.2 mmol), propyl iodide (6 ml, 60.00 mmol), potassium carbonate (2.25 g, 16.28 mmol) and deionised H_2O (11 ml) were poured in a microwave glass vessel creating a biphasic system. The closed vessel was irradiated for 2 h at 80 ºC setting the maximum irradiation power at 100 W. After the irradiation, the crude appeared to be a triphasic system being the desired product in between the aqueous and the organic phase. The water phase was eliminated from the top with a pipette. Then, hexane (20 ml) were added and the crude was filtered. Hexane (3 x 20 ml) were used to clean the product and the crude was dried under vacuum obtaining **3** as a yellow solid (64 %). **^{1}H NMR** (500 MHz, CD_3OD) δ (ppm): 7.33 (d, *J* = 7.2 Hz, 2 H, Ar,), 7.16 (d, *J* = 7.2 Hz, 2 H, Ar,), 3.38 (m, 2 H, CH_2-N), 3.23 (m, 6 H, 3 x CH_2-N), 2.92 (m, 2 H, *o*-CH_2), 1.97 (m. 6 H, 3 x CH_2),

1.45 (s, 9H, 3 x CH_3), 0.96 (t, *J* = 1.0 Hz, 9 H, 3 x CH_3). **MS** (ESI): m/z 363.3 [M^+] $C_{22}H_{39}N_2O_2^+$ requires 363.60. Negative MS 126.7 [I^-] I^- requires 129.9.

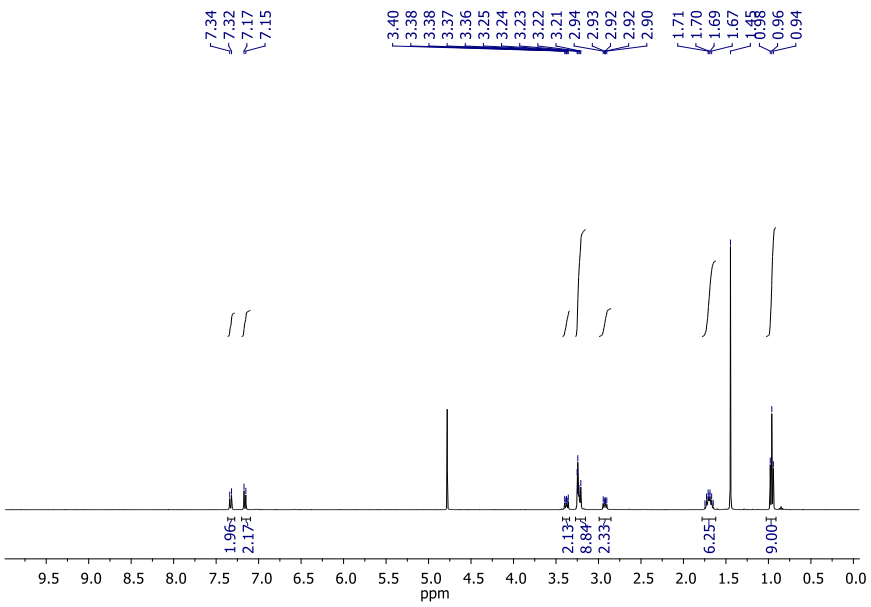

Figure 5.5. ^{1}H-NMR spectra of 3 in CD_3OD.

4-aminophenethyltripropyl ammonium hydroxide (**4**)

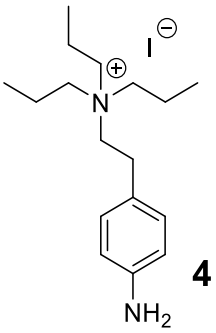

4

3 (520 mg, 1.0 mmol) was refluxed in deionised water (50 ml) for 2 h. The crude of reaction was freeze-dried obtaining **4** as a yellowish solid (85 %). **^{1}H NMR** (500 MHz, CD_3OD): δ 7.10 (d, *J* = 10 Hz, 2 H, Ar-H), 6.76 (d, *J* = 10 Hz, 2H, Ar-H), 3.44 (t, *J* = 10 Hz, Ar-CH_2), 3.33 (m, 6H, -CH2-N), 2.95 (t, *J* = 9 Hz, 2H, -CH_2-N), 1.80 (m, 6H, -CH_2-), 1.06 (t, *J* = 8 Hz, 3H, CH_3-). **^{13}C NMR** (125 MHz, CD_3OD) δ 148.3, 130.8, 126.1, 117.1, 61.5, 61.2, 28.8, 16.7, 11.1. **MS (ESI+)** *m/z* calcd for $C_{16}H_{14}N_2O_2^+$ 263.2, found *m/z* 263.6 [M]$^+$, MS (ESI-) *m/z* calcd for I^- 126.9, found *m/z* 127.2 [I^-].

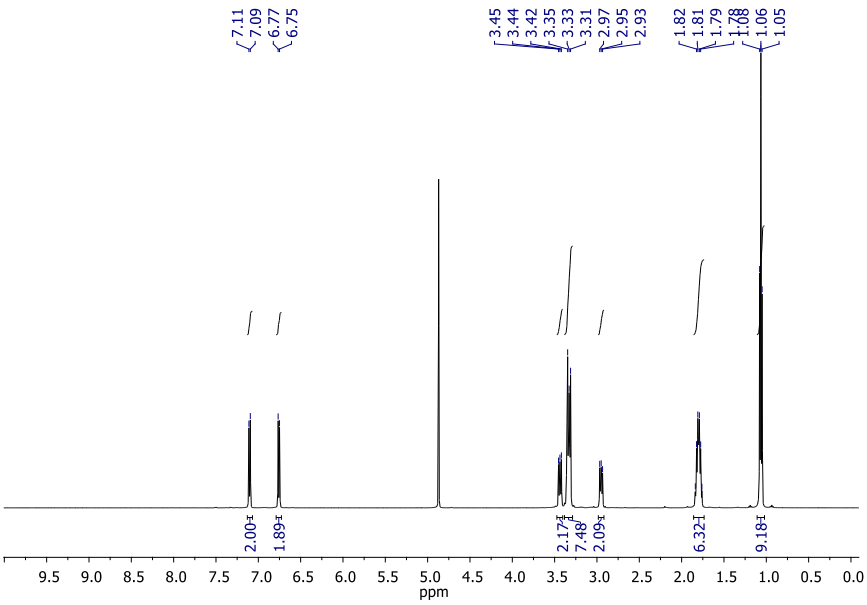

Figure 5.6. ^{1}H-NMR spectra of 4 in CD_3OD.

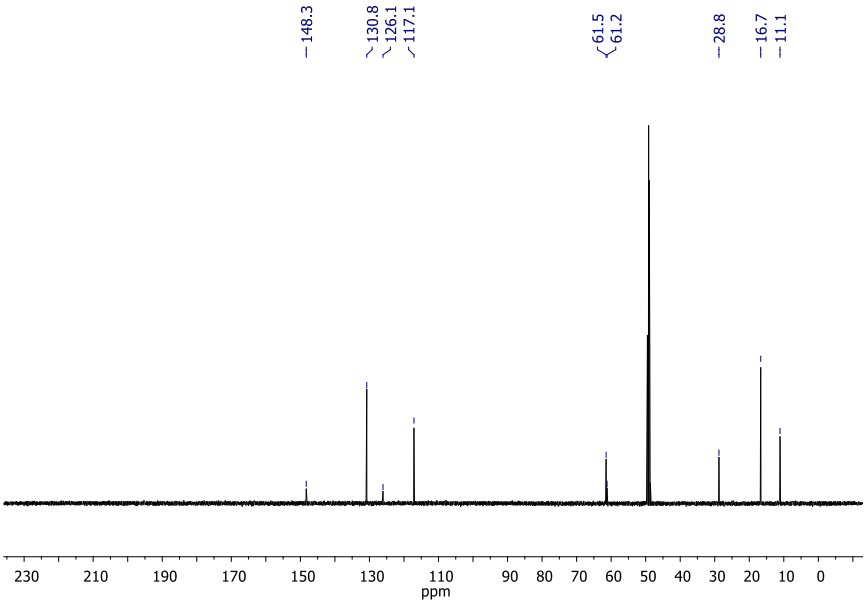

Figure 5.7. ^{13}C-NMR spectra of 4 in CD_3OD.

4-aminophenethyltripropyl ammonium hydroxide (**5**)

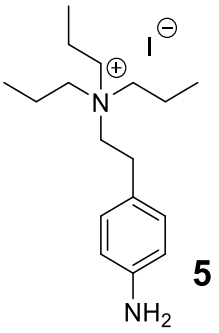

5

For the anion exchange process, KOH 1 M (5 ml) were passed through 2 ml of Dowex® resin (chloride form, 100-200 mesh). Next, the resin was washed with deionised water until its neutralisation. Then, a solution of product **4** (0.07 M) in H_2O/MeOH 4/1 was passed slowly through the resin and the resin was eventually washed with H_2O/MeOH 4/1 (20 ml). Finally, the solvent was eliminated under reduced pressure affording product **5** as a greenish product (0.29 g, 55 %). ^{1}H NMR confirmed the identity of product **5**. **MS** (ESI+) *m/z* calcd for $C_{16}H_{14}N_2O_2^+$ 263.2, found *m/z* 263.6 $[M]^+$, MS (ESI-) absence of I^-.

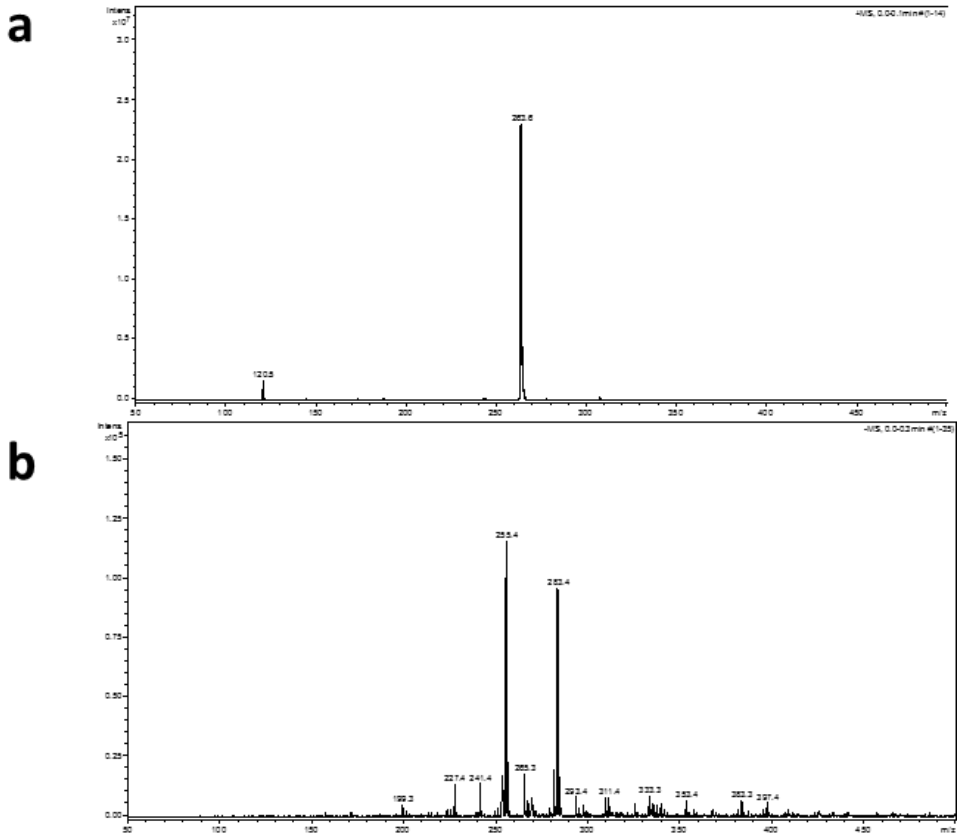

Figure 5.8. MS spectra of 5: (a) positive; and (b) negative mode showing the absence of iodide.

^{L}Leu-^{D}Phe-^{D}Phe (SPPS)

^{L}Leu-^{D}Phe-^{D}Phe was synthesised following Fmoc-based SPPS under dry and inert atmosphere. The swelling of the resin (2-chlorotrityl, 5 g) was done in dichloromethane (20 ml). Then $SOCl_2$ (0.4 ml) was added and the reaction was stirred under an Ar flow for 1 h. After that, the resin was washed with DMF (3 x 15 ml) and dicloromethane (3x 15 ml). Next, a solution of Fmoc-^{D}Phe-OH (2 g, 5.2 mmol), DIPEA (4.5 ml, 25.9 mmol) in DMF/dichloromethane 3/1 was added to the reactor and the reaction was stirred for 1.5 h. Then, MeOH (1 ml) was added before washing the reaction with DMF (3 x 15 ml) and dicloromethane (3x 15 ml). For the deprotection, piperidine 25 % in DMF (5 ml) was added to the reactor and was stirred at room temperature for 20 min. Then reaction was washed with DMF and dichloromethane. For the first coupling, Fmoc-^{D}Phe-OH (2.905 g, 7.5 mmol), DIPEA 1 M in DMF (6 ml), HBTU (2.275 g, 6 mmol) in DMF were ultrasonicated until the solution was clear and the mixture was added to the reactor and the coupling was stirred at room temperature for 1 h. Then, the crude was washed and deprotected as in the previous step. The coupling and deprotection of the last amino acid and was done exactly in the same way that the first coupling but adding Fmoc-^{L}Leu-OH (2.650 g, 7.5 mmol) instead of Fmoc-^{D}Phe-OH. Eventually, a solution of TFA/dichloromethane/H_2O/TIPS 49/49/1/1 (25 ml) was added to cleave the peptide from the resin. After 2 h of cleavage the solution was drain from the reactor and the solvent was evaporated under an air stream. The crude was purified by reversed-phase HPLC (Waters). The HPLC was equipped with a semi-preparative column C18 and a photodetector at 214 and 254 nm. For the solvent a mixture of CH_3CN:H_2O following the program: t = 0-2 min, 25% CH_3CN, t = 25 min, 95 % CH_3CN (t_R = 10-11 min). The peptide was freeze-dried and its identity was confirmed by ^{1}H-NMR, ^{13}C-NMR and ESI-MS. **^{1}H NMR** (500 MHz, DMSO-d_6) δ (ppm) 8.73 (d, *J* = 8.5 Hz, 1 H, NH), 8.62 (d, *J* = 8.6 Hz, 1 H, NH), 7.98 (broad s, 3 H, NH_3), 7.32 – 7.16 (m, 10 H, Ar), 4.72 (ddd, *J* = 10.6, 8.6, 4.5 Hz, 1 H, αCH), 4.47 (dt, *J* = 13.8, 6.8 Hz, 1 H, αCH), 3.64 (t, *J* = 7.2 Hz, 1 H, αCH), 3.11 (dd, *J* = 4.4 Hz, *Jgem* = 13.7 Hz, 1H, βCH_2), 2.95 (dd, *J* = 6.7 Hz, *Jgem* = 13.7 Hz, 1 H, βCH_2), 2.65 (dd, *J* = 7.8 Hz, *Jgem* = 13.7 Hz, 1 H, βCH_2), 2.78 (dd, *J* = 10.7 Hz, *Jgem* = 13.6 Hz, 1 H, βCH_2), 1.16 – 1.06 (m, 3 H, 2 x βCH, γCH_2), 0.68 (dd, *J* = 5.7 Hz, 6 H, 6 x δCH_3). **^{13}C NMR** (125 MHz, DMSO-d_6) δ (ppm) 172.7, 171.2, 168.7 (3 x CO); 137.5, 137.4, 129.3, 129.1, 128.3, 128.0, 126.5, 126.3 (Ar); 53.7, 53.6, 50.6 (3

x αC); 40.3, 38.1, 36.6 (3 x βC); 23.1, 22.5 (2 x γC); 21.7. (δC). **MS** (ESI): m/z 426.2 $[M+H]^+$ 448.2 $[M+Na]^+$ $C_{24}H_{31}N_3O_4$ requires 425.2.

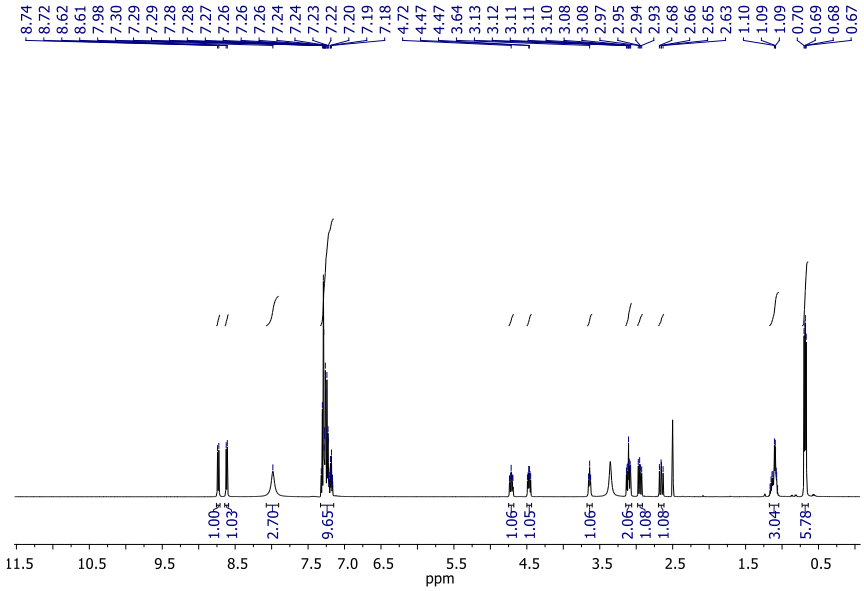

Figure 5.9. ^{1}H-NMR spectra of ^{L}Leu-^{D}Phe-^{D}Phe in DMSO-d$_6$.

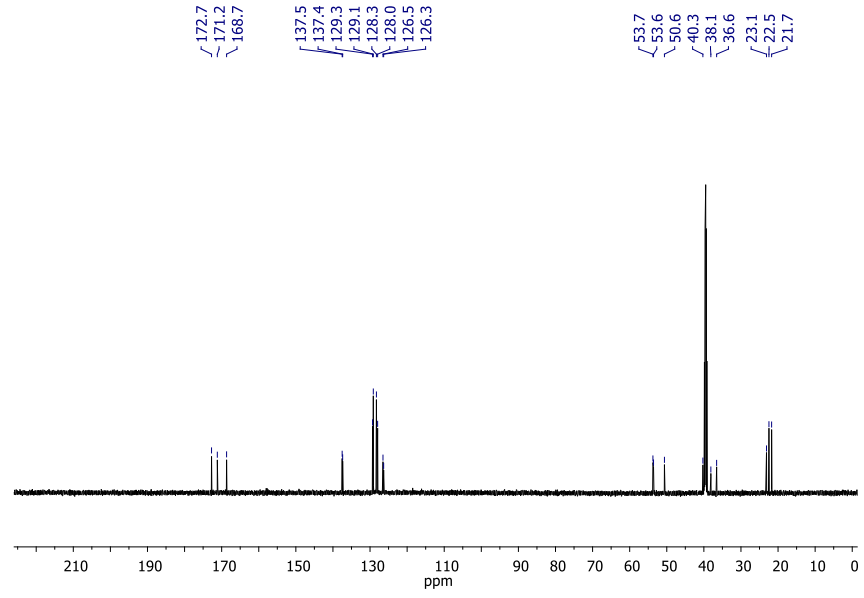

Figure 5.10. ^{13}C-NMR spectra of ^{L}Leu-^{D}Phe-^{D}Phe in DMSO-d$_6$.

5.2.2. Functionalisation of CNS

Short-Ox-MWCNTs

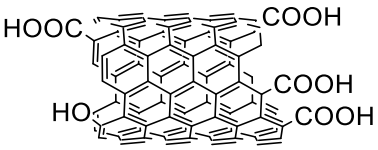

short-ox-MWCNTs

4 ml of HNO_3 (69 %) and 12 ml of H_2SO_4 (95 %) were mixed in a round bottom flask. Then, 100 mg of pristine MWNTs were added on top. The resulting mixture was sonicated for 5 h at room temperature. After that, the reaction was quenched with cold water (200 ml). The crude was filtered through Millipore membrane (JHWP, 0.45 µm) and washed with deionized water till neutralisation of the washings. The black powder was finally washed with MeOH and dried with Et_2O affording 99 mg of Short-Ox MWCNTs (TGA weight loss at 600 ^oC: 10 %).

Long-Ox-MWCNTs

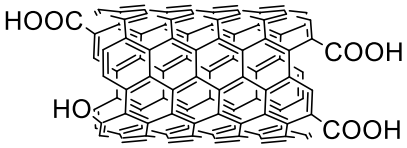

long-ox-MWCNTs

100 mg of pristine MWCNTs were sonicated in 100 ml for 3 h at room temperature. After that, the reaction was quenched with cold water (200 ml). The crude was filtered through Millipore membrane (JHWP, 0.45 µm) and washed with deionised water till neutralization of the washings. The black powder was finally washed with MeOH and dried with Et2O affording 100 mg of long-Ox MWCNTs (TGA weight loss at 600 ^oC: 3.5 %).

Phenol-MWCNTs

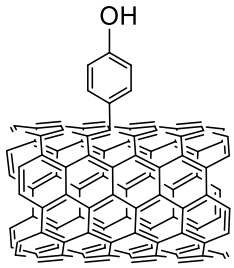

phenol-MWCNTs

100 mg of p-MWNTs were sonicated in 100 ml of deionized water for 15 min. Then, 4-aminophenol (272 mg, 2.5 mmol) were added and the mixture was sonicated again for 5 min. Finally, isopentyl nitrite (1.75 ml, 13.0 mmol) were added and the reaction was stirred at 80 ºC for 16 h. Once the reaction cooled down, the crude was filtered through a Millipore membrane (JHWP, 0.45 µm). The black powder was purified through several cycles of sonication/filtration with DMF, deionized water, EtOH and MeOH till the washings were clean. Eventually, the black powder was dried with Et2O affording 104 mg of phenol-MWCNTs (TGA weight loss at 600 ºC: 7.4%).

Isophthalic-MWCNTs

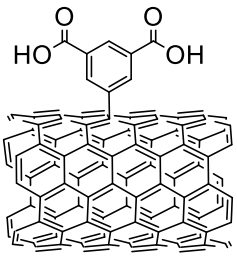

isophthalic-MWCNTs

100 mg of p-MWNTs were sonicated in 100 ml of deionized water for 15 min. Then, 5-aminoisophthalic acid (425 mg, 2.5 mmol) were added and the mixture was sonicated again for 5 min. Finally, isopentyl nitrite (1.75 ml, 13.0 mmol) were added and the reaction was stirred at 80 ºC for 16 h. Once the reaction cooled down, the crude was filtered through a Millipore membrane (JHWP, 0.45 µm). The black powder was purified through several cycles of sonication/filtration with DMF, deionized water, EtOH and MeOH till the washings were clean. Eventually, the black powder was dried with Et2O affording 102 mg of isoph-MWCNTs (TGA weight loss at 600 ºC: 6 %).

Isophthalic-G

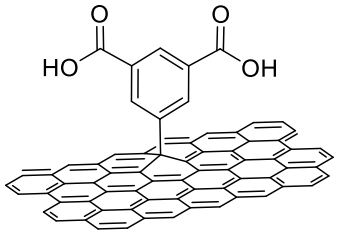

isophthalic-G

In a round-bottom flask, 35 ml of G dispersed in water (0.42 g l^{-1}) and 5-aminoisophthalic acid (680 mg, 3.775 mmol) were sonicated for 1 min. Then, isopentyl nitrite (0.35 ml, 2.5 mmol) was added and the mixture was microwave-irradiated at 80 ºC setting the maximum irradiation power at 100 W. After 30 min, a second aliquot of isopentyl nitrite (0.35 ml, 2.5 mmol) was added and the reaction was irradiated at 80 ºC for 1 h setting the maximum power at 30 W. Once the reaction cooled down, the crude was filtered through a Millipore membrane (JHWP, 0.45 μm). The black powder was purified through cycles of sonication/filtration with DMF, deionised water, EtOH and MeOH till the washings were clean. Eventually, the black powder was washed with Et_2O and dried under vacuum affording 15 mg of product. (TGA weight loss at 600 ºC: 12%).

Quaternary-G

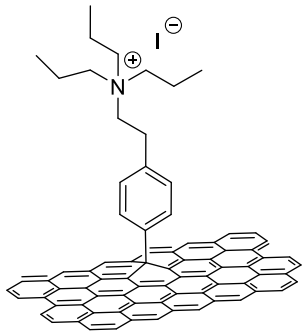

quaternary-G

In a round-bottom flask, 45 ml of G dispersion (0.84 g l^{-1}) and **4** (1.81 g, 4.62 mmol) were sonicated for 5 min. Then, isopentyl nitrite (0.35 ml, 2.5 mmol) was added and the mixture was irradiated with microwaves at 80 ºC setting the maximum irradiation power at 100 W. After 30 min irradiation, a second aliquot of isopentyl nitrite (0.35 ml, 2.5 mmol) was added and the reaction was irradiated at 80 ºC for 1 h setting the maximum power at 30 W. Once the reaction cooled down, the crude was filtered through a Millipore membrane (JHWP, 0.45 μm). The black powder was purified through several cycles of

sonication/filtration with DMF, deionized water, EtOH and MeOH till the washings were clean. Eventually, the black powder was washed with Et_2O and dried under vacuum affording 40 mg of quaternary-G (TGA weight loss at 600 ºC: 12%).

Quaternary(OH^-)-G

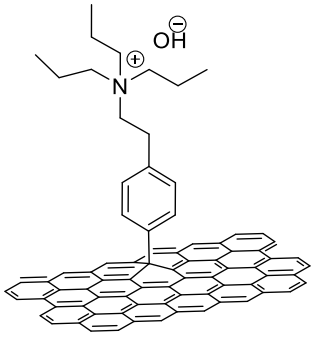

quaternary(OH^-)-G

In a round-bottom flask, 45 ml of G dispersion (0.84 g l^{-1}) and **5** (1.31 g, 4.68 mmol) were sonicated for 5 min. Then, isopentyl nitrite (0.35 ml, 2.5 mmol) was added and the mixture was irradiated with microwaves at 80 ºC setting the maximum irradiation power at 100 W. After 30 min irradiation, a second aliquot of isopentyl nitrite (0.35 ml, 2.5 mmol) was added and the reaction was irradiated at 80 ºC for 1 h setting the maximum power at 30 W. Once the reaction cooled down, the crude was filtered through a Millipore membrane (JHWP, 0.45 µm). The black powder was purified through several cycles of sonication/filtration with DMF, deionized water, EtOH and MeOH till the washings were clean. Eventually, the black powder was washed with Et_2O and dried under vacuum affording 40 mg of quaternary(OH^-)-G. (TGA weight loss at 600 ºC: 14%).

Blank-G

In a round-bottom flask, 17 ml of G dispersion (0.84 g l^{-1}) were sonicated for 5 min. Then, the mixture was irradiated with microwaves at 80 ºC setting the maximum irradiation power at 100 W. After 30 min irradiation, a second irradiation step was done at 80 ºC for 1 h setting the maximum power at 30 W. Once the reaction cooled down, the crude was filtered through a Millipore membrane (JHWP, 0.45 µm). The black powder was purified through cycles of sonication/filtration with DMF, deionised water, EtOH and MeOH till the washings were clean. Eventually, the black powder was washed with Et_2O and dried in vacuo affording 13 mg of product. (TGA weight loss at 600 ºC: 3%).

O_3 treatment of CNF

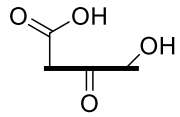

ox-CNT fibre

The functionalization of CNF was performed using a Cleaner ProCleaner™ Plus on top of the quartz support provided by the manufacturer. Initially, CNT ropes were subjected to different reaction times to follow the(*i.e.* λ = 185 nm) that produces ozone from atmospheric oxygen (*i.e.* there is no gas flowing kinetics of the process (*i.e.* 5 min, 15 min, 30 min or 2 h).

Ox-MWCNTs@PDA

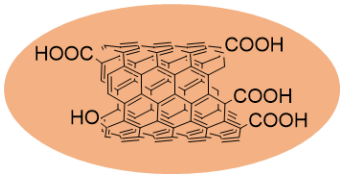

ox-MWCNTs@PDA

Dopamine hydrochloride (400 mg, 2.11 mmol) and ox-MWCNTs (10 mg) were ultrasonicated in deionized water (40 ml) for 30 min. Tris buffer pH 8.5 (10 ml, 50 mM) was then added and the reaction was stirred for 16 h at room temperature. The crude was filtered through a Millipore membrane (JHWP, 0.45 µm) and washed with cycles of ultrasonication/filtration in water (2 x 50 ml) and ethanol (2 x 50 ml). The black product was rinsed with Et_2O and dried under vacuum affording 43 mg of ox-MWCNTs@PDA. (ox-MWCNTs:PDA 21.9:78.1)

Ox-MWCNTs@PDA_{700}

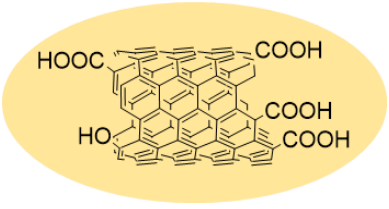

ox-MWCNTs@PDA_{700}

Ox-MWCNTs@PDA (154 mg) were annealed at 700 ^oC under Ar for 3 h to afford Ox-MWCNTs@PDA_{700} (91 mg). No further purification was required (59 %).

Ox-CNHs

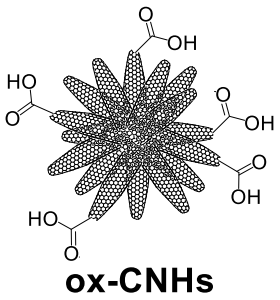

Pristine CNHs (100 mg) were sonicated in 100 ml of HNO_3 (69 %) for 15 min. The resulting dispersion was stirred for 3 h at 35 °C. Cold water (200 ml) was then added to the reaction and the crude was filtered through a Millipore membrane (JHWP, 0.45 µm) and washed with deionised water till neutralisation of the washings. The black powder was finally washed with MeOH and dried with Et_2O affording 99 mg of ox-CNHs (TGA weight loss at 600 °C: 10%).

Ox-CNHs@PDA

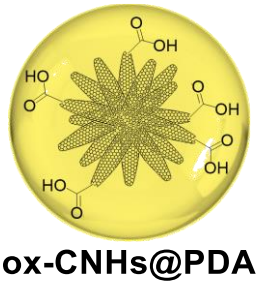

Dopamine hydrochloride (400 mg, 2.11 mmol) and ox-CNHs (10 mg) were ultrasonicated in deionized water (40 ml) for 30 min. Tris buffer pH 8.5 (10 ml, 50 mM) was then added and the reaction was stirred for 16 h at room temperature. The crude was filtered through a Millipore membrane (JHWP, 0.45 µm) and washed with cycles of ultrasonication/filtration in water (2 x 50 ml) and ethanol (2 x 50 ml). The black product was rinsed with Et_2O and dried under vacuum affording 50 mg of ox-CNHs@PDA (ox-CNHs:PDA 21.9:78.1).

Ox-CNHs@PDA$_{xxx}$

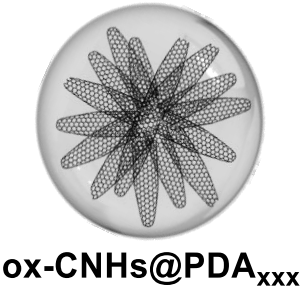

Ox-CNHs@PDA (xx mg) were annealed under Ar at 700 ºC, 800 ºC or 900 ºC, for 3 h to afford Ox-CNHs@PDA$_{700}$, Ox-CNHs@PDA$_{800}$ Ox-CNHs@PDA$_{900}$, respectively. No further purification was required.

Table 5.1. Yield of the calcination step at the different temperatures.

Sample	Initial mass (mg)	Final mass	Yield (%)
Ox-CNHs@PDA$_{700}$	140	92	66
Ox-CNHs@PDA$_{800}$	73	42	59
Ox-CNHs@PDA$_{900}$	64	27	42

GO

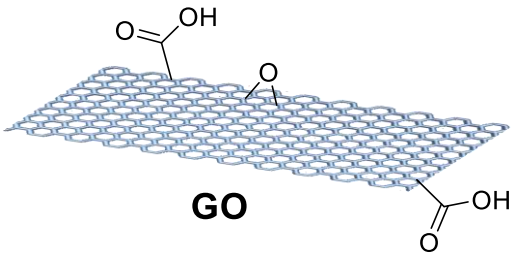

In a round bottom flask 100 ml volume containing $K_2S_2O_8$ (200 mg, 0.37 mmol), P_2O_5 (100 mg, 0.35 mmol) and H_2SO_4 (10 ml), pristine G (200 mg) was added. The reaction was stirred at 80 ºC for 4 h. The crude was cooled down, diluted with deionised water (50 ml), filtered through Millipore membrane (JHWP, 0.45 µm) and wash with deionised water until neutralisation of the washings. The black powder collected from the Millipore membrane was transferred into a round bottom flask and $KMnO_4$ (100 mg, 0.63 mmol) and H_2SO_4 (20 ml) were added at 0 ºC. The mixture was stirred at 35 ºC for 2 h. After that, deionised water (20 ml) and H_2O_2 30 % (2.4 ml) were added and the reaction was stirred for 15 min. The crude was filtered through Millipore membrane (JHWP, 0.45 µm) and washed with HCl 1 M (100 ml) and deionised water till neutralisation of the

washings. Eventually the black powder was washed with MeOH and dried with Et_2O affording 217 mg of GO (TGA weight loss at 600 ºC: 10%).

Ox-SWCNTs

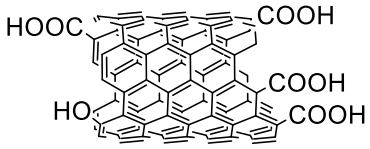

ox-SWCNTs

0.8 ml of HNO_3 (69 %) and 2.4 ml of H_2SO_4 (95 %) were mixed in a round bottom flask. Then, 20 mg of pristine SWCNTs were added on top. The resulting mixture was stirred at 60 ºC for 30 min. sonicated for 5 h at room temperature. After that, the reaction was quenched with cold water (100 ml). The crude was filtered through Millipore membrane (JHWP, 0.45 µm) and washed with deionized water till neutralization of the washings. The black powder was finally washed with MeOH and dried with Et_2O affording 19 mg of ox-SWCNTs (TGA weight loss at 600 ºC: 27%).

5.2.3. CNS-inorganic hybrids

5.2.3.1. Zeolites

The zeolitic materials were prepared by Dr. Paul Gebhardt at the University of Munster (Germany). Briefly, 731 µl of tetraethoxysilane (TEOS) and 28.3 µl of tetrabutyl titanate (TBOT) were added to 5 ml of EtOH (abs.) to yield a clear solution that was stirred for 4 h. 660 µL of this solution, corresponding to 30 mg of zeolite considering a quantitative yield, were added to 10 mg of functionalised G (*i.e.* quaternary-G or quaternary(OH^-)-G and stirred for 20 h, then aged (at r.t., without stirring) for 6 h. The black mixture was transferred into a teflon-lined autoclave and heat-treated at 150 °C for 15 h. After that, the solid material was collected via centrifugation at 4000 rpm for 10 min and collected in EtOH. The material was dryed at 80 °C. Eventually, the materials were calcined at 600 ºC for 5 h.

5.2.3.2. TiO_2 electrospun fibres

The electrospun fibres were prepared by Alicia Moya at IMDEA Materials Institute (Getafe, Spain).[8] Briefly, a homogeneous solution was prepared mixing PVP 10 wt. % in ethanol, titanium ethoxide 63.5 wt. %, 5-6 drops of acetic acid and a solution of the corresponding f-CNS when applicable. This solution was electrospun in a Nanon 01A, MECC Co., Ltd., at 2 ml min^{-1}, with an applied potential of 18 kV. The calcination of the samples was done first under air at 400 ºC for 150 min and then under Ar at 500 ºC for 60 min.

5.3. References

(1) V. Reguero, B. Alemán, B. Más, J. j. V. *Chem. Mater.* **2014**, *26*, 3550–3557.

(2) Seah, M. P.; Gilmore, I. S.; Spencer, S. J. *J. electron Spectrosc.* **2001**, *120*, 93–111.

(3) Tanuma, S. *Surf. interface Anal.* **2015**, *38*, 178–180.

(4) Spurr, R. A.; Myers, H. *Anal. Chem.* **1957**, *29* (5), 760–762.

(5) Patterson, A. L. *Phys. Rev.* **1939**, *56*, 978–982.

(6) Victoria, M.; Melchionna, M.; Giuliani, A.; Nasi, L.; Tavagnacco, C.; Prato, M.; Fornasiero, P. *Sensors Actuators B* **2017**, *239*, 923–932.

(7) Perron, V.; Abbott, S.; Moreau, N.; Lee, D.; Penney, C.; Zacharie, B. *Synthesis* **2009**, *2*, 283–289.

(8) Moya, A.; Cherevan, A.; Marchesan, S.; Gebhardt, P.; Prato, M.; Eder, D.; Vilatela, J. J. *Appl. Catal. B Environ.* **2015**, *179*, 574–582.